JPL Quarterly Technical Review

Volume 2 April 1972 Number 1

Contents

JPL Quarterly Technical Review Volume 2, Number 1 April 1972

Index: Apollo Project, lunar interior, lunar surface, meteors, soil sciences, solar phenomena

A View of the Moon

R. G. Brereton

Advanced Technical Studies Office

Apollo information on lunar science is now voluminous, and NASA has recognized the need for a task that would collate and interpret Apollo results and provide a synthesized view of the Moon. The initial conclusions of such a task carried out at JPL are reviewed here. In summary, whereas most of the Earth's surface is highly mobile because of dynamic endogenic and exogenic processes, the lunar surface is old, stable, and coexists with the ambient environment of space.

The Moon is essentially quiet seismically, does not have a heavy solid or liquid core, and has a much cooler internal temperature than Earth. The lunar lithosphere is both old and strong and appears to have been little modified by volcanic or tectonic activity for more than three billion years.

Introduction

This paper presents some of the pertinent facts of our present knowledge about the Moon. From these facts conclusions about the Moon's origin, history, structure, and processes can be deduced. The most recent source for lunar scientific information was the Third Lunar Science Conference held at the Manned Spacecraft Center, Houston, Texas, January 10 through January 13, 1972. Proceedings of the First Lunar Science Conference, held in 1970, have now been published by Pergamon Press (Reference 1). Summaries of the scientific achievements of Apollos 11 through 15 have been published in *Science* (Reference 2), and special NASA publications (References 3–6).

Geology and Lunar Rocks

Geomorphically the surface of the Moon can be divided into the dark mare regions and the lighter-appearing highland regions. The Apollo 11 and 12 samples, as well as the Russian Luna 16 samples, were taken from the dark mare regions. Apollo 14 Fra Mauro samples appear to represent material that was gouged out of the lunar crust during the event that formed the Imbrium Basin. It is highly brecciated and broken, and it is not like the mare basalts in either composition or texture. The Apollo 15 rocks from around the Hadley Rille are typically basaltic; however, rocks collected

closer to the Apennine Front are breccias like the Apollo 14 rocks but with differences in composition and texture.

The surface of the Moon at the Apollo, Surveyor, Luna 16, and Luna 17 landing sites consists of a regolith of fine particulate material and rocks of varying size. Weathering is occurring due to the impacts of primary and secondary particles, and so with prolonged exposure sharp features become subdued; rocks are progressively comminuted; bright rays fade; and the regolith thickens. Small primary impacts with velocities of greater than 2 km/s are responsible for the microscopic glass-lined "zap" craters found on the surfaces of the returned lunar rocks. Larger primaries may have caused the meter-sized craters with glass on the bottom. The round glass spherules in the lunar soil are probably melted crater ejecta that froze in flight. Green glassy spherules can be recognized in all the Apollo 15 soil samples. Some rocks are also partly covered with glass that hit the rock while molten and froze later. The seismometer data indicate that impacts are still occurring.

The fragmental debris layer comprising the lunar "soil" or regolith varies from perhaps one to several meters deep in the mare landing sites. Most of the debris layer is comprised of material from local mare rocks; however, evidence for a foreign component, possibly derived as ejecta from distant impacts, is very strong. The regolith at the Fra Mauro site is considerably thicker than at the mare sites. The Active Seismic Experiment suggests a depth of 8½ m. The greater depth of soil here probably represents a greater age for Fra Mauro than for the maria; however, the fragmental nature of the whole Fra Mauro formation has probably made it more susceptible to lunar surface comminution processes. The regolith at the Apollo 15 site ranged in thickness from a surface exposure of bedrock along the rim of Hadley Rille to several tens of meters in areas receiving debris from the Apennine mountains. The surface exposure of bedrock at the Apollo 15 site was of great interest, as this was the first time such a feature has been accessible to direct sampling. The soil from the Hadley Rille area is composed primarily of reworked mare-type basaltic material, but the soils from sites closer to the Apennine Front appear to be composed of debris from bedded deposits with very little mare material evidenced.

The carbon concentration in lunar soils appears to be of the order of 200 parts/10^6 with much of the carbon appearing in the form of carbon monoxide. Analysis by several techniques has failed to show organic compounds in lunar soils. No viable organism has been found in the lunar samples, and there is no evidence of fossil material. Evidently the lunar regolith has always been devoid of life.

The Apollo 11 samples from Tranquillity Base consisted of basaltic igneous rocks, soil, and microbreccias, which are a mechanical mixture of the soil and small rock fragments compacted into a coherent rock. The age of the igneous material is about 3.7 billion years. With regard to the major elements and texture, the lunar igneous material resembles terrestrial basalts, with the notable exceptions of high titanium and iron, and low silica and sodium content. Relative to both cosmic and terrestrial abundances,

lunar basalts are depleted in water and other volatile elements and contain a higher proportion of refractory elements, including titanium and rare-earth elements. The main mineral phases are pyroxene, plagioclase, olivine, and ilmenite. The plagioclase in the Moon basalts, however, is almost pure anorthite, whereas the plagioclase in terrestrial basalts is a solid solution series formed of a mixture of albite and anorthite. Laboratory studies indicate that the magma from which the lunar basalts formed was very dry and highly reducing. Crystallization occurred quickly over the temperature range of 1100 to 1000°C. The viscosity of the magma was an order of magnitude less than terrestrial basalts, so it probably flowed very easily. The constant association of ilmenite, troilite, and native iron in these rocks suggests that these minerals are an equilibrium assemblage, and one that must have formed in a strongly reducing environment with low oxygen fugacity. This information, in conjunction with the conspicuous absence of any hydroxyl-bearing minerals, very low alkali content, and probable high temperature of the magma, seems to indicate that the chemical composition of the source of the lunar mare basalts was significantly different from those that characterize terrestrial basalts.

The Apollo 12 samples from Oceanus Procellarum are very similar to the Apollo 11 samples, with the major exceptions that they contain significantly less titanium and are approximately 0.5 billion years younger. Generally, the Procellarum basalts exhibit a greater range in mineral composition and texture than other mare basalts. This range in properties can be attributed to sampling from several chemically distinct basalt units that were emplaced sequentially, and cooled at different rates. Evidently the dark regions of the Moon, the mare basins, were formed from many individual lava flows or near surface intrusions of basaltic material some 3 to 4 billion years ago.

The source of the mare basalts is a key scientific question. Studies of the systematics of both major and minor element distributions indicate that the lunar basaltic lava was generated as a partial melt of a primordial material several hundred kilometers deep in the lunar interior. Since the basalts probably cannot exist at depths greater than ~300 km without undergoing a phase transformation to a more dense mineral assemblage (one that is too dense for the Moon), it seems that most of what has been returned from the Moon so far probably represents a minute differentiated fraction of the lunar interior composition.

The Apollo 14 rocks are quite different from the Apollo 11 and 12 rocks, and also from the Luna 16 material, in color, texture, age, and composition. In general, the Fra Mauro sample is characterized by a scarcity of crystalline igneous rocks, much clastic material or breccia, and a lighter color. It is higher in silicon and aluminum and lower in iron, titanium, and magnesium than the basalts. The crystallinity and texture observed in many of the fragmental rocks is compatible with a derivation from a very large impact event in which much shock and subsequent annealing took place within a thick hot ejecta blanket or base surge. Aside from the shock and annealing effects, however, the differences in mineral and chemical composition

between the Apollo 14 material and the mare basalts are such that the Apollo 14 rocks must be regarded as representing a distinct type of lunar material. Whether or not the Apollo 14 rocks represent a sample from an extensive and homogeneous lunar source material cannot yet be specified. The sampling of other ejecta blankets of large events would be required to solve this problem.

Certainly the Fra Mauro material is not representative of upland material. The Surveyor 7 automated chemical analysis of upland material near Tycho shows the Fra Mauro material to be richer in titanium, iron, magnesium, and silicon. Orbital remote sensing instruments also show a difference.

The Apollo 15 samples can be generally classified as basalts, breccias, and soil. The basalts predominate at the rille collection sites, whereas breccias predominate at the sites closer to the Apennine Front. As indicated earlier, the soil in the area of the Hadley Rille appears to represent comminuted basalt, whereas the soils collected from sites closer to the Apennine Front are believed to be composed of debris from earlier bedded deposits.

The apparent bedding or terracing observed by the Apollo 15 astronauts, both from orbit and from the lunar surface, certainly suggests a layered Moon. Scott and Irwin vividly described and photographed the layering along the sides of the scarp of 4-km (13,000-ft) Hadley Delta, 4.6-km (15,000-ft) Mt. Hadley, and the sides of Hadley Rille. Similar features were observed by Worden in the central peak of the giant farside crater Tsiolkovsky, and they have been inferred from earlier orbiter photography. Whether this apparent bedding results from sedimentary processes, individual lava flows, or represents some type of foliation or lineation structure, is not yet certain. As the maria are believed to be layered by numerous lava flows and indurated regolith, so may the ancient pre-mare crust be layered, and the Imbrium event has exposed a great scarp of this rock that is more than 4 billion years old.

One of the most important contributions of Apollo to lunar science is that it has made possible the absolute age-dating of selected lunar material. Prior to the Apollo sample return flights, the energy-frequency distribution of meteorites and crater count statistics were used to determine the "relative" age and erosion rate for lunar stratigraphic units. Although this data is useful, it needs to be tied together by absolute age-dates. Isotopically derived age-dates, using a variety of techniques, have now been determined for several lunar events and rock units. The age of the Tranquillitatis basalts is reliably accepted as 3.7 billion years, the Procellarum basalts 3.2 billion years, while the Imbrium event, which scattered the Fra Mauro rocks, appears to date at 3.9 billion years.

The oldest and most complex rock yet acquired from the mare areas (Apollo 12, Rock 13) is composed of angular fragments of basalt contained in a matrix of lighter colored material, parts of which are granitic in composition. It is of interest in terrestrial geologic studies that granitic material apparently can form from igneous processes without going through

a geosyncline cycle of sedimentation and subsequent melting. The lighter material in Rock 12013 appears to have invaded and partially assimilated the basalt. The event occurred about 4 billion years ago and reset the radioactive clocks for both the basalt and the invading material.

The oldest rock yet acquired and dated, the so-called "genesis rock," was picked up by astronaut Scott on the second extravehicular activity (EVA) of the Apollo 15 mission while he and Irwin were exploring along the base of the Apennine Mountains. The rock has an apparent age of 4.15 billion years and is close to anorthosite in composition. The "Great Scott" basalt apparently dates with the Procellarum basalts at about 3.2 billion years old.

Our best model of lunar history suggests a major lunar-wide chemical fractionation at about 4.6 billion years ago. By analogy with meteorite samples and the Earth, both of which apparently formed approximately 4.6 billion years ago, one concludes that the Moon formed at the same time as these other bodies. It is believed that chemical differentiation formed an ancient low-density crust on the Moon. The uplands on the frontside and much of the backside are comprised of this material and form the oldest observable lunar terrain. Great meteorites impacted the ancient surface and formed the mare basins. The Imbrium event is dated by the Fra Mauro ejecta blanket which apparently had its radioactive time clock reset at about 3.9 billion years ago. Mare Humorum appears to be older than this, whereas the west-limb basin Mare Orientale appears to be younger. At any rate, the major basins on the Moon appear to date from the time of crust formation to nearly 4 billion years ago.

Sometime after the basins were formed, they were filled with basaltic lava. Basin filling was accomplished by many thin very fluid surface lava flows or shallow intrusions, and these may possibly alternate with welded regolith. The mare lava-flows were generated millions of years subsequent to basin formation and represent a major period of lunar volcanism, lasting from approximately 3.7 billion years ago to perhaps 3 billion years ago.

Crater count statistics suggest that many upland craters were filled with a higher albedo material, with morphological expressions similar to the mare basalts, prior to the major episodes of mare basalt flooding. The Descartes mission of Apollo 16 will be targeted to sample this type of material.

Geophysics

We have approximately two years of seismic data on the Moon. The Apollo 11 seismometer worked for about 21 days to give the first clue to the unusual seismic environment of the Moon. The Apollo 12 seismometer has been operating since November 1969. It was joined by the Apollo 14 instrument in February 1971, and the Apollo 15 instrument in early August 1971, to form a three-station array operating simultaneously on the Moon. The Apollo 12 and 14 instruments are separated by 181 km, while the Apollo 15 instrument is located approximately 1100 km to the north. This network of three stations now makes it possible to determine the distance and

location of both meteorite impacts and moonquakes, and it also provides more qualitative data for studying lunar interior structure and seismicity.

Several hundred seismic signals resulting from moonquakes and meteorites have now been observed. In addition to the natural events, several rather large artificial seismic events have been produced by the impact of the Apollo 12 lunar module (LM), the Apollo 13 S-IVB, the Apollo 14 S-IVB and LM, and the Apollo 15 S-IVB and LM. The overall characteristics of the signal for these events are not only mutually similar but also similar to many natural events. Generally the signals begin small and reach a maximum intensity after several minutes. The signals for the larger S-IVB impacts as compared to those for the LM are perhaps 20 to 30 times larger and 4 times longer (approximately 4 hours versus 1 hour). Similar signals on Earth would last about 5 min. Apparently the duration of a lunar seismic signal can be related to the magnitude of the source.

A significant fact revealed by the seismic data is that the Moon is seismically quiet as compared to the Earth. The detected average over the 24 months of operation is approximately 1.5 event per day (1 to 2 magnitude on the Richter scale). On Earth, several hundred such events occur every day. Some of these lunar events are caused by moonquakes and some by meteorites. There appears to be a correlation between events and the Moon's closest approach to the Earth. The absence of significant seismic activity within the Moon implies the absence of tectonic processes similar to those associated with major crustal movements on the Earth, and further implies lower specific thermal energy in the lunar interior than is present in the interior of the Earth.

The lunar seismic net has now located about a dozen epicenters for moonquakes. The depth of focus for one moonquake area now appears to be between 700 and 800 km. The deepest known earthquakes are at a depth of about 700 km. Moonquakes are triggered by the tidal effects of the Earth, but what processes are operating deep within the Moon to cause an apparently linear buildup of stress is unknown. The association of some small moonquakes into "swarms" or groups with characteristics similar to terrestrial volcanic earthquakes does suggest, however, that volcanic activity is still taking place on the Moon, and this may be related to the buildup of crustal stress.

A second significant fact is the ease with which the Moon transmits seismic energy. The Moon is a very efficient conductor of seismic energy, and its transmission properties are far superior to those of the Earth. For example, the impact of the Apollo 15 LM (26.36°N, 0.25°E) was detected at the Apollo 15 seismometer located some 93 km away, but it was also detected at both the Apollo 12 and 14 stations located more than 1000 km to the south. On the Earth, signals from such an impact would not be detected at a range of more than about 100 km.

The impact of a meteorite onto the lunar surface gives a seismic signature similar to those observed for the LM and S-IVB impacts. Many of these have

now been recorded and a cumulative mass spectrum for meteoroids impacting the Moon has been constructed from the data. It seems that the total meteoroid mass flux is a factor of 20 less than previously estimated. In terms of size and energy of the impacting bodies, these data indicate that the Moon gets several grapefruit-size meteorites every year, and approximately one impact per year with kinetic energy equal to that of the S-IVB impact. Smaller impacts, of course, are occurring. These impacts probably represent the primary agent for tilling the lunar regolith and gradually aging and subduing the outline of surface features.

The overall planetary magnetic field of the Moon is now very small. This was suspected from both theory and earlier data from automated probes, but it remained to be proven by Apollo. The Apollo 15 subsatellite magnetometer data, and also the Explorer 35 orbital magnetometer measurements, indicate a lunar magnetic field and perhaps as much as 3 gamma; however, localized fields that are much higher have been measured on the surface. It seems probable that the overall lunar magnetic field, as measured by orbiting spacecraft, is made up of localized fields caused by magnetized material that acquired remanence during an ancient lunar epoch when inducing fields were present at the Moon.

Measurements of the magnetic field on the lunar surface by the 3-component Apollo 12 magnetometer show a steady field of approximately 38 ± 3 gamma, and located within 200 km from the measuring site. The portable magnetometer used by the astronauts on Apollo 14 measured a steady magnetic field of 103 ± 5 gamma at a site near the LM, and a steady magnetic field of 43 ± 6 gamma 1.12 km distant from the first site along the traverse in the direction of cone crater. The steady magnetic field being recorded at the Apollo 15 site is apparently very small, measuring less than 10 gamma.

It seems quite probable that the lunar field as now observed by orbital and Apollo surface missions represents a fossil remnant of a stronger field originally frozen into the lunar lavas. Magnetic measurements on lunar samples indicate that they possibly cooled in a magnetic environment amounting to about one tenth of the present Earth's field—about 3000 gammas. The source of this ancient inducing field may have been a lunar magnetic field or electric currents from solar plasma.

Transient solar magnetic fields measured by the Apollo surface magnetometer have been analyzed to determine the electrical conductivity of a three-layered model of the Moon. Analysis of many transients indicates a best fit to the model for an outer nonconducting layer less than 87 km thick, an inner spherical shell between 1042 and 1651 km in radius, and a highly conducting inner core. Putting this in another way, the interplanetary magnetic field of the solar wind causes a potential difference between the dark and light side of the Moon, resulting in currents that may be as large as 100,000 A to flow in and through the Moon.

The magnetic signals generated from such currents can be interpreted in terms of the Moon's electrical conductivity, temperature, composition, and depth. An approximate calculation for an olivine Moon presently suggests a temperature gradient in the outer part of the Moon of 2°C/km and a maximum central temperature of about 1000°C. On Earth the average crustal gradient is approximately 30°C/km and the central temperature is of the order of 3000°K.

The Laser Ranging Retroreflector (LR3) at the Apollo 15 site is made up of 300 corner prisms. The Apollo 11 and 14 LR3 each have 100 corners. The McDonald Observatory is now ranging successfully on all three arrays. The Apollo 15 array is the key array in the network and is used first in each session, since it is more easily acquired and permits a quick calibration of the ground-based instrumentation, thus simplifying ranging to the other arrays. Recent returns from the Apollo 11 array indicate that there has been no measurable degradation to the reflector since its emplacement. Apollo 15 completed plans for emplacing this experiment, with retroreflectors displaced in both latitude and longitude on the lunar surface. The initial data from the Apollo 11 retroreflector provided ranging accuracies of a few meters, but continued observations using the three stations have reduced this to a few centimeters. The significance of these data is very great for providing information on the motions, interactions, and body physics of both the Earth and the Moon. These data may eventually provide a much better definition of the oscillation of the axis of the Earth (known as Chandler's wobble), and on the present rate of continental drift.

Several Apollo experiments are designed to provide information about the fields and particles environment of the Moon. We have already discussed the magnetometer data, but three other experiments—the Suprathermal Ion Detector Experiment (SIDE), the Solar Wind Spectrometer (SWS), and the Cold Cathode Gauge Experiment (CCGE)—also have provided important information.

The SIDEs, in addition to providing data on natural lunar ion phenomena, have proved to be so sensitive that they also detect ions generated by impact events. Thus impacts of all the Apollo stages, as well as a relatively large meteorite impact that was also recorded by the Apollo 14 seismometer, have now been studied. Of particular interest in the SIDE data is the reported detection of what is believed to have been a transient cloud of water vapor. The phenomenon was detected on both the Apollo 12 and 14 SIDE instruments. The cloud persisted for a period of about 14 hours, and seems to have occurred simultaneously with an extended period of moonquakes. It is speculated that the lunar quaking permitted water in some form to find its way to the surface where it was immediately vaporized in the lunar vacuum and subsequently ionized by solar radiation.

The Cold Cathode Gauge Experiment, also referred to as the lunar atmosphere detector, has produced some interesting data on the density of neutral atomic particles at the lunar surface and the variations in density that occur as a result of lunar phases, solar activity, meteorite impact and

perhaps surface gas venting. The instrument measures the neutral particle density and the ambient temperature and from this data the lunar atmospheric pressure can be calculated. Ambient pressure on the lunar surface appears to be about 6.7×10^{-10} N/m^2 (5×10^{-12} torr), however, there appear to be many transients in this value. Some of these pressure changes have been correlated with activities on the other particle detectors, and with seismic activities.

The surface SWS at the Apollo 12 Procellarum site has now been operating for approximately two years. It was joined by the Apollo 15 instrument in August 1971 to form a two-station array. Analysis of the SWS data shows that the plasma environment of the lunar surface changes during a lunation as a function of the positions of the Sun, Earth, and Moon. Four plasma regions or periods have now been recognized. Thus during two periods of a typical lunation the SWS instruments detect no plasma. One of these, called the lunar wake, occurs during the entire 14-day lunar night when the Moon itself shields the instrument site from the Sun. The second, lasting for 4.5 days, occurs when the body of the Earth is between the Moon SWS site and the Sun. In this configuration the geomagnetic tail region of the Earth excludes the bulk of the plasma. On either side of the tail region is a transition region where plasma that has been less strongly perturbed by the Earth's field is measured for a duration of about three days. Finally, there are five days when the observed plasma parameters are consistent with those that have been observed on various space probes far away from any planetary body, confirming that the undisturbed solar plasma does reach the lunar surface during these periods.

As indicated, transient gas clouds have been measured by some of the Apollo Lunar Surface Experiments Package (ALSEP) instruments. Astronaut Worden, during his time in orbit, spotted volcanic cinder cones at several points on the surface. This information, plus numerous color flashes and gas clouds previously observed from Earth and the moonquake swarms, suggest that local volcanic activity may still be taking place on the Moon. A site which apparently displays such volcanic manifestations is a candidate for the Apollo 17 mission.

Orbital Science

All data now show that the farside of the Moon is different from the frontside in many significant ways—structurally, chemically, and topographically. The Laser Altimeter on Apollo 15, along with precision tracking information, clearly shows that the frontside of the Moon is depressed between 2 and 5 km below what might be called the lunar geoid or sea level, while the farside is elevated by a similar amount. Also the lunar center of mass appears to be displaced about 2 km in a direction 37°E of the direction of the Earth. There are also smaller-scale topographic differences. The craters on the farside appear to be steeper walled than frontside craters. The deepest crater yet measured, Gagarin, is located on the farside, and it is about 6.5 km deep. There are other large farside circular basins such as

Apollo, Hertzsprung, and Korolev, to name only a few; however, these craters are not filled with dark mare material as similar frontside structures are, but rather they are apparently "dry," or at most only partially filled with material of higher albedo than mare basalt.

The subsatellite magnetometer, launched by Apollo 15, confirms the presence of a small regional backside magnetic anomaly, and this is certainly consistent with the previous data in indicating a fundamental difference in the crustal structure between the two hemispheres of the Moon.

The name "mascon" was originally coined as an acronym for the apparent mass concentrations found within certain frontside circular mare basins. The subsatellite S-band transponder launched by Apollo 15 is providing new mascon data. Numerous gravity anomalies resulting from these features have now been mapped. Mascons represent a load on the lunar crust that has apparently been maintained for several billion years. This suggests that the crust of the Moon is comparatively stable, rigid, and strong. In contrast, the Earth's crust is mobile, overlies a subjacent asthenosphere, and is renewed over a time cycle of a few hundred million years. The heat engine of the Moon is much less active than the Earth's.

The X-Ray Spectrometer, carried by Apollo 15 in orbit around the Moon, shows the highlands of the Moon to be richer in aluminum than the mare basins. The eastern highlands are two to three times higher in aluminum content than are the mare basins. The aluminum–silicon ratios for the highlands east of the Sea of Fertility correspond to those for anorthosite or gabbroic anorthosite. The lunar farside highlands are apparently very high in aluminum content, whereas the Apennine highlands are lower in aluminum than eastern frontside highlands, but higher than any of the circular maria.

From all of these observations, a picture of the Moon has emerged which, though much more definitive than previous knowledge would permit, still leaves unanswered some major questions as to the origin and constitution of the Moon. In particular, the question of fission, capture, or joint accretion with Earth remains unsettled. However, our acceptable range of models for the Moon has been greatly narrowed, and this is important progress in the field of planetology.

References

1. *Proceedings of the Apollo 11 Lunar Science Conference*, Vols. I, II, and III, Pergamon Press, New York, 1970.

2. *Science*, Vol. 167, No. 3918, Jan. 30, 1970.

3. *Apollo 11 Preliminary Science Report*, NASA SP-214, National Aeronautics and Space Administration, Washington, D.C., 1969.

4. *Apollo 12 Preliminary Science Report*, NASA SP-235, National Aeronautics and Space Administration, Washington, D.C., 1970.

5. *Apollo 14 Preliminary Science Report*, NASA SP-272, National Aeronautics and Space Administration, Washington, D.C., 1971.

6. *Apollo 15 Preliminary Science Report*, NASA SP-289, National Aeronautics and Space Administration, Washington, D.C. (in press).

Index: Mariner Venus–Mercury
1973 Project, solar phenomena

Mariner Venus–Mercury 1973 Mission Solar Proton Environment: Fluence and Dose

J. R. Thomas

The Boeing Company

The solar proton environment of Mariner Venus–Mercury 1973 (MVM73) may be the most severe yet encountered in space missions, because the trajectory by Mercury brings the spacecraft significantly closer to the Sun than that of any previous exploration. This study presents a derivation of proton fluence over the duration of the mission in terms of a relatively constant low-energy component, the solar wind, and a probabilistic high-energy component from discrete solar events. An updated correlation of yearly energetic proton fluence with yearly average sunspot number is presented. This correlation and sunspot cycle forecasts for the period of the MVM73 mission (late 1973 through early 1975) form the basis for the high-energy proton fluence estimates with various confidence levels. Uncertainties in the probability estimates and in calculation of the scaling with distance from the Sun are discussed. Selection of a particular 95-percentile model as the design constraint is recommended along with reasons for not using the worst-case model. Interior fluences are calculated and expressed in terms expected to be useful for spacecraft design.

Introduction

The solar proton flux is the major possible radiation hazard to the MVM73 mission, for the following reasons:

(1) MVM73 will fly closer to the Sun than any previous mission.

(2) The physics of proton acceleration by the Sun and proton propagation from Sun to Earth is not well understood.

(3) On occasion (albeit infrequently) the Sun has produced hazardous fluxes of energetic protons (typically 1 MeV to 1 GeV) in flare events.

(4) The proton component of the steady solar wind (around 1 keV) is sufficiently intense in the vicinity of Mercury to impose design constraints on spacecraft surfaces.

In the following sections, a derivation of expected proton fluences is presented with estimated probabilities that these fluences will not be

exceeded. Fluence is the flux integrated over the duration of the mission and is, of course, a function of proton energy. Specifically, integral fluence (fluence of protons of energies greater than a given energy E) is tabulated and graphed in the following sections. Since the average proton energy spectrum is relatively soft (i.e., the integral fluence decreases rapidly with energy), the description of the radiation environment can be conveniently divided into two categories: the low-energy solar wind fluence and the energetic solar proton fluence.

The fluence, by definition, depends on the mission. For the following calculations the mission is assumed to include the extended mission to second encounter. Thus, launch from Earth is assumed to be about November 1973, followed by a five-month trip to Mercury, a six-month solar orbit, and then returning to Mercury about February 1975.

Solar Wind Fluence

The solar wind protons ($\lesssim 10$ keV) flow rather steadily, and their flux varies on a yearly average only by a factor of about 2. The average density and velocity at Earth are 5 protons/cm^3 and 400 km/s corresponding to a yearly fluence of 6×10^{15} protons cm^{-2} (References 1, 2). Hence, during the time of the MVM73 mission, the probability for this solar wind fluence to exceed 10^{16} cm^{-2} is quite low (estimated to be $\leqslant 0.05$). Furthermore, the solar wind flow is quite well understood (Reference 3). Continuity of flow implies that a given parcel of solar wind expands so that its flux is inversely proportional to the square of the distance r from the Sun. Therefore, on a long-term (yearly) average the solar wind flux scales as r^{-2}. An average of r^{-2} along the trajectory from Earth past Venus to Mercury in five months, plus an additional six months to second encounter at Mercury, yields a mission fluence of approximately six times the fluence observed at Earth in one year. Thus, the fluence of protons with energies $E \geqslant 1$ keV during the mission is estimated to be 6×10^{16} cm^{-2} for both 95-percentile and worst-case models.

Prediction of Solar Event Protons

The moderate-to-high-energy component of solar protons is called variously by such names as solar event protons, solar cosmic rays (high energy) and solar energetic storm particles (moderate energy), or solar flare protons. The last name is least suitable because, although energetic protons are emitted only as an accompaniment of solar flares (i.e., optical brightening of local regions), the flux of protons is not well correlated with flare size or brightness. In fact, the large majority of flares produce no energetic protons at Earth. The predictability of the occurrence and magnitude of a solar proton event is very poor, even on a short-term (~ 1 day) basis. However, a reasonable correlation of yearly energetic proton fluence with yearly average sunspot number has been found (References 4, 5). Physically, this result may be interpreted as meaning that the average sunspot number, a known general indicator of solar activity, provides a fair measure of the

product of expected number of solar proton events times the fluence per event.

Figure 1 shows the correlation as established by Webber and Thomas (Reference 4) on data for the years 1956 through 1965. Data (Reference 6) at 10 and 30 MeV for the years 1966 through 1969 have been added during this study and are indicated by circles with radial ticks. These points further substantiate the apparent correlation. The dashed lines are used here as the basis for prediction. Note that most of the data points lie slightly below the curves. However, data for the years 1956 through 1958 were derived from ground-based measurements and are probably lower than true values that would have been obtained with good measurements in space. The years 1962 and 1963 are somewhat anomalous. Since the prediction is based on a rather arbitrary yearly division, this anomaly may be partly resolved if 1962 and 1963 are averaged over their total two-year span.

Several other points should be made concerning Figure 1. First, note that there is nearly an order of magnitude difference in fluence between the peak year of cycle 19 (i.e., 1959) and the peak years of cycle 20 (i.e., 1968 to

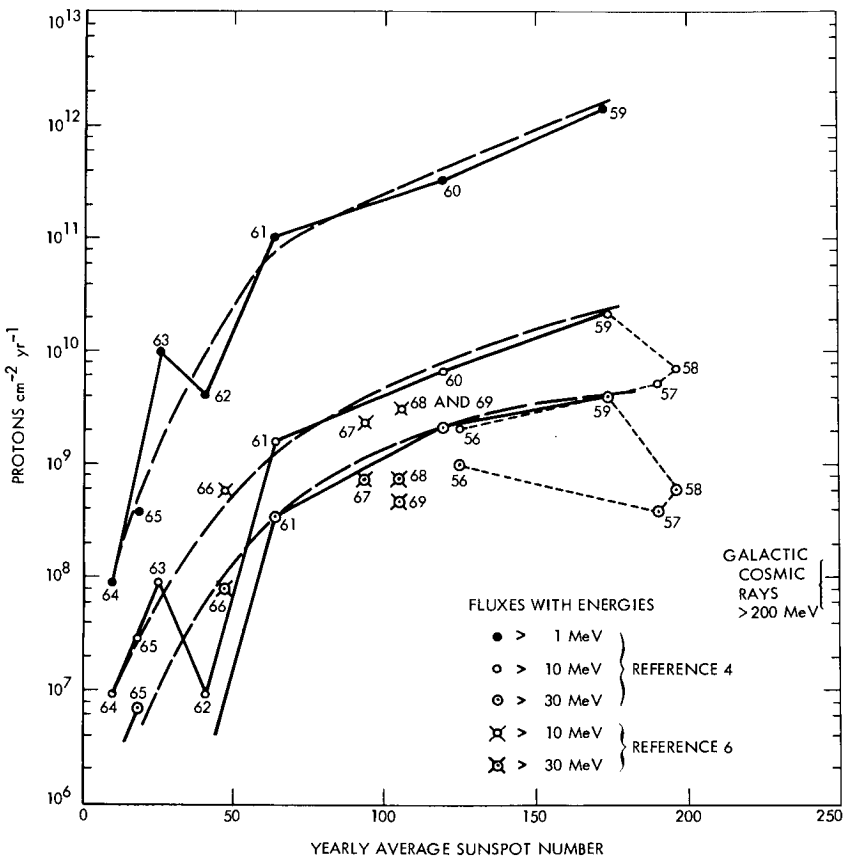

Figure 1. Yearly solar proton fluxes at Earth as a function of sunspot number for the years 1956 to 1969

1969). This provides further evidence of correlation of energetic proton emission with solar activity as indicated by sunspot number. Thus, a fluence of $\sim 10^{12}$ protons per cm^2 above 1 MeV corresponds to the peak of the exceptionally high sunspot cycle (namely 19) and represents not only: (1) a worst case since observations have been recorded, but also, (2) based on the correlation, probably the worst case over a period of ~188 years—the long-period solar cycle. Finally, the integral galactic cosmic ray flux above 200 MeV varies over a small range, around 10^8 cm^{-2} yr^{-1} (Reference 7), in anticorrelation with solar activity. This flux in any case represents a lower bound on the level to which spacecraft must be resistant.

Further evidence of the correlation of sunspot number and yearly fluence and some indication of the predictability of these quantities a few years in the future is provided by Table 1. The predictions were formulated in the summer of 1966 (Reference 4). However, the documented predictions referred to fluxes above 10 and 40 MeV, and an interpolation to 30 MeV was necessary for comparison with the data. The predicted values for 1965 were really preliminary values of observed data. Proton flux observations are included only through the first quarter of 1970, and the first quarter numbers should be multiplied by a factor of 4 for comparison with prediction.

The fluences in Table 1 depend on sunspot number prediction through the correlations previously discussed. At the beginning of a new cycle, prediction of the forthcoming sunspot peak is rather uncertain. However, prediction of the next sunspot minimum level and time from the current point in the decreasing portion of the cycle is possible with considerably greater confidence. The general nature of the regularity of the sunspot cycle is illustrated in Figure 2. It shows that time between sunspot minima is regular to about ±1 year and that there are several longer-period cycles imposed on the basic 11-year cycle. Figure 3 then shows details of sunspot number variations during the last two cycles superimposed on typical high, medium, and low cycles as derived by Waldmeier (Reference 8). Cycle 19 had a peak sunspot number of ~200 (off scale at the top of the graph), which is *much* higher than the peak during a typical high sunspot number cycle. In contrast, the peak of cycle 20 is only slightly above a typical medium peak, although the duration of the peak of cycle 20 is longer than usual. Thus, on the grounds that sunspot number is a rough indicator of absolute solar activity as established by a variety of correlations, predictions based on peak values of cycle 19 are not appropriate to cycle 20.

Probability Estimates

Two methods are used here to obtain estimates of the probability that the fluence at Earth will not exceed certain levels during the MVM73 mission. The first method is based on the shape of recent sunspot cycles. From our study of prediction methods for future cycles, the following deductions have been drawn:

(1) The average sunspot number during the MVM73 mission (late 1973 through 1974) will be less than 30, with a probability of 0.5.

Table 1. Observed and predicted sunspot number and yearly fluences at Earth

Year	Yearly mean sunspot number		J(>10 MeV), cm^{-2}		J(> MeV), cm^{-2}	
	Observed	Predicted*	Observed	Predicted*	Observed	Predicted*
1965	15.1	16	7.4×10^7	3.5×10^{7}**	6.8×10^6	6×10^{6}**
1966	47.0	48	5.8×10^8	3.0×10^8	8.2×10^7	1×10^8
1967	93.8	85	2.3×10^9	2.5×10^9	7.5×10^8	9×10^8
1968	105.9	110	3.1×10^9	5.0×10^9	7.3×10^8	2×10^9
1969	105.5	92	3.2×10^9	3.0×10^9	4.8×10^8	1×10^9
1970	104.5	74	1.7×10^8 (1st quarter)	1.5×10^9	3.2×10^7 (1st quarter)	6×10^8
1971		58		7.0×10^8		2×10^8
1972		38		1.5×10^8		5×10^7

* (Reference 4).
** Preliminary observed data.

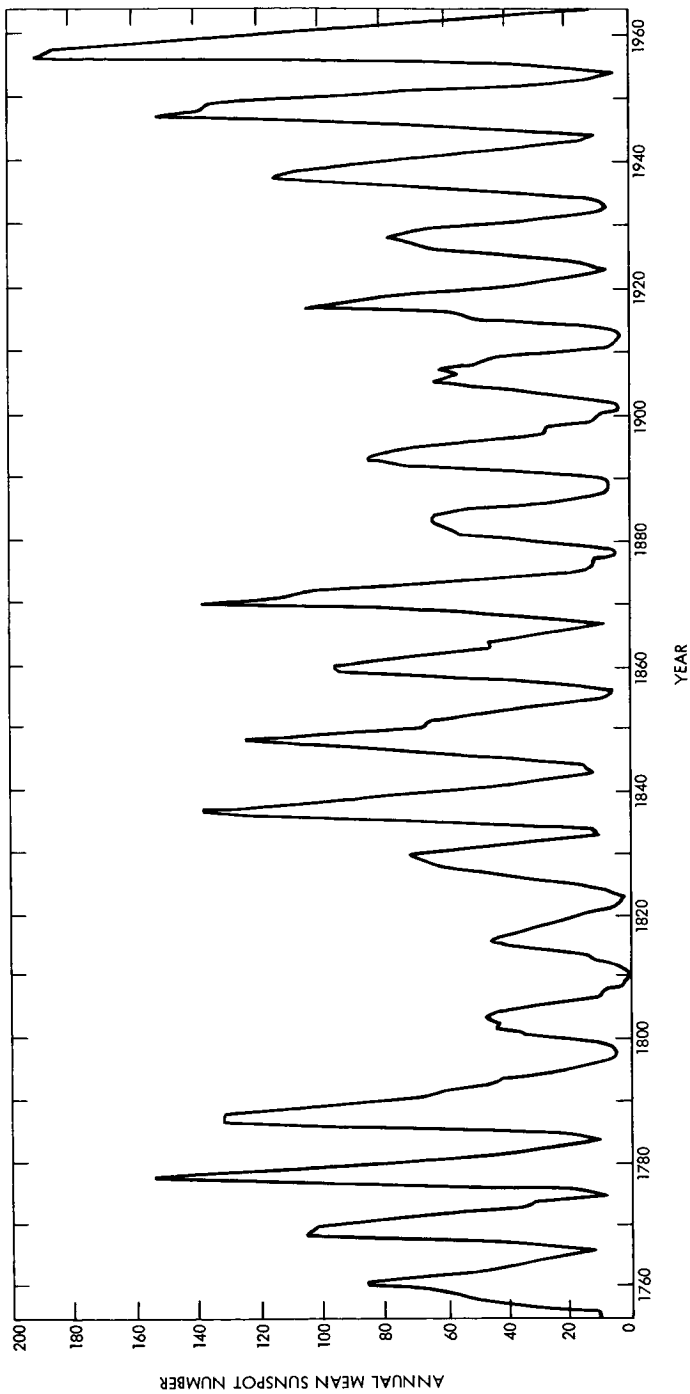

Figure 2. Mean yearly sunspot numbers since 1760

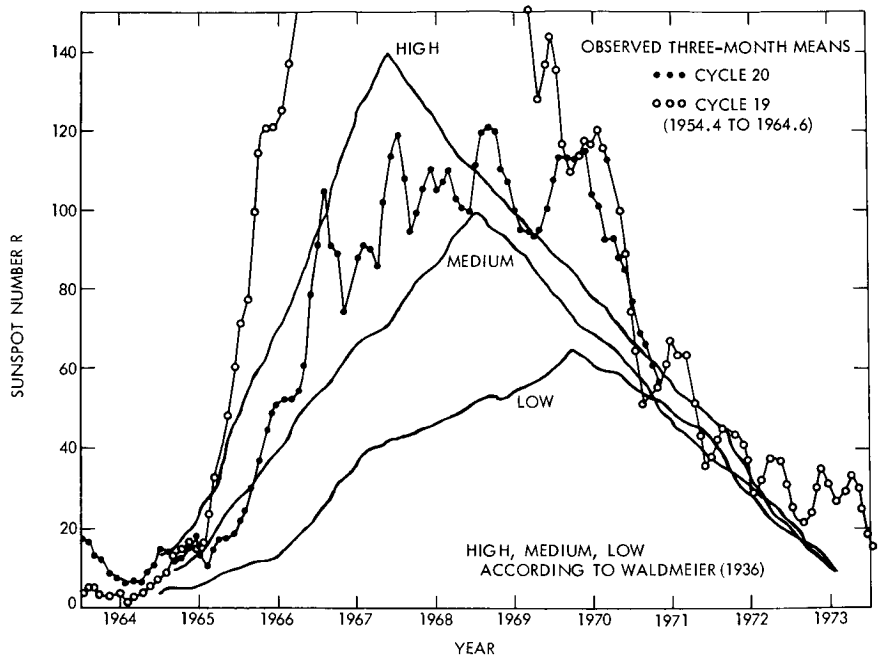

Figure 3. Temporal variation of sunspot number placed on a time scale for cycle 20

(2) By comparison with cycle 19, which oscillated to sunspot numbers approaching 40 very late in the cycle, and from the unusual character of cycle 19, which places the probability of such occurrence roughly above the standard deviation in the upper tail of the (assumed gaussian) distribution, the sunspot number will be less than 40 with a probability of 0.84.

(3) From consideration of the maximum observed variation in both time of occurrence and level of minimum in all the past 20 cycles (Figure 2), the average sunspot number is found to be less than 50 with a probability of 0.95.

The fluence levels at Earth (Table 2) are derived from the correlations shown in Figure 1 and assigned probabilities according to the foregoing deductions (1), (2), and (3). Note that the sunspot predictions of Figure 3 are in essential agreement with predictions based on the method of McNish and Lincoln (Reference 9). The latter predictions are derived from a regression analysis based on cycles 8 through 19, and are published in *Solar-Geophysical Data.* According to the July 1971 issue, the predicted values are decreasing throughout the period of the MVM mission from 24.2 ± 21 in November 1973 to 11.0 ± 15 in February 1975. The ± figure represents the 90% confidence interval.

The second method of estimating probabilities is based on the calculated root-mean-square deviation in logarithm of the fluence about the dashed

curves for the data points shown in Figure 1 (except data for 1956 through 1958 were not used). This sample standard deviation was approximately the same for each curve, and the value obtained by including data points from all the curves in one sample set is

$$\sigma\,(\log_{10}\text{ yearly fluence}) = 0.47 \approx \log_{10} 3$$

It has been suggested that the distribution of event fluences within a solar cycle follow a log-normal distribution. If we assume that the yearly fluence distribution is also log normal with a mean that depends on sunspot number (e.g., as given by correlation of Figure 1) and a constant standard deviation, then the probability of exceeding the most probable fluence (i.e., 50-percentile fluence based on a normal distribution) by a factor of 3 is 0.5 + 0.34 = 0.84 or a factor of $3^2 \approx 10$ is 0.5 + 0.475 = 0.975. Hence, if the 50-percentile fluences are taken as in the foregoing from the most probable projection of the current solar cycle, then the 84- and 95-percentile fluences should be larger by factors of about 3 and 10, respectively. The at-Earth fluences in Table 2 agree reasonably with this second method also.

Scaling to Mercury

The final step in establishing solar proton estimates for MVM73 involves scaling the predicted fluences from the vicinity of Earth to that along the spacecraft trajectory, which travels to within about 0.4 AU of the Sun. The propagation of energetic protons from solar events is only partially understood, but several physical processes affect the propagation. The radial flow of the solar wind and the rotation of the Sun draw the solar magnetic field lines into the well-known "garden-hose" or Archimedes spiral. In addition, fluctuations in the solar-wind flow induce stochastic variations in the field. The high-energy particles (of much lower total energy density) are then channeled in this spiral field but with anisotropic energy-dependent diffusion caused by the variations.

Several models have been formulated to describe this propagation and diffusion. Webber and Thomas (Reference 10) pointed out that isotropic diffusion, filling a conical volume, leads to a $1/r^3$ dependence of peak flux and total fluence, while highly anisotropic (radial dominant) diffusion leads to a $1/r^2$ dependence. Englade (Reference 11) has formulated a much more detailed computational model that includes anisotropic energy-dependent diffusion in a stochastic interplanetary magnetic field and adiabatic deceleration produced by the solar wind, plus many other physical mechanisms. Deceleration can be a significant mechanism in changing the radial dependence of flux above a given energy with the typical steeply falling spectra of solar proton events. In any case, the model of Englade depends on a considerable number of input parameters, and the impact of the choice of these has not been fully explored. However, for some "typical" choice, Englade (Reference 12) found an increase from 1 to 0.4 AU in expected event fluence of a factor of 15 for 10 MeV protons and a factor of

Table 2. Estimated proton fluence probability for 1973-1974 (one-year mission)

Probability $\{F < F_0\}$	Fluence F_0, protons/cm^2							
	At Earth				At Mercury			
	>1 MeV	>10 MeV	>30 MeV	>100 MeV	>1 MeV	>10 MeV	>30 MeV	>100 MeV
Worst case (July 10–16, 1959)	1.0×10^{12}	1.5×10^{10}	3.0×10^{9}	3.5×10^{8}	1.5×10^{13}	2.2×10^{11}	3.0×10^{10}	3.5×10^{9}
0.95 (SS = 50)	3.0×10^{10}	6.0×10^{8}	2.0×10^{8}	2.0×10^{7}	5.0×10^{11}	1.0×10^{10}	2.0×10^{9}	2.0×10^{8}
0.84 (SS = 40)	1.0×10^{10}	3.0×10^{8}	6.0×10^{7}		1.5×10^{11}	5.0×10^{9}	6.0×10^{8}	
0.50 (SS = 30)	3.0×10^{9}	1.0×10^{8}	2.0×10^{7}		5.0×10^{10}	1.0×10^{9}	2.0×10^{8}	
	>1 keV	>10 keV	>100 keV		>1 keV	>10 keV	>100 keV	
0.95	1.0×10^{16}	1.0×10^{14}	1.5×10^{12}		6.0×10^{16}	1.0×10^{15}	2.5×10^{13}	

Fluence: time-integrated flux.
SS = Yearly average sunspot number.

10 for 100 MeV protons. These factors correspond to scaling in proportion to r^{-3} and $r^{-2.5}$, respectively. Therefore, we have scaled to Mercury orbit as r^{-3} for the 1 and 10 MeV fluences in Table 2 and as $r^{-2.5}$ for the 30 and 100 MeV fluences.

These calculations probably tend toward the severe end of the range of hazard estimates. In a similar way the use of the probability levels at Earth for those at Mercury is severe, because the mission spends its duration over a range of distances from Earth to Mercury and this would bias the mission probability to lower fluences (i.e., between Mercury and Earth fluences).

Worst Case

In addition to fluences associated with estimated probabilities discussed above, a worst-case fluence has been included in Table 2. This worst case at Earth is the fluence observed during the week of July 10–16, 1959 (Reference 13). A continuing series of three events in that week produced about 75% of the energetic proton fluence observed in 1959, and the proton fluence in 1959 is the largest occurring in one year since particle fluxes have been recorded.

Although the possibility of occurrence of a similar event during the MVM73 mission cannot be disproved (perhaps because of incomplete knowledge of solar physics), the likelihood of such occurrence appears extremely remote. It would be contrary to: (1) the correlation of proton flux with solar activity, (2) the fact that solar cycle 19 with the highest average sunspot number observed in over 200 years of recorded data produced about 8 major proton events, whereas the current cycle 20 with a near-average peak has produced no events within a factor of ≈ 5 in fluence of those 8 major ones, and (3) mission schedules, in which the MVM73 launch date in November 1973 is just 16 months before the next predicted solar minimum, because no major events have been observed at such solar quiet times. Two solar proton events, namely those of March 1942 and February 1956 have been cited as evidence for the invalidity of point (3). However, the average sunspot number in February 1956 was 97, and the event in March 1942 at an average sunspot level of 54 (2 years before minimum) was probably not a major event in the sense of the 8 proton events in cycle 19. (Fluence data on these pre-space-era events were obtained chiefly from ground-based neutron monitors and are consequently much less accurate.)

For these reasons, we do not believe the worst-case model should be chosen as a design model. It should be realized that such a choice does depend on our (somewhat intuitive) knowledge that the worst case would impose severe penalties in terms of cost and weight. We recommend the 95-percentile model as offering a chance of success at least as good as that associated with several other essential systems, yet probably without major design penalties.

Interior Environment

The Boeing SPARES (Space Radiation Environment and Shielding) code was utilized to calculate interior environments and conversion to dose and damage equivalent fluence for the 95-percentile and worst-case models. Figures 4 and 5 present the interior environment corresponding to the worst-case and 95-percentile exterior environments, respectively. Figures 6 and 7 provide conversion of these fluences to ionization dose in silicon and an equivalent fluence of 15 MeV protons for displacement damage to P-type silicon of resistivity 1 Ω-cm. Equivalent damage is defined as the same decrease in minority carrier lifetime as that produced by 15-MeV protons. This damage depends on proton energy, material resistivity and temperature, etc.

This equivalent fluence is a typical measure of the proton displacement damage to semiconductor devices, especially 1-Ω-cm N/P solar cells. On the other hand, surface damage is better correlated with ionization dose than with displacement damage and is strongly dependent on operating conditions.

All the dependent variables in Figures 4 through 7 are given as a function of spherical aluminum shield thickness. However, the result is relatively insensitive to shield material if thickness is measured in terms of mass per unit area, as shown. For a first-order correction, the area density thickness of aluminum equivalent to a shield of some other material (also spherical) may be calculated by multiplying by the ratio of

$$\frac{(Z/A)_{\text{other}}}{(Z/A)_{\text{Al}}}$$

where Z/A is the average ratio of atomic number Z to atomic weight A. The average is weighted according to the number of atoms of each element in the chemical formula. For example, aluminum has $Z = 13$, $A = 27$ and, hence, $Z/A = 0.481$. Similarly silicon has $Z = 14$, $A = 28$, and oxygen has $Z = 8$, $A = 16$. Thus, the average Z/A for SiO_2 is 0.5. A 20-mil (0.0508 cm) spherical shell of SiO_2 at a density of 2.2 g/cm^3 has an area density thickness of $2.2 \times 0.0508 = 0.112$ g/cm^2. Hence, it is equivalent to an aluminum shield of thickness $(0.112)(0.5/0.481) = 0.116$ g/cm^2.

Usage

Figures 4 and 5 may be used to obtain an integral energy spectrum at any (reasonable) depth, from which differential spectra and other damage equivalent fluences may be calculated. The format of Figures 4 through 7 is also useful for evaluating the fluences or doses under planar and other nonspherical shields. In general, the dose (or fluence) under a nonspherical shield may be evaluated by summing over contributions from sections of different shield depth. Each sector contributes a dose which is the product of the dose shown in the appropriate figure for that shield depth times the

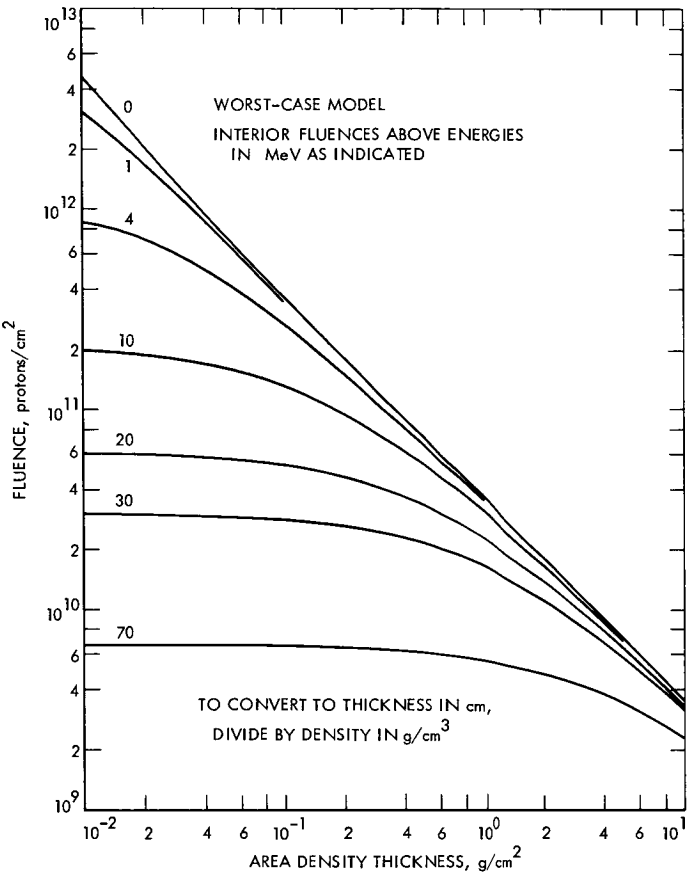

Figure 4. Interior fluences as a function of shield thickness for worst-case model

fraction of the total 4π solid angle subtended by that sector about the dose point.

Calculation of dose, for example, under a planar shield may be done easily if the dose versus depth is approximated satisfactorily by a straight line on a log–log plot. Inspection of Figures 6 and 7 show that this approximation is reasonable for the fluences or doses presented here. In such a case, the differential dose dD from a sector of solid angle $2\pi \sin\theta\, d\theta$ (where θ is the angle of incidence of the proton as measured from normal to the plane) through a planar shield of thickness t is given by

$$dD = D_{\text{sph}}\,(t/\cos\theta)\,\frac{2\pi \sin\theta\, d\theta}{4\pi}$$

$$= D_{\text{sph}}\,(t)\,\cos^n\theta\,\frac{\sin\theta\, d\theta}{2}$$

where $D_{\text{sph}}\,(t)$ is the spherical dose function of Figure 6, and n is its negative slope in log–log form. (That is, $D_{\text{sph}}\,(t) \propto t^{-n}$. For thicknesses > 0.2 g/cm^2,

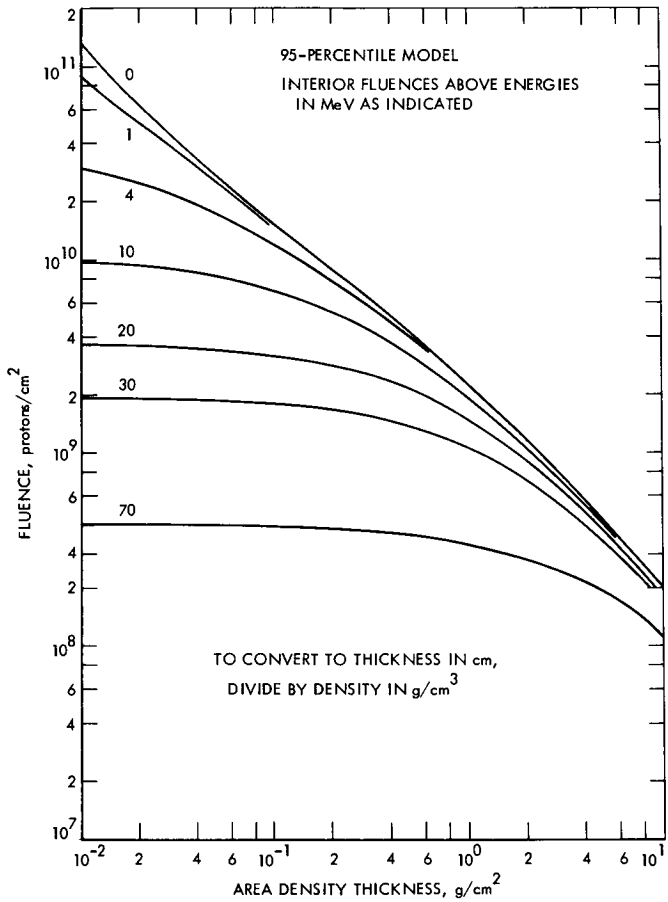

Figure 5. Interior fluences as a function of shield thickness for 95-percentile model

the 95-percentile case in Figure 6 is well approximated by $n = 1.34$). The differential dose may then be integrated to obtain the dose at a point sandwiched between two large planar shields, each of thickness t, as

$$D_{pl}(t) = \frac{D_{sph}(t)}{n+1}$$

Again, more complicated cases of combination of sectors including a planar shield and other shapes may be handled by adding the contributions of each.

Effect of Solar Latitude on Proton Fluence

Since the MVM73 mission will proceed to higher solar latitudes (~11°) than any previous space mission, a question arose as to whether latitude dependence of proton fluence could affect the foregoing estimates. The solar equator is inclined 7° 15′ to the ecliptic, and so a range of ±7° has been explored from Earth without the finding of a noticeable latitude effect. Possible detection of a scarcely measurable effect on the solar wind has been

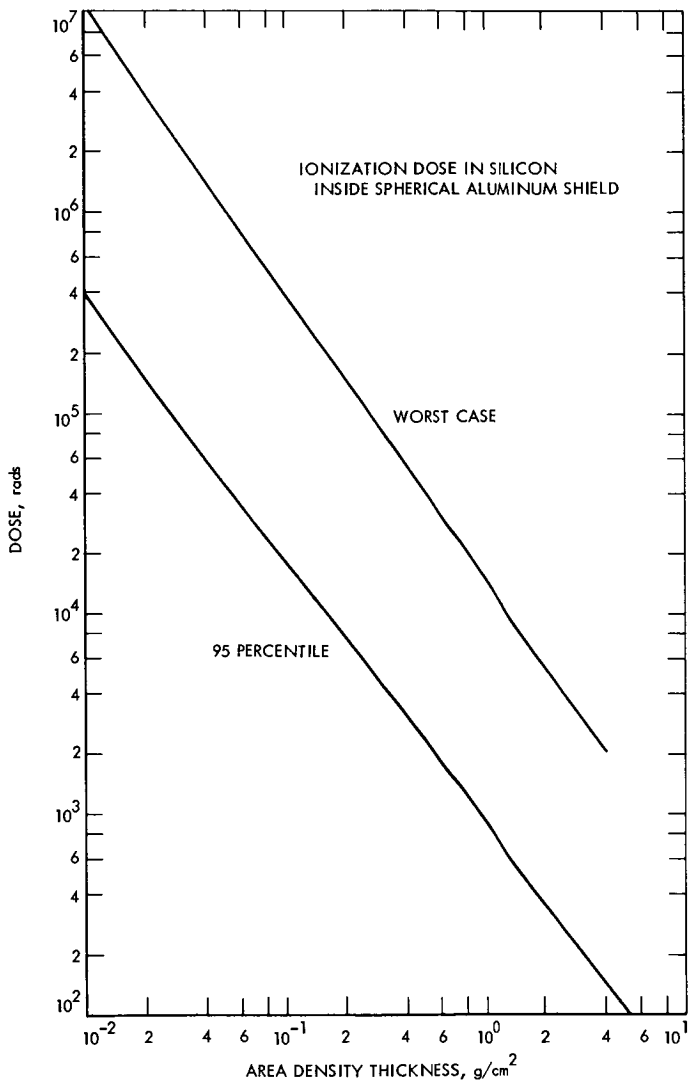

Figure 6. Ionization dose as a function of shield thickness

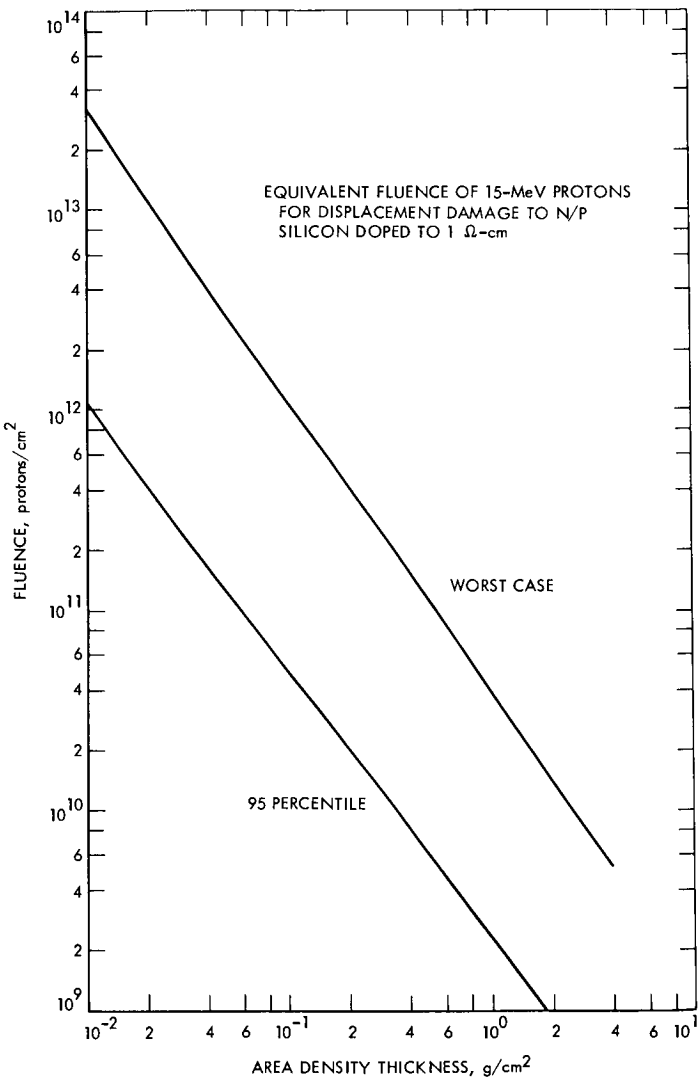

Figure 7. Damage equivalent fluence as a function of shield thickness

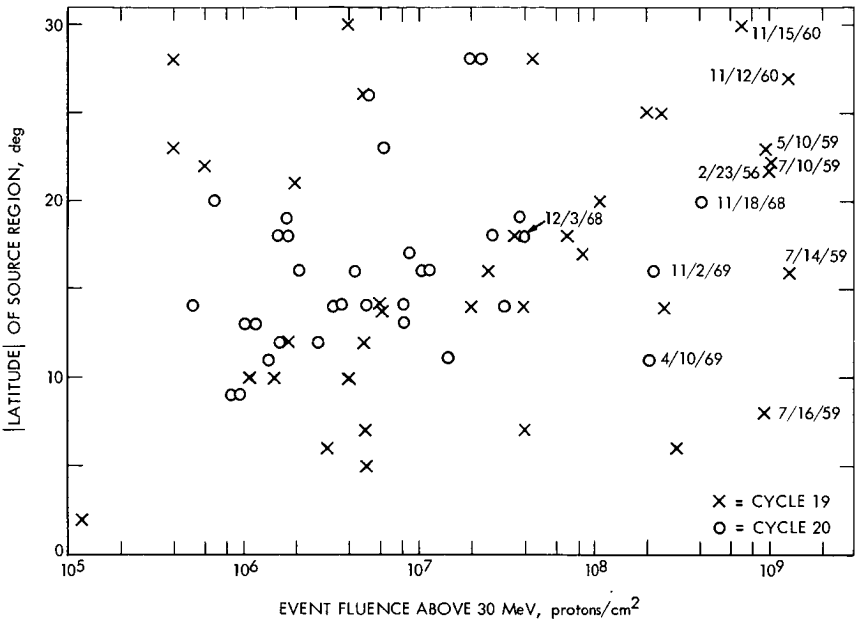

Figure 8. Scatter plot of heliocentric latitude of source flare versus proton fluence

reported recently (Reference 14). Furthermore, any possible small correlation between observed event fluence and latitude of the flare source region is overwhelmed by the large variation in event size, as Figure 8 illustrates. The fluence of protons at Earth is plotted for all the recorded proton events of cycles 19 and 20. (Many more optical flares produced no protons detected at Earth.) The latitude plotted is absolute value of heliocentric latitude of the optical source flare on the visible disk. Note also that the largest events are listed by date on Figure 8 to illustrate that cycle 20 events have been significantly smaller than the largest ones of cycle 19.

References

1. Dessler, A. J., "Solar Wind and Interplanetary Magnetic Field," *Rev. Geophys.*, Vol. 5, pp. 1–41, 1967.

2. Hundhausen, A. J., "Composition and Dynamics of the Solar Wind Plasma," *Rev. Geophys. Space Phys.*, Vol. 8, pp. 729–791, 1970.

3. Parker, E. N., "Recent Developments in Theory of Solar Wind," *Rev. Geophys. Space Phys.*, Vol. 9, pp. 825–835, 1949.

4. Webber, W. R., and Thomas, J. R., *Sunspot Number and Solar Cosmic Ray Predictions for Cycle 20 (1965–1975) with Preliminary Estimates for Cycle 21*, Document D2-113522-1. The Boeing Company, Seattle, Wash., May 1967.

5. Lanzerotti, L. J., "Solar Flare Particle Radiation," in *Proceedings of the National Symposium on Natural and Man-Made Radiation in Space*, held in Las Vegas, Nev., March 1971, NASA TMX-2440. National Aeronautics and Space Administration, Washington, D.C., January 1972.

6. Atwell, W., "The Significant Solar Proton Events in the 20th Solar Cycle for the Period October 1964 to March 1970," in *Proceedings of the National Symposium on Natural and Man-Made Radiation in Space*, held in Las Vegas, Nev., March 1971, NASA TMX-2440, pp. 329–335. National Aeronautics and Space Administration, Washington, D.C., January 1972. (See also Document 645D.21.070. Lockheed Electronics Company, Houston, Texas, March 1971).

7. Webber, W. R., "The Spectrum and Charge Composition of the Primary Cosmic Radiation," *Handbuch der Physik*, Vol. XLVI/2, pp. 181–264, 1967.

8. Waldmeier, M., "Prognose fur das nachste Sonnenfleckenmaximum," *Astron. Nachrichten*, Vol. 259, p. 267, 1936.

9. McNish, A. G., and Lincoln, J. V., "Prediction of Sunspot Numbers," *Trans. Am. Geophys. Union*, Vol. 30, pp. 673–685, 1949.

10. Webber, W. R., and Thomas, J. R., *Spatial Variations in Solar-Cosmic-Ray Intensities in Interplanetary Space*, Document D2-114459-1. The Boeing Company, Seattle, Wash., February 1969.

11. Englade, R. C., "A Computation Model for Solar Flare Particle Propagation," *J. Geophys. Res.*, Vol. 76, pp. 768–791, 1971.

12. Simpson, J. A., et al., *Energetic Particle Measurements at the Environment of Mercury and Venus*, Final Report of the Energetic Particles Experiment Team for the Venus/Mercury Flyby in 1973, Document 615-5, April 1970 (JPL internal document).

13. Webber, W. R., *An Evaluation of the Radiation Hazard Due to Solar Particle Events*, Document D2-90469. The Boeing Company, Seattle, Wash., December 1963.

14. Hundhausen, A. J., Bame, S. J., and Montgomery, M. D., "Variations of Solar-Wind Plasma Properties: Vela Observations of a Possible Heliographic Latitude Dependence," *J. Geophys. Res.*, Vol. 76, pp. 5145–5154, 1971.

Index: industrial processes and equipment, power sources

JPL Lithium-Doped Solar Cell Development Program

P. A. Berman

Guidance and Control Division

One of the most significant problems encountered in the use of silicon solar cells in space has been the sensitivity of the device to electron and proton radiation exposure. A major advancement was achieved when the P diffused into N-base solar cells were replaced with the more radiation-tolerant N diffused into P-base solar cells. Another advancement in achieving greater radiation tolerance was the discovery that the addition of lithium to N-base silicon resulted in what appeared to be annealing of radiation-induced defects. This phenomenon is being exploited to develop a high-efficiency radiation-resistant lithium-doped solar cell. In this investigation, lithium-doped solar cells fabricated from oxygen-lean and oxygen-rich silicon have been obtained with average initial efficiencies of 11.9% at air mass zero and 28°C, as compared to state-of-the-art N/P cells fabricated from 10-Ω-cm silicon with average efficiences of 11.3% under similar conditions. Lithium-doped cells have demonstrated the ability to withstand three to five times the fluence of 1-MeV electrons before degrading to a power equivalent to state-of-the-art solar cells. This article discusses the principal investigations carried out with respect to fabrication of high-efficiency radiation-resistant lithium-doped cells, including starting material, P/N junction diffusion, lithium source introduction, and lithium diffusion.

Introduction

Increasing the radiation tolerance of solar cells is important in any solar array system since it results in greater reliability, reduction in array size and weight, and, if cell costs do not increase significantly, greater economy. While these factors are important for all missions, they become extremely important for those missions which require large-area solar arrays (such as manned orbiters, electric propulsion missions, and Jupiter flyby missions) because a specific percentage reduction in the number of cells required represents a significant absolute cost reduction. The amount of radiation anticipated for a particular mission is, of course, dependent upon the mission trajectory, time of launch (with respect to the solar cycle), and mission duration. However, there is *always* a probability of exposure to a

significant amount of radiation from such sources as the Van Allen belts and solar proton flares.

State-of-the-art solar cells used in spacecraft solar array power systems degrade with electron and proton irradiation which occurs in near-Earth space as a result of the Van Allen belts and in deep space as a result of solar proton flares. The amount of degradation is quite dependent upon the irradiation spectrum and fluence. This problem is presently circumvented by overdesigning the panels with respect to the initial power output, so that the degraded output will meet or exceed mission requirements. This approach is oftentimes used in conjunction with thick coverglasses which attenuate some of the radiation. Thus, tradeoffs must be made between the power and useful lifetime of a solar array and its allowable size, weight, and cost. Effort has therefore been directed to develop an improved radiation-hardened solar cell, and there has been significant progress to date to suggest that the lithium-doped solar cell can be developed to the status of a practical device. Preliminary tests have shown that lithium-doped P/N solar cells can be designed and fabricated to be significantly more radiation-resistant than conventional silicon N/P solar cells at temperatures above 30°C. They can also be made reproducibly with initial conversion efficiencies equal to or better than those of the state-of-the-art cells. The present data indicate that these lithium-doped solar cells, when properly optimized for a particular mission environment, can be effectively 3 times more radiation-resistant to electrons and 10 times more radiation-resistant to protons and neutrons than present-day conventional 10-Ω-cm N/P solar cells, with little increase in cost.

The JPL lithium-doped cell program has been in existence for about 4 yr and has involved subcontracts to 10 industrial organizations and 5 universities. Due to the summary nature of this document, the information reported here is concerned only with the most pragmatic aspects of lithium-doped cell fabrication and does not include the underlying physics of the interaction among lithium, silicon, oxygen, and radiation-induced effects.

The advancements made with respect to lithium-doped cell development have clearly shown the power of the interdisciplinary approach which was adopted throughout the life of the program. Problems such as cell instability, low efficiency, poor process control, unpredictability of recovery characteristics, variations in recovery rate, cell size limitations, etc., that at one time appeared to be all but insoluble, appear to be falling by the wayside. These problems could not have been solved without the involvement of the multi-expert team represented by the organizations participating in this program. Each organization isolated the problems with respect to its own area of expertise, and the resultant body of information was coordinated and distributed to the other organizations by JPL. It is strongly felt that such an approach is applicable to many other programs (e.g., application of space technology to the economic generation of terrestrial power by means of solar energy conversion) and should prove to be of immense value in the majority of cases.

The results of the investigations carried out during the past two years represent the most significant achievements attained thus far with respect to the lithium-doped solar cell program. Lithium-doped solar cells fabricated from oxygen-lean and oxygen-rich silicon have been obtained with average initial efficiencies of 11.9% at air mass zero and 28°C, as compared to state-of-the-art N/P cells fabricated from 10-Ω-cm silicon with average efficiences of 11.3% under similar conditions.

Objectives

The major objectives of the program discussed in this article were to optimize the P/N lithium-doped solar cell with respect to initial efficiency and efficiency after recovery from exposure to electron radiation, and to compare these characteristics with those of the state-of-the-art N/P solar cells.

In order to achieve these major objectives, it was necessary to determine the effects of cell design and processing parameters on the pre- and post-irradiation cell characteristics and to develop methods of reproducibly effecting the desired cell design. This involved yet another objective, namely, development of analytical techniques to correlate cell design and processing with the observed effects on the pre- and post-irradiation cell characteristics. During the course of the program it became clear that understanding and/or improvements of four major aspects of lithium-doped cell design would be required if the P/N lithium-doped solar cell were ever to be competitive with the N/P state-of-the-art solar cell; namely, (1) starting material, (2) P/N junction diffusion, (3) lithium source introduction, and (4) lithium diffusion schedule. The successful attainment of these goals is described below.

Lithium-Doped Cell Fabrication

Starting Material

Three major forms of silicon were investigated for use in lithium-doped cell fabrication: crucible grown, float zone refined, and Lopex. The latter two types of silicon are quite similar to one another except that the dislocation density of Lopex silicon is much lower.

The general characteristics of the crucible-grown silicon are:

(1) High oxygen content.

(2) Low dislocation count.

(3) Economical production.

(4) Amenability to large-area cells.

(5) Slow recovery of lithium-doped cells.

(6) No apparent instability of resultant lithium-doped cells.

Crucible-grown silicon is particularly adaptable to use in large-area cells because it can be grown with relatively large diameters. There is no apparent degradation of cells fabricated from crucible silicon after storage at room temperature for periods exceeding 500 days.

The general characteristics of float-zone silicon are as follows:

(1) Low oxygen content.

(2) High dislocation count.

(3) Less economical than crucible-grown material.

(4) Less amenable to use in large-area cells because of smaller diameters.

(5) Fast recovery rate of highly doped lithium cells.

(6) Instability of highly doped lithium cells, especially after recovery of radiation-induced damage.

Lopex silicon has the same characteristics as float-zone silicon with the exception that it has a low rather than high dislocation count.

Extensive analysis has been performed on the effect of starting material on the action of lithium in irradiated silicon, but the results and conclusions are too complex to be reported in detail in this summary paper. Suffice it to say that the lithium interacts with radiation-induced defects to form configurations which are dependent upon the oxygen content of the silicon. However, the major difference, as far as cell behavior is concerned, is a slower recovery rate in lithium-doped oxygen-rich silicon due to a higher activation energy and correspondingly lower lithium diffusion constant. That is to say, it takes longer for the lithium to diffuse through the silicon and associate itself with the radiation-induced defect in oxygen-rich silicon (crucible grown) than it does for the lithium to diffuse through oxygen-lean silicon (float zone and Lopex). On the other hand, lithium-doped cells fabricated from oxygen-rich silicon are far more stable than those fabricated from oxygen-lean silicon and appear to be more uniform in their electrical characteristics.

P/N Junction Diffusion

Lithium-doped solar cells are produced by diffusing the lithium into N-type silicon. Prior to the introduction of the lithium, a P/N junction is formed in N-doped silicon by high-temperature (of the order of 1000°C) diffusion of boron to a depth of approximately 300 nm (3000 Å), thus giving a P/N cell configuration. When cells are fabricated in this manner, significant low-temperature (28 to 100°C) annealing of radiation damage induced by exposure to electrons having an energy of 1 MeV has been observed. Similar results have also been obtained after exposure to neutrons and protons.

One of the original problems encountered with lithium-doped solar cells was an initial cell efficiency so low that even after complete recovery, the

cells had much less power after irradiation than the state-of-the-art cells. Recently, lithium-doped cells have been fabricated which have initial efficiencies significantly higher than the state-of-the-art N/P cells.

One of the primary areas of investigation was concerned with the diffusion of boron into the silicon blank to form the P/N junction. The state-of-the-art boron trichloride (BCl_3) source results in an undesirable etching action and induces strains and dislocations in the silicon material. Investigations were carried out to develop an alternate boron junction diffusion technique, preferably one which would not etch the silicon blank surfaces and which would introduce fewer strains.

Two major investigations of alternative diffusion techniques were undertaken: (1) investigation of boron tribromide (BBr_3) as a diffusion source, and (2) investigation of modification of BCl_3 source deposition time schedule. The results of the BBr_3 source investigation indicated that while the number of etch pits and the amount of induced strains were greatly reduced, the resultant cell outputs were lower than obtained with the standard diffusion. The results of the second investigation also showed a very great reduction in dislocation density and induced stresses, but in this case significant improvements in cell efficiencies were also obtained, especially for cells fabricated from oxygen-lean silicon. Consequently, work on the BBr_3 diffusions was terminated and emphasis was placed on optimizing the boron deposition time in the BCl_3 diffusions.

As a result of the P/N junction diffusion investigation, lithium-doped silicon solar cells having dimensions as large as 12 cm^2 are now possible, due to the improved boron-diffusion techniques, which stress the cells far less than techniques used previously. A large increase was observed in the short-circuit current measured in tungsten (long wavelength) light for cells that were fabricated using the improved diffusion techniques as compared with previous cells, indicating a preservation of minority carrier diffusion length in the base region of the former cells. Sintering (at about 600°C) of the contacts of lithium-doped cells fabricated from Lopex silicon resulted in large increases in maximum power (of between 1 and 4 mW), mainly due to an open-circuit voltage improvement, over non-sintered cells. Efficiencies as high as 12.8% were observed, with the average efficiency being about 11.9%. The sample is small, but the efficiency is significantly higher than the average efficiency of 10-Ω-cm N/P cells (state-of-the-art), which is about 11.3%.

Lithium Source Introduction

One method of introducing lithium into silicon is to utilize a paint-on source which consists of lithium powder suspended in an oil. After the lithium is painted on the back surface of the cell, the cell is heated in a furnace to alloy the lithium and drive it into the silicon. In many cases the cell is then removed from the furnace, the lithium alloy region removed by etching, and the cell returned to the furnace for additional heat treatment.

This is termed *redistribution*, since it redistributes the lithium within the base region and changes the lithium concentration profile.

Painting the lithium-oil suspension onto the back surface of the cell is a critical operation, since thick layers can form spheres of lithium which cause the formation of large alloy pits when the lithium-coated cells are heated in the diffusion furnace. These alloy pits can result in large stresses which in extreme cases are of sufficient magnitude to break the cell. Even when the painted layer is kept thin, it is still possible for conglomerations of lithium, small pits, and possible stressing of the cell to develop. To a great extent the use of a lithium aluminum hydride solution has alleviated most of the problems associated with the oil suspension method, except for the cumbersome task of individually painting the solution on the back face of each cell.

While the paint-on technique is quite adequate for fabrication of cells in small lots, it presented a bottleneck for larger lots and was highly operator-dependent (more of an art than a science). Consequently, a major effort was expended to develop a technique for evaporating the lithium onto the back surface of cell batches. While high-efficiency cells were attainable using this technique, initially the yield of such cells was lower than obtained from the paint-on technique. Through additional effort, however, the yields were increased so that they now are equal to or better than those obtained from the paint-on technique. The evaporation technique is more amenable to high-volume production and should, if properly controlled, give greater reproducibility than the paint-on technique which has been used in the past.

Lithium Diffusion Schedule

As mentioned above, one technique for lithium diffusion involves a two-cycle lithium alloy-redistribution schedule. The major investigation during the course of this program was centered around optimizing the lithium diffusion to achieve highest initial and post-irradiation-recovered cell efficiency. The time and temperature of both cycles were systematically varied and it appeared that the best result was achieved for an alloy cycle of 90 min and a redistribution cycle of 60 min, both carried out at a temperature of 425°C.

Subsequently, efforts were directed toward investigation of single-cycle lithium diffusion schedules. Again, the times and temperatures were systematically varied and the resultant cells analyzed with respect to initial- and post-irradiation recovery characteristics. It was found that lowering the diffusion temperatures to between 350 and 380°C and increasing the diffusion time to between 180 and 480 min yielded cells with higher initial- and post-irradiation-recovered power than those obtained from the best two-cycle schedules. The single-cycle lithium diffusion technique not only reduced the complexity of the lithium diffusion over the two-cycle technique, but resulted in a greater degree of uniformity in the resultant cell characteristics.

The time–temperature schedule of lithium diffusion determines the distribution of the lithium within the body of the cell. A very convenient method for determining the lithium concentration near the junction is measurement of capacitance versus voltage as the cell is reversed-biased. This technique is applicable to a distance of up to 10 nm from the junction, depending upon the silicon resistivity, after which the cell goes into "reverse breakdown." As a result of very thorough and extensive analysis, it is possible to predict quantitatively the lithium-doped cell radiation recovery characteristics by measurement of the lithium concentration gradient within this narrow region adjacent to the P/N junction by means of the non-destructive and relatively convenient capacitance–voltage measurement. (It should be noted that the modifying term "relatively convenient" applies because the measurement does take some time to make, and while it is possible to measure small quantities of cells on a 100% basis, it would be prohibitive for large production lots except on a sampling basis.) Once the power of the capacitance–voltage relationship was fully realized and utilized, many of the results which previously appeared to be anomalous became readily explainable. The most important of these was the different recovery behavior among cells from the same lot (which were supposedly identical). It was found that, in fact, the cells were not identical, but that the lithium density gradient could vary by a factor of up to 70. When the cells were reordered to correspond to their lithium density gradient rather than their lithium diffusion schedule, the results were found to be entirely predictable. This led to the selection of lithium diffusion schedules which not only gave cells with high initial efficiencies but also with similarly high radiation recovery capabilities. The capacitance–voltage analysis, the single most important breakthrough of the program, showed that two-cycle lithium diffusion schedules, and single-cycle lithium diffusion schedules utilizing times greater than 3 h, can result in high-efficiency, high-recovery cells, but also tend to yield wider variations in lithium density gradient and consequently in cell recovery capabilities. On the other hand, single-cycle lithium diffusion schedules for times between 2 and 3 h give very uniform (within about a factor of two) lithium density gradients and high recovery capability.

Concluding Remarks

The results of the investigations carried out during this program represent significant achievements with respect to the lithium-doped solar cell. Lithium-doped solar cells fabricated from oxygen-lean and oxygen-rich silicon have been obtained with average initial efficiencies of 11.9% at air mass zero and 28°C, as compared to the state-of-the-art N/P cells fabricated from 10-Ω-cm silicon with average efficiencies of 11.3% under similar conditions. Improvements in cell-processing techniques have made possible the fabrication of large-area lithium-doped cells. Excellent progress has been made in quantitative predictions of post-irradiation lithium-doped cell characteristics as a function of cell design by means of capacitance–voltage measurements, and this information has been used to achieve further

improvements in cell design. Specifically, analysis of irradiated lithium-doped cells has shown that the recovery characteristics can be very well predicted by the lithium density gradient near the junction and that very good cell-to-cell reproducibility of lithium density gradient can be obtained with single-cycle 2- to 3-h lithium diffusion schedules.

Since the radiation damage annealing rate for lithium cells is a function of cell operating temperature and oxygen concentration in the silicon, the design of the lithium-doped cell must accommodate the desired annealing rate with respect to the cell operating temperature. Lithium-doped cells would probably not be appropriate for missions involving extended equilibrium temperatures below 30°C unless some means of auxiliary cell heating is provided.

The lithium-doped solar cell represents the most significant improvement in solar cell radiation resistance since the advent of the N diffused into P-base solar cell developed in the early 1960s.

Index: electronic components and circuits, power sources, electric propulsion

Methods for Utilizing Maximum Power From a Solar Array

D. K. Decker

Guidance and Control Division

Ion thrusters are being considered for outer-planet spacecraft propulsion for future missions. In a typical mission, the spacecraft primary energy source may be required to deliver as high as 16 kW of power to the thruster system. This power level is quite high compared to system power levels developed in the past. It is therefore very important to utilize the maximum available power from the energy source at all times.

A preliminary study of maximum power utilization methods was performed for an outer-planet spacecraft using an ion thruster propulsion system and a solar array as the primary energy source. The problems which arise from operating the array at or near the maximum power point of its I–V characteristic are discussed. Two closed-loop system configurations which use extremum regulators to track the array maximum power point are presented. Also, three open-loop systems are presented that either (1) measure the maximum power of each array section and compute the total array power, (2) utilize a reference array to predict the characteristics of the solar array, or (3) utilize impedance measurements to predict the maximum power utilization. The advantages and disadvantages of each system are discussed and recommendations for further development are made.

Introduction

This article summarizes the results of a preliminary study of maximum power utilization methods for an outer-planet spacecraft using an ion thruster propulsion system and a solar array as the primary energy source. A block diagram of a typical power system with ion thruster power conditioning circuitry and spacecraft "housekeeping" subsystem is shown in Figure 1. Power required by the ion thrusters is regulated by dc-to-dc converters within the propulsion power conditioner. In a typical mission, the total array power required by the thruster power conditioner can be as high as 16 kW, which is quite large compared to power systems developed in the past. The spacecraft loads typically require 500 to 1000 W of power. If the total power required by the spacecraft exceeds the available array power, the

battery will support only the spacecraft loads since a battery large enough to provide 16 kW for any significant period of time is too bulky to be desirable.

Maximum Power Point Operating Problem

The I–V characteristics of a typical converter input, along with the corresponding output characteristics of a solar array, are shown in Figure 2. The voltage V_R in the figure is the solar array voltage above which the converter regulates its output voltage. During the regulating mode of operation, the converter functions as a constant power load on the solar array. Note, also, that the converter exhibits a negative resistance characteristic in this mode. Below V_R, the converter output voltage is not regulated, and the converter simulates a resistive load on the solar array. When voltage is initially applied to the converter input, the current required by the converter at V_R must be less than the available solar array current at V_R to obtain the regulating mode. This condition is illustrated by load line curve 1 in Figure 2, and point A is the resultant operating point. If the converter load power is increased after initial startup, load line curve 2 with three possible operating points can be obtained. Point B is the desirable operating point. Point C is an unstable operating point due to the negative resistance characteristic of the converter and the high resistance of the solar array at that point (see Reference 1). A converter operating at point C can be driven to either point B or D depending upon the direction of the perturbating signal. Point D is a stable operating point on the nonregulating portion of the curve. Curve 3 illustrates a converter load line with two possible operating points. Point E is the maximum power point of the solar array. Any incremental increase in power from curve 3 will cause the converter to snap to point F, which would be the nonregulating operating point. The system power demand would then need to be reduced to curve 1 to allow a desirable operating point on the solar array (I–V) curve.

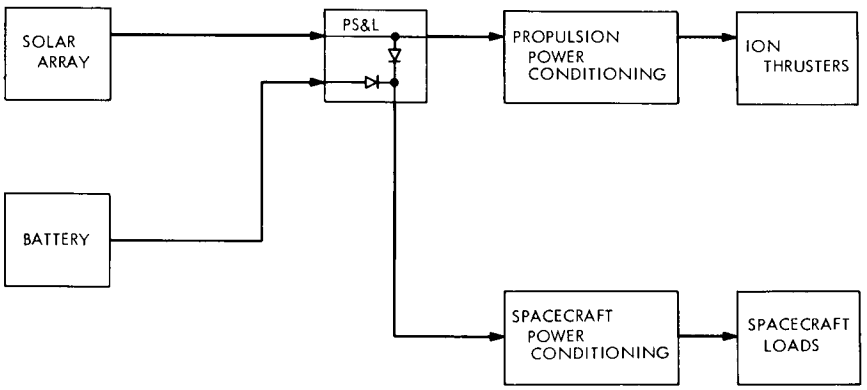

Figure 1. Block diagram of a solar electric propulsion spacecraft

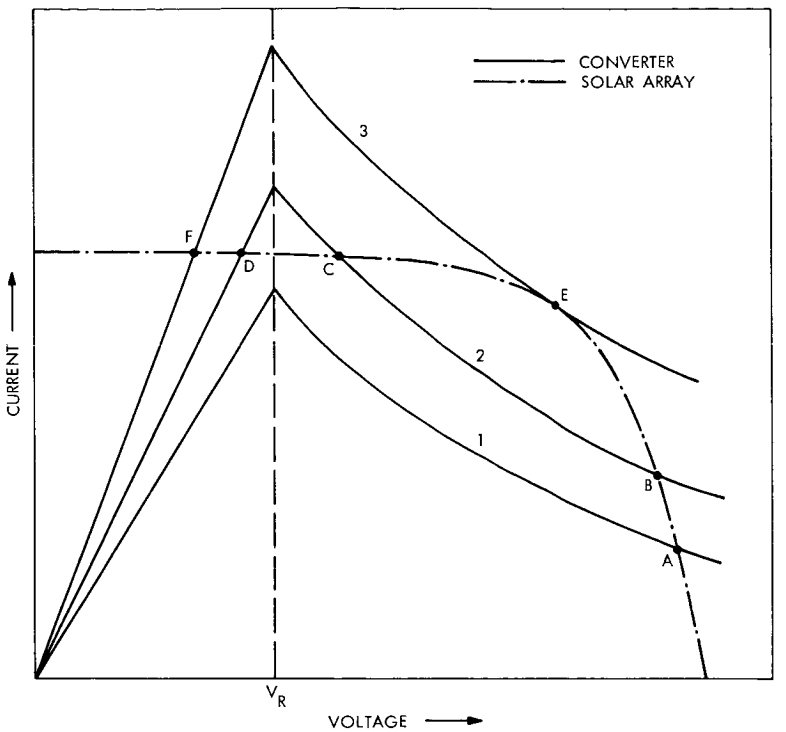

Figure 2. Solar array-converter operating points

The above discussion leads to the conclusion that active electronic systems are needed to operate at or near the solar array maximum power. To operate at the maximum power point, the active system can be a closed-loop system where a device is employed within the power system to "track" the array maximum power and constantly adjust the power system characteristics. Such a system must utilize a variable load in conjunction with the converter constant load to adjust for system fluctuations. An alternative approach that allows operation near the maximum power point is to use an open-loop system that either (1) measures the maximum power of an array section and computes the total array power, (2) utilizes a reference array to predict the characteristics of the solar array, or (3) utilizes impedance measurements to predict the maximum power utilization.

Closed-Loop Systems

Maximum power point trackers (MPPTs) fall into a general category of control systems called adaptive control systems. The MPPT is more precisely known as an extremum regulator. The extremum regulator differs

from a normal regulator which compares a controlled parameter (voltage or current) to a fixed reference. The extremum regulator continuously searches for the extremum position of the controlled parameter (power in this case) and maintains the system at that point regardless of the extremum variations.

There are two system configurations that can be considered for this application: a series tracker (Figure 3) and a parallel tracker (Figure 4). The block labeled MPPT in Figures 3 and 4 can be expanded into the functional block diagram in Figure 5 to provide a basic understanding of MPPT design principles (References 2–4). The block labeled T is a transducer which measures either the deviation of solar array power from the maximum power point or the derivative of power with respect to voltage. The output of T is called the search error signal. Block C is a control device which reverses the search direction. The control device must also determine either the time or sign of the search reversal, or produce an output proportional to the search error signal, depending on the type of system. Block E, the effector, produces the automatic search signal from either a small external continuous perturbation signal or directly from the feedback properties of the control loop. The effector must provide a constant output, about which the search signal oscillates, that corresponds to the extremum position. The effector is therefore an integrator. Block R is the regulator unit. This regulator is a pulse-width modulator. The regulator duty cycle is varied by the effector output such that the load impedance is matched to the array impedance and maximum power is thereby transferred. The accuracy of the extremum regulator depends primarily on the amplitude of the search oscillation. This amplitude is a function of transducer sensitivity and time delays within the control loop. System noise, in turn, determines the minimum allowable search oscillation amplitude. Extremum regulators are usually low frequency devices for this reason. Previously designed systems have tracked the maximum power within 1% (References 5–13).

Comparison of Series and Parallel Trackers

The series tracker's most desirable feature is operating point stability. Power detecting problems are reduced since system noise is isolated from the power detecting transducer by the series configuration. Also, since the *total* system power is controlled by the series tracker, the maximum power point can always be recovered after load transients (assuming that the variable load power remains greater than zero). This condition is not true for the parallel tracker. The parallel tracker is susceptible to the stability problem previously discussed (Figure 2). Heavy load transients may cause the parallel tracker system to "lock-up" at point D or F of Figure 2, since the power delivered to the thruster power conditioning is not controlled by the tracker. A parallel tracker system requirement, therefore, is that the system response time is fast enough to prevent the instability under all load transient and system noise conditions. This requirement could be quite severe since the extremum regulator is typically a low-frequency device as previously discussed.

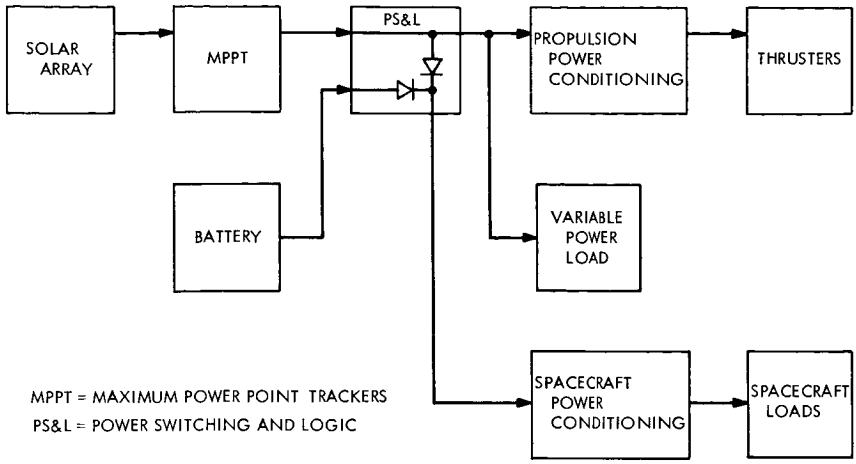

Figure 3. Series MPPT configuration

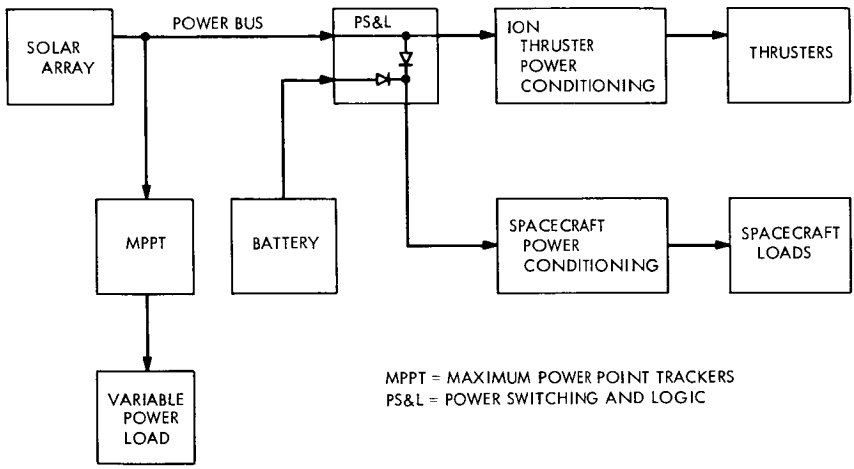

Figure 4. Parallel MPPT configuration

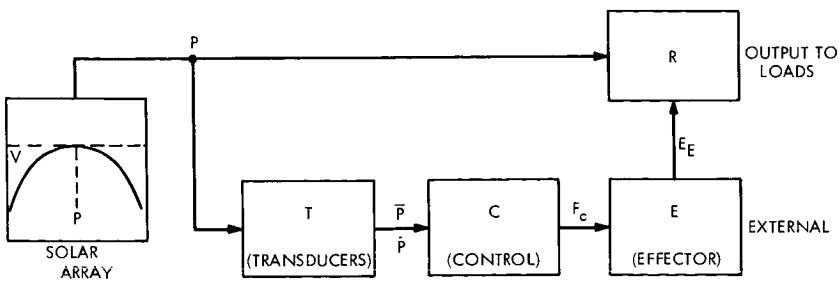

Figure 5. Extremum regulator functional block diagram

The main disadvantage of the series tracker is that the total array power must flow through the tracker. A pulse-width-modulated regulator is typically 90% efficient. Therefore, a maximum of 1440 W will be dissipated by the series tracker. This amount of power creates a severe thermal problem which requires heavy heat sinks and large electronic components. The series tracker design does not appear feasible for this reason. Also the 10% power loss compares unfavorably with open-loop systems which could probably predict the maximum power point within 10% with smaller, less dissipative circuitry.

The size of the parallel tracker depends primarily upon the power margin. The power margin can be defined as the difference between the maximum array power and the power consumed by the thruster and spacecraft power conditioning. The variable power load must then equal the power margin to allow the maximum power point operation. The minimum allowable power margin is determined as follows:

Power margin (min) = transient power + noise power + tracking error

where

Transient power = maximum system instantaneous step load change

Noise power = maximum instantaneous power from system noise

Tracking error = maximum error of the power tracking system

The power margin due to transients and noise is estimated to be 2%. If the tracking error is 1%, then the variable power load must be 16 kW × 3% = 480 W minimum at beginning of life. A variable power load of 1 kW appears reasonable. This load is quite large and there is no useful load on the spacecraft which could be employed; therefore, a dummy load must be used. This load could possibly cause thermal problems if it were constantly drawing power. A solution to this problem would be to track the maximum power just long enough to obtain a reading and adjust the system accordingly.

In summary, the series tracker has been determined to be unfeasible because of its thermal problem and excessive power loss. Further analysis of the parallel tracker instability problem is required to determine the feasibility of the parallel tracker. Its main advantage is its lower power dissipation. The parallel tracker approach will be compared to open-loop systems later.

Open-Loop Systems

Open-loop systems measure one or more array parameters and determine or predict the array maximum power point from this data. Three types of open-loop systems are discussed here: array section measurements, reference array measurements, and source-to-load impedance comparison. Other

methods such as array temperature and illumination measurements were reviewed and appeared to be too indirect for this application.

Array Section Measurements

One method of maximum power point detection is to measure the power of each array section and add the results. This method is presently being developed at JPL. A brief description of this method follows. The solar array to be measured is divided into a number of sections. Each section is normally connected to the solar array bus through an isolation diode. A transistor load is connected to one section at a time and the load is increased until the maximum power point of that section is traversed. The maximum power is measured with a peak detector and recorded. The load is stepped through each section and the process is repeated. As each section is loaded, its power is removed from the solar array bus by the isolation diode. The spacecraft power demands must therefore be reduced by the corresponding power contribution of each section prior to loading so that the remaining array power is not exceeded.

If the section maximum power points do not occur at the same voltage, they cannot be directly added to determine the total array maximum power since each array section is forced to operate at the same voltage during actual system operation. Each section must then be remeasured to determine its power at the established operating voltage of the array. The maximum power point voltage is primarily a function of temperature. Therefore, if large temperature gradients across the array are present during the power measurements, inaccuracies in the summation process are possible.

Reference Array

A second method of predicting the array characteristics is to place test cells at representative positions within each array section. The cells are connected to form a reference array which is electrically isolated from the actual array. The reference array can then be scanned to determine the maximum power point. The accuracy of the system depends mainly on the ability of the reference array to simulate actual array conditions. The size and location of the reference array sections are therefore very critical. The array cost is the primary factor that limits the size. The cost[1] is estimated at \$350/W. Therefore, to be practical, the array size is limited to the 50-W range, which is 0.25% of the actual array size. The electronic circuitry required to measure the maximum power point of a 50-W reference array can be quite simple and lightweight. A peak power detector and a scanning circuit are basically all that is required.

[1] Personal communications from W. A. Hasbach, JPL Photovoltaics Group, Spacecraft Power Section.

Impedance Comparison

A third method of maximum power prediction is accomplished by comparison of the load impedance and the solar array impedance. The array power can be expressed as

$$P_A = VI \tag{1}$$

and

$$\frac{dP_A}{dV} = \frac{V dI}{dV} + I\frac{dV}{dV} \tag{2}$$

At the maximum power point,

$$\frac{dP_A}{dV} = 0 \tag{3}$$

Therefore,

$$V\,dI + I\,dV = 0$$

or

$$\frac{V}{I} = -\frac{dV}{dI} \tag{4}$$

Equation 4 states that the load resistance determined by the dc operating point is equal to the dynamic resistance, or slope, of the solar array I–V curve at the maximum power point. It can be concluded that the load impedance to array impedance ratio is an index of the power mismatch. The degree of mismatch is dependent upon the shape of the solar array I–V curve. If the array I–V characteristics were linear, the power mismatch could be calculated within the accuracy of the impedance measuring devices. Unfortunately, this is not the case. For the case under consideration, the solar array characteristic may vary from the curve of Figure 2 to almost a straight line. Some additional information about the array characteristic, such as end points, is therefore needed to determine the shape of the I–V curve. Possibly the array open-circuit voltage and short-circuit current data from the transducers already on the spacecraft would provide sufficient accuracy.

The technique for measuring the solar array dynamic resistance is shown in Figure 6. A small perturbing signal e_{ac} is introduced onto the array bus through the transformer T. If the reactance of C is much less than the load resistance R_L at the perturbing frequency, the solar array is, in effect, directly across the secondary of T. If e_{ac} is constant in amplitude, then $1/r_a$,

the solar array conductance, is proportional to i_s. Therefore, i_s can be measured to determine the array dynamic resistance r_a.

Comparison of Open-Loop Systems

In this section the various open-loop measuring techniques are examined and the advantages and disadvantages presented in the system operation are discussed. The array section measurement system is probably the most accurate of the three systems if the temperature of each section is the same. The system accuracy then depends upon the sweep rate and the sensitivity of the power measuring circuitry. This system is the most complex of the three and must dissipate the array section power (up to 1.5 kW) for short periods of time. The necessity of reducing the power demands of the system during the maximum power measurement is also a disadvantage. However, this reduction in power is not a serious disadvantage if the maximum power measurements are infrequent.

The accuracy of the reference array system is questionable. The reference array maximum power can be calibrated to the actual array maximum power at the beginning of a mission. However, degradation due to space irradiation is unknown and damage from micrometeorites, etc., will always remain uncertain. The main advantage of this system is that the circuitry involved can be lightweight and easily designed.

The main advantage of the impedance comparison system is that it presents an actual array measurement which provides an index of power mismatch while the system is operating. A disadvantage is that the accuracy depends upon some outside knowledge of the array I–V characteristics which may be difficult to predict. It appears that the development of the actual hardware will also present some difficulties. The capacitor C of Figure 6 must be quite large and withstand an array voltage of up to 400 V. Also system noise may affect the accuracy of the dynamic resistance measurement.

In summary, further investigation of the reference array and impedance comparison system accuracies is required to determine the feasibility of the systems. The array section measurement system appears to be the most accurate of the three. However, this system is much more complex than the

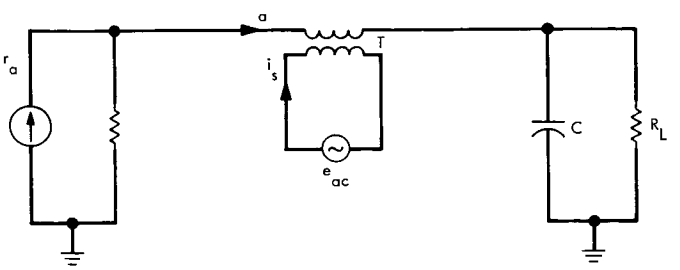

Figure 6. Solar array dynamic resistance measurement

other two and is larger in size and weight. The reference array system is the least complex and smallest in size and weight.

Comparison of Closed-Loop and Open-Loop Systems

The main advantage of the closed-loop system is the continuous accurate tracking of the maximum power point. However, the application of a maximum power point tracker design to an outer-planet spacecraft presents a number of problems. The solar array power output continuously varies with time which requires variable tracker characteristics and reference inputs. To accomplish this requirement, complex circuitry must be employed in conjunction with continuous power dissipating elements to force the system to operate at the maximum power point. Another disadvantage is the susceptibility of the tracker design to the anticipated high noise and transients present on the power lines from the thruster subsystem.

The array section measurement system compares closely with the tracker accuracy if the solar array section temperatures are all the same. This system is equally as complex as the parallel tracker and also has the disadvantage of system power reduction during operation. The system must dissipate the array section power which is approximately 1.5 kW. Therefore, it probably will require larger and heavier components than the parallel tracker, depending upon the time required for measurement.

The reference array and impedance comparison systems are much less complex and are much lighter than the parallel tracker. Again, the feasibility of these two systems depends upon further investigation of their accuracies.

Table 1. Summary of open-loop and closed-loop systems

Method	Type	Advantages	Disadvantages
Series tracker	Closed loop	Continuous accurate tracking of the maximum power point	Thermal problem, excessive power losses, requires dummy load, and complex circuitry
Parallel tracker	Closed loop	Continuous accurate tracking of the maximum power point	Complex circuitry, requires dummy load, operating point stability problem
Reference array	Open loop	Simplicity, lightweight	Accuracy is difficult to determine
Impedance comparison	Open loop	Provides power mismatch index	Accuracy is difficult to determine, possible component problems
Direct array measurement	Open loop	Provides actual array measurement	Power reduction is required, circuitry is complex, and array section temperatures must be the same

Summary

The various types of systems are listed in Table 1 with their advantages and disadvantages. Unfortunately, not one single system uniquely provides a solution to the power tracking problem. As previously stated, the direct array measurement system is presently being developed. Further development of the other systems is required before a conclusion can be made as to which system is best for this application.

References

1. Millman, J., and Taub, H., *Pulse, Digital, and Switching Waveforms*, Chapter 13, p. 476. McGraw-Hill Book Co., Inc., New York, 1965.

2. Ostrovski, Iv. I., "Extremum Regulation," *Automat. Rem. Contr.*, Vol. 18, No. 9, p. 900, 1957.

3. Morosanov, I. S., "Methods of Extremum Control," *Automat. Rem. Contr.*, Vol. 18, No. 11, p. 1077, 1957.

4. Wescott, J. H., "An Exposition of Adaptive Control," in *Proceedings of Symposium Held at the Imperial College of Science and Technology, London, 1961.* Pergamon Press, New York, 1962.

5. Dumont, A., et al., *Development of an Advanced Control Circuit for Satellite Power Systems*, First Progress Report. European Space Research Organization, Charleroi, Belgium, 1969.

6. *Non-Dissipative Solar Array Optimum Charge Regulator*, First Quarterly Report No. P65-125. Hughes Aircraft Co., Culver City, Calif., Oct. 1965.

7. Engelhardt, R. A., "Optimized Solar-Array-Battery-Space Power System," IEEE Twelfth East Coast Conference on Aerospace and Navigational Electronics, Oct. 1965.

8. Paulkovich, J., *Slope Detection as a Method of Determining the Peak Power Point of Solar Arrays*, X-636-64-282. Goddard Space Flight Center, Greenbelt, Md., Oct. 1964.

9. Boehringer, A. F., "Self Adapting dc Converter for Solar Spacecraft Power Supply," *IEEE Trans. Aerospace and Electronic Systems*, Vol. AES-4, No. 1, Jan. 1968.

10. *Final Report for Optimum Charging System Study Program*, Report No. 1906. Gulton Industries, Hawthorne, Calif., Aug. 1, 1966.

11. *Advanced Voltage Regulator Techniques as Applied to Maximum Power Point Tracking for the NIMBUS Meteorological Satellite*, Final Report AED R-3221. Radio Corporation of America, New York, Oct. 1967.

12. Knauer, P., "Automatic Impedance Matching in dc Circuits," *IEEE Trans. Aerospace and Electronic Systems*, Vol. AES-2, No. 6, Nov. 1966.

13. Hartman, D. A., "Adaptive Power Conditioning for Solar Cell Arrays," *IEEE Trans. Aerospace and Electronic Systems*, Vol. AES-2, No. 6, Nov. 1966.

Index: control and guidance, Mariner Mars 1971 Project, scientific instruments

Mariner Mars 1971 Scan Platform Pointing Calibration

G. D. Pace, G. I. Jaivin, and R. A. Virzi

Guidance and Control Division

Accurate calibration is required to meet the pointing accuracy requirements of science instruments mounted on a spacecraft scan platform. Calibration methods used on previous missions required excessive system-test time and did not achieve the desired accuracy. Therefore, a new technique was devised for the Mariner Mars 1971 mission wherein both ground and in-flight calibrations were performed. A more analytical approach was used for ground calibration, and in-flight calibration was performed using narrow-angle television pictures of stars. The results were outstanding, indicating the potential of this technique for future missions when imaging experiments are flown. The Mariner Mars 1971 calibration technique and results are summarized in this article.

Introduction

A 2-deg-of-freedom scan platform is utilized to point the Mariner Mars 1971 science instruments. Pointing of the platform relative to the spacecraft is accomplished by articulating the platform about its two control axes, clock and cone. The spacecraft attitude is stabilized in three axes by orienting celestial sensors to the Sun and the star Canopus. The locations of the scan platform, science instruments, and sensors on the spacecraft are shown in Figure 1.

One axis of the scan control subsystem is shown in Figure 2. Commands are received to step the platform in 0.25-deg steps. A stepper motor moves the wiper on a reference potentiometer to create a reference voltage. The analog servo loop responds until the feedback voltage cancels the reference voltage. Potentiometers geared to the gimbal provide feedback and telemetry measurements.

Errors in pointing the platform are caused by attitude sensor electromechanical offsets, clock and cone gimbal offsets and misalignments, spacecraft and platform structural misalignments, and scan control loop offsets. Determination of these errors by accurate calibration of platform pointing

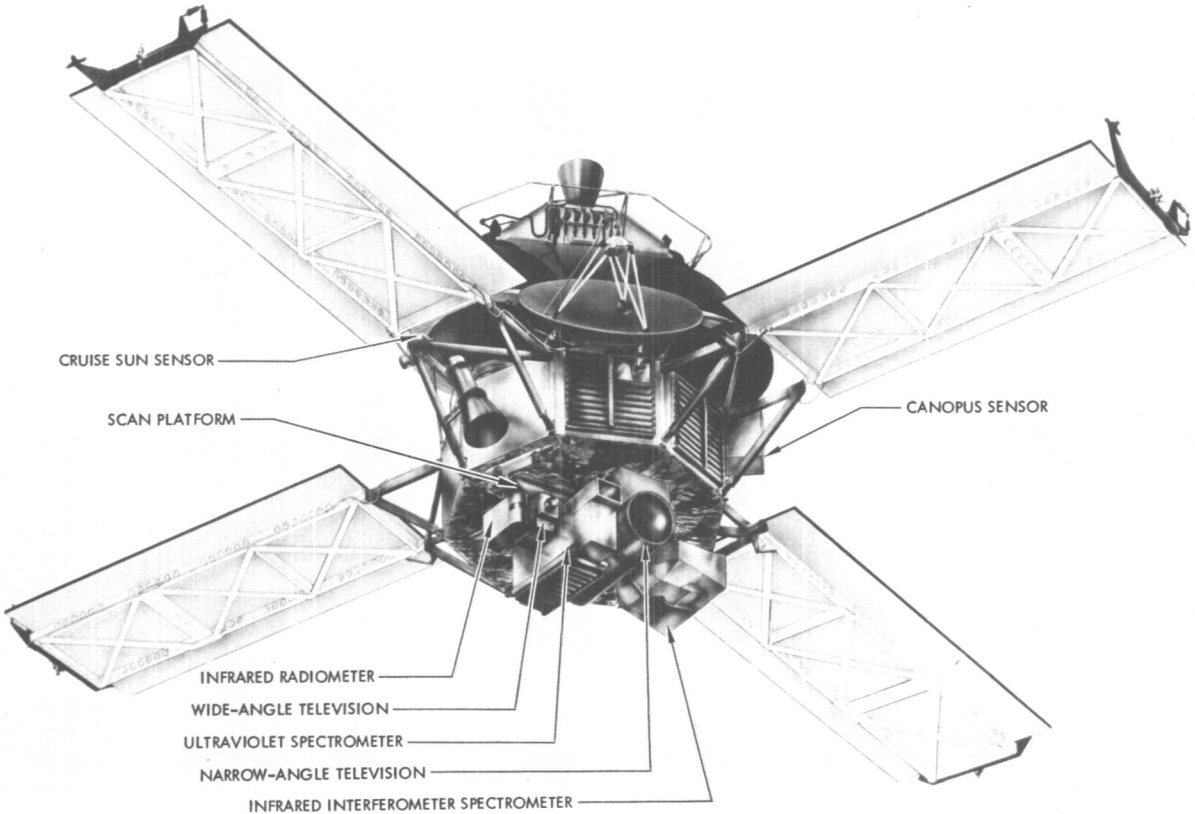

Figure 1. Mariner Mars 1971 spacecraft, showing scan platform, science instruments, and sensors

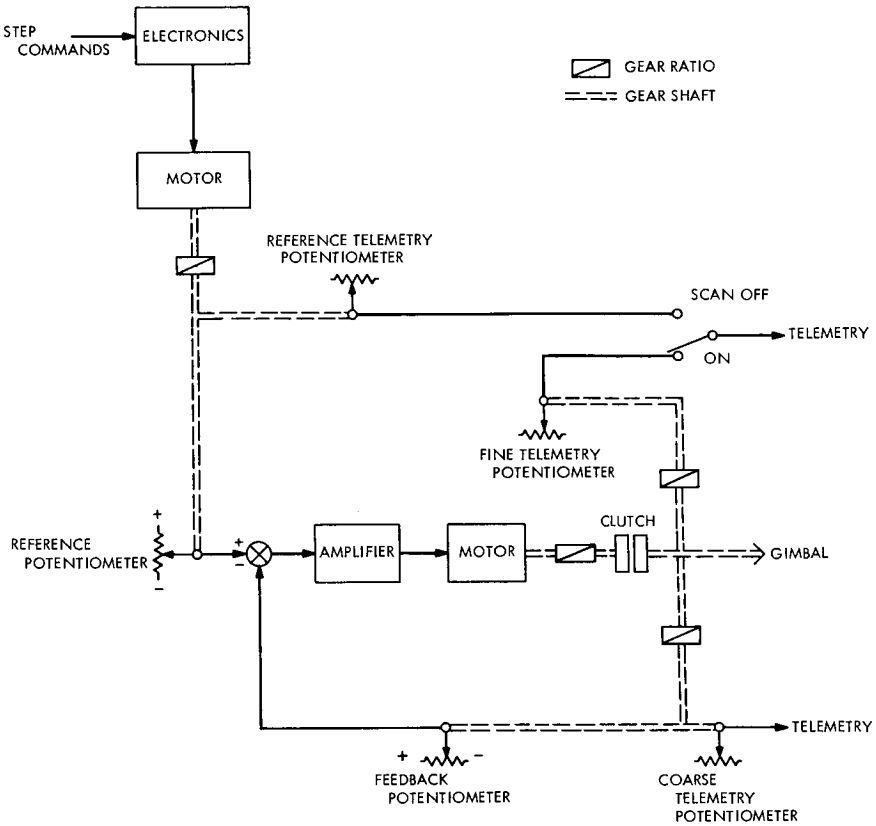

Figure 2. Single-axis scan control loop

was necessary to meet the pointing accuracy requirements of the science instruments. An *a priori* pointing control accuracy of 0.5 deg (3σ) and an *a posteriori* knowledge of where the platform pointed of 0.25 deg (3σ) were desired.

Experience on previous missions dictated that a new calibration technique be devised to meet these requirements. Most calibration data from previous missions were obtained by taking numerous electrical and mechanical measurements with the spacecraft in a full system configuration. This involved much effort and consumed much system-testing time. In addition, the results did not achieve the desired accuracy. Inaccuracies arose from the test instrumentation and from the fact that the scan actuators could not support the platform weight in a 1-g field. The test setup devised to support the platform was found to introduce mechanical distortions in the spacecraft and platform structure on the order of the biases being measured.

To overcome these drawbacks for the Mariner Mars 1971 mission, a two-part scheme was devised wherein the offsets and misalignments that cause pointing errors were combined into eight biases to be estimated in both

ground and in-flight calibrations (References 1 and 2). The ground calibration combined analytically the separate calibrations of the scan pointing elements. This allowed calibration to proceed simultaneously among several subsystems independently. System-level tests were limited to determining subsystem electromechanical interactions and verifying the analysis. The in-flight calibration, which utilized narrow-angle television pictures of stars, provided an end-to-end system calibration with an accuracy sufficient to ensure that science instrument pointing requirements could be met.

Ground Calibrations

The ground calibration plan consisted of three parts: telemetry calibration, control loop calibration, and calibration of the fixed electromechanical offsets. The subsystems and elements involved in the calibrations are illustrated in Figure 3 and discussed below.

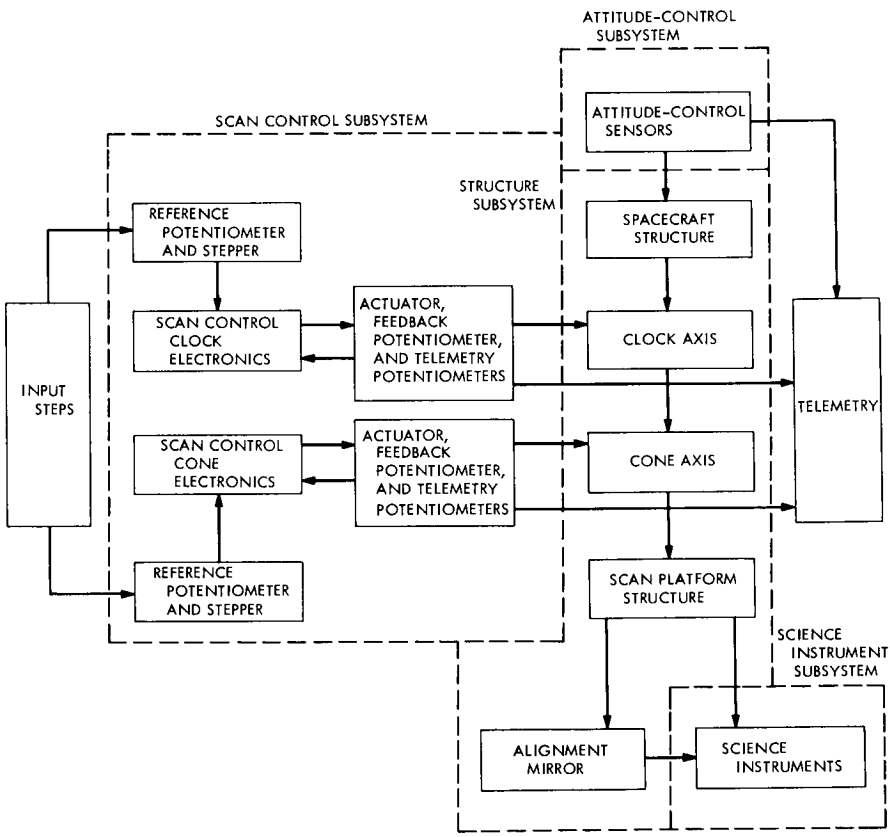

Figure 3. Subsystems and elements involved in scan platform ground calibration

Telemetry Calibration

Accurate telemetry calibration was required as part of the ground calibration, since limited improvement was possible in the in-flight calibration. The attitude-control sensor telemetry output versus error angle was fitted with a third-order polynomial to an accuracy of 0.015 deg. The scan coarse telemetry potentiometer output versus actuator output angle was fitted with a third-order polynomial to an accuracy of 0.08 deg.

Calibration of the fine telemetry potentiometer was complicated by the gear train system. Undefined resistance regions occurred on the potentiometer as it completed a revolution. Center-to-center gear radius variations and ellipticity introduced harmonics which affected the calibration. A sequential minimum-variance estimator with interactive data editing was programmed to provide a third-order fit and account for these factors. The resulting fine telemetry potentiometer calibration accuracy was 0.06 deg.

During telemetry calibration, two scan actuators exhibited high hysteresis. These were interchanged with actuators with low hysteresis. No recalibration was necessary since the plan allowed for exchange of subsystem elements.

Control Loop Calibration

Control loop calibration data were obtained on the reference and feedback potentiometers. Nonlinearities in the feedback potentiometers were causing errors of 0.3 deg when the data were fitted with a third-order polynomial. This polynomial fitting was replaced by a table lookup routine so that in-flight data could be included. The resulting accuracy was 0.1 deg.

Electromechanical Offset Calibration

Calibration data to determine the fixed electromechanical offsets were obtained from the structure, science instruments, and attitude-control sensors. Attitude-control sensor and science instrument offsets were measured relative to the mounting surface. Mechanical misalignments of the mounting surfaces relative to the spacecraft and platform structure were measured. Also, misalignments between the spacecraft and platform structure were measured. These measurements were analytically combined to provide overall instrument pointing offsets. These offsets were related to the scan gimbal telemetry in the final system-level testing. The overall accuracy of these calibrations indicated an uncertainty as large as 0.5 deg could exist. This was subsequently confirmed in the in-flight calibration.

The attitude-control Sun sensor nulls were expected to change by aging as much as 0.1 deg, with 90% of the change expected to occur after 6-wk operation. In-flight calibration was required to measure this change.

In-Flight Calibrations

Calibration Plan

To enhance the limited accuracy of the ground calibration, in-flight calibration was to be performed prior to Mars encounter. The spacecraft-based measurements to be used in the in-flight calibration were the attitude-control celestial sensor angles, scan platform gimbal angles, and the television pictures from the science television cameras. The attitude-control celestial sensors measure the orientation of the spacecraft with respect to the Sun and the star Canopus. The scan platform gimbals measure the orientation of the platform and television field-of-view with respect to the spacecraft. A television picture of a known object provides the true pointing direction of the television field-of-view. Stars were chosen as calibration objects primarily because their orientation relative to the spacecraft can be accurately determined.

The calibration was to be accomplished by calculating the expected image location of a star in a television picture from trajectory data and attitude-control and platform gimbal measurements. When the calculated location was compared to the observed television star image location, an estimate of the pointing biases could be determined.

Data Processing

To provide sequence planning, facilitate data handling, and perform the estimation of biases, an extensive system of computer software was developed. Software developed for the Mariner Mars 1971 optical navigation demonstration (Reference 3) was utilized as much as practical to reduce development time and cost.

Planning software used star catalogs and trajectory data to provide star geometry in spacecraft coordinates and star brightness information. In order to identify the images appearing in the television pictures, computer-generated overlays were produced for each picture that showed the stars visible in the camera's field-of-view. The overlays indicated both the position and the visual magnitude of the stars and facilitated the identification of the star images observed in the television pictures. A television picture taken during the Mariner 9 mission and its computer-generated simulation are shown in Figure 4.

The software developed to command the platform to the desired picture-taking position was also used to process the engineering telemetry data to obtain the celestial sensor and platform gimbal angles.

Pictures of the stars and planets were obtained using the narrow-angle science television camera. The vidicon's active target raster is electronically scanned in 700 lines and sampled at 832 picture elements (pixels) per line. The 500-mm focal-length lens results in a 1.1- × 1.4-deg field-of-view with an angular resolution of 6 arc sec. Each video sample is digitized to 9 bits (512 intensity levels) prior to transmission to Earth. In order to accurately

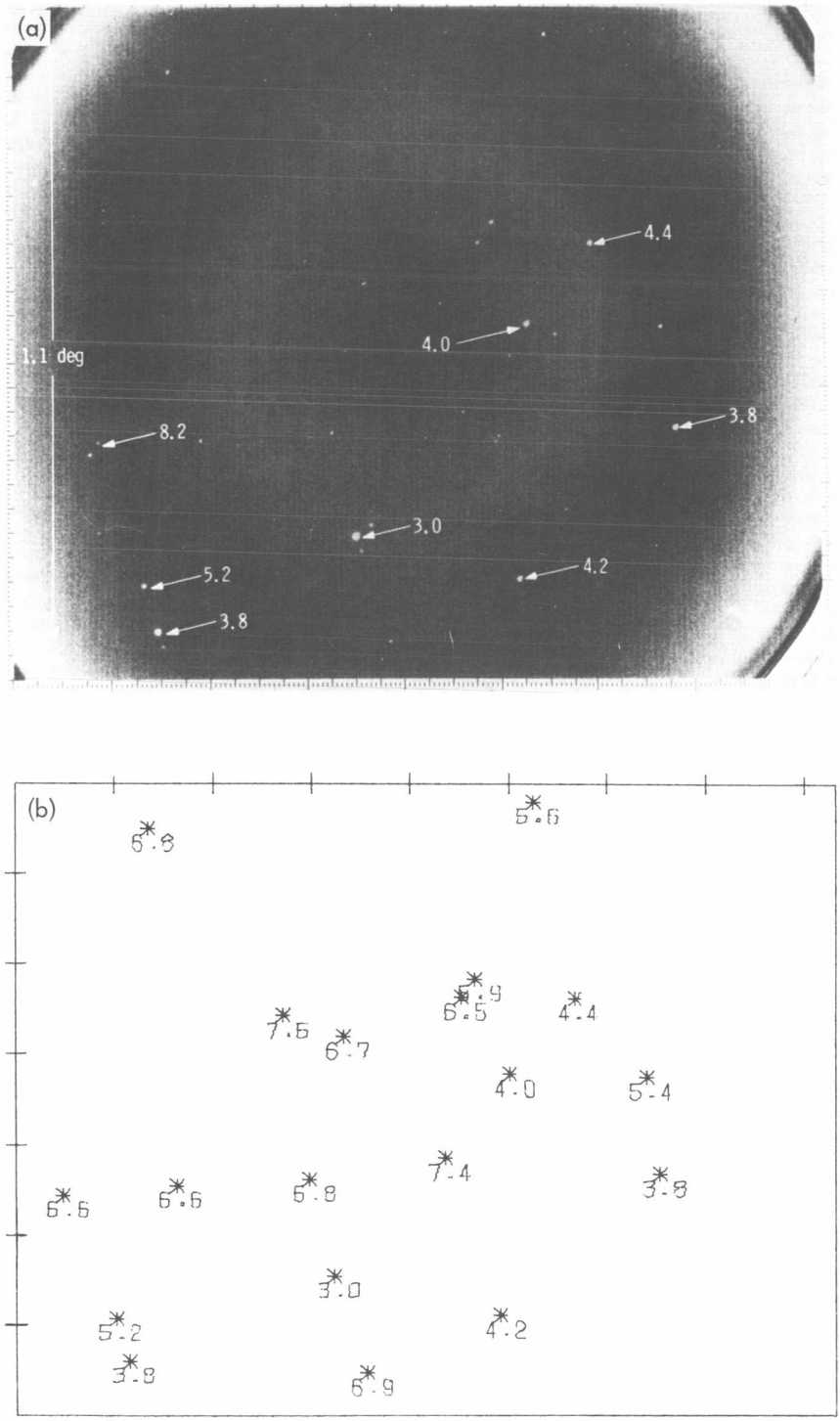

Figure 4. Star cluster Pleiades: (a) Mariner 9 television picture, (b) computer-generated simulation

measure the location of star images on the television picture, an image processing computer program was used to examine each picture in detail. This program generated both tabulated digital television data and contour maps of each star image (Figure 5). By this means, it was possible to determine the center of star images to ±1 pixel.

An estimation program provided a minimum-variance estimate of the biases in selected error parameters from the observed and expected positions of the images in the television pictures. An *a posteriori* estimate of the pointing error and its associated covariance matrix and an updated set of television picture orientation angles were computed for each picture.

Calibration Sequences During the Mission

Two calibration sequences were performed. The first sequence, performed 40 days prior to Mars encounter, consisted of taking 31 pictures targeted at bright stars, Saturn, and a bright compact star cluster. An overlapping picture pattern was chosen for this sequence to ensure the acquisition of an initial set of data that would allow the determination of any gross biases in the platform pointing system. A typical television picture from the first scan calibration sequence was shown in Figure 4a. The results of this calibration indicated a 0.5-deg post-launch bias in the platform cone gimbal null offset.

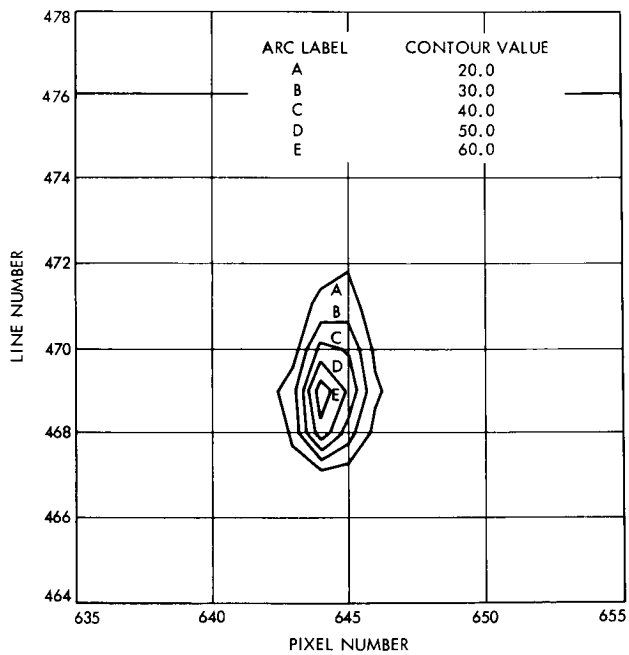

Figure 5. Video intensity contour plot of a 6.9-magnitude star

Achievement of an initial recalibration of the platform pointing system and the excellent vidicon sensitivity observed in the first set of pictures permitted some retargeting to optimize the second calibration sequence of pictures 7 days later. Targets for these 31 pictures were selected so as to require camera pointing over the entire dynamic range of scan platform motion. Two or more images were detected in 28 of these pictures, while a single image was observed in the remaining three.

Results and Conclusion

The ground calibrations were combined to provide the eight pointing offsets. The estimated accuracy of the ground calibration was 0.8 deg (3σ) for scan pointing control and 0.6 deg (3σ) for pointing knowledge. The accuracy was limited by the polynomial fitting errors in the control loop calibration and the large uncertainties in the calibration of the electromechanical offsets.

Of the eight separate biases determined from the in-flight calibration, major ones were a cone gimbal null offset of 0.48 deg and a clock gimbal null offset of 0.28 deg. Had the in-flight calibration not been performed, a scan pointing control error of 0.7 deg would have existed. Analysis of the second calibration sequence, using the biases determined in-flight, indicated that a scan pointing control accuracy of 0.49 deg (3σ) and a pointing knowledge accuracy of 0.16 deg (3σ) had been achieved, as compared to the desired values of 0.5 and 0.25 deg (3σ), respectively.

Thus, the results of the combined ground and in-flight calibrations were outstanding. The ground calibration technique saved a considerable amount of system-test time. In addition, it isolated problems and allowed subsystem elements to be interchanged without having to repeat major calibration tests. The in-flight calibration technique provided accuracy better than that required. On the basis of the success achieved for the Mariner Mars 1971 mission, it can be concluded that these techniques will be valuable on future missions when imaging experiments are flown.

References

1. "[Mariner Mars 1971] Scan Calibration Plan," in *Flight Projects*, Space Programs Summary, 37-61, Vol. I, pp. 12–14. Jet Propulsion Laboratory, Pasadena, Calif., Jan. 31, 1970.
2. *Mariner Mars 1971 Scan Platform Control Calibration and Alignment Plan*, 610-126, June 18, 1970 (JPL internal document).
3. Acton, C. H., *Processing On-Board Optical Data for Planetary Approach Navigation*, AIAA Paper 72-53, presented at the AIAA 10th Aerospace Sciences Meeting, San Diego, Calif., Jan. 17–19, 1972.

Index: control and guidance, mathematical sciences

Analysis of Morgantown Vehicle Steering Control

H. S. Lin and E. L. Marsh

Guidance and Control Division

The proposed Morgantown public transportation system will use a fleet of computer-controlled vehicles operating on a separate dedicated network of roadways called a "guideway." An automatic steering system on each vehicle will enable the traversal of the proposed route of various guideway sections.

This article describes a preliminary study made at JPL to analyze the steering control for the Morgantown vehicles. The primary requirement was to design an automatic steering system that would achieve a smooth ride and simultaneously eliminate the need for excess margin in the guideway width, a significant factor in overall system cost. Front- and rear-wheel steering and front and rear sensing capabilities were assumed in the analysis. The system finally adopted—front- and rear-wheel steering and front sensing—was shown by computer simulations and by Boeing Company vehicle steering experiments to be adequate.

Introduction

The proposed Morgantown public transportation system will use a fleet of computer-controlled vehicles operating on a separate dedicated network of roadways called a "guideway." An automatic steering system on each vehicle will enable the traversal of the proposed route of various guideway sections.

A preliminary study was made at JPL to analyze the steering control for the Morgantown vehicles. The primary requirement was to design an automatic steering system that would achieve a smooth ride and simultaneously eliminate the need for excess margin in the guideway width, a significant factor in overall system cost.

The analysis presented here begins with a derivation of the basic equations of motion governing the vehicle's travel along the guideway and proceeds through a discussion of the stability of a linearized system, the determination of the appropriate system control law, and a description of the system response.

Equations of Motion

The terms relevant to this analysis of the Morgantown vehicle and guideway are defined in Figure 1 and below:

B_0 = vehicle body designation

B_i = wheel designation
i = 1,3 for front wheels
i = 2,4 for rear wheels

S_i = sensor–guideway contact designation

p^* = vehicle mass center

$\mathbf{V}$ = velocity vector of p^*

$\mathbf{v}_i$ = velocity vector of center of wheel

$f(x)$ = equation for left edge of guideway

$g(x)$ = equation for right edge of guideway

α_i = wheel sideslip angle

β = vehicle sideslip angle

δ_i = wheel steering angle

In Figure 1, axes X and Y are fixed in an inertial reference frame N, with unit vectors $\mathbf{n}_X$ and $\mathbf{n}_Y$. Unit vectors $\mathbf{n}_1$, $\mathbf{n}_2$, and $\mathbf{n}_3$ are fixed in the vehicle body B_0. With $\mathbf{n}_3$ also fixed in N, the vehicle can experience neither roll nor pitch motion. Thus, only those forces and torques that can influence yaw–lateral motion are shown in Figure 1.

A wind force $\mathbf{W} = W\mathbf{n}_2$ is assumed to act parallel to $\mathbf{n}_2$. Forces exerted over the contact patch of a single wheel can be replaced by the equivalent system of a single force passing through the contact patch center and a couple. In Figure 1, the component parallel to the X–Y plane of the resultant force exerted on wheel B_i is denoted $\mathbf{F}_i$, and the component parallel to $\mathbf{n}_3$ of the couple exerted on wheel B_i is denoted $\mathbf{T}_i$. Forces exerted on S_i are equated to a single force and couple, where the surface plane and $\mathbf{n}_3$ components are denoted $\mathbf{f}_i$ and $\mathbf{t}_i$, respectively.

Usually, $\mathbf{F}_i$ is further resolved into a component parallel to the wheel plane (the traction force) and a component normal to the wheel plane (the lateral force). In the ensuing analysis, the traction force is ignored. Furthermore, $\mathbf{T}_i$ is assumed to be negligible. As a final simplification, the sensor reaction forces and couples $\mathbf{f}_i$ and $\mathbf{t}_i$ are assumed to be small. The vehicle yaw attitude and lateral displacement are then governed entirely by the lateral wheel forces.

The equations of lateral and yaw motion are:

$$\left(\sum_{i=1}^{4} \mathbf{F}_i + \mathbf{W} - M\dot{\mathbf{V}}\right) \cdot \mathbf{n}_2 = 0 \tag{1}$$

$$\left(\sum_{i=1}^{4} \mathbf{r}_i \times \mathbf{F}_i - I\ddot{\psi}\mathbf{n}_3\right) \cdot \mathbf{n}_3 = 0 \tag{2}$$

where M and I are the mass and yaw-axis inertia, respectively, of B_0, and $\mathbf{r}_i$ is the position vector of the center of the wheel contact patch with respect to p^*. More explicitly, when the following relationships are established:

(1) $\mathbf{F}_i$ expressed as a function of slip angle α_i.

(2) $\dot{\mathbf{V}}$ expressed in terms of the kinematic variables β and ψ.

(3) Slip angle α_i expressed in terms of the kinematic variables β and ψ and steering angles δ_i.

(4) Steering angles δ_i related to sensor errors via the steering control law.

then, upon linearizing along the nominal trajectory of the vehicle center, which in this case is the center of the guideway, the following two equations result:

$$\begin{aligned}\left[-2\frac{Ca}{V} + \frac{2C(L-a)}{V} - MV\right]\dot{\psi} - 2C\,[(K_1 + K_3)(a+c) \\ + (K_2 + K_4)(L - a + d)]\,\psi - MV\dot{\beta} - 4C\beta \\ - 2C(K_1 + K_2 + K_3 + K_4)y = -W\end{aligned} \tag{3}$$

$$\begin{aligned}I\ddot{\psi} - 2\frac{C}{V}[a^2 - (L-a)^2]\,\dot{\psi} - 2C\,[a(a+c)K_1 - (L-a)(a+c)K_3 \\ + a(L - a + d)K_2 - (L-a)(L - a + d)K_4]\,\psi - 2C(L-a)^2\beta \\ - 2C\,[aK_1 + aK_2 - (L-a)K_3 - (L-a)K_4]\,y = 0\end{aligned} \tag{4}$$

The parameter C is referred to as the wheel cornering power coefficient, the variable y is the distance between the center of the vehicle and the center of the guideway, and the K_i's are control-system gain parameters associated with the assumed control law

$$\left.\begin{aligned}\delta_F &= K_1 D_F + K_2 D_R \\ \delta_R &= K_3 D_F + K_4 D_R\end{aligned}\right\} \tag{5}$$

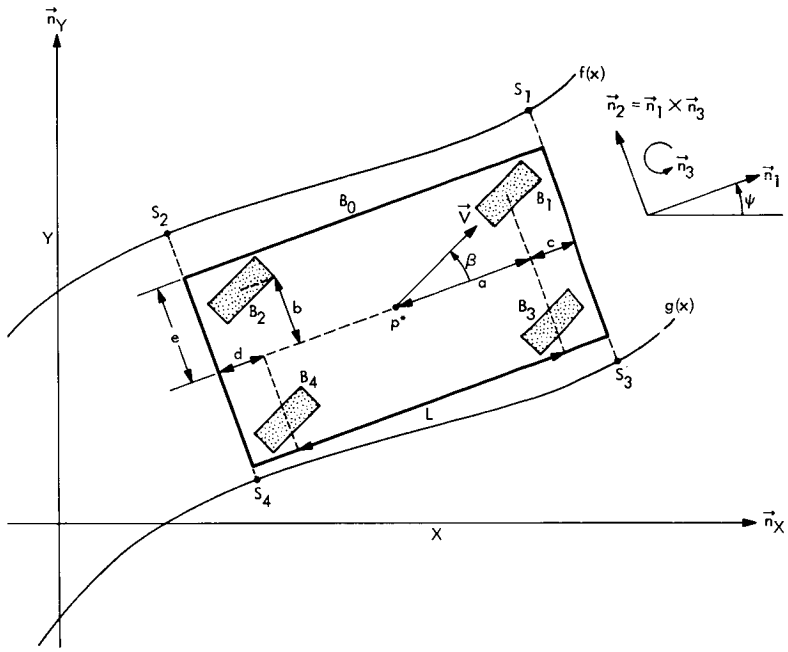

WHEEL VARIABLES WHEEL FORCES

(ILLUSTRATIONS SHOW WHEEL B_1)

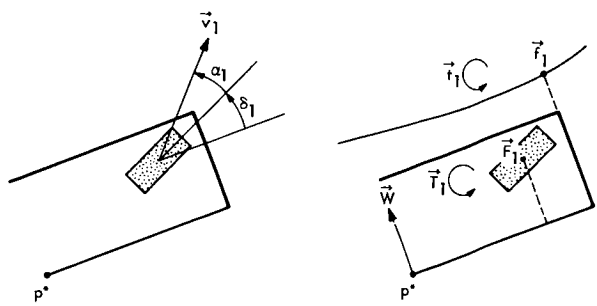

Figure 1. Definition of terms for vehicle and guideway in inertial reference frame

where δ_F and δ_R are the front and rear steering angles, respectively (i.e., $\delta_F = \delta_1 = \delta_3$, $\delta_R = \delta_2 = \delta_4$), and D_F and D_R are the front and rear sensing errors. On a straight guideway, D_F and D_R can be further expressed as

$$\left.\begin{aligned} D_F &= -[y + (a + c)\psi] \\ D_R &= -[y - (L - a + d)\psi] \end{aligned}\right\} \tag{6}$$

The kinematical relationship

$$\dot{y} = V(\psi + \beta) \tag{7}$$

together with Equations 3 and 4 form a consistent set of equations that can be rewritten in vector form as

$$\dot{u} = Au \tag{8}$$

where u is a (1 × 4) vector with components

$$u_1 = \psi, \quad u_2 = \dot{\psi}, \quad u_3 = \beta, \quad u_4 = y \tag{9}$$

and A is a constant (4 × 4) matrix whose elements are functions of the following system parameters[1]:

L = 2.794 m (9.167 ft)

a = 1.397 m (4.584 ft)

c,d = 0.59 m (1.92 ft)

e = 0.9145 m (3.0 ft)

V varies parametrically ($0 \leq V \leq 13.4$ m/s)

M = 3409.1 kg (233.6 slugs)

I = 3607.4 kg-m^2 (2658.33 slug-ft^2)

C = 87,273.7 N (19,620 lb)

W = 0

Stability of the Linearized System

The system of Equations 8 is asymptotically stable if the eigenvalues of A have negative real parts. This can easily be determined by applying the Routh criteria to the characteristic equation

[1] Values in customary units are included in parentheses after values in SI (International System) units if the customary units were used in the measurements or calculations.

$$|A - sI| = 0 \tag{10}$$

In more detail, the general characteristic equation derived from the equations of motion is[2]

$$\begin{aligned} C(S) = {} & 0.00008432VS^4 + 0.08177S^3 \\ & + S^2[18.304/V + 0.01478V(K_1 + K_2 + K_3 + K_4) \\ & + 0.0371V(K_1 - K_2 - K_3 + K_4)] \\ & + S[9.152(K_1 + K_2 + K_3 + K_4) + 13.000(K_1 - K_2 - K_3 + K_4)] \\ & + 2.000V(K_1 + K_2 - K_3 - K_4) + 26.000V(K_1K_4 - K_2K_3) \end{aligned} \tag{11}$$

The five special cases of practical interest that were investigated in detail are:

(1) Front-wheel steering based on front sensing ($K_2 = K_3 = K_4 = 0$).

(2) Front- and rear-wheel steering based on front sensing ($K_2 = K_4 = 0$).

(3) Front- and rear-wheel steering based on front and rear sensing, respectively ($K_2 = K_3 = 0$).

(4) Front- and rear-wheel steering through the same angle, but in opposite directions, based on front and rear sensing ($K_1 = -K_3$, $K_2 = -K_4$).

(5) Front- and rear-wheel steering in parallel, based on front and rear sensing ($K_1 = K_3$, $K_2 = K_4$).

The stability regions for cases 2–4 are shown in Figures 2–4. Case 1 is a special case of case 2 or 3; case 5 is always unstable (in the sense that asymptotic stability can never be achieved), as can be shown from the system equations of motion (Equations 8). In the above cases, the speed of the vehicle, V, is assumed to be 13.4 m/s (44 ft/s). It can be shown by a direct application of the Routh criteria that, for this configuration, if the steering system is stable for $V = 13.4$ m/s, it is stable for all $0 < V \leq 13.4$ m/s (44 ft/s). The stability plots provide a convenient reference for choosing gain parameters K_i, since only the sets of K_i within the stable regions would guarantee a stable system. In selecting K_i, the system transient response and its steady-state errors should also be taken into consideration.

[2] All coefficients in Equation 11 were calculated in the slug-ft-s system.

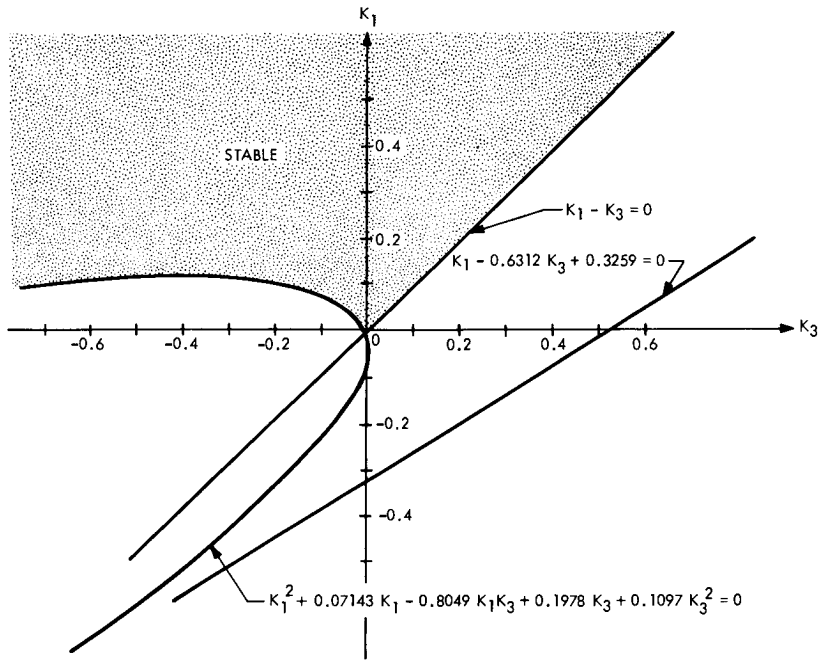

Figure 2. Stability region for case of front- and rear-wheel steering based on front sensing

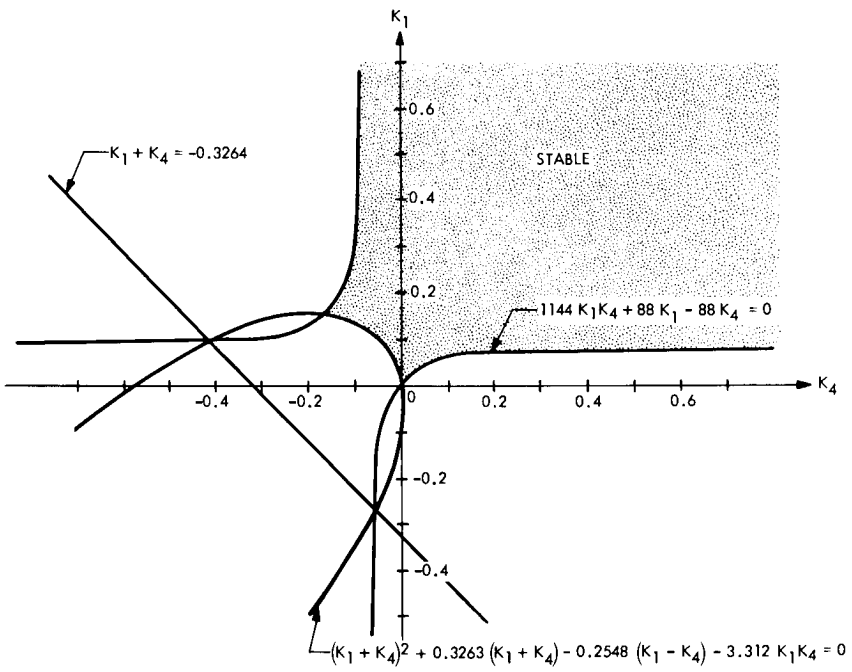

Figure 3. Stability region for case of front- and rear-wheel steering based on front and rear sensing, respectively

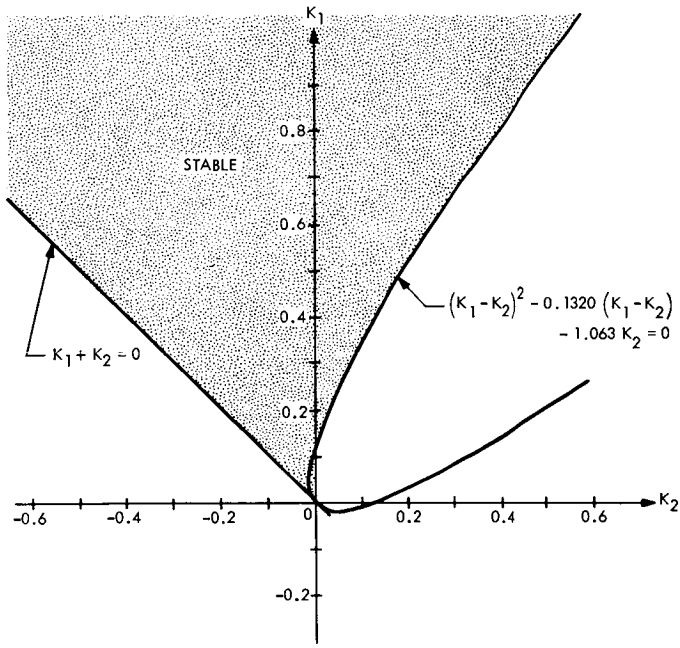

Figure 4. Stability region for case of front- and rear-wheel steering through same angle, but in opposite directions, based on front and rear sensing

System Control Law

Since the width of the guideway is the major consideration in the present design, a possible "best candidate" of the control laws can be determined by the following procedures: Assume that the vehicle is traveling at a constant speed of 1.829 m/s (6 ft/s) along a guideway with a 9.144-m (30-ft) constant radius of curvature ρ (Figure 5). In this case, it is clear that $\ddot{\psi} = 0$, $\dot{\beta} = 0$, and $\dot{\psi} = V/R_c$, where R_c is the distance between the center of curvature and the center of the vehicle (Figure 5). Further, assume

$$\delta_R = k\delta_F \tag{12}$$

where k is a constant to be determined.

The angle β can be determined from the vehicle dynamic equations as

$$\beta \cong \left[\frac{-MV}{4C} + \frac{a(1+k)}{V(1-k)}\right]\frac{V}{R_c} \tag{13}$$

From geometrical reasoning, it is obvious that the guideway width can be minimized if and only if $\beta = 0$ or $k = -0.954$.

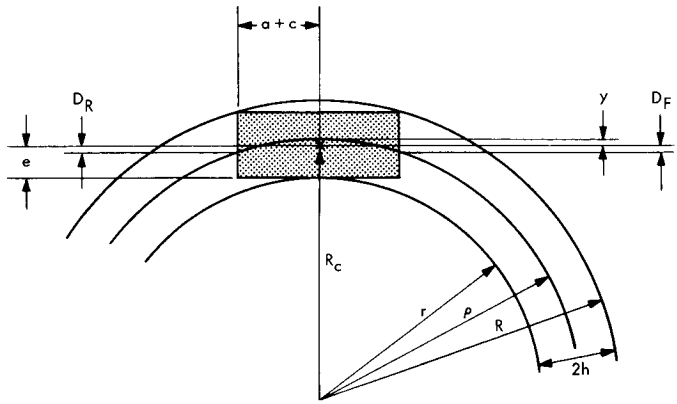

Figure 5. Definition of terms for vehicle on guideway with constant radius of curvature ρ

For convenience in hardware mechanization, the factor k is chosen to be -1; i.e., the rear wheels would be steered through an angle of the same magnitude but in the opposite direction with respect to the front wheels. The value of β in this case turns out to be approximately -0.0035 rad.

Using the value $\beta \cong 0$ and the geometry of Figure 5, the values of r, $2h$, R, and y can be determined to be

$$\left.\begin{aligned} r &= 8.132 \text{ m } (26.679 \text{ ft}) \\ 2h &= 2.024 \text{ m } (6.642 \text{ ft}) \\ R &= 10.156 \text{ m } (33.321 \text{ ft}) \\ y &= -0.0978 \text{ m } (-0.321 \text{ ft}) \end{aligned}\right\} \tag{14}$$

The front- and rear-wheel steering angles corresponding to the case $k = -1$ and $\beta \cong 0$ are

$$\delta_F = -\delta_R \cong \frac{a}{R_c} = 0.154 \text{ rad} \tag{15}$$

For the sake of simplicity, front sensing (i.e., $K_2 = K_4 = 0$) will be assumed. The front sensing error D_F can also be determined from the geometry shown in Figure 5.

$$D_F \cong \frac{(a+c)^2}{2 \times 9.144} + y$$

$$= 0.117 \text{ m } (0.384 \text{ ft}) \tag{16}$$

Thus, the control law can be determined to be

$$\left.\begin{aligned} K_1 &= -K_3 = \delta_F / D_F = 1.312 \text{ m}^{-1} \ (0.4 \text{ ft}^{-1}) \\ \delta_F &= 1.312 D_F \\ \delta_R &= -1.312 D_F \end{aligned}\right\} \tag{17}$$

System Response

The transient response of the steering system was predicted from root-locus plots generated by a computer.[3] In these plots, only the positive imaginary axis appears since root loci are symmetrical to the real axis. Reproductions of two such plots corresponding to vehicle speeds V = 1.829 and 13.4 m/s (6 and 44 ft/s) are shown in Figures 6 and 7, respectively. From these figures, it was concluded that the system is well damped at low speed (1.829 m/s); however, at high speed (13.4 m/s), the damping factor decreases to approximately 0.38. The fact that the system tends to be less stable at a higher speed can easily be understood from the variation of the system's open-loop poles and zeros positions as a function of speed V (Table 1).

[3] All quantities in the root-locus plots were calculated in the slug-ft-s system.

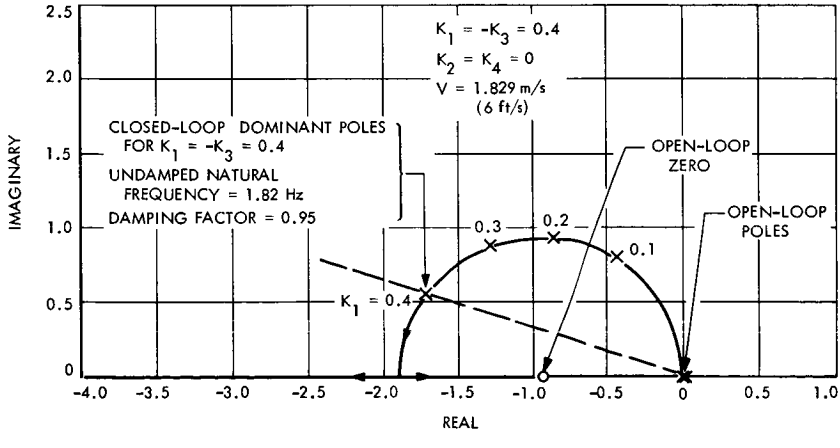

Figure 6. Root loci for low-speed travel with front- and rear-wheel steering (positive imaginary axis only)

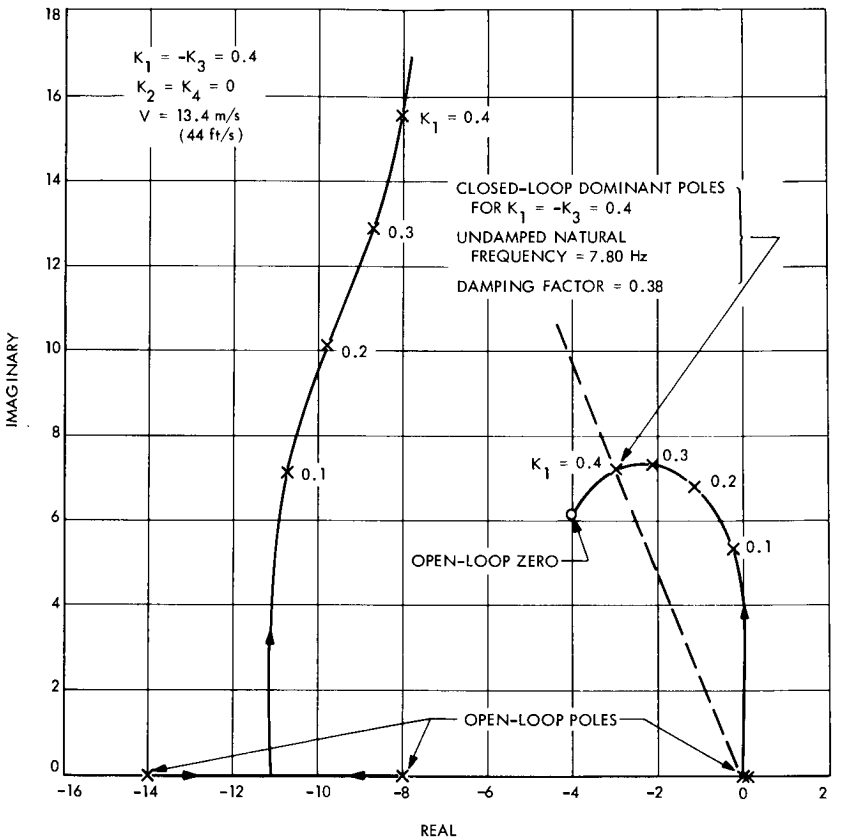

Figure 7. Root loci for high-speed travel with front- and rear-wheel steering (positive imaginary axis only)

Table 1. Open-loop poles and zeros for steering system

Case	Speed V m/s	Speed V ft/s	Open-loop poles Real	Open-loop poles Imaginary	Open-loop poles Order	Open-loop zeros Real	Open-loop zeros Imaginary	Open-loop zeros Order
Front- and rear-wheel steering	1.829 (Figure 6)	6	0	0	2	-0.938	0	1
			-58.461[a]	0	1	-57.463[a]	0	1
			-103.140[a]	0	1			
	3.353	11	0	0	2	-1.793	0	1
			-31.872	0	1	-30.062	0	1
			-56.289	0	1			
	7.273	23.86	0	0	2	-7.343	0	2
			-14.695	0	1			
			-25.950	0	1			
	10.058	33	0	0	2	-5.309	5.072	1
			-10.602	0	1	-5.309	-5.072	1
			-18.780	0	1			
	13.411 (Figure 7)	44	0	0	2	-3.984	6.170	1
			-7.968	0	1	-3.984	-6.170	1
			-14.072	0	1			
Front-wheel steering only	13.411 (Figure 8)	44	0	0	2	-4.854	3.874	1
			-7.968	0	1	-4.854	-3.874	1
			-14.072	0	1			

[a] Not shown on Figure 6.

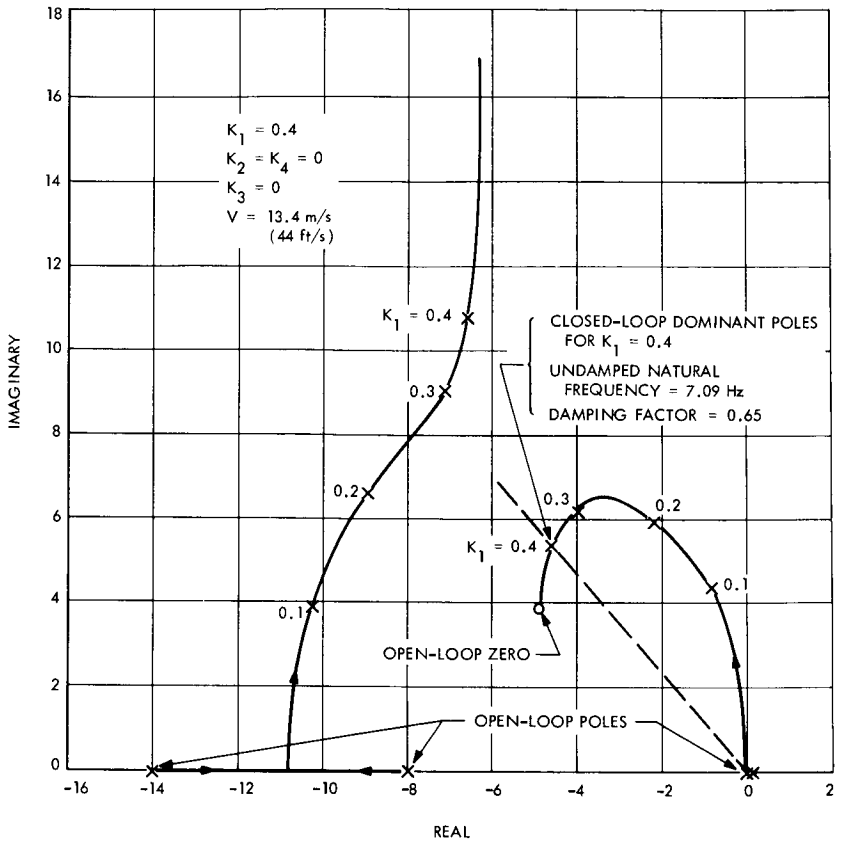

Figure 8. Root loci for high-speed travel with front-wheel steering only (positive imaginary axis only)

To improve the system response, it is suggested that the rear-wheel steering capability be switched off at high speed. The improvement in this case can be determined from the root-locus plot in Figure 8, where a satisfactory damping factor of 0.65 is indicated.

The dynamic response of the steering system was further verified by an extensive computer simulation study (Reference 1) and by vehicle steering experiments conducted at the Boeing Company.

Concluding Remarks

From the above analysis and the simulation and experimental results, it is concluded that a satisfactory control law can be implemented by setting

$$\left.\begin{aligned} \delta_F &= 1.312 D_F \\ \delta_R &= -1.312 D_F \text{ at low speed} \\ &= 0 \text{ at high speed} \end{aligned}\right\} \tag{18}$$

However, it should be noted that the control law was analyzed and simulated under idealized conditions:

(1) A linearized model of vehicle dynamics was assumed.

(2) The speed of the vehicle was assumed to be constant.

(3) The sensing device was considered to be perfect, i.e., no sensor lag and perfect calibration (no mismatch).

(4) No coupling of the yaw-lateral motion with other degrees of freedom (e.g., roll) was considered.

Any variation from these conditions could have serious impact on the guideway width determination.

Reference

1. Lin, H. S., and Marsh, E. L., *Steering Problems Associated With the Morgantown Vehicle*, Engineering Memorandum 344-339-HSL/ELM, Apr. 14, 1971 (JPL internal document).

Index: chemistry, energy storage, nonmetallic materials

Lifetime Estimates for Sterilizable Silver–Zinc Battery Separators

E. F. Cuddihy, D. E. Walmsley, and J. Moacanin

Propulsion Division

The lifetime of currently employed separator membrane in the electrolyte environment of JPL silver–zinc batteries has been estimated at 3 to 5 yr. The separator membranes are crosslinked polyethylene film containing grafted poly(potassium acrylate) (PKA), the latter being the hydrophilic agent which promotes electrolyte ion transport. The lifetime was estimated by monitoring the rate of loss of PKA from the separators, caused by chemical attack of the electrolyte, and relating this loss rate to a known relationship between battery performance and PKA concentration in the separators.

Introduction

Sterilizable separator membranes for silver–zinc batteries can be prepared by grafting poly(potassium acrylate) (PKA) onto a thin film of crosslinked polyethylene (PE). The crosslinked PE film provides the mechanical strength and heat stability while the PKA provides the required hydrophilic character for electrolyte ion transport. In service, the separators become black because of the oxidizing effect of the 45% KOH electrolyte solution which contains dissolved silver ions (≈30 mg/liter). The resulting silver deposition (References 1–8) within the membrane is paralleled with a continuous loss of PKA. Inasmuch as battery performance depends on ion transport through the hydrophilic PKA phase, deterioration of battery performance is tied directly to the rate of loss of PKA.

Details of the loss of PKA, the relationship between PKA concentration and battery performance, and the interrelationship between these two which forms the basis for the lifetime estimate are discussed. Also presented are recent experimental data which are not in concert with the accepted mechanism of PKA loss, causing a re-examination of the loss mechanism. Finally, preliminary results are given which indicate that a new potential hydrophilic agent, poly(potassium methacrylate), may be more stable to battery electrolyte than PKA.

Results and Discussion

Separator Lifetime

The half-life of these separators (identified as GX-152 membranes), expressed in terms of PKA loss, has been found to be 957 days (2.62 yr) at 25°C. This was determined experimentally by monitoring the loss of PKA at 135, 95, and 65°C. These data (Table 1) were found to obey first-order kinetics and are shown plotted in Figure 1. Rate constants were determined and plotted in Figure 2 according to the Arrhenius relationship.

Details of the experimental techniques and method of analysis of PKA in the separators have been previously discussed (References 6, 7, and 8).

Battery performance

The ease of electrolyte ion transport through a separator membrane can be measured in terms of a parameter called *membrane resistance.* This parameter is measured as follows. The resistance of a 40% KOH electrolyte solution between two electrodes is first measured. A separator membrane is then placed between the electrodes and the additional resistance which is measured above the separator-free value is taken as the *membrane resistance.*

In Figure 3 a plot of membrane resistance versus percent PKA graft is reproduced from the literature (Reference 9). This data shows that minimum resistance is achieved above 40% PKA, whereas as PKA decreases below this value, the resistance begins to increase rapidly. At 20% PKA, the resistance curve rises almost vertically, implying a shutoff of battery performance as PKA concentrations go below 20%.

The current JPL separators are prepared with an initial PKA concentration of near 45%. Using the half-life data, the PKA concentration will drop at ambient to near 22.5% in 957 days (2.62 yr) and to near 11% in another 957 days. The implication of Figure 3 is that the current JPL separator will cause a cessation of battery operation after 3–5 yr of service.

PKA Loss Mechanism

Heretofore it has been accepted that the PKA loss mechanism occurred through oxidative attack of the dissolved silver ions, resulting in deposition within the membrane of reduced metallic silver and chemical cleavage of the PKA. It was also known that some PKA was lost through exposure of the membranes to sterilization for 120 h at 135°C in 45% KOH, but it was felt that this PKA was residual homopolymer left after the grafting reaction.

Some recent experimental data, however, have necessitated a reexamination of this simple picture of PKA loss by silver ion oxidation. Samples of pure poly(potassium acrylate) homopolymer were dissolved in 45% KOH and a silver-oxide-saturated 45% KOH solution, and the specific viscosities monitored as a function of time at 95°C. The specific viscosities are related to the molecular weight of the dissolved polymer, and decreases in

Table 1. Poly(potassium acrylate) loss and silver accumulation in sterilized[a] GX-152 membranes exposed to Ag_2O-saturated 45% KOH battery electrolyte solution

135°C			95°C			65°C		
Time, h	Initial[a] PKA remaining in separator, %	Silver[b] accumulation	Time, h	Initial[a] PKA remaining in separator, %	Silver[b] accumulation	Time, h	Initial[a] PKA remaining in separator, %	Silver[b] accumulation
0	100	0	0	100	0	0	100	0
12	85	1.8	69	85	1.0	1720	94	1.8
140	68	0.9	316	78	4.7	2804	88	3.0
360	54	2.6	800	65	1.6	5200	83	4.7
700	38	1.8	1728	48	1.6			
840	33	2.9	3150	40	2.9			
			4950	27	4.7			

[a] Sterilized by exposure to 45% KOH solution for 120 h at 135°C. Average PKA loss from sterilization was near 20 wt %. PKA remaining in separator samples after sterilization was taken as the levels at the beginning of the exposure to the Ag_2O-saturated solution.

[b] Expressed as an equivalence ratio, silver atoms deposited per molecule of potassium acrylate lost.

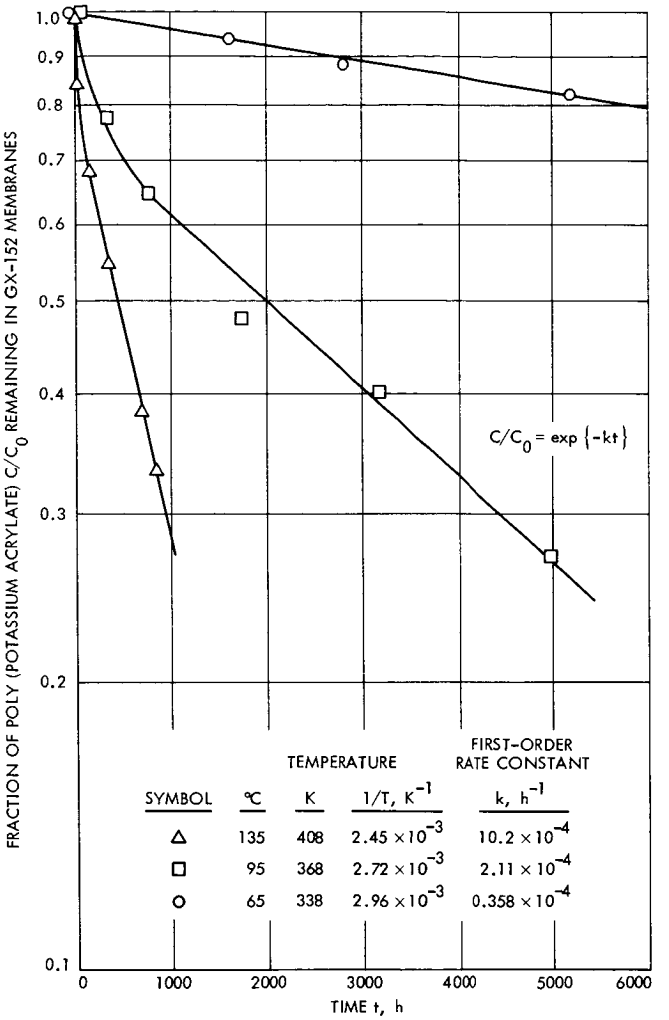

Figure 1. Loss of poly(potassium acrylate) from GX-152 membranes exposed to Ag_2O-saturated 45% KOH battery electrolyte solution

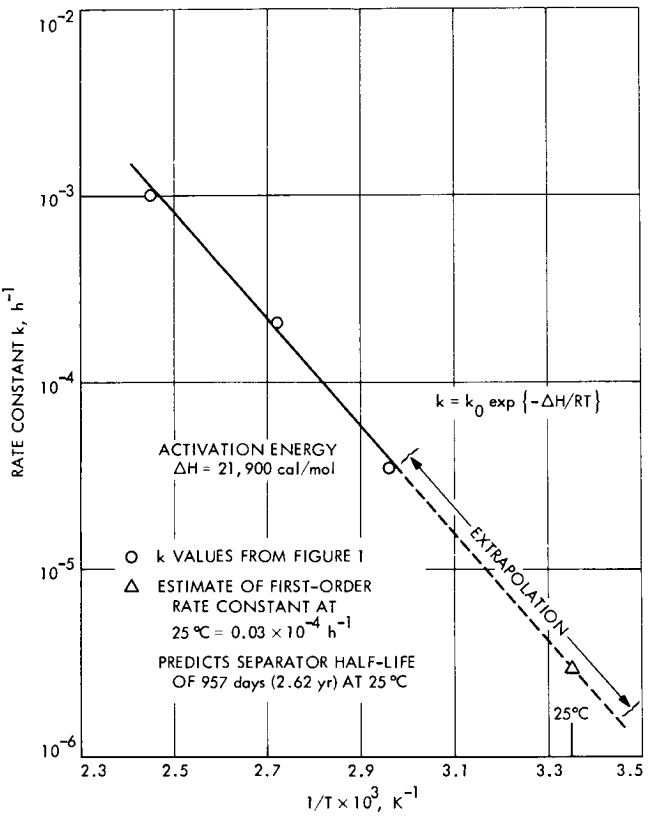

Figure 2. Arrhenius plot of first-order rate constants for loss of poly(potassium acrylate) from GX-152 membranes in Ag_2O-saturated 45% KOH battery electrolyte solution

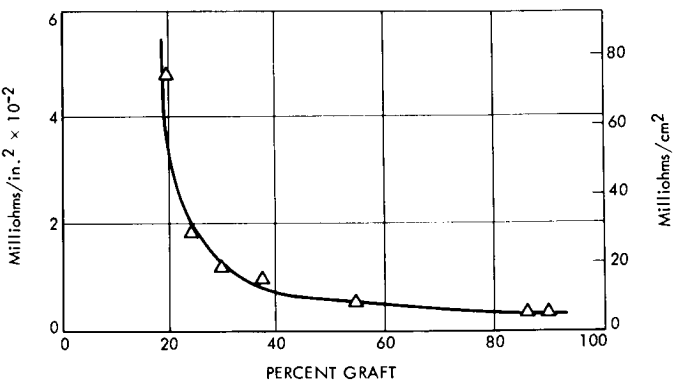

Figure 3. Effect of percent graft on resistance in 40% KOH (reproduced from Reference 9)

viscosity are caused by the degradation of the polymer in the solution. The specific viscosity results are given in Table 2, with the surprising and unexpected result that the decreases in specific viscosity are the same for both the silver-oxide-free and silver-oxide-saturated KOH solutions. This means that KOH alone appears to be the predominant degrader of PKA, not dissolved silver. This does not mean that silver is not oxidatively attacking PKA; the results only mean that PKA is so dominating that the contribution of silver is lost in the data.

Some further evidence for this can be found in Figure 4 and Table 3 for the loss of PKA at 135 and 95°C from membranes in KOH solution containing no silver. At 135°C, the loss of PKA from membranes in silver-free and silver-saturated solution is almost identical. At this temperature, dissolved silver has some but very little additional degradation effect above KOH, thus providing additional support for the KOH degradation mechanism. At 95°C, however, silver apparently has control with negligible KOH degradation. The cause of this effect must lie in the difference in accessibility of PKA in the membrane as controlled by the crystalline melting (110°C) of the polyethylene matrix. Below the melting point, PKA is strongly held within the crystalline structure, where it is sterically protected, thus permitting the slower attack of silver ion in its passage through the membrane to have dominance. Above the melting point, however, KOH accessibility to the PKA is increased, but not quite to the same extent as for free PKA homopolymer in solution. This is evident by comparing the 135°C results in Figure 4 with the specific viscosity results in Table 2.

Table 2. Change in specific viscosities of solutions of poly(potassium acrylate) and poly(potassium methacrylate) in battery electrolyte at 95°C

Poly(potassium methacrylate)[a]		Poly(potassium acrylate)[b]		
Time, h	Specific viscosity in 45% KOH solution	Time, h	Specific viscosity in 45% KOH solution	Specific viscosity in Ag_2O KOH solution
0	0.25	0	1.04	1.04
312	0.25	168	0.70	0.83
480	0.28	336	0.56	0.69
		504	0.49	0.38
		774	0.36	0.40

[a] Initial mol wt, 42,200; solution concentration, 0.420 g/100 ml.
[b] Initial mol wt, 820,000; solution concentration, 0.380 g/100 ml.

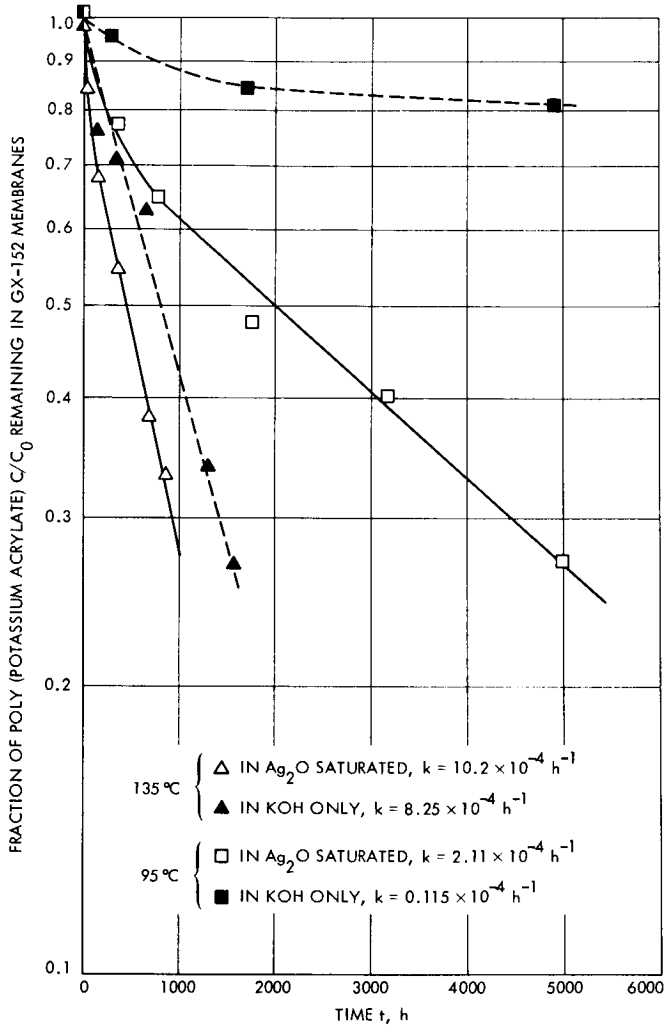

Figure 4. Comparison of loss rate of poly(potassium acrylate) from GX-152 membranes exposed to 45% KOH and Ag_2O-saturated 45% KOH battery electrolyte solutions

Table 3. Loss of poly(potassium acrylate) from sterilized[a] GX-152 membranes exposed to silver-free 45% KOH battery electrolyte solution

135°C		95°C	
Time, h	Initial[a] PKA remaining in separator, %	Time, h	Initial[a] PKA remaining in separator, %
0	100	0	100
120	76	288	96
340	71	1704	84
630	63	4912	81
1300	34		
1560	27		

[a] See Footnote a, Table 1. PKA remaining in separator samples after sterilization was taken as the *initial* levels.

The foregoing has demonstrated that KOH is a stronger degrader of PKA as compared to silver ion. But the relative rate of attack is dependent on accessibility of PKA. With increasing inaccessibility of PKA within the membrane, the degradation by KOH is diminished, and can be so decreased to such an extent that the slower degradation by silver ion can emerge as the dominant mechanism.

Silver Paradox

Simultaneously with the PKA loss, there is deposition within the separator of metallic silver, presumably the end product of the oxidation reaction. Because of this, silver deposition has been conventionally expressed as a ratio of silver deposited to PKA lost. These ratios are given in Table 1, which shows that the amount of silver depositing at 135 and 95°C is the same for the same loss of PKA. Yet at 135°C, PKA is being lost from the membrane almost exclusively by KOH. It is no longer exactly clear how silver deposits into the membranes. Its understanding is important, however, because battery performance, as influenced by electrolyte ion transport, is affected by both PKA loss and blockage of the separator by silver deposits. The effect of the latter and the full mechanism of silver deposition certainly has not been completely explored.

Stability of Poly(Potassium Methacrylate)

The PKA studies have demonstrated that if increases in separator lifetime are to be achieved, the PKA would have to be replaced with another hydrophilic polymer having increased KOH stability. Very preliminary work

has been initiated by monitoring the specific viscosity at 95°C of poly(potassium methacrylate) in KOH solution. The results, given in Table 2, are very promising in showing that this polymer has not undergone a change in specific viscosity after 480 h, compared to a 50% reduction in viscosity as experienced by PKA.

Summary

Investigations on sterilizable membranes to date have resulted in establishing that the current JPL system will seriously affect battery performance after 3 to 5 yr of service. There is a strong possibility for a major improvement by replacing the currently employed hydrophilic agent poly(potassium acrylate) with poly(potassium methacrylate).

References

1. Cuddihy, E. F., and Moacanin, J., "Investigations on Sterilizable Polymeric Battery Separator," in *Supporting Research and Advanced Development*, Space Programs Summary 37-50, Vol. III, pp. 166–169. Jet Propulsion Laboratory, Pasadena, Calif., Apr. 30, 1968.

2. Cuddihy, E. F., and Moacanin, J., "Investigation on Sterilizable Polymer Battery Separators, Part II," in *Supporting Research and Advanced Development*, Space Programs Summary 37-52, Vol. III, pp. 98–100. Jet Propulsion Laboratory, Pasadena, Calif., Aug. 31, 1968.

3. Cuddihy, E. F., and Moacanin, J., "Investigation on Sterilizable Polymer Battery Separators," in *Supporting Research and Advanced Development*, Space Programs Summary 37-54, Vol. III, pp. 100–104. Jet Propulsion Laboratory, Pasadena, Calif., Dec. 31, 1968.

4. Cuddihy, E. F., and Moacanin, J., "Investigation on Sterilizable Battery Separators," in *Supporting Research and Advanced Development*, Space Programs Summary 37-56, Vol. III, pp. 186–188. Jet Propulsion Laboratory, Pasadena, Calif., Apr. 30, 1969.

5. Cuddihy, E. F., Walmsley, D. E., and Moacanin, J., "Investigations on Sterilizable Battery Separators," in *Supporting Research and Advanced Development*, Space Programs Summary 37-59, Vol. III, pp. 200–204. Jet Propulsion Laboratory, Pasadena, Calif., Oct. 31, 1969.

6. Cuddihy, E. F., Walmsley, D. E., and Moacanin, J., "Investigation of Sterilizable Battery Separator Membranes," in *Supporting Research and Advanced Development*, Space Programs Summary 37-61, Vol. III, pp. 213–216. Jet Propulsion Laboratory, Pasadena, Calif., Feb. 28, 1970.

7. Cuddihy, E. F., Walmsley, D. E., and Moacanin, J., "Investigation of Sterilizable Battery Separator Membranes," in *Supporting Research and Advanced Development*, Space Programs Summary 37-64, Vol.

III, pp. 136–138. Jet Propulsion Laboratory, Pasadena, Calif., Aug. 31, 1970.

8. Cuddihy, E. F., Walmsley, D. E., Moacanin, J., and Tom, H. Y., "Investigation of Sterilizable Battery Separators," in *Supporting Research and Advanced Development*, Space Programs Summary 37-65, Vol. III, pp. 171–176. Jet Propulsion Laboratory, Pasadena, Calif., Oct. 31, 1970.

9. D'Agostino, V., "Procedures and Controls in Preparing Grafted Membranes," *Proceedings of the Symposium on Battery Separators*, The Columbus Section of the Electrochemical Society, Battelle Memorial Institute, Columbus, Ohio, Feb. 1970.

Index: information storage devices, Mariner Mars 1971 Project, non-metallic materials

Analysis of the Failure of a Polyester Peripheral Drive Belt on the Mariner Mars 1971 Flight Tape Recorder

E. F. Cuddihy

Propulsion Division

A polyester peripheral drive belt on the Mariner Mars 1971 flight tape recorder failed when a thin longitudinal strip separated off along one edge. Analysis showed that the most probable cause of failure occurred from flexural fatigue initiating in mechanically weak locations which are introduced into the belt during fabrication. Also, methyl ethyl ketone (MEK), which is employed as a cleaning solvent during fabrication, was found to cause permanent reduction in engineering properties of polyester and could have contributed to the reduction of the fatigue resistance. This article reviews fatigue properties of the polyester drive belt for the specific operating condition, as well as the sensitivity of polyester to cleaning solvents and the origin of the mechanically weak locations introduced during fabrication.

Introduction

The failure of a polyester peripheral drive belt (p-belt) on the Mariner Mars 1971 flight tape recorder precipitated a general investigation of the cause involving both a study of material and mechanical reasons for the failure. The results of the material investigation are detailed in this article. It should be pointed out that parallel with this activity additional p-belts were subjected to tape recorder operation without failure, although these belts did develop the same symptoms and appearance which characterized the failed p-belt. The studies which are reported here do not prove the cause of failure but strongly suggest the mode of failure in highlighting those weaknesses of polyester which were in operation at the time of the failure. At the very minimum, this article should contribute to avoiding certain problems associated with polyester in future use by JPL for flight applications.

A review of the conditions imposed on the p-belt during use and of the techniques of manufacturing suggests that, if failure occurred because of a material limitation, the most probable causes would be:

(1) Failure from flexural fatigue.

(2) Damage to material from sensitivity to methyl ethyl ketone (MEK) cleaning solvent.

(3) Nick in edge of p-belt.

(4) Combinations of above.

Analyses of these factors demonstrate that only the flexural fatigue properties of polyester film could be correlated with the failure history of the failed p-belt. In the absence of any other demonstrable cause, failure by flexural fatigue must be considered as primary.

Although not the primary cause of failure, MEK cleaning solvent can damage polyester film even to the extent where partial, but permanent, loss of engineering properties occurs after exposure. Its contribution to weakening the flexural fatigue resistance of polyester film can be significant. Its use as a cleaning solvent has been eliminated and replaced with the compatible solvent Freon-TE.

Failure from the growth of a nick in the edge of the belt is always a possibility. Its presence could have been missed during inspection. Nick studies showed that for the stress levels in the p-belt during operation, failure occurs when the nick depth is approximately 10% of the belt width. Since this depth is almost equal to the width of the longitudinal strip which peeled off the failed p-belt, an argument against a nick failure mechanism emerges. At 10% nick depth, the belt cannot support the stress level and would have failed by catastrophic tearing across the width. Failure by a nick, considering this argument and the many inspection steps, seems unlikely.

Background

This section reviews the p-belt operation on a tape recorder and the cause of the flexing mode. Also discussed is the technique of belt fabrication and the cause of mechanically weak locations fabricated into the belt. The fatigue properties and sensitivity to MEK cleaning solvent of the weak locations are discussed in subsequent sections.

Recorder Operation

Thin plastic belts [10.2mm (0.4 in.)[1] wide × 23.4μm (0.00092 in.) thick] prepared from polyester material are employed on JPL flight tape recorders as the means of driving the reels of recording tape. A typical flight recorder equipped with a polyester drive belt is shown in Figure 1, where it can be seen that the belt path carries it over the back side of the reels and in direct contact with the recording tape. When the belt is moving, the direct contact is the mechanism for driving the reels of recorder tape. The two hollow guides shown in Figure 1 are the driving idlers for the belt, while the two

[1] Values in customary units are included in parentheses after values in SI (International System) units if the customary units were used in the measurements or calculations.

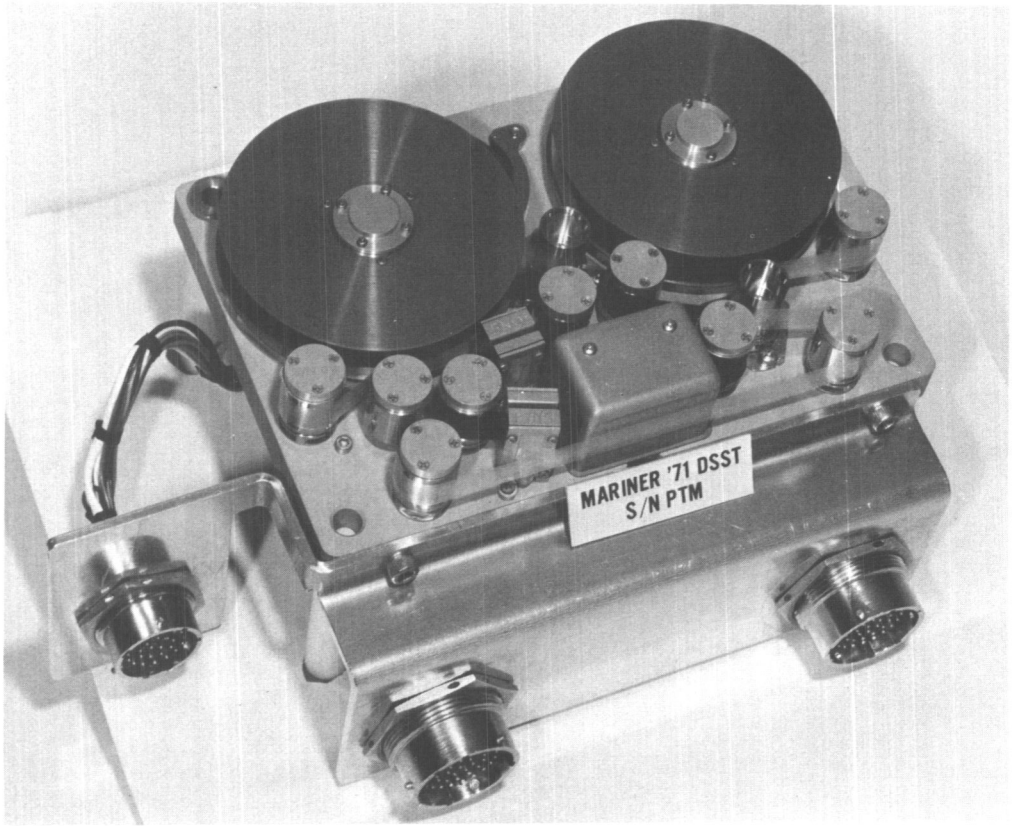

Figure 1. Mariner Mars 1971 flight tape recorder

guides in the front of the recorder (between which runs the long portion of the belt) are crowned guiding idlers which act to keep the belt centered as it traverses the recorder.

Examination of an operating p-belt on the flight tape recorder revealed that as the belt passed over the crowned guiding idlers, the polyester material was undergoing extensive wrinkling and that the edges of the belt were being lifted off the surface of the idler. The width of the lifted edges was about 1.27 mm (0.050 in.). With continued operation, two frost lines began to develop longitudinally at these edge locations, and the failure was caused by a splitting off of a longitudinal strip around the belt along one of the frost lines.

Further examination revealed that the belts were flat and wrinkle-free on all other guides and idlers. Thus, as the belt travelled around the recorder, the edges were experiencing flexure by being cyclically wrinkled and lifted off the crowned guiding idlers. These observations strongly suggested failure from flexural fatigue.

Belt Fabrication

Belts for the Mariner Mars 1971 flight tape recorder were prepared from a 23.4-μm (0.92-mil) sheet of a polyester material (Mylar "A," DuPont) according to the scheme detailed in Figure 2. A washer of the proper dimension is cut from the sheet stock, placed on a stretching device, and stretched until the inside edge is brought equal to the outside edge. The stretching operation was carried out above 135°C. At various stages in the fabrication, methyl ethyl ketone (MEK) solvent was employed both as a cleaning agent and as a medium to draw off accumulated static electricity. The potential of solvent damage from MEK was considered and included for study.

Belt Properties

The mechanical properties of commercial Mylar "A" are not uniform when these properties are measured as a function of angle around a given point in the sheet. The commercial process for preparing polyester sheets results in a higher modulus in the machine direction (see Figure 3) as compared to the transverse direction. Mylar "A" of 23.4-μm (0.92-mil) thickness was found to have a machine direction modulus of near 3.72×10^5 N/cm^2 (540,000 psi) compared to 2.76×10^5 N/cm^2 (400,000 psi) in the transverse direction.

The absence of circular symmetry of modulus in Mylar "A" directly results in the occurrence of a mechanically unbalanced p-belt, where now the longitudinal properties of the final belt are exactly the starting circular properties of the Mylar "A." The process of stretching a washer to a belt above 135°C does not appear to change either the distribution or level of modulus in the belt from that in the sheet. The correlation between the

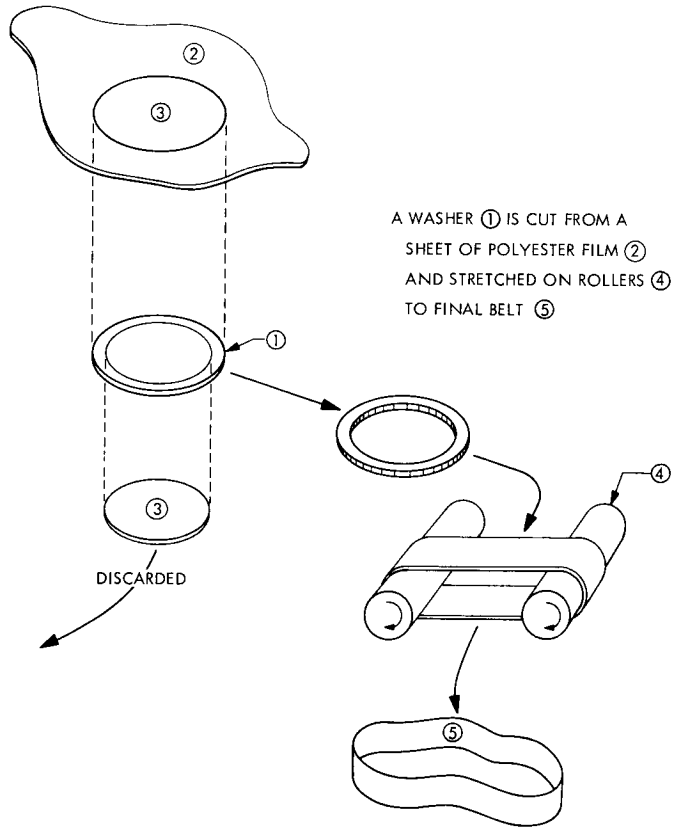

Figure 2. General details for preparing polyester seamless belts

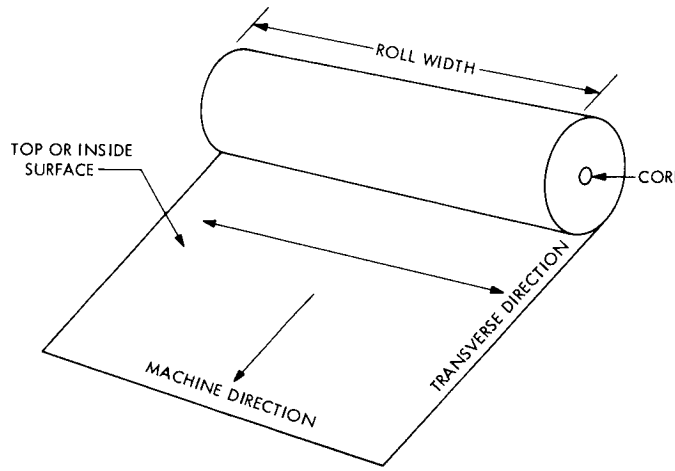

Figure 3. Nomenclature for rolls of polyester film

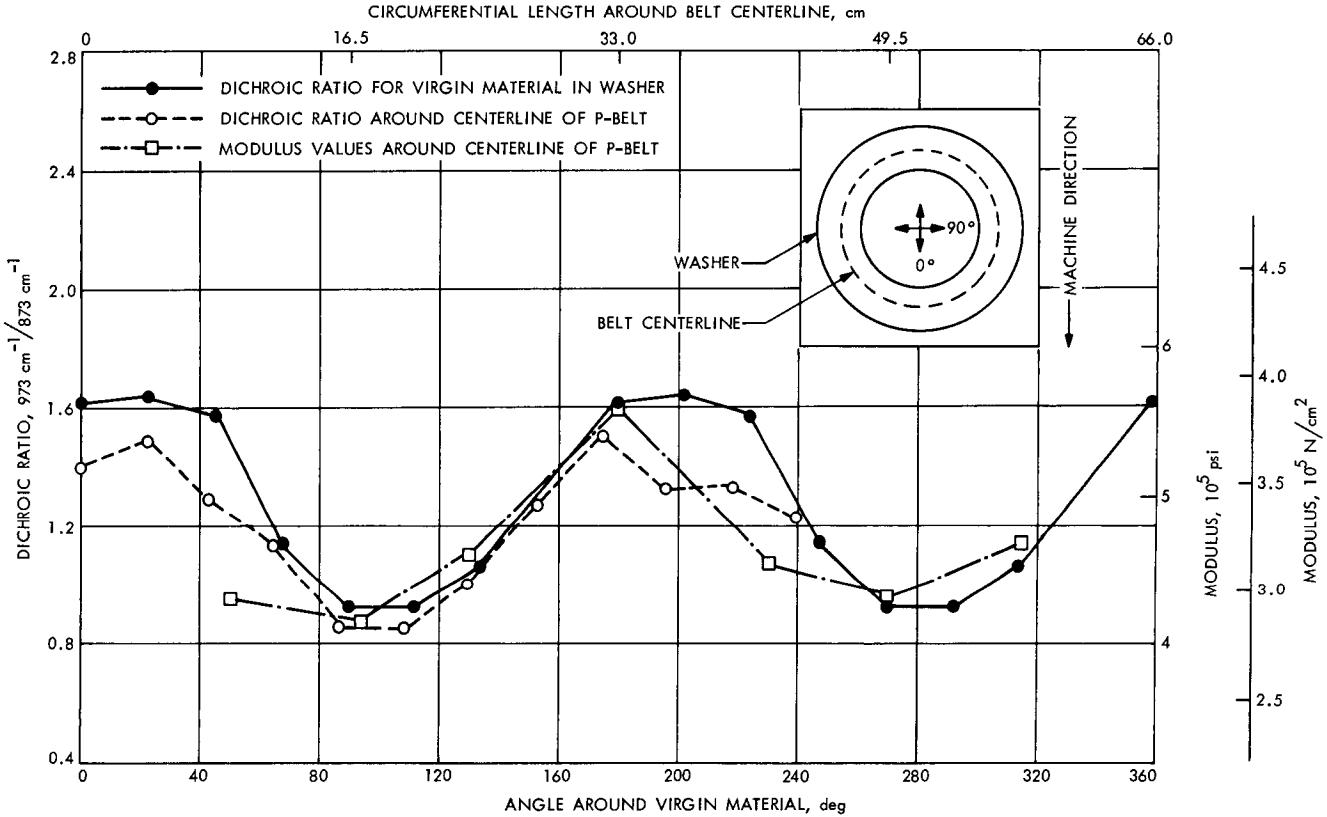

Figure 4. Modulus and dichroic ratio for Mylar "A" polyester film and Mariner Mars 1971 p-belt

circular dependence of modulus in the starting sheet and the longitudinal modulus in a final belt is given in Figure 4.[2]

It can be seen that as a result of the fabrication process p-belts are prepared having an unbalanced modulus distribution. This results in two weak locations (defined by low modulus) in the belt which are approximately 180 deg apart from each other. The studies carried out in this investigation demonstrated that the resistance of polyester to failure from flex fatigue and damage from MEK cleaning solvent decreased with decreasing modulus of the polyester. Thus, the two low modulus sites in the failed p-belt were highly susceptible to potential failure from the operational flexing and the use of MEK during fabrication.

Fatigue Characteristics of Polyester

The results presented in this section will argue a strong case in support of flexural fatigue as the primary cause of the p-belt failure. It is the only mode of failure which satisfactorily correlates with the known failure history of the belt. The correlation arguments are:

(1) The appearance of the strong frost lines running longitudinally around the belt where the material lifted off the Crown idlers. The frost lines are indications of material damage.

(2) The p-belt at failure experienced nearly 75,000 flexural cycles from wrinkling each time it passed over a Crown idler. In a laboratory test evaluating the flexural fatigue properties of polyester, it was found that for the conditions of flexing which created frostiness in the material the test specimens failed in flexural fatigue at this same number of cycles when the specimens were exposed to stress fields comparable to an operating p-belt.

For the fatigue studies, test specimens were cut out of a sheet of Mylar "A" in the modulus weak transverse direction. Preliminary flexural testing demonstrated that the low modulus direction was significantly weaker in resistance to flexural failure than the corresponding high modulus direction. The flexural fatigue studies were carried out by bending a strip of the material through some test angle while at the same time applying a tensile stress. The fatigue property was recorded as the number of cycles to failure as a function of the flexing angle and the applied stress.

Effect of Flexing Angle

The flexing angle, at constant stress, is related to the severity of flexure which the material experiences in application, and, therefore, it becomes

[2] Included in Figure 4 is a parameter called *dichroic ratio*, which was also measured on both the starting film and a p-belt. *Dichroic ratio* is measured from a nondestructive technique employing polarized infrared radiation and gives direct information on modulus. The technique, detailed in the section on *Infrared Dichroism*, became the principal method for monitoring modulus distribution in films and belts.

very important to properly select this angle such that a close approximation to application, i.e., the p-belt wrinkling and flexing in this case, is achieved. This is usually difficult, but polyester film fortunately exhibited a simple behavioral characteristic when the fatigue property was measured as a function of increasing flexing angle at constant stress. This is illustrated in Figure 5.

With increasing flexing angle at constant stress, the dependence of cycles to failure on angle decreased rapidly until a critical angle was surpassed, where a greatly reduced dependence was encountered. This latter zone, above the critical angle, also resulted in obtaining frostiness along the crease line. The severity of flexure on polyester thus divides conveniently into two zones: (1) the noncritical zone, where polyester strongly resists fatigue failure, and (2) the critical zone, where polyester is most affected by flexure, with the additional advantage of having very little dependence of flexing angle on cycles to failure. Thus, shoosing a bending angle within the critical zone to measure the cycles to failure versus stress should give behavior characteristic of this whole zone.

Fatigue Curve

The fatigue curve for polyester, defined as the number of cycles to failure versus stress at constant bending angle, is given in Figure 6. The bending angle selected was within the critical zone.

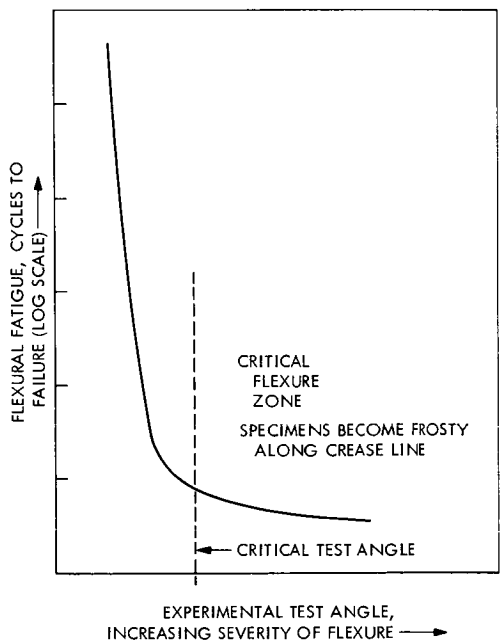

Figure 5. General fatigue characteristic of polyester as a function of experimental test angle at constant stress

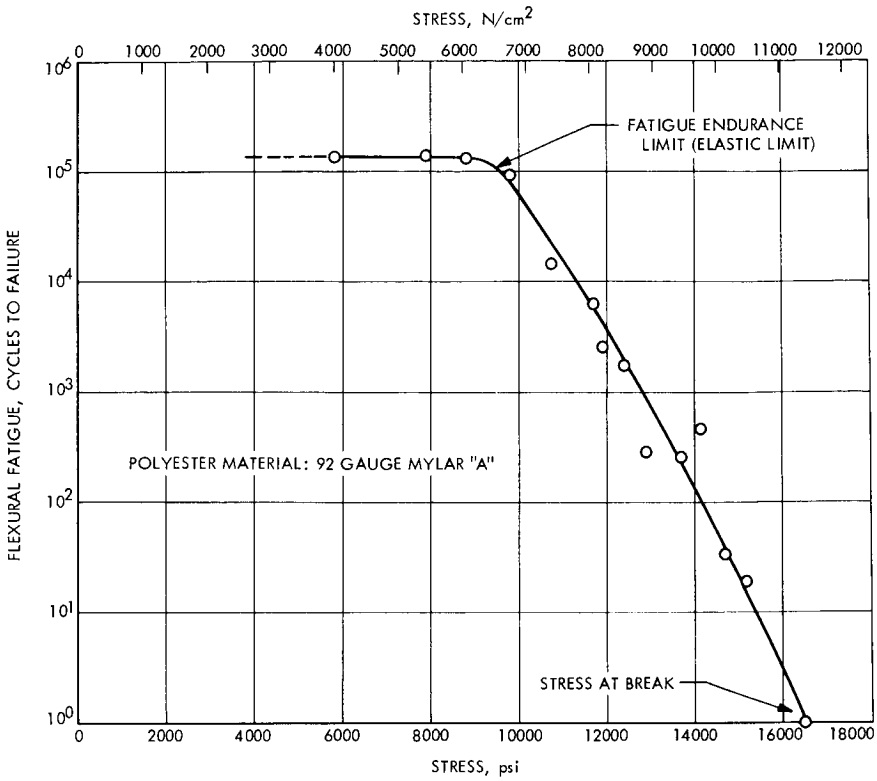

Figure 6. Fatigue curve for polyester tested at flexing angle within critical zone

This curve is characterized by two zones: the first at low stress, where the number of cycles to failure is essentially constant, until a stress, called the *fatigue endurance limit*, is exceeded at which point the cycles to failure falls rapidly with increasing stress.

The information in this curve is significant. The p-belt that failed had undergone 150 tape passes, which corresponds to around 75,000 flexural cycles.[3] Inspection of Figure 6 reveals that the stress levels required to fail the material at this number of cycles is in the stress region 6.21×10^3 - 6.89×10^3 N/cm^2 (9,000–10,000 psi) which the p-belt was operating when it failed. Since the data in this curve was measured within the critical flexural zone of polyester, operating at different bending angles would not greatly change the data. Only until the bending angle was decreased enough to approach the critical angle would there be a great departure from this basic data.

[3] Calculated as follows: The recording tape is 167.64 m (550 ft) long compared to the belt length of 67.15 cm (26.437 in.). Hence, each tape pass corresponds to (167.64) (100)/(67.15) = 250 belt passes [(550) (12)/(26.437) = 250 belt passes]. Since there are two Crown idlers, the belt at failure made (250) (2) (150) = 75,000 passes over the Crown idlers, each time experiencing a flexural cycle.

Hence, this data can provide a strong argument for failure from flexural fatigue, especially if the wrinkling and bending of the p-belt was sufficiently severe to locate the material within the "critical" flexural zone. That the material was indeed undergoing severe flexing is to be concluded from the strong frostiness that was observed in the failed p-belt.

A point on the relationship between laboratory testing and the recorder operation should be made. On the recorder, the belt experienced multi-axial bending and flexing, whereas only a uniaxial flex could be generated in the laboratory testing. Thus, the severity of flexure in the recorder is an accumulation of all the wrinkling and bending modes, more or less of which can shift the material's flexure response into or out of critical flexure behavior. The bending angle employed in laboratory uniaxial testing is only a means to create and study critical flexure behavior in the polyester material and bears no relationship to any actual wrinkling or bending angles which would be observed on the recorder. Strong frostiness did occur along the fracture line of laboratory samples tested within the critical flexure zone, but not for samples tested outside the critical zone. In fact, a sample of polyester was flexed at an angle outside the critical zone and at a stress level 10.3×10^3 N/cm^2 (15,000 psi) (this is within 10% of the normal stress-at-break for this material), and the material would not break. The test was finally terminated after 200,000 cycles when inspection of the material showed no signs of wear, fatigue, or frost.

Solvent Studies

The study of the effect of solvents, particularly MEK, on polyester are discussed in this section. The principal findings are:

(1) MEK can significantly damage polyester, with the following effects being observed:

   (a) In the presence of MEK, the stress-at-break of polyester is reduced from 11.4×10^3 to 5.9×10^3 N/cm^2 (16,500 to 8,500 psi). MEK is a strong solvent-stress-cracking agent.

   (b) Polyester, after exposure to MEK, was observed to have suffered partial, but permanent, loss of engineering properties.

(2) The use of MEK as a cleaning solvent should be avoided. Another solvent, Freon-TE, was found to be compatible with polyester for all cleaning applications.

The details of the solvent study and other observations are given below, and unless otherwise stated, all test specimens were cut from the low modulus direction of the polyester sheet stock.

MEK Sensitivity

The sensitivity of polyester to MEK was detected by measuring the stress–strain curve of this material while completely immersed in the solvent. In Figure 7 this curve is compared to a stress–strain curve measured in air. The

effect of MEK on polyester is readily apparent. MEK is a strong stress-cracking solvent which results in a significant reduction of the engineering properties. Its use as a solvent should be avoided.

Directional MEK Sensitivity

The effect of MEK on samples cut from the strong direction of Mylar "A" is shown in Figure 8. Very little effect is observed, demonstrating that the principal damage to polyester occurs along the material's low modulus direction.

Partial but Permanent Damage

Samples of polyester were exposed to MEK for periods ranging from 1 min to 96 h, after which the samples were removed from the solvent, air-dried 24 h, and then subjected to stress-strain measurements. The results, given in Figure 9, clearly demonstrate the occurrence of partial, but permanent, loss of engineering properties. Even after only 1 min of exposure, there was a significant decrease in the yield strength and stress at break.

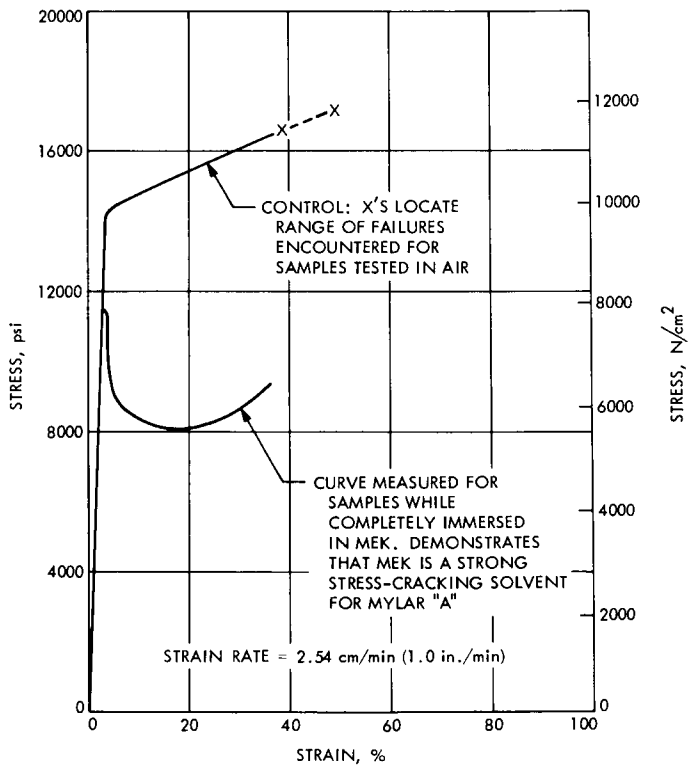

Figure 7. Effect of MEK on 92-gauge Mylar "A"

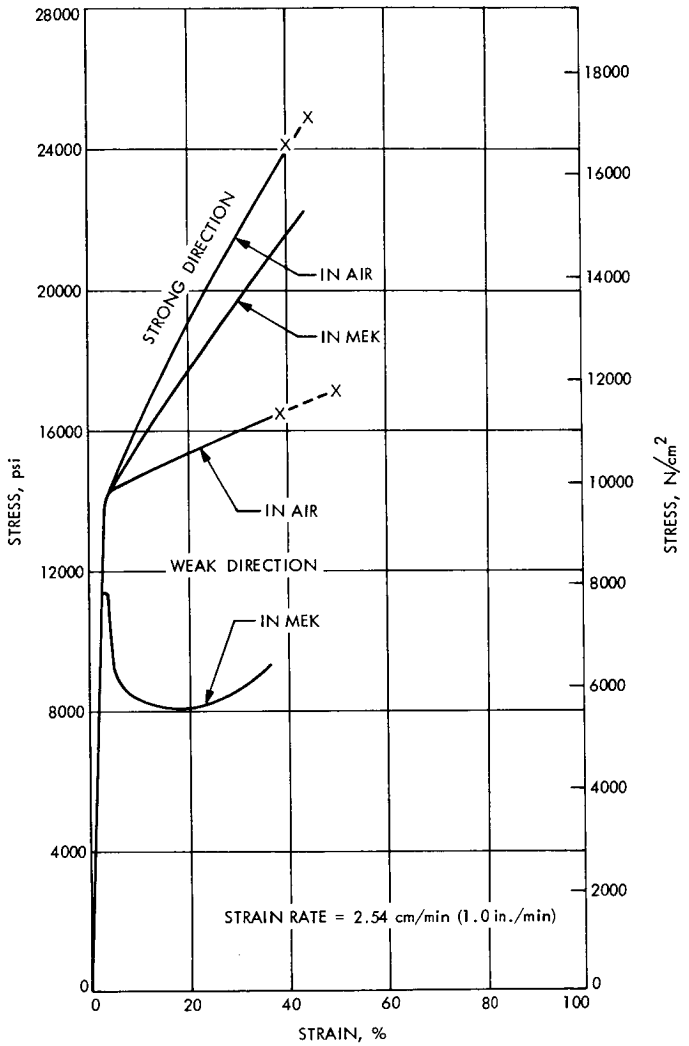

Figure 8. Effect of MEK on 92-gauge Mylar "A" directional properties

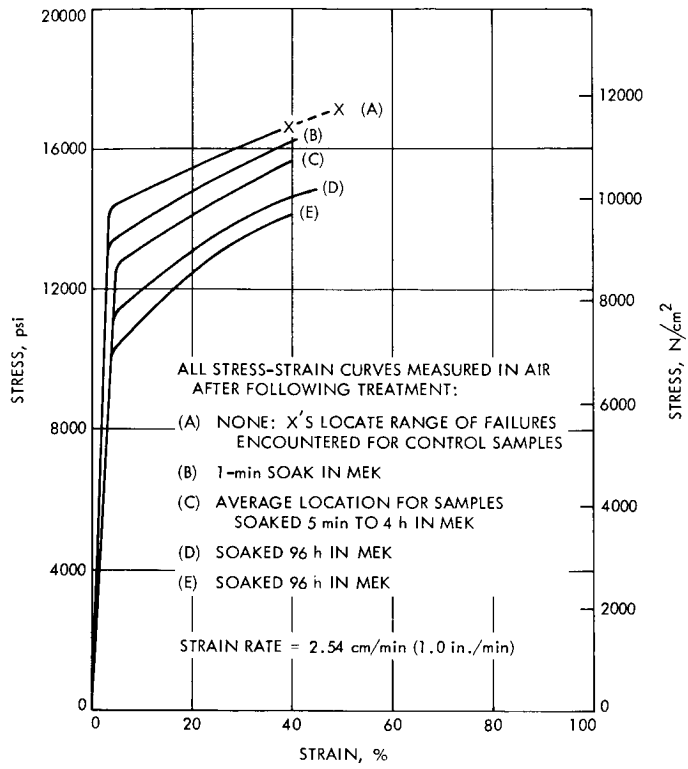

Figure 9. Change in properties of 92-gauge Mylar "A" after MEK exposure

Figure 10 compares in more detail the initial portions of the stress-strain curves of polyester tested with no exposure and the average curve (curve C, Figure 9) obtained after 5 min to 4 h of MEK exposure. Exposure resulted in a reduction in modulus and yield stress, respectively, from 2.76×10^5 and 8.27×10^3 N/cm^2 (400,000 and 12,000 psi) to near 2.24×10^5 and 6.89×10^3 N/cm^2 (325,000 and 10,000 psi). This reduction in modulus resulting from the MEK exposure would only act to further reduce the resistance to flex fatigue (Reference 1). It can only be conjectured that perhaps the failed p-belt experienced above average MEK exposure during fabrication, enough perhaps to affect the wrinkling characteristics and shift the material into critical flexure behavior.

Compatible Solvents for Polyester

The stress-strain curves of polyester were measured in a series of solvents with the intention of selecting compatible fluids. The results are documented in both Figure 11 and Table 1, which reveal that solvent effects on polyester can be broken down into three general classes. The first, called Class I solvents, which are shown in Figure 11a, is the worst, causing serious damage with loss of engineering properties. Their use on polyester should always be avoided. The second, called Class II solvents (Figure 11b), affects

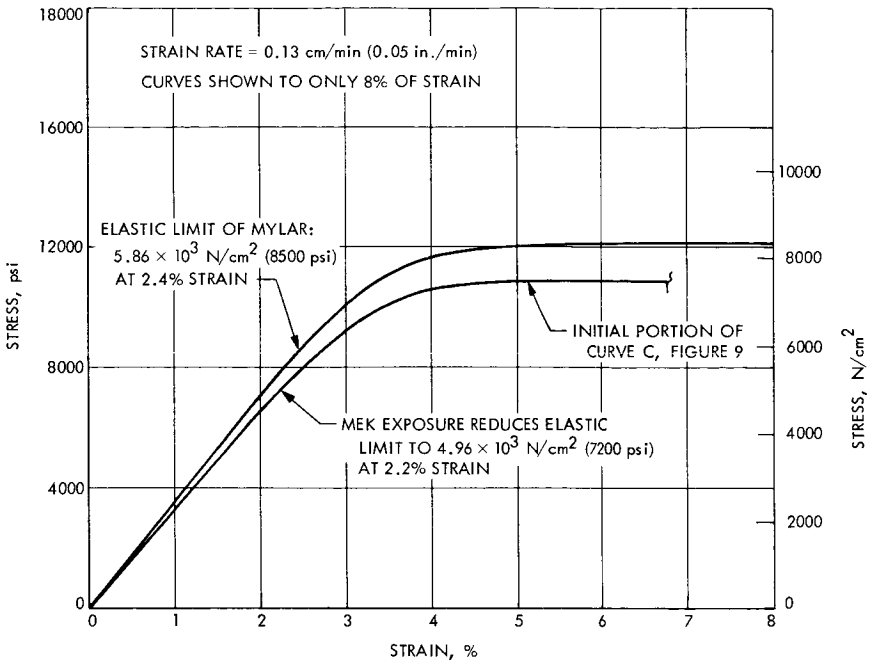

Figure 10. Comparison of initial portions of stress-strain curves for Mylar "A" in air and after 4-h exposure to MEK (both curves tested in air)

only the plastic draw region and do not result in a loss of engineering properties. These solvents may be used for brief exposure periods. The third, Class III solvents, may be safely used on polyester for all applications, with the result in Figure 11c indicating that the best cleaning solvent is Freon-TE.

Infrared Dichroism

This section describes the use of *infrared dichroism* as a nondestructive technique for measuring the modulus of polyester films.

The p-belt failure drew attention to the fact that these belts have highly anisotropic mechanical properties, particularly modulus, occurring in the longitudinal direction around the belt. Modulus values ranging from as low as 2.76×10^5 N/cm^2 (400,000 psi) to as high as 3.72×10^5 N/cm^2 (540,000 psi) have been measured. To measure modulus requires sacrificing a belt to prepare tensile specimens, a destructive practice not possible to do on a candidate flight belt. Therefore, a nondestructive test technique capability called *infrared dichroism* has been incorporated into the procedures of the JPL analytical group. This technique permits the measuring of a nondestructive parameter called *dichroic ratio*, which is directly related to the modulus of the material. Further, unlike tensile testing, the dichroic ratio can be measured as a point property, and, therefore, the modulus values of belts can be easily monitored at any position in both the longitudinal and transverse directions.

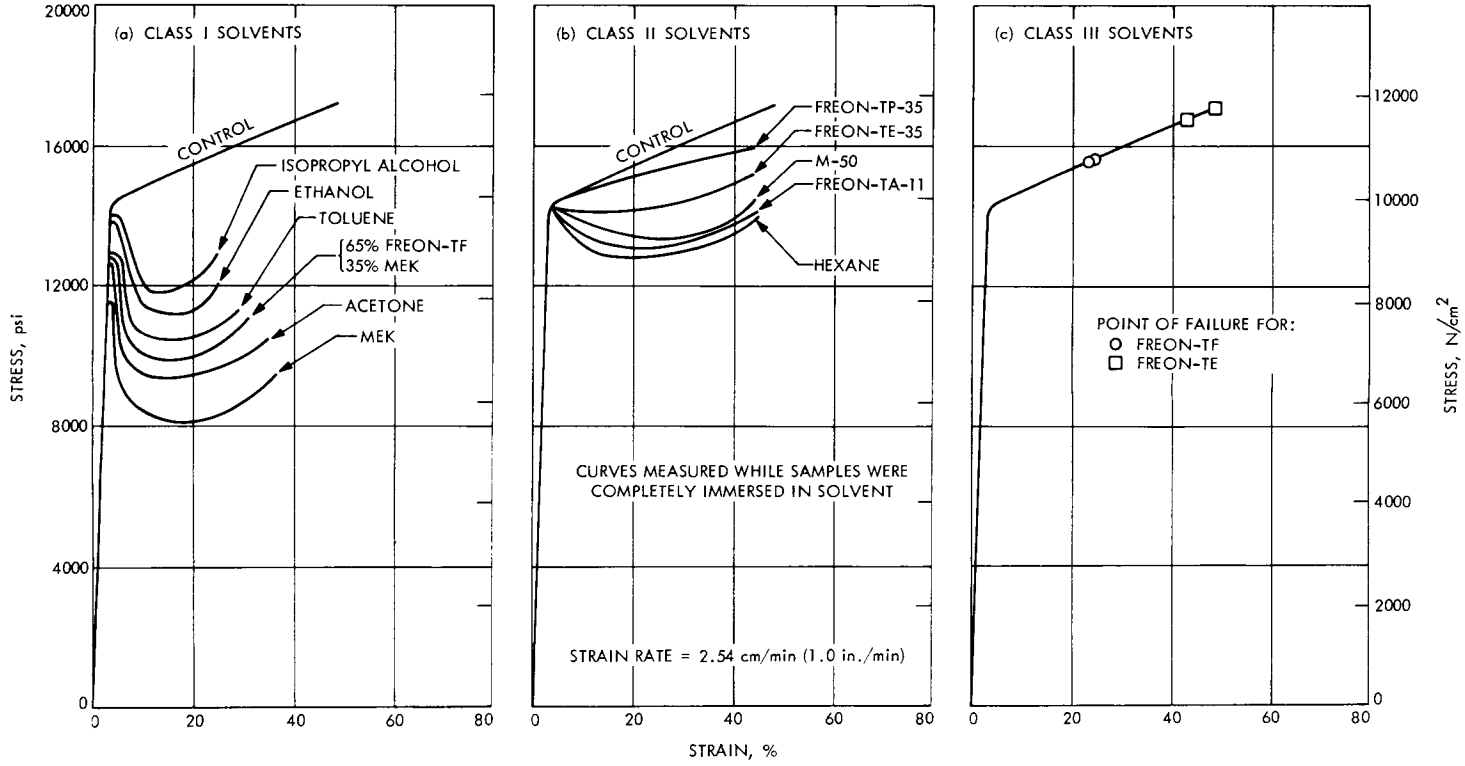

Figure 11. Effect of various solvents on 92-gauge Mylar "A"

Table 1. Ranking of solvents relative to compatibility with Mylar "A"

Class I:	Solvent stress cracking agents; use to be avoided.
(1) MEK	
(2) Acetone	
(3) MEK/Freon	
(4) Toluene	
(5) Ethanol	
(6) Isopropyl alcohol	
Class II:	Selectively compatible; exercise care in use.
(1) Hexane	
(2) Freon-TA-11	
(3) M-50 (1,1,1-trichloroethane)	
(4) Freon-TE-35	
(5) Freon-TP-35	
Class III:	Compatible for all applications.
(1) Freon-TF	
(2) Freon-TE	

Principles

The modulus level of polyester is directly related to the relative proportion of the molecules which are aligned or oriented in the same direction at which the modulus is being measured. It follows, therefore, that the distribution of the orientation of the molecules in the material directly controls the distribution of the modulus. Think of the molecules in polyester as pencils (see Figure 12). If all the pencils are lined up in the same direction, then the maximum tensile strength and modulus of the stack of pencils will be in the longitudinal direction, with essentially no strength existing at right angles. This situation describes "tensilized" polyester film where a very high proportion of the molecules are all aligned or oriented in the same direction. The modulus and strength in that preferentially oriented direction is very high compared to values measured at right angles.

If the pencils are now uniformly oriented (see Figure 12) as a function of angle, and since the proportions are the same in any direction contributing to strength, the modulus would be found to be uniform and invariant in any direction. This situation describes commercial polyester film where presumably the molecules, and therefore the modulus, are uniform. Thus, molecular orientation of the polyester molecules control the orientation characteristics of the material's modulus, and alternately measuring the modulus at various directions in polyester film gives direct information about the molecular orientation.

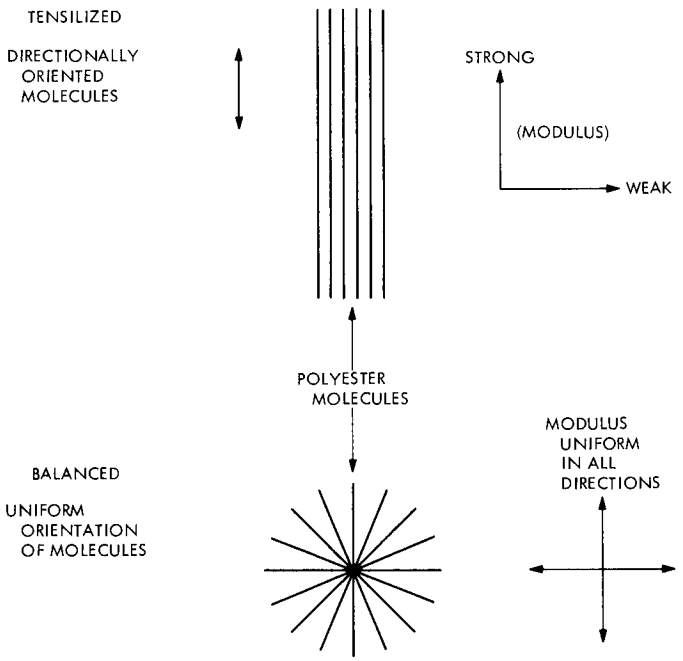

Figure 12. Relationship between molecular orientation and modulus

Now *infrared dichroism*, a technique employing *polarized* infrared light, also detects directly the molecular orientation of the polyester molecules, and, therefore, also the orientational characteristics of the modulus. It works as follows. A chemical grouping exists in the polyester molecule which strongly absorbs infrared radiation at a frequency[4] of exactly 973 cm^{-1}. Chemical groups absorb infrared radiation by having internal motions whose energy levels are related to a fixed frequency (energy, Plank's Law $E = h\nu$) in the infrared spectrum. When that frequency is employed, a resonance occurs with the group absorbing energy, causing an attenuation of the initial beam intensity. This attenuation can be detected, which provides testimony to the presence of the group as well as indicating the concentration of the group by the extent of attenuation. Now the internal motion of the chemical group in polyester which causes the resonance at 973 cm^{-1} is uniquely aligned along the long axis of the polymer molecules. Thus, the capability exists for measuring molecular orientation by employing polarized infrared frequency of 973 cm^{-1}. This polarized source will interact and resonate with only those chemical groupings which are also aligned in the direction of the plane of polarization of the incident infrared radiation. The extent of attenuation of the beam is now directly proportional to the proportion of polyester molecules which are aligned in the direction of the plane of

[4] This is really a frequency. Convention in infrared spectroscopy is to quote wavelengths or reciprocal wavelengths of the infrared radiation rather than its frequency. Common practice generally employs reciprocal wavelengths, $1/\lambda$ in cm^{-1}, because these values vary directly as frequency ($f \approx 1/\lambda$ from the relationship $f\lambda = C$), as well as providing a direct measure of wavelength which is preferentially desired for analysis by spectroscopists.

polarization. Hence, directional variations in the level of attenuation of the incident polarized infrared radiation are directly relatable to the variation in the modulus of the material.

One last remark is needed. Attenuation of the infrared radiation is also caused by the thickness of the polyester film. To eliminate thickness effects, absorbance at 973 cm^{-1} is divided by another absorption peak at 873 cm^{-1}; this ratio, called the *dichroic ratio*, is invariant to sample thickness and can be related linearly to modulus.

Summary

Commercial polyester films from which p-belts are prepared are not mechanically balanced, but are characterized by directional differences in modulus with usually the directions of highest and lowest modulus being perpendicular to each other. This study revealed that p-belts retain this modulus variation, and that the resistance of polyester to failure from flex fatigue and damage by MEK decreased with decreasing modulus. Thus, the failed p-belt, fabricated with low modulus locations, and operating with flexural modes after MEK exposure, had all the potential for failure.

Reference

1. Cuddihy, E. F., "Fatigue of Teflon Bladder Bag Materials," in *JPL Quarterly Technical Review*, Vol. 1, No. 1, pp. 57–63. Jet Propulsion Laboratory, Pasadena, Calif., Apr. 1971.

Index: information storage devices, metallic materials, nonmetallic materials

Studies on the Frictional Behavior of Magnetic Recording Tapes

S. H. Kalfayan and R. H. Silver

Propulsion Division

J. K. Hoffman

Astrionics Division

Magnetic tape recorders exhibit various failure modes. Those ascribable to friction between tape and magnetic head cause phenomena such as seizure (stick) and seizure and release (stick-slip). Methods have been developed at JPL for the measurement of frictional forces acting on the tape while in motion or at rest, as well as the extent of stick-slip. The effects of factors such as temperature, humidity, kind of gaseous atmosphere, tape speed, etc., on the frictional interaction between various tapes and heads have been investigated. Results were instrumental in the selection of a tape for Mariner Mars 1971 spacecraft. This article primarily discusses recent studies on the stick-slip behavior of tapes, and the performance of a metallic tape as compared to the usual plastic tapes.

Introduction

The frictional behavior of magnetic recording tapes have been under study at JPL for some time (Reference 1). The coefficient of friction, μ, or the quantity $\mu\beta$ (see below) of numerous candidate tapes was measured under experimental conditions using different kinds of magnetic heads. The following equation (Reference 2) for flexible band friction was used to calculate μ or $\mu\beta$:

$$F_2 = F_1 e^{\mu\beta} \tag{1}$$

where

F_2 = force necessary to sustain motion of tape

F_1 = supported weight

μ = coefficient of sliding friction

β = contact or wrap angle, rad

A diagram of the setup used for these measurements is shown in Figure 1.

For convenience, the quantity $\mu\beta$, rather than μ, was used for tape evaluation. Its value varied within a wide range, 0.2 to 3.4, depending upon the nature of the tape, the kind of magnetic head used, and the environmental conditions. Most tapes showed an increase in $\mu\beta$ with the number of passes. Moisture, even at 25% relative humidity level, increased the $\mu\beta$ values in a majority of cases. Brass- and Monel-bracketted magnetic heads showed higher $\mu\beta$ values than heads bracketted with aluminum or Havar shielded-aluminum.

The $\mu\beta$ value is indicative of the magnitude of the frictional (drag) forces in operation during the passage of the tape over the magnetic heads. Complete seizure (stick) and mechanical failure of the tape occur when it reaches high values.

Another phenomenon associated with tape friction is seizure-and-release (stick-slip). This can manifest itself in the variation of the tape-to-head speed. Sticking will decrease and slipping will increase the instantaneous speed of the tape as it passes over the magnetic heads. The determination of the instantaneous speed would, therefore, indicate the existence and the extent of stick-slip. The direct measurement of the instantaneous speed is difficult. An indirect method, namely, the measurement of the change in the apparent period of a signal prerecorded on the tape, is relatively simple.

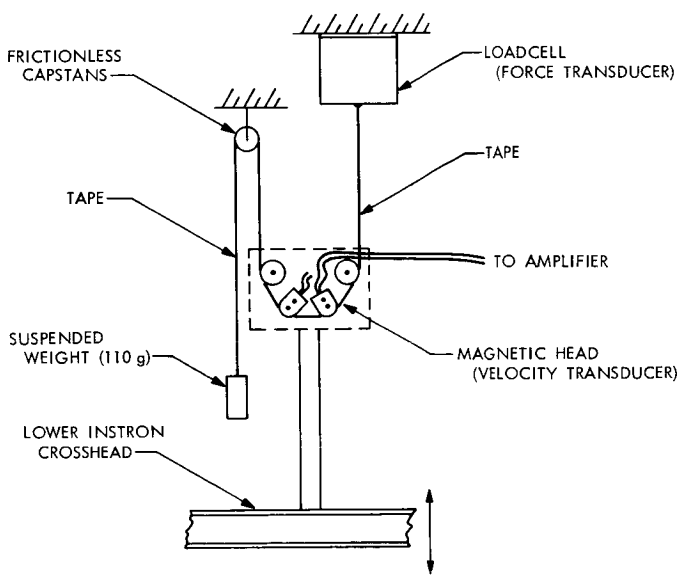

Figure 1. Diagram of setup for determination of coefficient of friction of tapes

The apparent period of a prerecorded signal will change with the speed of the tape. The amount of variation in the period, or the frequency of the signal will indicate the extent of stick-slip.

Environments under which tapes were tested included: dry argon, helium and nitrogen, moist argon, and air. Measurements were made mostly at 25 and 55°C, but other temperatures were used also. The effects of tape speed and outgassing of the tapes on the frictional behavior were also studied.

Results of these experiments showed that one of the tapes, i.e., 3M 20250, a tape backed with Mylar (polyethylene terephthalate), surpassed others in performance. This magnetic tape was eventually selected for flight on the Mariner 9 mission, taking into consideration other factors as well.

The results of the study of the frictional behavior of tapes and magnetic heads is discussed in detail in Reference 3. In the present article recent studies correlating the data obtained for the determination of stick-slip from velocity (or frequency) and frictional force measurements will be discussed, as well as the evaluation of a metallic tape, known as the Univac Magnetic Tape.

Results from Velocity and Frictional Force Measurements

Earlier in this study, a fluctuation in the electrical output of the loadcell was observed, which meant that the frictional force was changing. It was suspected that this might be due to the so-called stick-slip phenomenon. Recently the output of the loadcell or the "force transducer" was amplified, for a clearer examination of these fluctuations. Meanwhile, the "velocity transducer," consisting of a magnetic head and a tape specimen with a prerecorded signal, was used to detect the instantaneous variations in tape speed. The change in tape speed would be manifested in the change of the frequency of the prerecorded signal. Sticking would decrease and slipping would increase the frequency of the prerecorded signal.

The simultaneous electrical outputs of the velocity and force transducers are shown by graphs I and II, respectively, in Figure 2. They were obtained by using 3M 20294 tape and brass-bracketted magnetic heads at 22 ± 1°C, in air. This particular combination was chosen as a worse situation, so that results would be pronounced. The data of Figure 2 was gathered when the 110-g weight was moving downward, a situation that simulates the tension on a tape in an actual spacecraft tape recorder. The tape was not allowed to contact the magnetic heads when the weight was moving upward. Outputs from only runs 4–7 are shown. Runs 1–3 being similar to run 4, and those following run 7 being similar to it, were omitted. The construction of the recorder caused an apparent lag in the graphical output of the force transducer.

Figure 2 allows the following observations and deductions:

(1) Fluctuations in both the frequency and the force graphs point to the existence of stick-slip.

(2) Even during a smooth run like No. 4, there is a variation in frequency of ±1 Hz. This indicates that stick-slip is always present, although to a small extent (graph I). A similar variation in the frictional force (graph II) is not as obvious, because of the lesser sensitivity of the force transducer.

(3) When there is a decrease in the frictional force there is an increase in frequency (or speed) and vice versa. (Compare points p_1, p_2, and p_3, p_4). This result would be expected if the tape experienced stick-slip.

(4) The magnitude of the perturbations increases with the number of runs, indicating significant changes on the surface of the magnetic coating.

(5) The frictional force exerted on the tape approaches but never exceeds 110 g. Reaching this value would mean complete seizure. Similarly, the frequency approaches zero; reaching it would also mean complete seizure.

Evaluation of the Univac Metallic Tape

This magnetic tape is phosphor-bronze based and cobalt-nickel plated. Samples lubricated with Vac-Kote, as well as unlubricated ones, were tested. The amount of available tape limited the number of experiments. Tests were conducted in dry argon at 25 and 55°C, using only heads that were Monel bracketted and aluminum bracketted with Havar shields. Results are shown in Figures 3 and 4. For comparison, curves obtained for 3M 20250 (the tape used in the Mariner 9 mission) tested under the same conditions and with the same magnetic heads used with Univac tape, are also included.

The following observations may be made from Figures 3 and 4:

(1) The $\mu\beta$ values obtained for the lubricated and unlubricated Univac tape, at both temperatures, with both magnetic heads, ranges between 0.35 and 0.55. This is within the range of experimental error. The significance of this fact is that the difference between the frictional performance of the lubricated and unlubricated metallic tape is not much; the temperature change does not affect the $\mu\beta$ values significantly, nor does the kind of magnetic head make a difference. On the other hand, the frictional behavior of 3M 20250, a plastic-backed tape with an organic polymer coating, is significantly affected by the change in temperature ($\mu\beta$ values are much lower at 55°C), and the type of magnetic head influences its frictional performance considerably. (Monel bracketted heads show higher $\mu\beta$ values than aluminum-bracketted heads with Havar shields).

(2) The frictional performance of the metallic tape is comparable to that of 3M 20250 at 55°C, and is superior to the latter at 25°C.

(3) Whereas the $\mu\beta$ value of the 3M 20250 tape increases with the number of passes, that of the metallic tape remains constant,

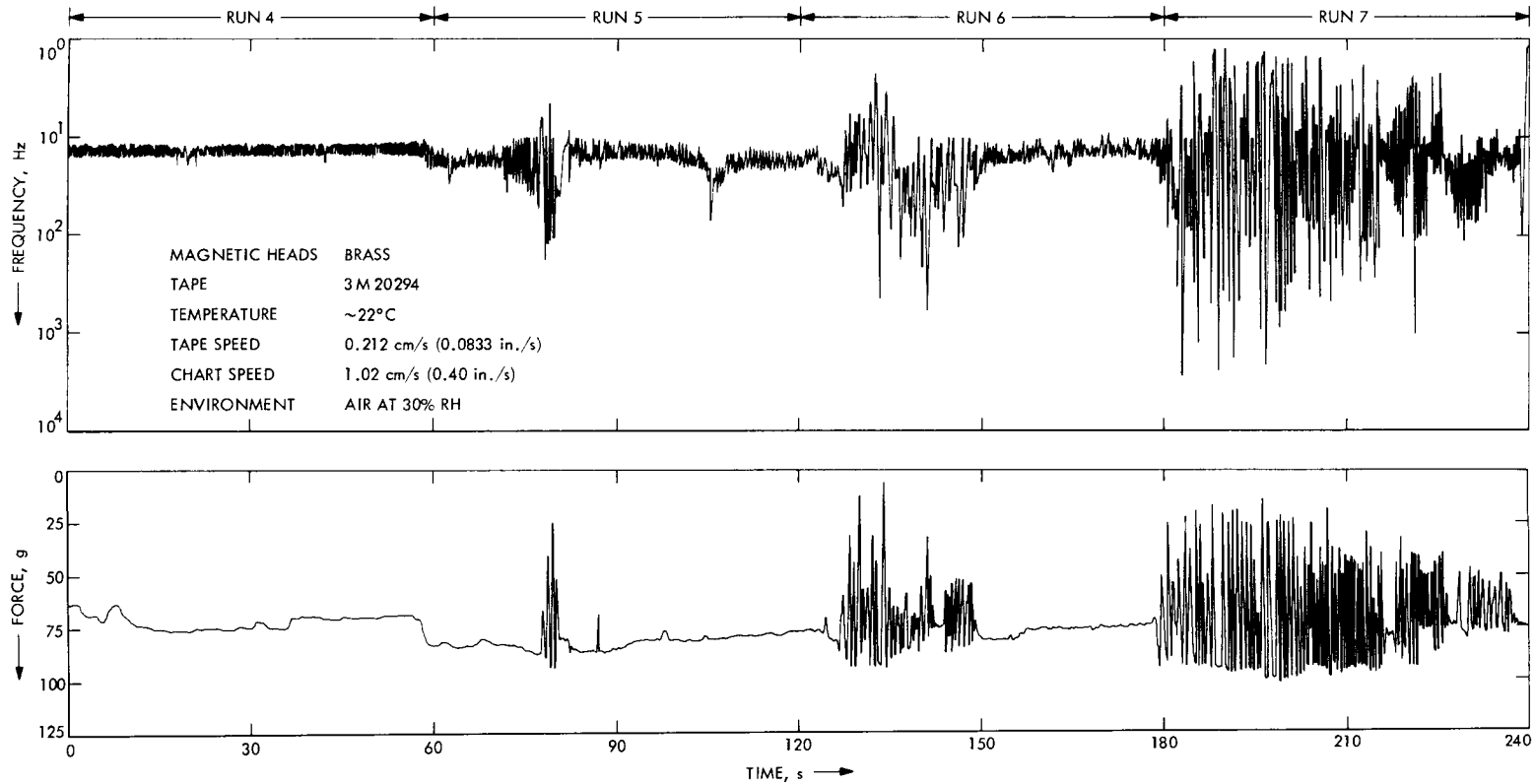

Figure 2. Comparison between the frequency (velocity) and force outputs, measured simultaneously

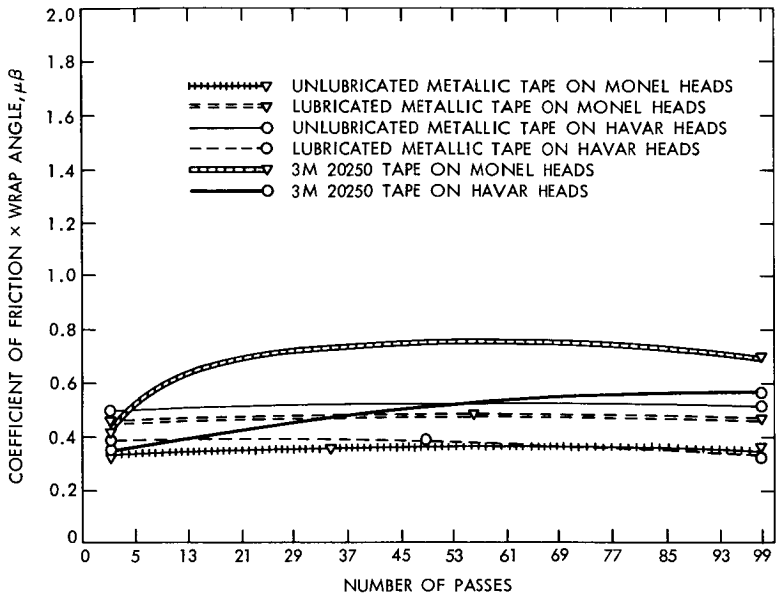

Figure 3. Frictional behavior of metallic tape compared with 3M 20250 tape at 25°C

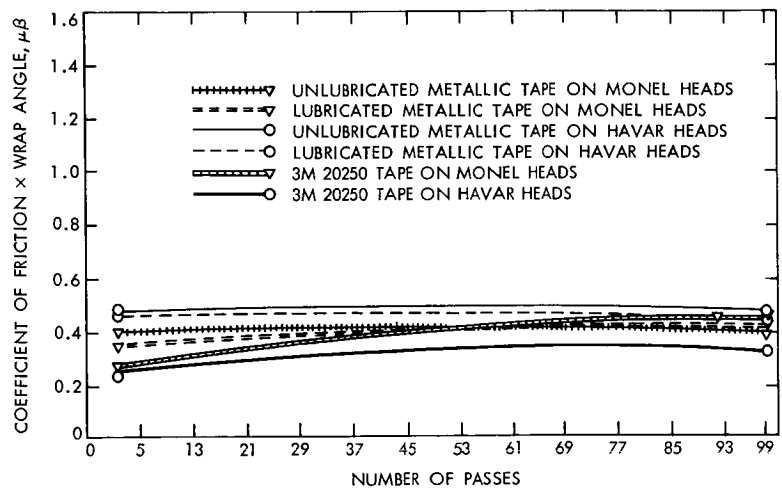

Figure 4. Frictional behavior of metallic tape compared with 3M 20250 tape at 55°C

indicating that changes on the contacting surface of the tape are absent or insignificant, during the test period.

Conclusions

The results of these tests indicate that:

(1) The phenomenon of stick-slip can be detected and measured by either a force transducer (loadcell) or a velocity transducer; the latter is the preferred method.

(2) Stick-slip is always present in plastic tapes in motion, although it may be to a small extent and without deleterious effects.

(3) Factors that increase the drag properties (or the $\mu\beta$ values) of plastic tapes, also increase the extent of stick-slip.

(4) Environmental factors have minimal effects on the frictional performance of the Univac metallic magnetic tape.

(5) Unlike the plastic-backed tapes, the metallic tape does not show any increase in the coefficient of friction with the number of passes used in these tests.

References

1. Kalfayan, S. H., Silver, R. H., and Hoffman, J. K., "Evaluation of Spacecraft Magnetic Recording Tapes," in *Supporting Research and Advanced Development*, Space Programs Summary 37-63, Vol. III, pp. 209–214. Jet Propulsion Laboratory, Pasadena, California, June 30, 1970.

2. Cox, C. N., and Plumtree, W. C., *Engineering Mechanics*, Second Edition p. 117. D. Van Nostrand Co., Inc., New York, February 1959.

3. Kalfayan, S. H., Silver, R. H., and Hoffman, J. K., "A Study of the Frictional and Stick-Slip Behavior of Magnetic Recording Tapes," Technical Report 32-1548. Jet Propulsion Laboratory, Pasadena, Calif., April 1, 1972.

Index: control and guidance, liquid propulsion

Minimum Impulse Tests of 0.45-N Liquid Hydrazine Catalytic Thrusters

P. I. Moynihan

Propulsion Division

Many studies have identified the need for high-performance low-total-impulse chemical thrusters for attitude-propulsion applications on spacecraft with limit cycle attitude control. Specifically, studies for outer planet spacecraft have identified a need for thrusters with a steady-state thrust of 1.3×10^{-1} to 4.5×10^{-1}N (0.03 – 0.1 lbf)[1] and a pulsed "impulse bit" of 4.5×10^{-4} to 4.5×10^{-3}N-s (10^{-4} to 10^{-3} lbf-s). No data on small catalytic thrusters with this capability has heretofore been available. Therefore, in support of an attitude-control tradeoff study performed under the TOPS project, an exploratory test series was conducted on three types of 0.45-N (0.1 lbf) liquid hydrazine thrusters to ascertain the minimum impulse bit capability for this class of engine. This article describes this test series and discusses the results. The testing was performed at 21 and 145°C (70 and 300°F) while maintaining nominal 0.45 N (0.1 lbf) upstream conditions. Valve on-times as low as 0.008 s were applied. Impulse bits as low as 1.0×10^{-3}N-s and 2.6×10^{-3}N-s (2.3×10^{-4} lbf-s and 5.7×10^{-4} lbf-s) were observed for thruster temperatures of 21 and 145°C (70 and 300°F), respectively.

Introduction

In support of an attitude-control tradeoff study that was performed under the TOPS project and for which the limit cycle mode was being considered, tests were conducted (under vacuum conditions) to explore the minimum impulse bit capability of each of three 0.45 N (0.1 lbf) thrusters purchased by JPL. A capability to deliver small impulse bits is imperative if a thruster system is to be effective in limit cycle operations. Since no minimum impulse bit capability data had heretofore been available for 0.45 N (0.1 lbf) catalytic thrusters, these test results were to supply empirical data for this study. These tests were purposely conducted on thrusters that had already experienced extensive test history.

[1] Values in customary units are included in parentheses after values in SI (International System) units if the customary units were used in the measurements or calculations.

Test Objectives

The objective of this test series was to impart a single pulse to the thruster valve for the desired valve on-times given in Table 1. Valve on-time is defined as the time the valve is actually open during an actuation. An impulse bit was obtained for each valve on-time at both 21 and 145°C (70 and 300°F). The 21°C (70°F) temperature was obtained by chilling the thruster body with an external GN_2 purge. The 145°C (300°F) temperature was obtained by a firing of each thruster for approximately one second so that the thruster temperature exceeded 145°C (300°F) slightly. The pulse data was taken when the thruster temperature decayed to 145°C (300°F).

At the time of this series the Rocket Research and Hamilton-Standard thrusters had each accumulated about 1000 cold starts, with the thruster and propellant temperature below 32°C (90°F). The Marquardt unit, which was the one selected to demonstrate 2600 cold starts, had accumulated more than 1700 at this time.

Test Results

Figures 1 through 3 show impulse as a function of actual valve on-time for the Hamilton-Standard, Marquardt, and Rocket Research 0.45-N (0.1 lbf) thrusters, respectively. The impulse was calculated by multiplying the integral of chamber pressure by the thrust coefficient C_f and thrust area A_t. The C_f and A_t used in this calculation were based on a 30-s steady-state test

Table 1. Valve on-time for minimum impulse bit tests of three 0.45-N (0.1-lbf) thrusters

Commanded valve on-times, s	Actual valve on-times, s		
	Moog valve (Rocket Research thruster)	Parker valve (Hamilton-Standard thruster)	Parker valve (Marquardt thruster)
0.100	0.105	0.115	0.124
0.070	0.074	0.085	0.095
0.050	0.059	0.065	0.074
0.040	0.043	0.053	0.065
0.030	0.033	0.044	0.055
0.025	0.028	0.040	0.051
0.020	0.023	0.033	0.045
0.015	0.017	0.030	0.041
0.010	0.013	0.024	0.033
0.005	0.007	0.011	0.015

that was conducted on each thruster after obtaining the impulse data, and hence render a more conservative (i.e., slightly larger) impulse bit than really existed. However, for comparison, the corresponding integral of chamber pressure (P_c bit) is presented on the opposite axis. The variance in $C_f A_t$ for each thruster is reflected by the different locations of the P_c bit scales in the three figures.

Figures 4 and 5 are "normalizations" of these results for which the nominal 0.45-N (0.1-lbf) thrust level has been factored out to enable one to more readily estimate minimum impulse bits for thrusters with an average thrust other than 0.45-N (0.1-lbf). Although thrust-level limitations below 0.18-N (0.04 lbf) have not been thoroughly explored for these thrusters, they are being approached with the present designs. However, lower nominal operating points are obtainable with minimal design changes. Since the Rocket Research thruster operated at approximately twice the chamber pressure as the other two thrusters and has, therefore, incorporated a thicker body design (larger thermal mass), the data spread in Figure 4 appears to reflect a difference in utilization of available energy for the lower impulse bits at 21°C (70°F) between the Rocket Research thruster and both the Hamilton-Standard and Marquardt thrusters, which operate at approximately the same chamber pressures. However, the minimum impulse bit per unit thrust at elevated temperatures (Figure 5) appears to be independent of thruster design.

There was very little chamber pressure response at 21°C (70°F) for valve actuations below 0.015 s. However, the actual impulse bit for given inlet conditions at the elevated bed temperature appears to be limited primarily

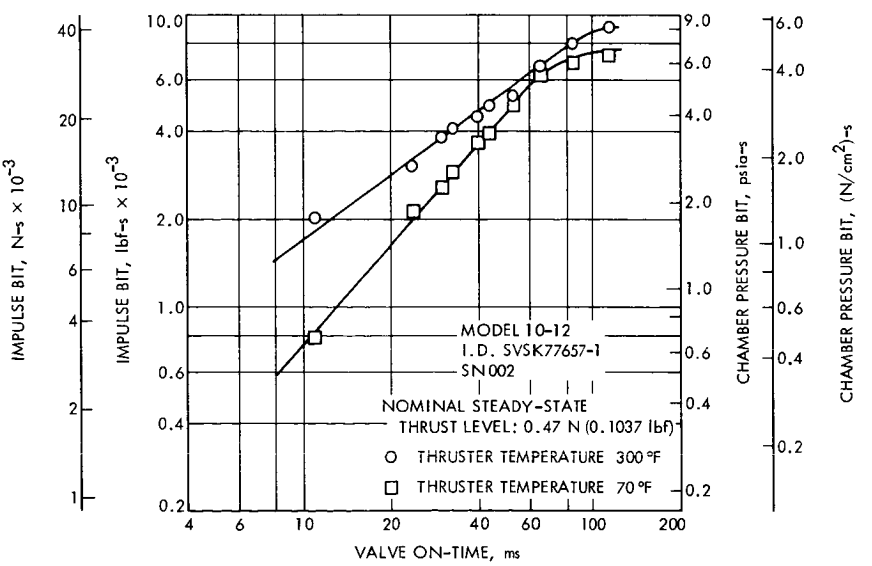

Figure 1. Hamilton-Standard 0.45 N (0.1-lbf) thruster impulse bit as a function of valve on-time at thruster temperatures of 145 and 21°C (300 and 70°F)

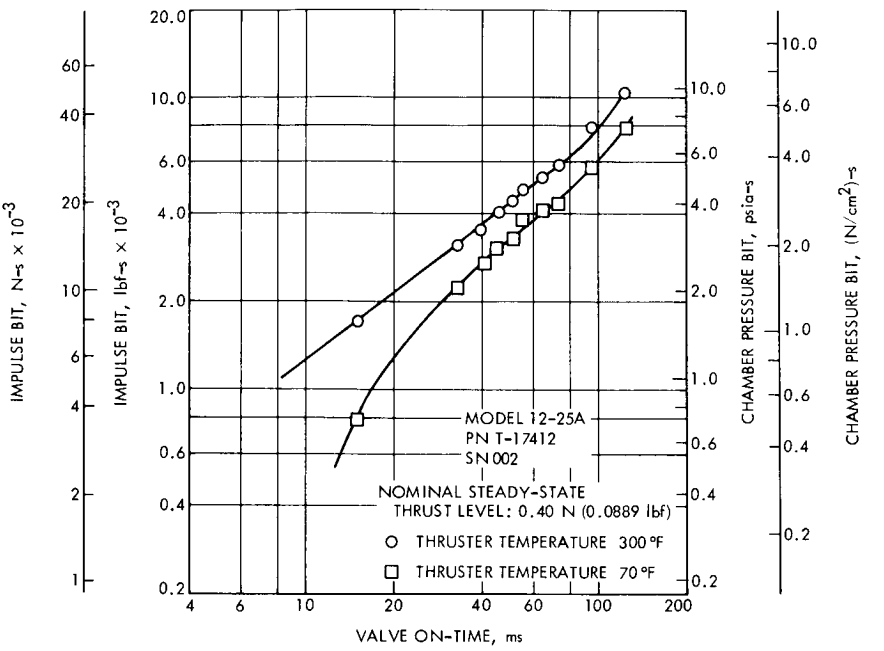

Figure 2. Marquardt 0.45 N (0.1-lbf) thruster impulse bit as a function of valve on-time at thruster temperatures of 145 and 21°C (300 and 70°F)

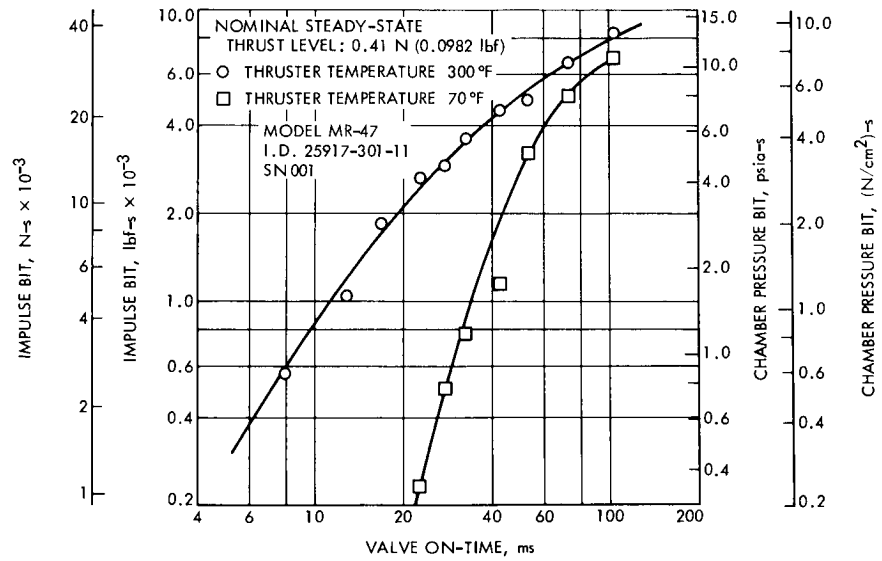

Figure 3. Rocket Research 0.45 N (0.1-lbf) thruster impulse bit as a function of valve on-time at thruster temperatures of 145 and 21°C (300 and 70°F)

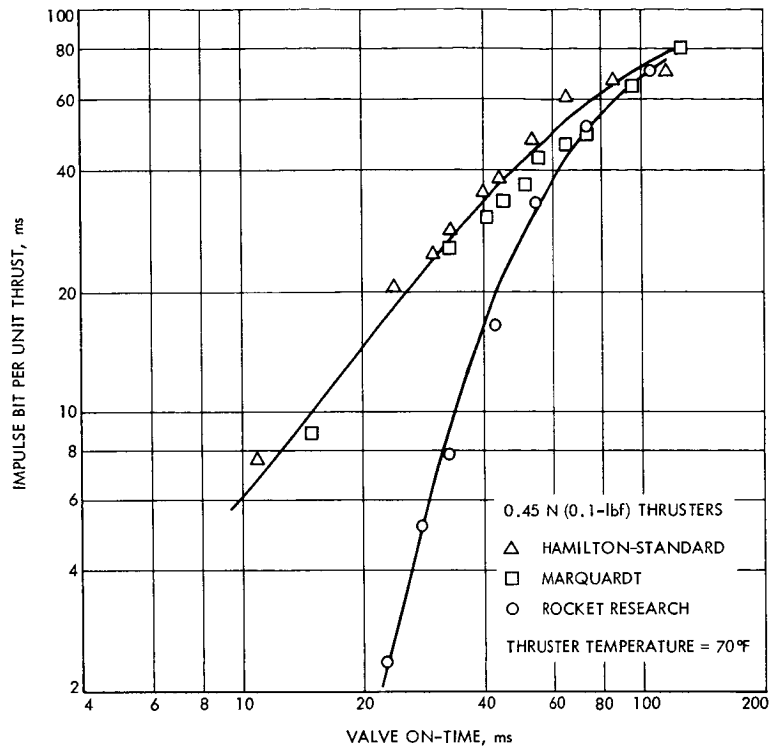

Figure 4. Impulse bit per unit thrust for three thruster designs as a function of valve on-time at thruster temperature of 21°C (70°F)

by valve response. Chamber pressure response was experienced at 145°C (300°F) at a valve on-time as low as 0.008 s for the Rocket Research thruster, which utilized the Moog in-line solenoid valve P/N 010-58723-1. This valve has an opening response of approximately 0.0035 s and a closing response of 0.003 s from command initiation to valve actuation. Both the Hamilton-Standard and Marquardt thrusters are equipped with a version of the Parker-Hannifin valve (P/N 5696050 for Hamilton-Standard and P/N 5675207 for Marquardt) with opening and closing responses on the order of 0.007 s.

Conclusions

These tests have demonstrated the small impulse bits that are readily obtainable for liquid hydrazine catalytic thrusters of the 0.45-N (0.1 lbf) size, and have inferred a practical lower level approaching 4.5×10^{-4}N-s (10^{-4} lbf-s). Although smaller impulse bits are realized for a cold thruster [1.1 N-s $\times 10^{-3}$ (2.5×10^{-4} lbf-s) for the Rocket Research thruster] than were obtained for a warm thruster, the total life is expected to be less than that of a similar duty cycle with a heated catalyst bed.

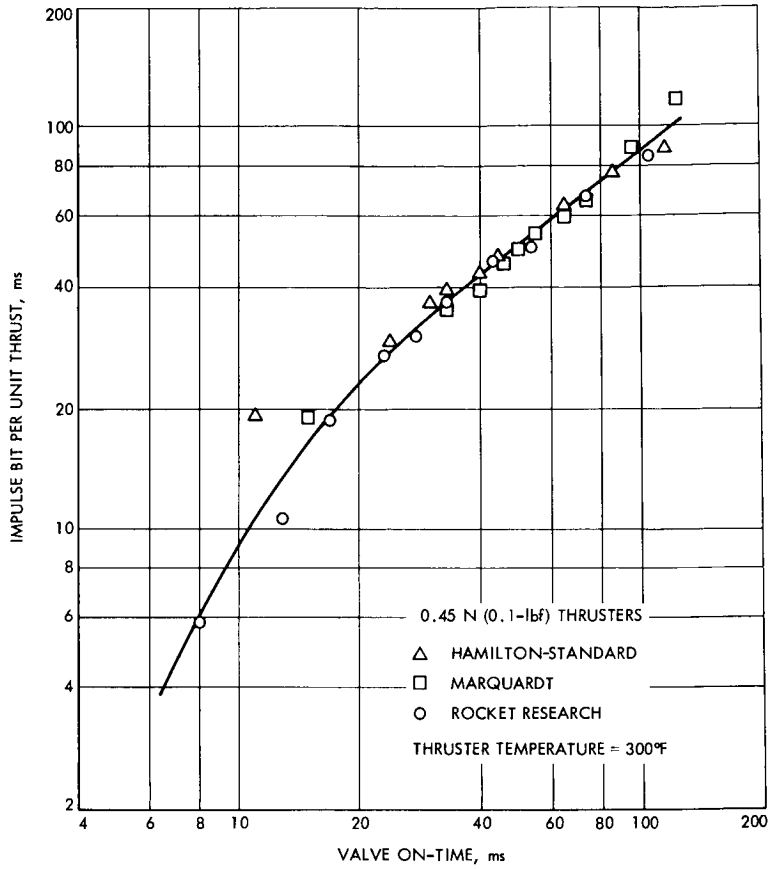

Figure 5. Impulse bit per unit thrust for three thruster designs as a function of valve on-time at a thruster temperature of 145°C (300°F)

An impulse bit of 2.25×10^{-3} N-s (5×10^{-4} lbf-s) was obtained for a catalyst bed temperature of 145°C (300°F), which, in a properly designed thermal control environment, can be maintained for less than a half watt per thruster.

JPL Quarterly Technical Review Volume 2, Number 1 April 1972

Index: computer programs, Mariner Mars 1971 Project, liquid propulsion

Mariner 9 Propulsion Subsystem Performance During Interplanetary Cruise and Mars Orbit Insertion

M. J. Cork, R. L. French, C. J. Leising, and D. D. Schmit

Propulsion Division

On November 14, 1971, the Mariner 9 1334-N (300-lbf)[1] thrust rocket engine was fired for just over 15 min to place the first man-made satellite into orbit about another planet. Propulsion subsystem data gathered during the 5-mo interplanetary cruise and orbit insertion are of significance to future missions of this type. Specific results related to performance predictability, zero-g heat transfer, and nitrogen permeation, diffusion, and solubility values are presented.

Introduction

The Mariner 9 spacecraft was designed to use the basic spacecraft employed on previous Mariner (fly-by) missions with the incorporation of a new and larger propulsion subsystem to accomplish in-transit trajectory corrections and to decelerate the spacecraft from a hyperbolic approach trajectory into an elliptical orbit about Mars (Reference 1). The schematic diagram of this pressure-fed, bipropellant subsystem is shown in Figure 1. The hypergolic propellants, fuel (monomethylhydrazine) and oxidizer (nitrogen tetroxide), are carried in separate tanks, and each is contained within a Teflon expulsion bladder. A regulated supply of filtered nitrogen gas is used to force the propellants from the propellant tanks through a filter, a Teflon-lined flexible hose, and a bipropellant control valve to the rocket engine. The flexible hoses permit gimballing of the rocket engine to provide spacecraft pitch–yaw control. Positive isolation of the pressurant and propellants during long cruise periods is achieved with pyrotechnic-operated gate valves which are actuated by ground commands.

The Mariner 9 sequence of propulsion-related events is listed in Table 1. Although four propulsive maneuvers have been accomplished, only the orbit

[1] Values in customary units are included in parentheses after values in SI (International System) units if the customary units were used in the measurements or calculations.

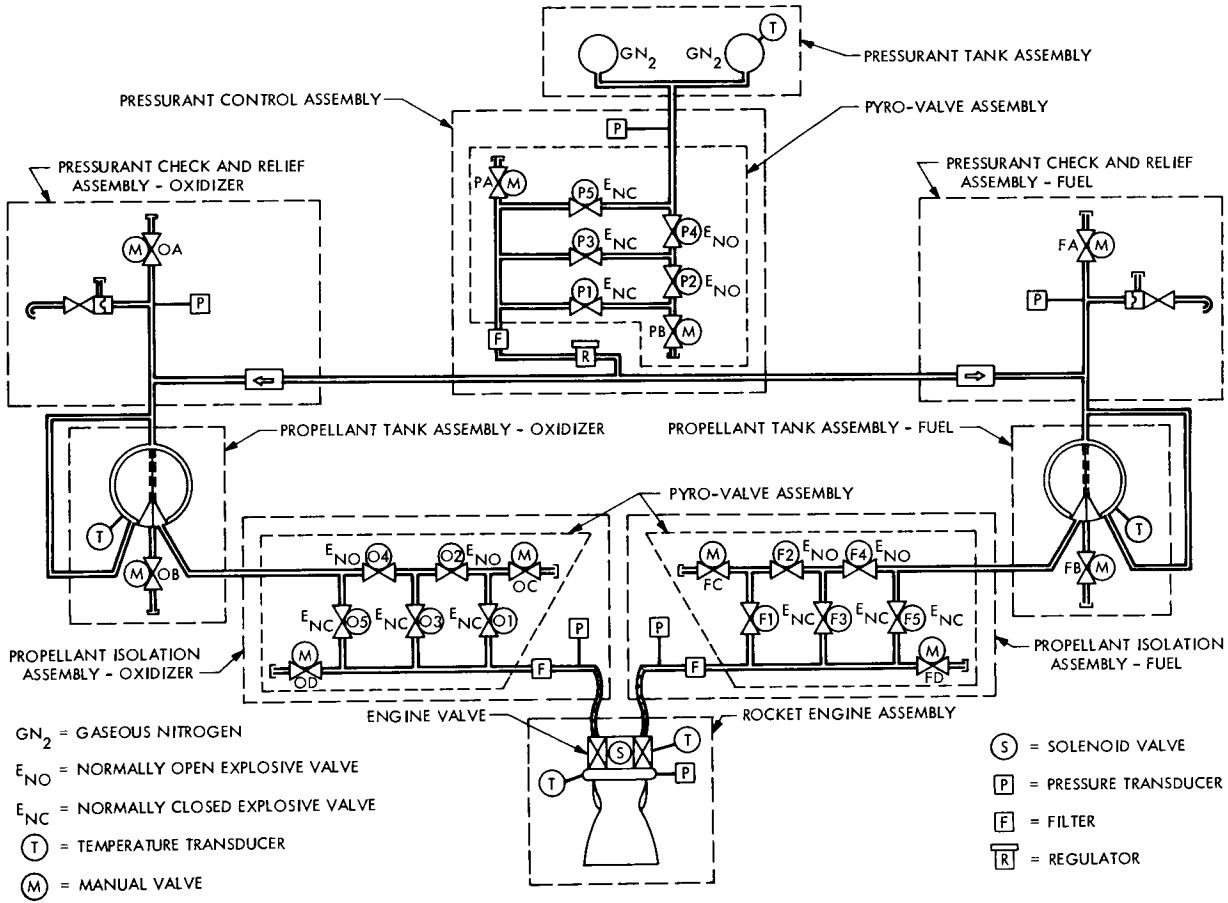

Figure 1. Schematic of Mariner 9 propulsion subsystem

insertion maneuver was long enough to provide sufficient data for a thorough comparison with pre-flight predictions. The tank pressures during the interplanetary cruise period (events 5 to 7 of Table 1) provided data for analyses of nitrogen mass transport properties.

Mars Orbit Insertion Results

A Propulsion Subsystem Operation and Performance (PSOP) digital computer program was developed to support Mariner 9 flight analysis (Reference 2). PSOP is a low-frequency simulation model of the complete propulsion subsystem which predicts system pressures, temperatures, propellant and pressurant flow rates, thrust, spacecraft mass distribution, acceleration, total velocity change, and thrust pointing angles as functions of time. PSOP was used with empirical input data obtained from the Mariner 9 and similar propulsion subsystems to calculate the pre-orbit insertion predictions of Table 2. All parameters are average values for the burn period.

A review of the computer inputs after orbit insertion revealed a regulator-data input error; this is corrected in the second column of Table 2. A weighted-least-squares fit of the flight data and predictions resulted in the best-fit data list of Table 2. Also listed is the estimated 1-σ uncertainty of each parameter in the best-fit column. Burn time, chamber pressure, and engine mixture ratio are all within 0.5% of pre-burn predictions. The flight

Table 1. Propulsion event sequence

Event	Date
1. Launch with propellant tanks at low pressure	May 30, 1971
2. Vent air from liquid lines	Jun 1, 1971
3. Pyro valves open (P1, O1, F1) to pressurize tanks and lines	Jun 3, 1971
4. Midcourse 1 firing (5.1 s)	Jun 4, 1971
5. Pyro valve closed (P2) to isolate gas supply from propellant tanks	Jun 6, 1971
6. Pyro valves closed (O2, F2) to isolate propellants from engine	Jun 14, 1971
7. Pyro valves open (P3, O3, F3) to repressurize system	Nov 1, 1971
8. Orbit insertion firing (915 s)	Nov 13, 1971
9. Orbit trim 1 firing (6.4 s)	Nov 15, 1971
10. Pyro valve closed (P4) to isolate gas supply from propellant tanks	Nov 17, 1971
11. Orbit trim 2 firing (17.3 s) in blowdown mode	Dec 30, 1971

Table 2. Orbit insertion propulsion performance summary for velocity change of 1.6005 km/s[a]

Parameter	Pre-maneuver predict	Corrected predict[b]	Best-fit data	1-σ uncertainty
Burn time, s	919.8	912.8	915.4	0.03
Regulator outlet pressure, N/m^2 ($lbf/in.^2$)	1.74×10^6 (252.2)	1.76×10^6 (255.1)	1.75×10^6 (254.5)	6.89×10^3 (1)
Engine chamber pressure, N/m^2 ($lbf/in.^2$)	7.93×10^5 (115.0)	7.99×10^5 (115.9)	7.97×10^5 (115.6)	6.89×10^3 (1)
Oxidizer resistance, $N\text{-}s^2/m^5\text{-}kg$ ($lbf\text{-}s^2/in.^5\text{-}lbm$)	1.632×10^{10} (17.6)	1.632×10^{10} (17.6)	1.632×10^{10} (17.6)	1.85×10^8 (0.2)
Fuel resistance, $N\text{-}s^2/m^5\text{-}kg$ ($lbf\text{-}s^2/in.^5\text{-}lbm$)	2.429×10^{10} (26.2)	2.429×10^{10} (26.2)	2.447×10^{10} (26.4)	2.78×10^8 (0.3)
Mixture ratio, kg (ox)/kg (fuel)	1.574	1.575	1.582	0.011
Specific impulse, N-s/kg (lbf-s/lbm)	2817 (287.3)	2817 (287.3)	2816 (287.2)	6.8 (0.7)

[a] Burn was controlled by on-board accelerometer to produce this change in velocity.
[b] Post-burn analysis revealed error in regulator data input to model.

data were not sufficiently accurate compared to engine acceptance tests to improve knowledge of specific impulse, so little change was noted there. The increases in mixture ratio and burn time compared to the corrected prediction were attributed to a 0.8% increase in fuel resistance. Note, however, that the fuel resistance change required to provide a data match is less than the 1-σ uncertainty of that parameter. The excellent agreement between flight data and predictions provides a validation of the prediction tools used.

Pressurant gas transfer from the pressurant tanks to the propellant tanks is primarily controlled by the regulator. The contributions of heat transfer are small, but the effects of small heat transfer rate variations can be observed by carefully monitoring the nitrogen tank pressure decay during the 15-min Mars orbit insertion burn.

PSOP was run with the heat transfer equations of Reference 3 and with several variations in the basic heat transfer rates. Three of these runs are summarized in Figure 2 along with flight data. Curve A, the pre-burn prediction, matches ground test data in a simulated altitude chamber. An internal heat transfer film coefficient a factor of 5 larger than those recommended by Reference 3 was required to produce this curve with the assumption of negligible heat transfer to the tank external surfaces. This assumption was recognized to be a potential error source, but no flight systems had been previously fired in the test chamber which could provide a calibration point. Also, the program PSOP had not been used previously, so its performance was not verified. It was therefore decided to use the ground test results for a flight prediction, recognizing that some error could be induced, but with the knowledge from parametric computations that the magnitude of error would not be critical to flight operations.

The flight data plotted on Figure 2 show a pressure 6.89×10^5 N/m^2 (100 lbf/in.^{2}) lower than predicted at the end of orbit insertion. This error had no

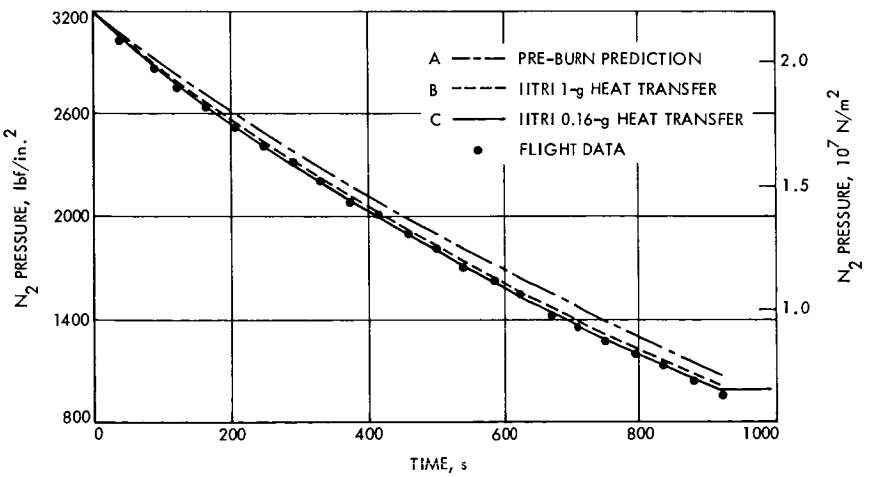

Figure 2. Nitrogen tank pressure during orbit insertion

impact on system operation, but the flight data provide an opportunity to calibrate the test cell and model. Curve C, which incorporates the film coefficients recommended in Reference 3 for internal heat transfer under a 0.16-g environmental acceleration as existed in flight, shows excellent agreement with flight data. Curve B was calculated with Reference 3 heat transfer coefficients modified for 1-g test conditions to evaluate the acceleration-field effect on internal convective heat transfer. The change between curves B and C is small compared to that between curves A and C. It is concluded that the primary error source was convective heat transfer outside the pressurant and propellant tanks but within the test cell. Correlation of the rocket engine valve post-burn temperature transient with similar test data also indicates test cell heat transfer greater than inflight. For future ground testing, careful evaluation of the environment should precede any modifications to the basic Reference 3 equations.

Nitrogen Mass Transport Properties

A portion of the nitrogen pressurant gas used in the Mariner IX propulsion subsystem went into solution during the interplanetary cruise phase. The actual amount in solution was of interest because full saturation of the oxidizer at a tank pressure of 1.72×10^6 N/m^2 (250 lbf/in.^{2}) will decrease operating mixture ratio about 6% from the unsaturated operation point. Pre-flight testing with an oxidizer flow bench which simulated the propulsion subsystem hydraulic circuit showed that (1) the engine injector is the only component which exhibits significant resistance increase due to the two-phase flow caused by gas coming out of solution, and (2) such a resistance increase does not occur until the partial pressure of N_2 in solution exceeds the injector inlet pressure, less vapor pressure.

The injector resistance increase is plotted in Figure 3 as a function of gas out of solution. This same curve was found to apply to the fuel circuit, but lower solubility causes the effect of fuel saturation to be only about 25% that of the oxidizer. Gas out of solution may be calculated as follows:

$$M_{out} = M_{tank} - K\,(P_{inj} - P_v)$$

where

M_{out} = specific mass of N_2 out of solution, kg (N_2)/kg (prop)

M_{tank} = specific mass of N_2 in solution at the propellant tank, kg (N_2)/kg (prop)

K = Henry's solubility constant, kg (N_2)-m^2/N-kg (prop)

P_{inj} = injector inlet pressure, N/m^2

P_v = propellant vapor pressure, N/m^2

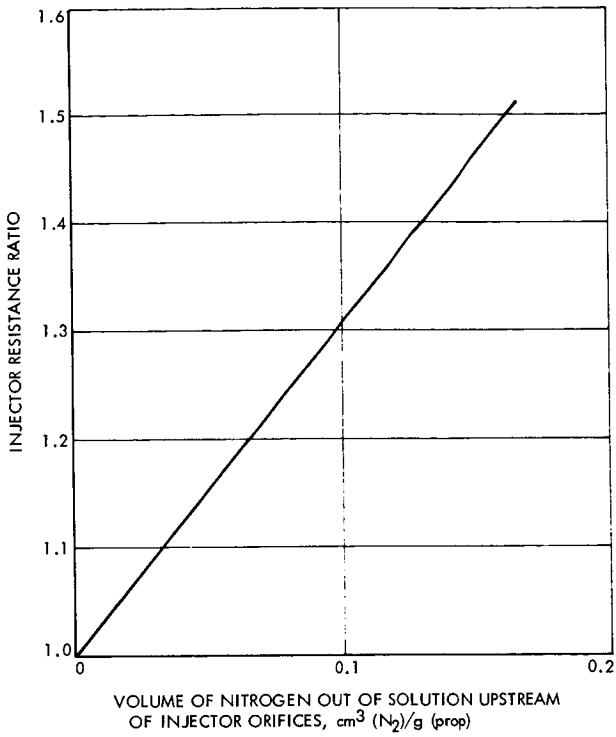

Figure 3. Injector resistance ratio for nitrogen-saturated propellants

Knowledge of injector inlet pressure and gas properties allows calculation of specific volume of gas out of solution and the corresponding resistance factor. This model was included in PSOP for simultaneous solution with the other equations required to define system operating characteristics. Predictions of saturation level were input to the program for each burn.

Pre-flight predictions of saturation level at orbit insertion were calculated using the spherical permeation/diffusion model described in Reference 4 and the parameter values listed in Table 3. Launch saturation levels were equal to the observed propellant tank pad pressures, less vapor pressure. Average saturation level was calculated as a function of time by integrating the mass transfer equations through a constant pressure period (Items 3 to 5 of Table 1), a constant mass period (Items 5 to 7), and another constant pressure period (Items 7 to 8). Predicted propellant tank pressures obtained from this analysis for the constant-mass period are plotted, along with flight data, in Figures 4 and 5 for the oxidizer and fuel tanks, respectively. Note that a significant difference in curve shape and final pressure exists in Figure 4, while only the rate of pressure decay is different in Figure 5.

Since orbit-insertion saturation predictions were calculated by integrating from the end of the constant-mass period, it was desirable to update the model to match the observed pressure decay curves. Pressure profiles which matched the flight data were obtained with the permeation/diffusion

Table 3. Nitrogen permeation, diffusion, and solubility constants

Parameter	Pre-flight assumption	Post-flight estimate
Bladder permeation coefficient, kg (N_2)-m/N-s [lbm (N_2)-in./lbf-h]	7.9×10^{-18} (1.1×10^{-11})	Oxidizer: 4.24×10^{-17} (5.9×10^{-11}) Fuel: 7.9×10^{-18} (1.1×10^{-11})
Portion of bladder area available	1.0	Oxidizer: 0.8 Fuel: 1.0
Diffusivity into oxidizer, m^2/s ($in.^2/s$)	6.45×10^{-9} (10^{-5})	3.87×10^{-9} (6.0×10^{-6})
Solubility in oxidizer, kg (N_2)-m^2/kg (N_2O_4)-N [scc (N_2)-$in.^2$/g (N_2O_4)-lbf]	1.71×10^{-9} (0.01)	1.37×10^{-9} (0.008)
Diffusivity into fuel, m^2/s ($in.^2/s$)	1.35×10^{-8} (2.1×10^{-5})	1.93×10^{-9} (3.0×10^{-6})
Solubility in fuel, kg (N_2)-m^2/kg (MMH)-N [scc (N_2)-$in.^2$/g (MMH)-lbf]	4.46×10^{-10} (0.0026)	3.26×10^{-10} (0.0019)

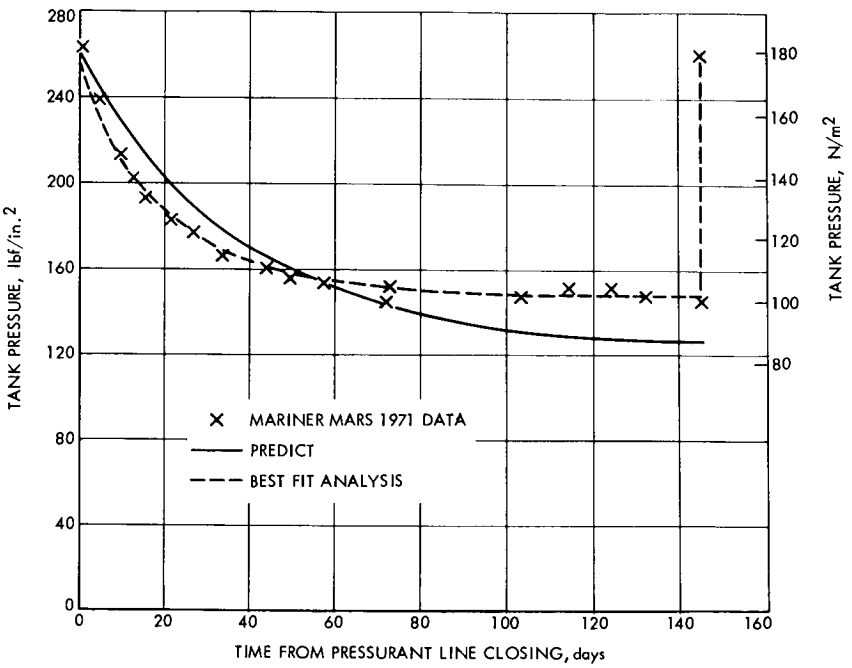

Figure 4. Oxidizer tank pressure during interplanetary cruise

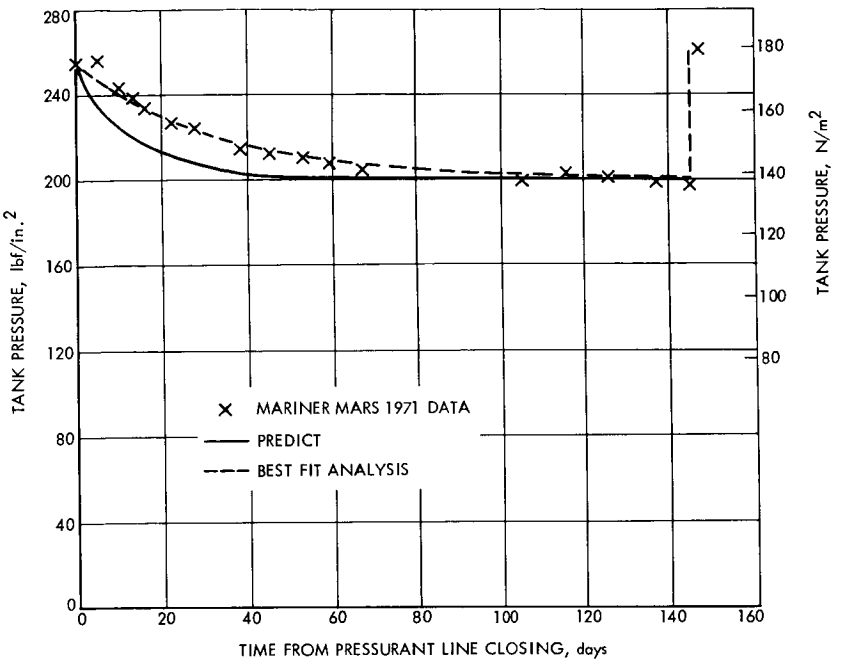

Figure 5. Fuel tank pressure during interplanetary cruise

computer model by assuming different values for bladder area available, diffusion rate, and solubility. Table 3 lists the final solubility and rate constants used to match the data. The increase in N_2 permeation rate for Teflon in N_2O_4 is a result of laboratory data (obtained after Reference 4) which showed that Teflon saturated with N_2O_4 had larger N_2 permeation rates than dry Teflon. Diffusion constants were reduced from the upper edge of the pre-flight uncertainty band toward the lower edge in order to obtain a better data fit. The specific values used were obtained from theoretical diffusion rate calculations. The changes in solubility between the pre- and post-flight estimates are within the range of variation in laboratory test data. Although some uncertainty exists in any one of the parameters listed in Table 3, the set of values listed provides a good data fit and exhibits consistency between the fuel and oxidizer solutions.

The revised constants were used to calculate N_2 saturation pressures at orbit insertion of 1.17×10^6 N/m^2 (170 lbf/in.^{2}) for the oxidizer and 1.47×10^6 N/m^2 (213 lbf/in.^{2}) for the fuel. The oxidizer saturation level is very nearly equal to injector inlet pressure, so only a small amount of excess N_2 would be expected to come out of solution. No mixture ratio shift which could be attributed to excessive saturation was observed during orbit insertion. The flight data tend to enforce the ground-test-derived model of a saturation effects threshold as previously discussed, but they do not allow an evaluation of saturation effects per se because the threshold was not exceeded. The combination of ground and flight data, however, should be especially useful to future programs which use N_2 as a pressurant gas.

Conclusions

The excellent agreement between observed engine performance during orbit insertion and pre-flight predictions lends credence to the characterization of propulsion performance parameters obtained from development and qualification test programs. The demonstrated ability to match flight data by making small adjustments to independent variables in analytical models demonstrated the validity of those models. These results should improve the predictability of similar propulsion subsystems used in future programs.

References

1. Stocky, J. F., "Mariner Mars 1971 Orbiter Propulsion Subsystem Type Approval Test Program," in *JPL Quarterly Technical Review*, Vol. 1, No. 2, pp. 47–53. Jet Propulsion Laboratory, Pasadena, Calif., July 1971.

2. "Propulsion Subsystem," in *Flight Projects*, Space Programs Summary 37-62, Vol. I, pp. 25–26. Jet Propulsion Laboratory, Pasadena, Calif., Mar. 31, 1970.

3. *Design Guide for Pressurized Gas Systems: Task 7*, Report No. IITRI-C6070-20. Illinois Institute of Technology Research Institute (IITRI), Chicago, Ill., June 1967.

4. "Analysis of Pressurant Gas Solubility in the Mariner Mars 1971 Propellant Tanks," in *Flight Projects*, Space Programs Summary 37-65, Vol. I, pp. 35–38. Jet Propulsion Laboratory, Pasadena, Calif., Sept. 30, 1970.

Index: chemistry, liquid propulsion, test facilities and equipment

Surface Tension of Propellants

R. Razouk[1]

Propulsion Division

The design and successful performance of surface tension type propellant management systems for spacecraft necessitate the knowledge of propellant surface tension and contact angle values, and of the behavior of these parameters under various conditions of temperature, pressure, gravitational forces, and aging. The present work is concerned with the measurement of surface tension. An apparatus is described for determining the surface tension of propellants by measuring the maximum bubble pressure using two capillaries of different bores. The innovation is the use of a pressure transducer coupled to a bridge supply and a strip chart recorder for registering the development of the pressure difference as the bubble is formed and released. This enables the measurements to be made under controlled atmospheres and to be remotely operated. Preliminary experiments were done on propellant-grade hydrazine and monomethylhydrazine, and on purified hydrazine, at temperatures between 275.4 and 353.2 K. Straight-line expressions and logarithmic expressions reproduce equally well the variation of surface tension with temperature. Contaminated hydrazine, pre-exposed to coupons of 6Al–4V titanium alloy for long periods, gives slightly higher values of surface tension.

Introduction

Surface tension technology has been applied in recent years to the retention and control of propellants for liquid propulsion systems used in space vehicles. The reason is that propellant management devices based on the capillary concept possess the features of light weight, simplicity in design, and good reliability. They are also characterized by high expulsion efficiency under the conditions of zero- or low-g encountered during coast, attitude control maneuvers, trajectory correction, and orbit injection.

Capillary retention and control devices utilize the familiar phenomena involved in the rise of liquids in capillary tubes, and in the retention of bubbles of gas in liquids by means of screens. The behavior of such systems is primarily determined by the surface tension of the liquid, and the contact angle that the liquid forms with the wetted surface.

[1] Professor, Chemistry Department, California State College at Los Angeles

The design and successful performance of surface tension type propellant acquisition systems for spacecraft necessitate, therefore, an informed knowledge of the surface tension of the propellant, and of the propellant/container (usually metallic) contact angle, and, in addition, the behavior of these parameters under various conditions of temperature, pressure, and reduced gravity. Furthermore, the propellant/tank material compatibility is a dominant factor for long-life missions of several years; thus, it is of prime importance to ascertain the effect of any resulting decomposition and contamination of the propellant on these properties.

Limited work has been done on the determination of the surface tension and contact angles of Earth-storable and space-storable propellants, and there are occasionally discrepancies in some of the published data. The effect of temperature over a wide range has scarcely been investigated, and no studies have yet been made on the effects of gas evolution and of contamination accompanying extended contact of the propellant with the equipment.

The present work is confined to the measurement of surface tension. An apparatus for measuring the surface tension of propellants is described, and preliminary results of experiments on hydrazine and monomethylhydrazine (MMH) are reported.

The apparatus is based on the principle of Sugden's maximum bubble pressure method involving two capillaries of different radii immersed in the liquid to the same depth (Reference 1). The method has the advantage that it does not depend on contact angle and that the depth of the capillaries and the radius of the narrow capillary need not be known. Only the radius of the larger capillary and the density of the liquid must be known, but not necessarily to a high degree of exactness, since they appear as correction terms.

According to Sugden (Reference 1) the surface tension is given by

$$\gamma = A \cdot \Delta P \left(1 + 0.69 \frac{r g D}{\Delta P}\right) \tag{1}$$

where γ is the surface tension (N-m^{-1}), ΔP the difference in the maximum pressures necessary to form the bubbles at the narrow and wide tubes (N-m^{-2}), r the radius of the wide tube (m), g the acceleration due to gravity (9.807 m-s^{-2}), D the density of the propellant (kg-m^{-3}), and A a characteristic constant of the apparatus (m).

The innovation in the present method is the use of a pressure transducer coupled to a bridge supply and strip chart recorder for registering the pressure differences as the gas bubbles are formed and detached at the tips of the two tubes alternately. This arrangement circumvents the difficulty of simultaneous reading of the two levels of an ordinary manometer, and eliminates the errors arising from the lag of the manometer fluid. It also enables the measurements to be made under controlled atmospheres and to

be remotely operated. These features are of particular interest because of the noxious nature of propellants, and because of the adaptability of the method to the study of surface tension under high-pressure conditions which require an all-metal apparatus.

Experimental

Apparatus

Measurements of surface tension were made with the aid of the apparatus shown schematically in Figure 1. A double-jacketed cylindrical pyrex cell (a) with a carefully ground long and wide neck contained the propellant at constant temperature. The ground joint stopper had two similar tubes (b and b′) passing through it. Tube b was fitted with a Teflon stopcock at its upper end. The lower end of tube b′ was sealed to a short capillary of 3×10^{-3}-m length. The lower tips of the two tubes were cut sharply at right angles to their axes at exactly the same level and were finely ground. The diameters of the tubes were 4.070×10^{-3} and 0.269×10^{-3} m. The tubes were connected together above the stopcock into a common tube (c) which led to the pressure side of the transducer (d). A side tube (e) allowed the introduction of a stream of nitrogen gas. The stopper also had a ground joint opening (f) for a thermometer, and an outlet tube (g) connected to the reference side of the transducer. The outlet tube contained a small vent to maintain the pressure of the surrounding atmosphere on this side of the transducer.

The pressure transducer used was a Statham Type PM60TC ± 1-350. It was connected to a Dynamics bridge supply Model 6343A. The electric signal was recorded on a Hewlett-Packard Moseley 7100B strip chart recorder Model 17501A.

The transducer was excited by an electric potential difference of 10 V. It was calibrated by measuring the electric output for different pressure standards. The bridge and recorder were adjusted so that a signal of 2.54 cm (1 in.) on the chart corresponded to a pressure difference of 1.730×10^2 N-m^{-2} (1.730×10^3 dyne-cm^{-2}). This arrangement permitted measurements of surface tension to an accuracy of 10^{-4} N-m^{-1}, which corresponded approximately to 0.2% of the surface tension measured (*vide infra*).

Procedure

The measurements were carried out in an atmosphere of dry nitrogen in order to eliminate errors resulting from absorption of water vapor by the propellant and oxidation with atmospheric oxygen.

A slow stream of dry nitrogen regulated by a system of needle valves was passed through a copper coil at the temperature of the experiment and then through the capillaries of the cell. The rate was adjusted to 2–4 bubbles of nitrogen per minute. The gas was first allowed to pass through the wider tube, and the development of the pressure difference was recorded for several cycles of growth and release of the bubbles. The stopcock of tube b

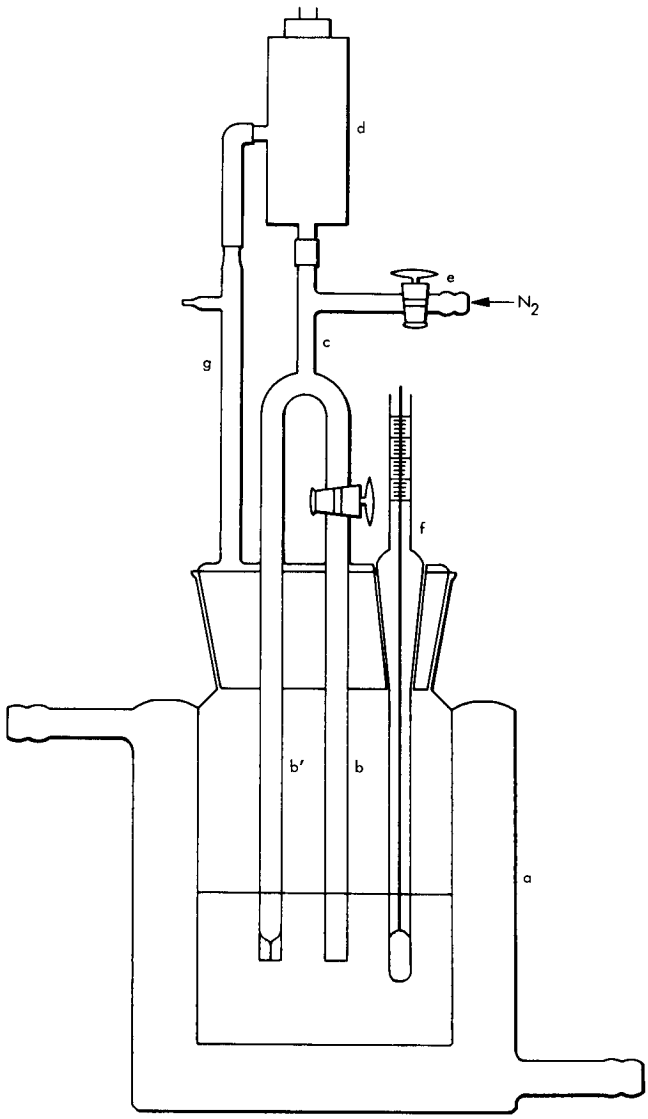

Figure 1. Surface tension apparatus

was closed next and nitrogen was passed through the narrow tube, and again the development of the pressure difference was recorded.

Figure 2 shows typical recordings of two experiments on hydrazine at 283.2 and 343.2 K. As the gas bubbles were formed and detached, the pressure increased to a maximum and then decreased. But the cyclic pressure changes depended on the bore of the capillary, the depth of the orifice, and the rate of gas bubbling. The pressure in the narrow tube increased steadily to a maximum, when the bubble assumed the hemispherical shape, and then dropped sharply as the bubble was released. On the other hand, the pressure in the larger tube increased to a maximum and diminished slowly as the bubble grew and flattened and finally became unstable and detached; the pressure then showed a sudden drop. This behavior is frequently overlooked in the familiar bubble point experiments for determining surface tension by measuring the gas pressure at the instant of detachment of a gas bubble.

Materials

Experiments were carried out on samples of propellant-grade, purified, and contaminated hydrazine, and of propellant-grade monomethylhydrazine.

Hydrazine I was propellant-grade Mathieson quality. Analysis showed that at the time of the experiments it contained 0.2% water, 0.1% ammonia, and 0.2% aniline.

Hydrazine II was a purified sample prepared as follows. Propellant-grade hydrazine was treated with barium oxide for several hours; then the vapor and gases were pumped off until the volume of the liquid was reduced by 20%. The liquid was then distilled from the mixture *in vacuo* at ambient temperature, and collected at dry-ice temperature. Finally, hydrazine was redistilled *in vacuo* into bulbs which were sealed off and stored at dry-ice temperature until used. The bulbs were broken in a glove box under an atmosphere of dry nitrogen and the hydrazine transferred into the surface tension cell. Typical analysis gave 0.1% water, 0.06% ammonia, and less than 5-ppm aniline.

Contaminated hydrazine was a product obtained from hydrazine compatibility experiments of a current program. Propellant-grade hydrazine was introduced into capsules containing a coupon of 6Al–4V titanium alloy, and the capsules were kept at dry-ice temperature, degassed, and sealed. They were stored at 316.5 K until a pressure of about 3.5×10^5 N-m^{-2} was developed inside the capsules, at which time they were moved to a box at dry-ice temperature. The capsules were broken, the pressure released, and the liquid transferred to the surface tension apparatus. The contaminated hydrazine had a brownish color and a density about 5% higher than that of the parent liquid. It also contained considerable amounts of particulate matter in suspension visible to the naked eye. Samples were taken from

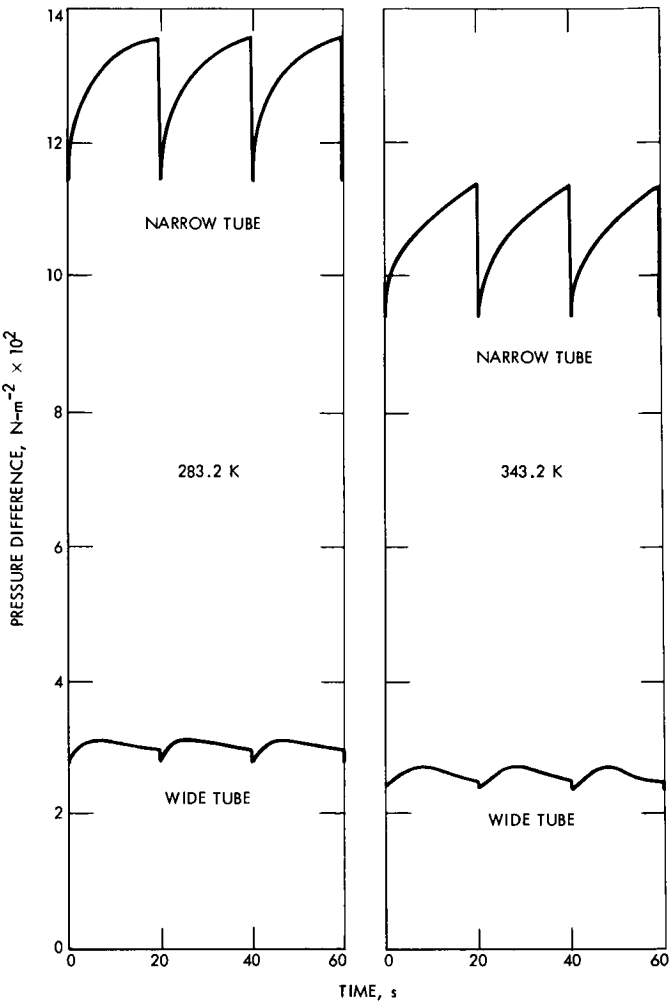

Figure 2. The development of pressure difference in cycles of growth and detachment of gas bubbles

three capsules. The ammonia content of the propellant at the end of the experiments was 0.2, 2.8, and 1.5%.

Propellant-grade monomethylhydrazine was Olin-Mathieson quality. It contained 0.2% water and 0.2% ammonia at the time of the experiment.

Results and Discussion

The apparatus constant A was determined by measuring the maximum bubble pressure differences for liquids of known surface tension at 303.2 K. The following results were obtained: water, 6.80×10^{-5} m; methanol, 6.73×10^{-5} m; benzene, 6.74×10^{-5} m; carbon tetrachloride, 6.80×10^{-5} m; 10% by volume aqueous ethanol solution, 6.79×10^{-5} m; and 20% by volume aqueous ethanol solution, 6.75×10^{-5} m. The average value of 6.77×10^{-5} m was used.

Table 1 shows the results of measurements of the surface tension of hydrazine and monomethylhydrazine over a temperature range of about 80 K. Contamination appears to produce small changes in the surface tension of hydrazine. Both the propellant-grade quality and contaminated hydrazine obtained from compatibility experiments have surface tensions that differ slightly from the value of the purified propellant. Such small differences should have little effect on the performance of surface tension type acquisition devices designed on the basis of surface tension values for pure hydrazine, provided that the contact angle of the hydrazine/container material is not sensibly altered in the meantime. However, the experimental results do not necessarily imply that there is no deterioration of the surface tension of hydrazine when the latter is saturated with ammonia, nitrogen, and hydrogen under the high pressures which may be developed during extended periods of propellant contact with the tank material. Measurements of surface tension under these conditions have to be made before drawing definite conclusions. Furthermore, it is more likely that difficulties would arise from the narrowing or clogging of the capillaries and the screen perforations of the equipment by the particulate materials which have been observed in the contaminated propellant.

Surface tension values for Hydrazine II and MMH are also plotted in Figures 3 and 4. Good linear relations are found between surface tension and temperature. For Hydrazine II the relationship is represented by

$$\gamma\ (\text{N-m}^{-1}) = 129.1 \times 10^{-3} \left(1 - \frac{T\,(\text{K})}{632}\right) \tag{2}$$

$$[\gamma\ (\text{dyne-cm}^{-1}) = 73.3 - 0.2044t\ (^{\circ}\text{C})]$$

where γ is the surface tension at temperature T in kelvin (t in degrees Celsius). For MMH the relationship is

$$\gamma\,(\text{N-m}^{-1}) = 65.8 \times 10^{-3}\left(1 - \frac{T\,(\text{K})}{606}\right) \tag{3}$$

$$[\gamma\,(\text{dyne-cm}^{-1}) = 36.1 - 0.1088t\,(^{\circ}\text{C})]$$

The constants of Equations 2 and 3 differ somewhat from the values calculated for hydrazine (138.7×10^{-3} N-m^{-1}, 572 K) and for MMH (63.2×10^{-3} N-m^{-1}, 641 K) using the data of Bernard and Goudeau (Reference 2) and Lawrence (Reference 3, Table 18), respectively.

The surface tension of pure liquids decreases with rise of temperature, and it should vanish at the critical temperature T_c. Based on Equations 2 and 3, the critical temperatures of hydrazine and MMH would be 632 and 606 K, respectively. These values are much closer to the corresponding experimental critical temperatures of 653.2 K (Reference 4) and 585.2 K (Reference 3, Table 3) than the values of 572 and 641 K calculated from the data of Bernard and Goudeau (Reference 2) and Lawrence (Reference 3, Table 18), respectively.

Nevertheless, it is obvious that although the linear relation fits the data over the temperature range of the experiments, it is inadequate at higher temperatures. A better empirical relation between surface tension and temperature has been developed on the basis of the principle of corresponding states, namely,

$$\gamma = \gamma_0\left(1 - \frac{T}{T_c}\right)^{1+r} \tag{4}$$

where r is a constant equal to 0.234 (van der Waals, Reference 5), 0.21 (Ferguson, References 6 and 7), and 2/9 (Guggenheim, Reference 8). This relationship is assumed to apply only to spherically symmetrical homopolar molecules. Cahn and Hilliard (Reference 9) pointed out that $r = 0.21$ in the region $T/T_c = 0.6$ but that in the neighborhood of T_c it approaches 0.5. Grosse (Reference 10) found that for metals r varies between 1.28 (sodium) and 0.25 (cadmium).

Equation 4 has been tested by plotting log γ versus log $(1 - T/T_c)$ in Figures 5 and 6. The straight lines are very satisfactorily represented by

$$\gamma\,(\text{N-m}^{-1}) = 130.5 \times 10^{-3}\,(1 - T/653.2)^{1.065} \tag{5}$$

$$[\gamma\,(\text{dyne-cm}^{-1}) = 0.1311\,(380 - t)^{1.065}]$$

for hydrazine II, and by

Table 1. Surface tension of hydrazine and MMH

Temperature, K	Surface tension $\gamma \times 10^3$ N-m^{-1}			
	Hydrazine I (propellant-grade)	Hydrazine II (purified)	Contaminated hydrazine	MMH
275.4	71.8	72.8		35.9
283.2	70.3	71.2		35.0
293.2	68.5	69.2		34.0
303.2	66.5	67.2	68.5; 68.8; 67.3	32.9
313.2	64.6	65.1		31.8
323.2	62.7	63.0		30.7
333.2	60.7	61.0		29.6
343.2	58.7	58.9		28.5
353.2	56.7	57.0		27.4

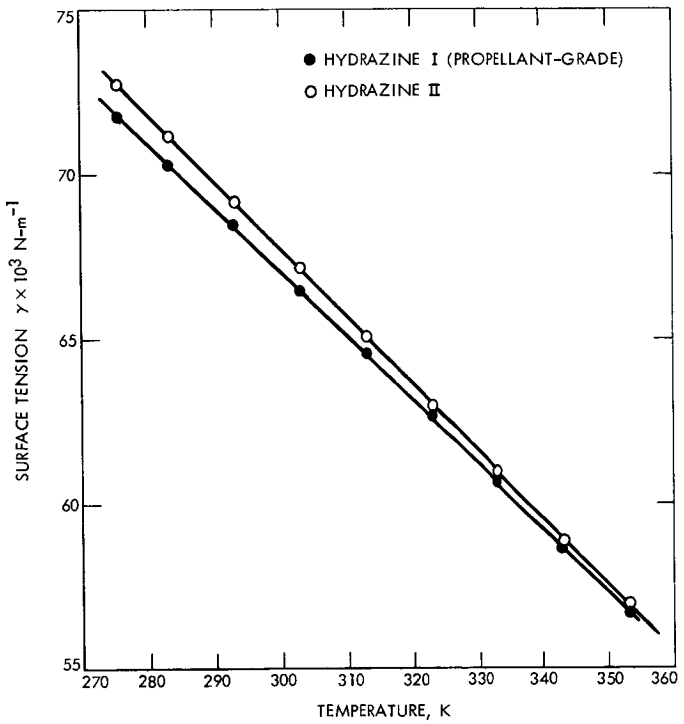

Figure 3. Linear variation of the surface tension of Hydrazine I (propellant-grade) and Hydrazine II with temperature

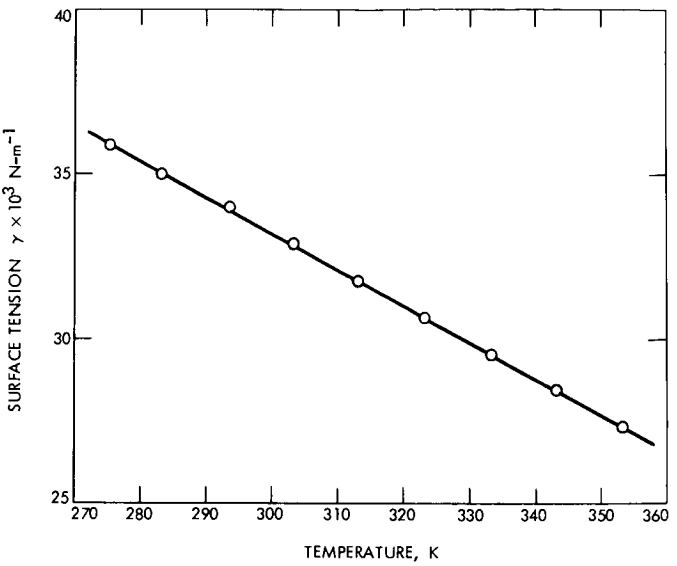

Figure 4. Linear variation of the surface tension of MMH with temperature

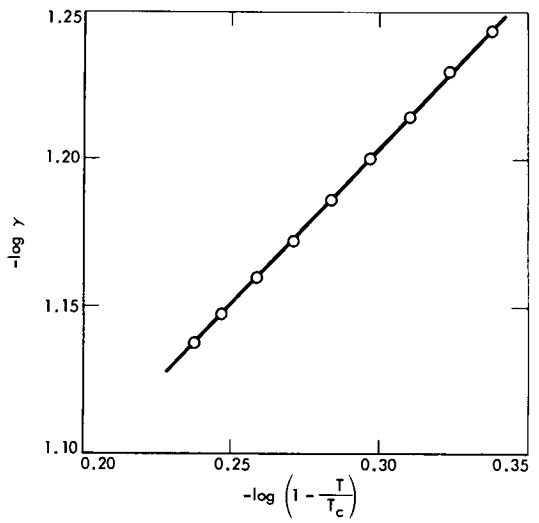

Figure 5. Logarithmic relationship between the surface tension of Hydrazine II and temperature

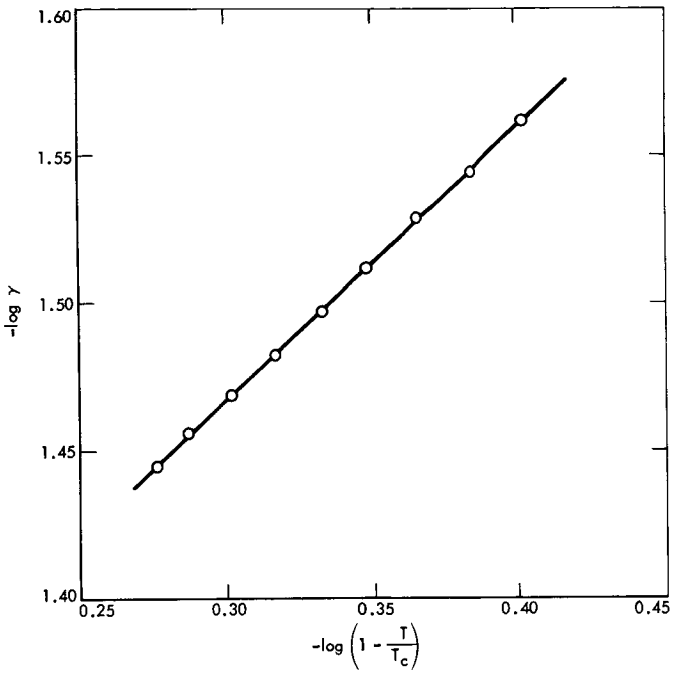

Figure 6. Logarithmic relationship between the surface tension of MMH and temperature

$$\gamma\ (\text{N-m}^{-1}) = 65.2 \times 10^{-3}\ (1 - T/585.2)^{0.937}$$

$$[\gamma\ (\text{dyne-cm}^{-1}) = 0.1668\ (312 - t)^{0.937}] \qquad (6)$$

for MMH.

Both the straight-line expressions (Equations 2 and 3) and the logarithmic expressions (Equations 5 and 6) reproduce the experimental results equally well, and give values of γ_0 close to within 1%. However, at higher temperatures one would expect that the logarithmic expression fits the results better, since the surface tension vanishes at the true critical temperature.

The Eötvös constant (Reference 11) and the parachor (Reference 12) were calculated for hydrazine and MMH by using the respective expressions; both values indicated considerable association of the molecules of the two liquids, and the decrease of the extent of association with rise of temperature.

Acknowledgment

The author wishes to express his thanks to Mr. Stephen P. Vango for the preparation of purified hydrazine, and his appreciation to Mr. George Yankura for useful discussions.

References

1. Sugden, S., *J. Chem. Soc.*, Vol. 125, p. 1177, 1924.
2. Bernard, M. L., and Goudeau, J. C., *J. Chim. Phys.*, Vol. 62, p. 732, 1965.
3. Lawrence, R. W., *Handbook of the Properties of Unsymmetrical Dimethylhydrazine and Monomethylhydrazine*, Aerojet Project No. 1292. Aerojet-General Corporation, El Monte, Calif., May 1958.
4. Clark, C. C., *Hydrazine*, p. 21. Mathieson Chemical Corporation, Baltimore, Md., 1953.
5. van der Waals, J. D., Z. *Physik. Chem.*, Vol. 13, p. 657, 1894.
6. Ferguson, A., *Trans. Faraday Soc.*, Vol. 19, p. 407, 1923.
7. Ferguson, A., *Proc. Phys. Soc.*, Vol. 52, p. 759, 1940.
8. Guggenheim, E. A., *J. Chem. Phys.*, Vol. 13, p. 253, 1945.
9. Cahn, J. W., and Hilliard, J. E., *J. Chem. Phys.*, Vol. 28, p. 258, 1958.
10. Grosse, A. V., *J. Inorg. Nucl. Chem.*, Vol. 24, p. 147, 1962.
11. Von Eötvös, R., *Ann. Physik*, Vol. 27, p. 448, 1886.
12. Sugden, S., *J. Chem. Soc.*, Vol. 125, p. 32, 1924

JPL Quarterly Technical Review Volume 2, Number 1 April 1972

Index: computer applications and equipment, computer programs, tracking

Operating Executive for the DSIF Tracking Subsystem Software

P. L. Poulson

Data Systems Division

The advanced engineering model of the DSIF tracking subsystem (DTS) is currently being developed by the Deep Space Instrumentation Facility. The DTS will provide effective and reliable tracking and data acquisition support for the complex planetary and interplanetary spaceflight missions planned for the 1970 decade. The nucleus of the subsystem is a Honeywell H832 digital computer. This article describes the design and capabilities of the real-time operating executive software being developed for this subsystem.

Introduction

The DSIF tracking subsystem comprises the digital capabilities required at a deep space station for the purposes of tracking data acquisition and validation and subsequent transmission to the SFOF. Initial requirements include the real-time handling and control of doppler, ranging, angle, predict, validation, and others. The subsystem must handle a variety of digital and analog input and output as well as provide control services to many DSIF subassemblies. This multifunctional environment of data and services is being centrally controlled by the H832 computer, which, in turn, requires a unified software operating system or executive. The primary purpose of the operating executive (EXEC) is the management of computer resources, such as central processing unit (CPU), memory, and input–output. The real-time environment, with its multiplicity of asynchronous events and quasi-servo processes, imposes stringent design constraints upon the operational software. The DTS EXEC must handle high- and low-rate asynchronous input and output, activate the appropriate processing, respond to a host of configuration control messages, service display requests, insure that all time-critical requirements are met through a time-dependent priority structure, and provide services for data storage and retrieval. Finally, an important consideration in the design philosophy of the EXEC was the fact that it would operate within a relatively stable and unchanging complement of functional software.

For a more detailed description, see Reference 1.

Hardware

Much of the computer hardware is of the everyday variety. However, there are certain features that require special mention because of their impact upon the design of the EXEC.

The H832 is a multi-processor computer, with the present configuration consisting of two CPUs and two input-output processors (IOPs), each operating as dictated by stored and sequentially ordered instructions (program). Additionally, both the CPU and the IOP can each operate at sixteen priority states or levels, which, in effect, is a hardware determined queue of software. The EXEC incorporates a two-dimensional program queuing structure based upon this characteristic and is described in more detail later on.

Control of CPU or IOP activity is accomplished by the multi-process controller (MPC) which specifies the level at which CPU or IOP is to operate. Both CPU and IOP are equipped with control process orders (instructions) which, when executed, are delivered to the MPC, which, in turn, effects a change of state in the CPU or IOP. Thus, through software, either CPU or IOP can effect the operating level of any of the computer processors. Each CPU operating level has a priority position and operates in one of four activity states: stopped, enabled, committed, or sequencing. Likewise, each IOP level can operate in one of four activity states: stopped, waiting, engaged, or sequencing. The hardware can thus accommodate the various interruptive and I/O traffic.

Finally, the computer establishes its interface with the external DSIF environment through the digital/analog input/output (DAIOS) subsystem which provides a capability of transferring data between an IOP and a large number of discrete and analog lines, including GCF traffic. The DAIOS is the sole interface between the H832 and the DSIF subassemblies. It has 8 channels for each of 8 subsystems, with each channel having 64 subchannels, or 4096 subchannels in all.

Software

Like many such computer-based support facilities, the existence of independent and diverse programs, all operating at the same time, requires central controlling software. Such control is vested in the EXEC which, in turn, controls all functional support programs, the design of which is as much determined by the EXEC as by the hardware. The questions are: How much control should be exercised by an EXEC? How large should it be allowed to get? What are the limits of services it should provide? Such considerations are practically boundless, and it is a well-known phenomenon that nothing so proliferates as computer operating systems.

Design Philosophy

The hallmarks of the DTS EXEC are simplicity, adaptability, and efficiency, and the approach "better too little than too much" is taken. The EXEC is simple in that it encompasses all the basic features required for real-time operation, but explicitly excludes the myriad embellishments that are characteristic of the job-shop computer facility. It is adaptable to changing DSIF requirements because of its functionally independent nature, readily accommodating the addition or deletion of new real-time or non-real-time programs. It is efficient in its use of memory and processor utilization and makes full use of parallel execution of input-output and computation.

The salient and distinguishing feature of the software structure is the method by which computer resources, especially CPU and IOP cycles, are allocated. All functional programs requiring real-time status, must be structured into subprograms to accommodate the variety of time-critical requirements and at the same time cohabitate with other tasks having similar needs. The subprogram is, therefore, the largest unit of software which is entitled to CPU or IOP resources in the real-time environment. Through this method the maximum computer resources are utilized, and response times to external stimuli are minimized. All subprograms are assigned to various CPU operating levels and are subject to being interrupted by subprograms that have been assigned higher priority operating levels. Programs not segmented, or not having real-time requirements, will be assigned the lowest operating or background level.

The EXEC supplies the linkages between the various subprograms comprising a functional task. Control is passed to each subprogram by the EXEC, which regains control when either: (1) a higher priority subprogram at a higher level is enabled, or (2) the subprogram is completed. The EXEC supplies the linkages between input-output activity and the ongoing tasks, as well as the link between program and data.

The particular priority level assigned to a subprogram depends upon: (1) periodicity of execution and, (2) duration of execution. Interrupt handling routines are essentially high-level subprograms. The addition or deletion of subprograms is accomplished through the EXEC tables. Functional continuity is also accomplished through the EXEC tables by the enabling of one member subprogram by another.

Another important consideration in the design philosophy was the use of the multi-processor (CPU) capabilities of the H832. The present philosophy treats a processor as a resource rather than as one assigned to a task. The assignment of a processor to a task is not predetermined, and in the case of processor failure, the task will be assumed by any other available processor. Theoretically, this is considered to be the optimum backup approach, although there are practical considerations, such as memory conflicts, that will reduce the overall effectiveness.

Design Characteristics

Job Queue Controller

Control is assigned through the use of the job queue controller, which allocates CPU resources according to priority and status. This is accomplished through the use of a job queue which is merely an ordering of subprograms. Each entry in a queue represents a subprogram which may or may not be active. Processor control is allocated through the queue and never from one subprogram to another. The queue itself is a two-dimensional hierarchal ordering of subtasks within the CPU processing level structure. The H832 accomplishes level switching through control process orders to the multi-process controller (MPC). Execution of subtasks at different CPU operating levels, or interlevel ordered, is done automatically by the MPC. Execution of subtasks residing at the same CPU level, or intralevel ordered, is accomplished through a software queue of subprograms, each level having a separate job queue. All subprograms at CP level N have interruptive priority over any subprogram at CP level N + 1, N + 2, etc. Intralevel-ordered subprograms have noninterruptive priority at that level. The four lowest (12, 13, 14, 15) CP levels are reserved for execution of user subprograms. Level 15, being the lowest level, is always sequencing and operates in a batch-type mode (Figure 1).

Subprogram Entry Tables (SET)

This is the subprogram queue. There is a SET for levels 12, 13, 14, and 15, and scanning takes place only at that level. Each SET is scanned from the top by an EXEC processor that is re-entrant. Upon completion of a scan, the currently sequencing level is suspended and the next lower active level resumes sequencing. Subprograms in the SET are referred to symbolically with no restrictions as to their activation from other subprograms. Thus a subprogram at level 14 may activate, through the SET, another subprogram at level 12.

Table of Executive Directives (TOED)

The TOED comprises directives to be performed at fixed time intervals by the EXEC. The purpose of the TOED is to activate various internal processors and subprograms corresponding with the appropriate periodic external stimuli. Non-periodic stimuli will usually be handled by dedicated interrupt processors. Executive directives may be of three types: requests to log data, requests for DAIOS output, and requests to execute user subprograms. Each block in the TOED contains three types of entries: execution rate, execution time, and directives (i.e., subprogram, data log, or data output). All directives in any block are activated at the same time.

TOED scanning is accomplished by CP level 1 every 10 ms, and at CP level 2, every 1 s. These particular scan rates have been chosen more or less arbitrarily as most appropriate for the DSIF tracking function and are in no way a design constraint.

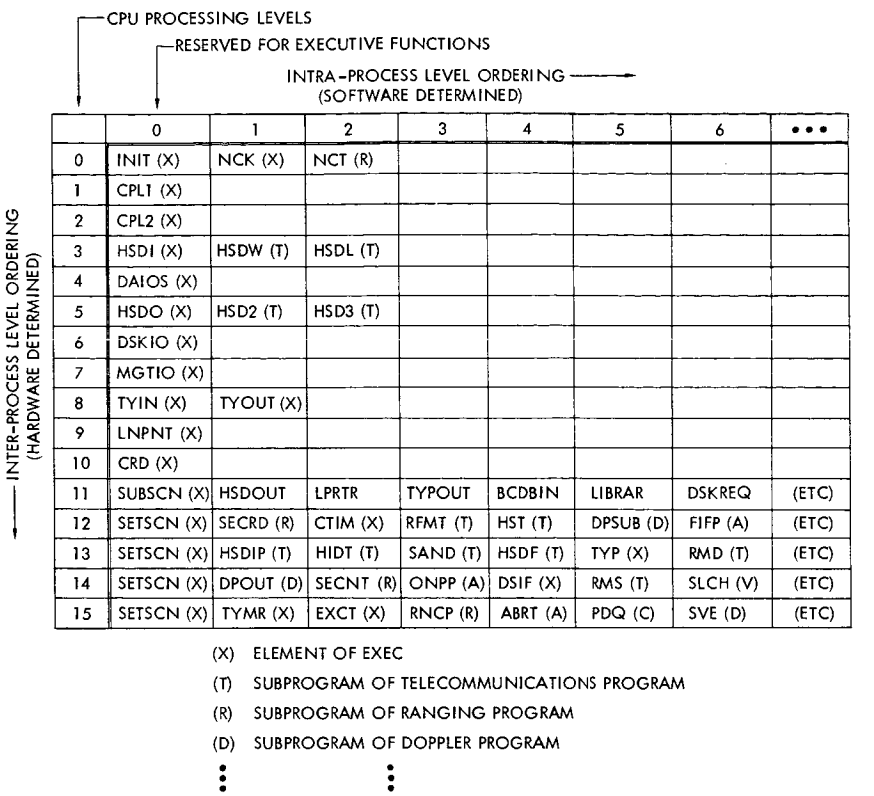

	0	1	2	3	4	5	6	• • •
0	INIT (X)	NCK (X)	NCT (R)					
1	CPL1 (X)							
2	CPL2 (X)							
3	HSDI (X)	HSDW (T)	HSDL (T)					
4	DAIOS (X)							
5	HSDO (X)	HSD2 (T)	HSD3 (T)					
6	DSKIO (X)							
7	MGTIO (X)							
8	TYIN (X)	TYOUT (X)						
9	LNPNT (X)							
10	CRD (X)							
11	SUBSCN (X)	HSDOUT	LPRTR	TYPOUT	BCDBIN	LIBRAR	DSKREQ	(ETC)
12	SETSCN (X)	SECRD (R)	CTIM (X)	RFMT (T)	HST (T)	DPSUB (D)	FIFP (A)	(ETC)
13	SETSCN (X)	HSDIP (T)	HIDT (T)	SAND (T)	HSDF (T)	TYP (X)	RMD (T)	(ETC)
14	SETSCN (X)	DPOUT (D)	SECNT (R)	ONPP (A)	DSIF (X)	RMS (T)	SLCH (V)	(ETC)
15	SETSCN (X)	TYMR (X)	EXCT (X)	RNCP (R)	ABRT (A)	PDQ (C)	SVE (D)	(ETC)

Figure 1. Typical software hierarchal structure

User Program Enable/Disable Table

This is an executive table of variable length entries used by the executive to determine the active status of the subprograms comprising a particular program. Whereas a TOED scan may request a variety of responses, this table selects which responses or activities are to be enabled or not. This table can be used to activate functions locally or remotely (from the SFOF) or to accommodate an extended system to activate programs from auxiliary storage.

Subroutines

A subroutine is a specialized nonfunctionally related set of software, usually commonly required, small in size, and of short duration. In this system they are handled like subprograms, and are available to all users.

System-supplied subroutines reside at CP level 11. When a user requires the services of a particular subroutine, a request is made to the resident controller which is located at the same level as the requesting subprogram at

levels 12, 13, 14, or 15. Control is then passed to CP level 11, insuring that completion takes place before other requests can be serviced. Upon completion, control returns to the lower level and to the requesting subprogram. By this method, subroutines may be used in common without requiring that they be coded re-entrant.

Input/Output Processor (IOP)

In a multiple real-time environment, input and output responses become the determining factors. DTS incorporates two I/O processors to handle input and output. Each IOP is a modified single-address word organized stored program computer that effects transfer of data between primary memory and input and output device controllers.

Input/Output Categories

The EXEC classes I/O into 3 categories: (1) peripheral, (2) synchronous, (3) asynchronous. All peripheral I/O, such as mag tape, disk, typewriter, CRT with keyboard, card reader, printer, etc., is handled by EXEC IOP channel programs and is available to any user. The user, in turn, is required to utilize the peripherals through the EXEC. Synchronous I/O is defined as that which is controlled by predictable and periodic interrupts, such as a 10-ms doppler sample. The EXEC will usually handle such traffic, although the user is allowed to supply his own interrupt and channel software. Asynchronous I/O is most often task peculiar and usually requires special interrupts and channel software supplied by the user under control of the EXEC to resolve possible I/O conflicts. Some DTS asynchronous I/O, such as the high-speed data, is handled as a service by the EXEC because of its commonality to other functions.

I/O Operation

All I/O within the DTS operates essentially as follows: user requests or external interrupts will cause the CPU to sequence (cycle) at a particular level. The resident EXEC processor at that level initiates an IOP channel program. The CPU continues with other work while data transfer takes place under control of the IOP. When data transfer is complete, IOP notifies the CPU and terminates, whereupon the appropriate CPU processing level is restarted.

Data-Handling Services

Data services supplied by the EXEC include the reception, storage, and retrieval of data for the purposes of recall, analysis, and archival histories. Such data may be either externally derived or internally generated. The services are used jointly by all user programs as well as the EXEC itself. Interface requirements between separate programs can easily be satisfied through the storage and retrieval services supplied on both disk and tape.

Data Librarian and Storage

The librarians, for disk and tape, are designed to coordinate and handle the required data bookkeeping and resolve apparent conflicts arising from multiple users of the disk and tape services. It is a two-sided approach: the EXEC supplies automatic storage of real-time data and at the same time allows the user the prerogatives of independent disk or tape usage.

Data within the system is classified as either real or non-real-time data. Real-time logging is identical for both tape and disk, and is stored in 900-word records or tracks, each track consisting of fifteen 60-word logical records. Real-time data is filled from memory in these 60-word records by data type and time, which also serve as the librarians' retrieve parameters. Cataloging is accomplished through internally maintained tables which refer to externally stored tables which, in turn, locate the desired data.

Non-real-time data, or any user data for that matter, is stored and retrieved according to files, which are opened and closed for the user through requests to the librarians.

Conclusion

The arrival of a new third-generation computer to be adapted to DSIF functions not yet computerized presented a good opportunity for a fresh approach to systems software development. The manufacturer had no applicable real-time system, supplying only the basic tools for software development. Some of the work remains undone, and a few areas have been implemented in an expedient fashion, but most of the features described herein have been implemented and are more or less operational. Programs currently operating under the EXEC, or that are in development, support the functions of dual doppler handling, telecommunications, ranging, and antenna pointing. The CPU and memory impact of the EXEC upon these programs is gratifyingly small and adheres to the basic design criteria of simplicity, adaptability, and efficiency.

One of the most fundamental features of software is its ability to adapt general-purpose hardware to specific applications. Attempts to fully generalize the software on top of generalized hardware results in reducing the power and versatility of the computer. Rather than achieving a functionally independent and negotiable product, this philosophy invariably results in a system with an overhead that continuously proliferates at great cost accompanied by increasing levels of uncertainty.

The DTS EXEC was designed in the middle ground somewhere between the philosophy of total generality and no philosophy at all. Unfortunately, the middle ground with its lack of definable boundaries and its inherent instability is vulnerable to the pressures of generalization on the one hand, or to the detailed requirements of the application on the other. Although not fully implemented, the EXEC is expected to contain all the features described herein and has the capability to accommodate any DSIF function without major modifications.

Reference

1. Urban, I., et al., *DSIF Tracking Subsystem*, Document 900-483, Nov. 30, 1971 (JPL internal document).

Index: mathematical sciences, telemetry and command, wave propagation

Interplex: An Analysis of Optimized Power Allocations for Two- and Three-Channel PSK/PM Telecommunications Systems

B. K. Levitt

Telecommunications Division

Under certain conditions, interplex modulation techniques can significantly improve the performance of a multichannel phase-shift-keyed/phase-modulated (PSK/PM) telemetry system by increasing the useful available power relative to conventional PSK/PM systems. However, previous efforts to compare the two modulation schemes and provide a measure of this improvement have occasionally fostered the false impression that the total average signal power and the channel modulation indices were common to both systems. In practice, in designing either modulation system for a deep space telecommunications link, optimal modulation indices are selected to minimize the total average signal power subject to certain minimum requirements on the average telemetry channel and carrier powers. This article illustrates these optimal design concepts for two- and three-channel telemetry modes in the context of the Mariner Venus–Mercury 1973 mission and provides a more realistic measure of the usefulness of interplex. These ideas are then applied as an example to one particular Mariner Venus–Mercury 1973 telemetry mode to demonstrate that interplex can reduce the required total average power by more than 2 dB in some cases.

Introduction

It has recently been suggested that, under certain conditions, the performance of a multichannel phase-shift-keyed/phase-modulated (PSK/PM) telemetry system can be significantly improved by the use of a new modulation technique called interplex (References 1–4). Relative to conventional PSK/PM systems, interplex reduces that portion of the total average signal power lost as cross modulation, thereby increasing the useful available power. However, quantitative comparisons of conventional and interplex modulation systems have fostered some false impressions which will be discussed below. It is the object of this article to provide some insight into the optimal design of two- and three-channel deep space PSK/PM telecommunications systems, and to produce a more realistic measure of the usefulness of interplex modulation.

Optimal Design Criteria

To illustrate the criticism leveled above, consider the conventional and interplex two-channel PSK/PM telemetry systems for the Mariner Venus–Mercury 1973 (MVM73) mission. In the conventional case, the phase-modulated RF signal has the form

$$r(t) = \sqrt{2P_T} \sin [\omega_C t + \theta_H S_H(t) + \theta_L S_L(t)] \quad (1)$$

where P_T is the total average RF signal power, ω_C is the carrier frequency, θ_H and θ_L are the modulation indices of the high- and low-power data channels, respectively, and $S_H(t)$ and $S_L(t)$ are the corresponding biphase-modulated squarewave subcarriers.

In the interplex version, $S_L(t)$ in Equation 1 is replaced by the cross-modulation product $S_H(t)\ S_L(t)$. Comparisons of these two modulation systems in the literature have generally left the mistaken belief that interplex modulation increases the average power P_L in the low-power channel by a factor of $\tan^2 \theta_H$ relative to the conventional modulation system. But this conclusion is only justified in the unlikely case where P_T, θ_H, and θ_L are constrained to be the same in both systems. A consequence of this constraint is that the average powers P_H in the high-power channel and P_C in the carrier remain unchanged as well. This implies that interplex is being used for the sole purpose of increasing P_L.

In practice, this is generally not the case. In designing either modulation system, modulation indices θ_H and θ_L are selected that are optimal with respect to a common design criterion which constrains P_H, P_L, P_C, and P_T. Independent of which design criterion is actually used, the optimal modulation indices for each system are not, in general, the same. And any valid comparison of the two modulation systems should be based on optimal design parameters.

In particular, for MVM73 telecommunications applications, the bit error rates for the two data channels are constrained to be below some given maximum design values. This constrains the signal-to-noise ratios P_H/N_0 and P_L/N_0 to exceed some threshold values P'_H/N_0 and P'_L/N_0, where N_0 is the one-sided power spectral density of the additive noise. Furthermore, in order to track the carrier frequency and phase reliably for coherent data demodulation, P_C/N_0 must exceed some threshold P'_C/N_0. The design criterion common to both modulation systems is, therefore, to select modulation indices that minimize P_T/N_0 subject to the threshold constraints above. Thus, interplex is used to provide an overall system power reduction instead of simply an improvement in the low-power channel. Consequently, a more realistic characterization of the improvement afforded by interplex is given by comparing the optimized values of P_T/N_0 for the two modulation systems satisfying the common threshold design constraint (see section on *Example*).

With the inclusion of a ranging channel, the MVM73 telemetry modes become three-channel PSK/PM systems. The conventional phase-modulated RF signal has the form

$$r(t) = \sqrt{2P_T} \sin [\omega_C t + \theta_H S_H(t) + \theta_L S_L(t) + \theta_R S_R(t)] \qquad (2)$$

where the subscript R denotes the ranging channel. In a partial interplex scheme, $S_L(t)$ in Equation 2 is replaced by $S_H(t)\, S_L(t)$. To realize the full potential of interplex, however, it may also be advantageous to replace $S_R(t)$ by $S_H(t)\, S_R(t)$, depending on the channel and carrier power requirements. Again, to provide reliable ranging information, P_R/N_0 must be constrained to exceed some threshold P_R'/N_0. The design procedure in the three-channel case is completely analogous to that for the two-channel situation.

Analysis

In this section the optimal power allocations are determined for the two- and three-channel MVM73 telemetry modes subject to the design criteria presented above.

Conventional Two-Channel System

The average powers P_H, P_L, and P_C can be expressed in terms of P_T, θ_H, and θ_L, using Equation 1. Eliminating θ_H and θ_L, it can then be shown that

$$\frac{P_T}{N_0} = \left(\frac{P_H}{N_0} + \frac{P_C}{N_0}\right)\left(1 + \frac{\dfrac{P_L}{N_0}}{\dfrac{P_C}{N_0}}\right) \qquad (3)$$

The optimization problem is to minimize P_T/N_0 subject to the threshold constraints on P_H/N_0, P_L/N_0, and P_C/N_0. From Equation 3, it is evident that P_T/N_0 is minimized over P_H/N_0 and P_L/N_0 when these two parameters are set to their threshold values, independent of P_C/N_0. Under this condition, P_T/N_0 need only be minimized over P_C/N_0, subject to a threshold constraint. Differentiating Equation 3 with respect to P_C/N_0, with P_H/N_0 and P_L/N_0 set to their threshold values, it is found that P_T/N_0 has an absolute minimum at

$$\frac{P_C}{N_0} = \sqrt{\frac{P_H'}{N_0}\,\frac{P_L'}{N_0}} \qquad (4)$$

As indicated in Figure 1, there are two cases to consider, depending on the relative values of the absolute minimum in Equation 4 and the threshold P_C'/N_0. The desired value of P_C/N_0 is

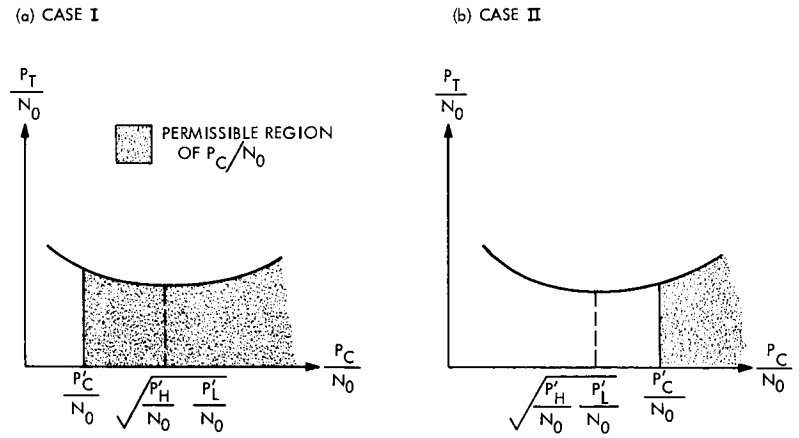

Figure 1. Diagram for optimization of power allocations in conventional two-channel telemetry systems

$$\sqrt{\frac{P_H'}{N_0}\frac{P_L'}{N_0}}$$

in Case I and P_C'/N_0 in Case II.

From Equation 3, it can be concluded that the optimized value of P_T/N_0 is given by

$$\frac{P_T}{N_0} = \begin{cases} \left(\sqrt{\frac{P_H'}{N_0}} + \sqrt{\frac{P_L'}{N_0}}\right)^2; & \frac{P_C'}{N_0} \leqslant \sqrt{\frac{P_H'}{N_0}\frac{P_L'}{N_0}} \\ \left(\frac{P_H'}{N_0} + \frac{P_C'}{N_0}\right)\left(1 + \frac{\frac{P_L'}{N_0}}{\frac{P_C'}{N_0}}\right); & \frac{P_C'}{N_0} \geqslant \sqrt{\frac{P_H'}{N_0}\frac{P_L'}{N_0}} \end{cases} \tag{5}$$

Having determined the optimal power allocations, the corresponding modulation indices θ_H and θ_L can be readily computed.

Interplex Two-Channel System

In place of Equation 3, the starting point is now

$$\frac{P_T}{N_0} = \left(\frac{P_C}{N_0} + \frac{P_H}{N_0}\right)\left(1 + \frac{\dfrac{P_L}{N_0}}{\dfrac{P_H}{N_0}}\right) \tag{6}$$

Comparing Equations 3 and 6, it is evident that the design analysis in this section mirrors that of the previous section with P_H/N_0 and P_C/N_0 interchanging their roles. Therefore, by inspection, the optimal system has P_L/N_0 and P_C/N_0 set to their threshold values, and P_H/N_0 set to either P_H'/N_0 or

$$\sqrt{\frac{P_L'}{N_0}\,\frac{P_C'}{N_0}}$$

depending on the relative magnitudes of these last two parameters. Then the optimum value of P_T/N_0 satisfies the relation

$$\frac{P_T}{N_0} = \begin{cases} \left(\sqrt{\dfrac{P_L'}{N_0}} + \sqrt{\dfrac{P_C'}{N_0}}\right)^2; & \dfrac{P_H'}{N_0} \leqslant \sqrt{\dfrac{P_L'}{N_0}\,\dfrac{P_C'}{N_0}} \\ \left(\dfrac{P_C'}{N_0} + \dfrac{P_H'}{N_0}\right)\left(1 + \dfrac{\dfrac{P_L'}{N_0}}{\dfrac{P_H'}{N_0}}\right); & \dfrac{P_H'}{N_0} \geqslant \sqrt{\dfrac{P_L'}{N_0}\,\dfrac{P_C'}{N_0}} \end{cases} \tag{7}$$

and again the optimal modulation indices can be computed.

Conventional Three-Channel System

From Equation 2, the relation

$$\frac{P_T}{N_0} = \left(\frac{P_H}{N_0} + \frac{P_C}{N_0}\right)\left(1 + \frac{\dfrac{P_L}{N_0}}{\dfrac{P_C}{N_0}}\right)\left(1 + \frac{\dfrac{P_R}{N_0}}{\dfrac{P_C}{N_0}}\right) \tag{8}$$

can be derived. As before, P_T/N_0 is minimized subject to threshold constraints on the remaining signal-to-noise ratios in Equation 8. Therefore,

P_H/N_0, P_L/N_0, and P_R/N_0 should be set to their respective threshold values P_H'/N_0, P_L'/N_0, and P_R'/N_0; then P_T/N_0 is minimized over P_C/N_0 subject to the constraint $P_C/N_0 \geq P_C'/N_0$. By differentiating P_T/N_0 in Equation 8 with respect to P_C/N_0 with the other signal-to-noise ratios at their threshold values, it is found that P_T/N_0 has an absolute minimum at

$$\frac{P_C}{N_0} = \left\{ \left[\left(\frac{P_H'}{N_0} \frac{P_L'}{N_0} \frac{P_R'}{N_0} \right)^2 - \frac{1}{27} \left(\frac{P_H'}{N_0} \frac{P_L'}{N_0} + \frac{P_H'}{N_0} \frac{P_R'}{N_0} + \frac{P_L'}{N_0} \frac{P_R'}{N_0} \right)^3 \right]^{1/2} + \left(\frac{P_H'}{N_0} \frac{P_L'}{N_0} \frac{P_R'}{N_0} \right) \right\}^{1/3}$$

$$- \left\{ \left[\left(\frac{P_H'}{N_0} \frac{P_L'}{N_0} \frac{P_R'}{N_0} \right)^2 - \frac{1}{27} \left(\frac{P_H'}{N_0} \frac{P_L'}{N_0} + \frac{P_H'}{N_0} \frac{P_R'}{N_0} + \frac{P_L'}{N_0} \frac{P_R'}{N_0} \right)^3 \right]^{1/2} - \left(\frac{P_H'}{N_0} \frac{P_L'}{N_0} \frac{P_R'}{N_0} \right) \right\}^{1/3} \equiv K \tag{9}$$

Then the optimal value of P_C/N_0 is either P_C'/N_0 or K (defined in Equation 9), depending on the relative magnitudes of P_C'/N_0 and K. The resulting optimized value of P_T/N_0 is specified by

$$\frac{P_T}{N_0} = \begin{cases} \left(\frac{P_H'}{N_0} + K \right) \left(1 + \frac{\frac{P_L'}{N_0}}{K} \right) \left(1 + \frac{\frac{P_R'}{N_0}}{K} \right); & \frac{P_C'}{N_0} \leq K \\ \left(\frac{P_H'}{N_0} + \frac{P_C'}{N_0} \right) \left(1 + \frac{\frac{P_L'}{N_0}}{\frac{P_C'}{N_0}} \right) \left(1 + \frac{\frac{P_R'}{N_0}}{\frac{P_C'}{N_0}} \right); & \frac{P_C'}{N_0} \geq K \end{cases} \tag{10}$$

and the optimal modulation indices θ_H, θ_L, and θ_R can be readily computed.

A commonly expressed belief is that turning on the ranging channel degrades the data channel and carrier signal-to-noise ratios by a factor of $\cos^2 \theta_R$ for the MVM73 telecommunications system under the conventional modulation scheme. However, if the optimization procedure above is followed, that contention is invalid. The degradation due to ranging should instead be expressed as the increase in the optimized required values of P_T/N_0 in going from the conventional two-channel system to the conventional three-channel system.

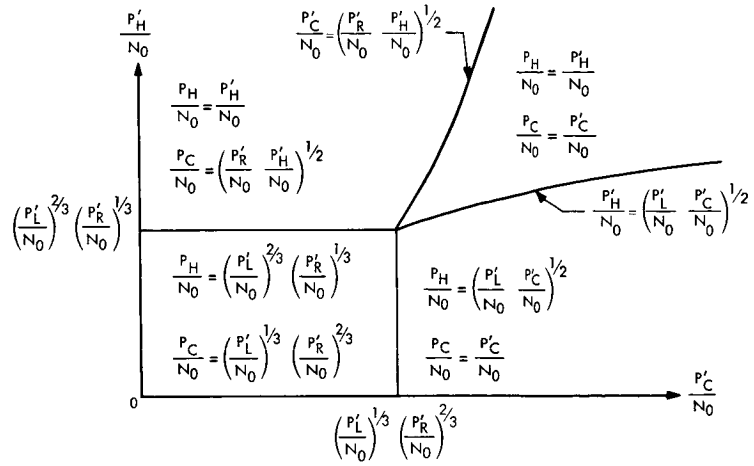

Figure 2. Optimal selection of high-power channel and carrier signal-to-noise ratios for partial interplex three-channel telemetry systems

Partial Interplex Three-Channel System

From Equation 2, with $S_L(t)$ replaced by $S_H(t)S_L(t)$, it can be shown that

$$\frac{P_T}{N_0} = \left(\frac{P_H}{N_0} + \frac{P_C}{N_0}\right)\left(1 + \frac{\frac{P_L}{N_0}}{\frac{P_H}{N_0}}\right)\left(1 + \frac{\frac{P_R}{N_0}}{\frac{P_C}{N_0}}\right) \tag{11}$$

According to the established design criterion, P_L/N_0 and P_R/N_0 must be set to their threshold values, leaving P_T/N_0 to be optimized jointly over P_H/N_0 and P_C/N_0 subject to their threshold constraints. Taking partial derivatives of P_T/N_0 with respect to P_H/N_0 and P_C/N_0, it is found that there are four cases to consider, each with a unique optimal P_H/N_0 and P_C/N_0, as shown in the diagram of Figure 2. The optimal values of P_T/N_0, θ_H, θ_L, and θ_R then follow.

Interplex Three-Channel System

The analysis here is similar to that for the conventional three-channel system. Using Equation 2 with $S_L(t)$ and $S_R(t)$ replaced by $S_H(t)\ S_L(t)$ and $S_H(t)\ S_R(t)$, respectively, it can be shown that

$$\frac{P_T}{N_0} = \left(\frac{P_H}{N_0} + \frac{P_C}{N_0}\right)\left(1 + \frac{\frac{P_L}{N_0}}{\frac{P_H}{N_0}}\right)\left(1 + \frac{\frac{P_R}{N_0}}{\frac{P_H}{N_0}}\right) \tag{12}$$

Therefore, P_L/N_0, P_R/N_0, and P_C/N_0 are set to their threshold values, and P_H/N_0 set to K' if P'_H/N_0 exceeds K', or to P'_H/N_0 otherwise; K' is equal to K in Equation 9, with P'_H/N_0 replaced by P'_C/N_0. Again, the corresponding optimal values of P_T/N_0, θ_H, θ_L, and θ_R can be readily calculated.

Example

To illustrate some of the ideas presented in this article, consider this example. A two-channel PSK/PM telemetry system for MVM73 is to be designed according to the following nominal specifications. The high-power channel must have a data rate R_H of 22.05 kbps, a threshold bit error rate of 5 in 10^2, and is uncoded. The low-power channel must have an information rate R_L of 2.45 kbps, a threshold bit error rate of 1 in 10^4, and use a (32,6) biorthogonal block code. The bit error rate requirements define minimum signal-to-noise ratios P_H/R_HN_0 and P_L/R_LN_0 of 1.32 and 5.24 dB, respectively; R_H and R_L can be expressed as 43.43 and 33.89 dB. Therefore, the threshold values of P_H/N_0 and P_L/N_0 are 44.75 and 39.13 dB. To ensure adequate carrier tracking for MVM73 telecommunications systems, a threshold value of P_C/N_0 of 30.80 dB is usually considered in the design.

Using the optimal design procedures developed for the conventional two-channel and interplex two-channel systems, the optimal conventional and interplex systems have the power allocations and modulation indices as listed in Table 1.

Thus, in this example, interplex reduces the nominal required value of P_T/N_0 by 2.44 dB, although P_H/N_0 and P_L/N_0 remain unchanged.

Concluding Remarks

This article has derived optimal design concepts for two- and three-channel PSK/PM telemetry systems for deep space applications. It was also demonstrated that a valid measure of the system improvement provided by interplex is the decrease in optimized total RF signal-to-noise ratio P_T/N_0

Table 1. Optimal power allocations and modulation indices for conventional and interplex two-channel MVM73 telemetry systems

Conventional	Interplex
P_H/N_0 = 44.75 dB	P_H/N_0 = 44.75 dB
P_L/N_0 = 39.13 dB	P_L/N_0 = 39.13 dB
P_C/N_0 = 41.94 dB	P_C/N_0 = 30.80 dB
P_T/N_0 = 48.41 dB	P_T/N_0 = 45.97 dB
θ_H = 54.1 deg	θ_H = 78.7 deg
θ_L = 35.9 deg	θ_L = 27.6 deg

relative to conventional modulation. Using a two-channel telemetry mode for MVM73 as an example, it was shown that the reduction in P_T/N_0 due to interplex could exceed 2 dB in some cases.

Acknowledgment

The author wishes to express his appreciation to Dr. S. Butman, JPL Telecommunications Division, for his contributions in the formulation of the identities in Equations 3, 6, 8, 11, and 12.

References

1. Butman, S., and Timor, U., "Coding and Synchronization Research: Interplex—An Efficient Two-Channel Telemetry System for Space Exploration," in *Supporting Research and Advanced Development*, Space Programs Summary 37-62, Vol. III, pp. 57–60. Jet Propulsion Laboratory, Pasadena, Calif., Apr. 30. 1970.

2. Butman, S., and Timor, U., "Coding and Synchronization Research: Efficient Multichannel Space Telemetry," in *Supporting Research and Advanced Development*, Space Programs Summary 37-63, Vol. III, pp. 34–37. Jet Propulsion Laboratory, Pasadena, Calif., June 30, 1970.

3. Timor, U., "Optimum Configurations for PSK/PM Systems," in *Supporting Research and Advanced Development*, Space Programs Summary 37-66, Vol. III, pp. 33–36. Jet Propulsion Laboratory, Pasadena, Calif., Dec. 31, 1970.

4. Butman, S., and Timor, U., "Interplex Modulation," in *JPL Quarterly Technical Review*, Vol. 1, No. 1, pp. 97–105. Jet Propulsion Laboratory, Pasadena, Calif., Apr. 1971.

Index: bioengineering, electronic components and circuits, packaging and cabling

Miniature Biotelemeter Gives Multichannel Wideband Biomedical Data

J. B. Carraway

Telecommunications Division

A miniature biotelemeter has been developed for sensing and transmitting multiple channels of biomedical data over a radio link. Doctors and biologists have expressed need for the ability to monitor vital physiological functions from human and animal subjects unrestrained by wires. JPL responded under NASA Technology Applications Office sponsorship in developing an advanced device suitable for a wide variety of medical and biological research applications. The design of this miniature, 12-cm^3, 10-channel, wideband (5 kHz/channel), pulse amplitude modulation/frequency modulation biotelemeter takes advantage of modern device technology (e.g., integrated circuit operational amplifiers, complementary symmetry/metal oxide semiconductor logic, and solid-state switches) and hybrid packaging techniques. The telemeter is currently being used for monitoring 10 channels of neuron firings from specific regions of the brain in rats implanted with chronic electrodes. Multichannel telemetry of electroencephalograms, electrocardiograms, electromyograms, state functions, and dynamic processes such as blood flow and body chemistry are all possible follow-on applications. Design, fabrication, and testing of an engineering model biotelemeter are described in this article.

Introduction

The remote measurement of biological parameters from animals and humans is an important requirement in many fields of biomedical research. Behavioral data from free moving animals, clinical data from unrestrained patients, and physiological data from implanted sensors are immediate examples. Phenomena to be measured include pressure, temperature, and various biopotentials that vary from microvolt neural impulses to myopotentials (muscular signals) in the tens of millivolts.

Collecting data by radiotelemetry offers experimenters several desirable features:

(1) Monitoring is permitted of subjects that are unrestrained by wires.

(2) The subject is isolated from power signal pickup and shock hazard.

(3) The telemeter signal sensor/amplifiers can be located on the subject, close to the signal source, giving the best possible signal-to-noise ratio.

(4) Cable flex artifacts and pickup are eliminated, resulting in maximum signal fidelity.

(5) Data from implanted sensors can be transmitted through the skin, eliminating the risk of infection inherent in running wires through the skin.

The goal of designing an advanced biotelemeter that is smaller, lighter, lower power, more sensitive, and of greater information bandwidth than examples in current use was met in the development of the biotelemeter pictured in Figure 1, which achieves the characteristics described in Table 1.

Figure 1. Miniature biotelemeter monitoring 10 channels of neuron firings from chronically implanted rat

Table 1. Telemeter specifications

Multichannel	10 channels of physiological data
Wideband	5-kHz data bandwidth per channel 20,000 samples/s per channel
High sensitivity	Less than 8-μV rms noise referenced to input
Miniature	12 cm^3 (3/4 $in.^3$) 16 g
Low power	7 mW
Wireless	Pulse amplitude modulation/frequency modulation (PAM/FM) single carrier radio link uses VHF frequencies

This device utilizes newly available, commercial monolithic, operational amplifiers, low-power complementary symmetry/metal oxide semiconductor medium scale integration (COS/MOS MSI) digital logic, and miniaturized chip components to achieve goals of low power, small size, and reliability. Packaging of the microelectronics employs state-of-the-art hybrid mounting techniques to achieve volumetric efficiency without compromising manufacturability or ease of maintenance. An example of this fact is that the integrated circuits (ICs) are individually replaceable.

System Description

A block diagram of the telemetry system is shown in Figure 2. The upper section of the figure shows the telemeter that is carried by the subject. The lower section of the figure shows the receiver/demultiplexer equipment that provides reconstructed output signals for recording or display purposes.

A pulse amplitude modulation/frequency modulation (PAM/FM) telemeter operates on multiple-signal inputs by sequentially sampling each, one at a time. This is accomplished through use of solid-state switches controlled by the sequencer, one switch for each input channel. The samples are combined with reference sync pulses to form a composite wavetrain of pulses which are amplitude modulated by input data. This waveform, in turn, frequency modulates a radio frequency (RF) transmitter.

The RF signal is sensed by a receiving antenna and demodulated by an FM receiver and discriminator to yield a composite PAM waveform. The sync pulse is detected from this pulse train and used as reference for the demultiplexer. The function of the demultiplexer is to unscramble the composite waveform and separate sample pulses corresponding to each input channel. Finally, each sampled waveform is passed through an

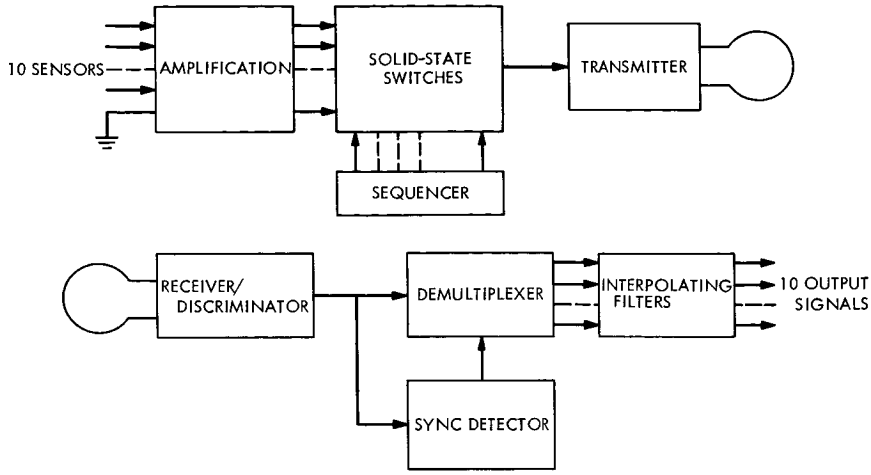

Figure 2. Telemetry system block diagram

interpolation filter for smoothing, and the data signal corresponding to that particular input is reproduced.

Telemeter Electrical Design

Input Signal Conditioning

Input signals can come from a variety of different sources. Some typical examples are surface electrodes contacting the skin through electrolytic paste [electrocardiograms (ECGs)], needle electrodes inserted directly into muscles [electromyograms (EMGs)], electrodes which just pierce the surface of the scalp [electroencephalograms (EEGs)], and microelectrodes less than 20 μm in tip diameter, carefully inserted into specific regions of the brain. The telemeter provides an operational amplifier for each input to permit signal conditioning tailored to each signal's characteristics. For instance, low-level, high-frequency neuron firings are amplified by a gain of 1500 and bandpassed between 350 Hz and 5 kHz. The low-frequency cutoff is chosen to filter out α and β wave frequencies (approximately 10 Hz and 30 Hz, respectively) as well as 60-Hz pickup frequency. The high-frequency cutoff filters out wideband noise and holds the input below the Nyquist frequency of the following commutator, while amplifying signals in the 2- to 3-kHz range (characteristic frequency range of neuron firings). The amplifiers also act as isolators between the source and the commutator switch transients. These switch transients could cause brain stimulation through the chronically implanted electrodes. Capacitive coupling is used to prevent cell polarization by amplifier leakage current.

Sampling Switches

Each input signal after amplification and band-limiting is sampled at the rate of 20,000 samples per second through field effect transistor (FET)

switches controlled by the sequencer logic. These are *n*-channel junction FETs with low pinch-off voltages (–1 V).

Sequencer

Switch control is provided by the sequencer shown in Figure 3, mechanized from three COS/MOS chips. The sequencer consists of:

(1) A 12-stage shift register that circulates a single 1 to sequence the sampling by the FET switches.

(2) A 4-stage shift register used as a ring counter to start the 12-stage register.

(3) A clock oscillator built from two NOR gates with an RC time constant added. The oscillator operates at 240 kHz with a stability of 0.1%.

Transmitter

The transmitter is a negative-resistance oscillator with an LC ringing circuit between transistor collectors. The inductive element of this, a 3.18-cm (1.25-in.)[1] diameter circular loop, also acts as the transmitting antenna. The oscillator configuration chosen offers several desirable features:

[1] Values in customary units are included in parentheses after values in SI (International System) units if the customary units were used in the measurements or calculations.

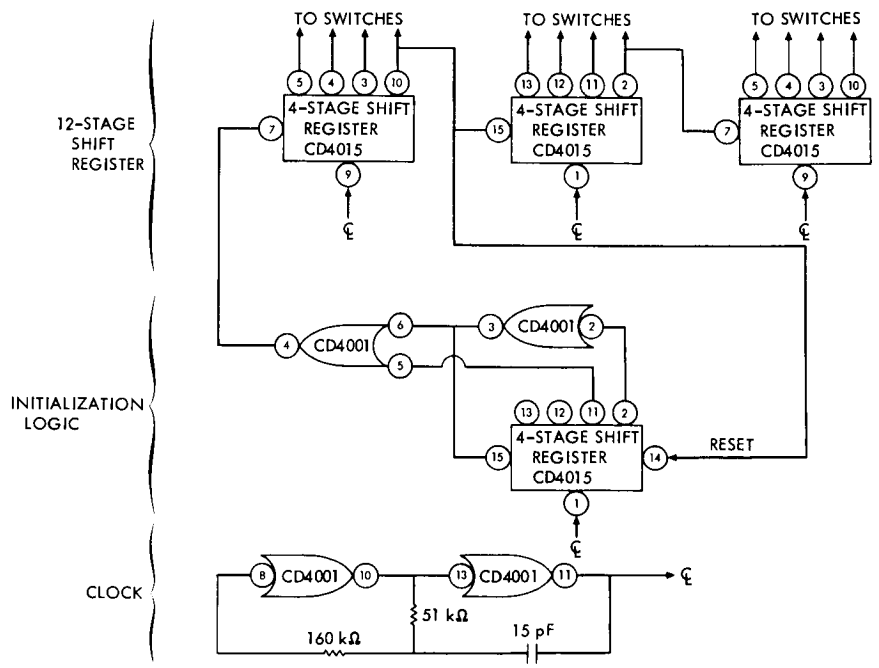

Figure 3. Telemeter sequencer

(1) The frequency tends to be independent of the bias voltage, since lower switchover voltage corresponds to lower drive voltage.

(2) Frequency stability is enhanced by operating the active elements either full-on or full-off.

(3) Power dissipation is minimized since either current or voltage is zero most of the time. Measured transmitter power dissipation is 1.8 mW.

The transmitter is frequency modulated by the PAM output of the switches. The modulating signal is applied across a transistor collector–base junction, causing its capacitance to vary. A high frequency of operation was required to provide a 1-MHz data bandwidth. The transmitting frequency chosen (185 MHz) lies in the middle of the commercial television spectrum (channel 8). This permits use of any readily available, inexpensive television front end as a receiver.

Telemeter Mechanical Design

The physical characteristics of a biotelemeter are of major importance. A device to be used to monitor biological data on unrestrained animals should not affect or inhibit natural behavior. The special environmental conditions associated with biological research and clinical medicine require creative packaging.

Efficient soldering, bonding, adhesive, and assembly techniques were used to achieve a miniature package with high volumetric efficiency, without sacrificing manufacturability or maintainability. An interesting comparison of packaging efficiency for space electronics that have flown is given in Table 2.

Miniaturization improves performance by locating amplifiers near critical points. Also, vulnerability to shock and vibration is reduced because of the reduction in mass and length of leads.

Packaging Approach

The packaging approach taken was to design a stack assembly of four miniature printed circuit boards (see Figure 4). The circuit boards each

Table 2. Packaging efficiency of various systems

System	Number of functioning parts per cubic inch
Surveyor electronics	20
Mariner 4 Cordwood module	37
Mariner Mars 1969 Data Acquisition System	41
JPL miniature biotelemeter	886

carry an electrical functional block of the total system so that they may be tested and tuned separately. They are laid out functionally as follows:

(1) Input components board (2-sided).

(2) Amplifier/commutator board (2-sided).

(3) Sequencer board.

(4) Transmitter board.

The circuit boards are flexible 0.4-mm (0.016-in.) copper clad epoxy boards etched with standard industrial techniques to 0.5-mm (0.020-in.) lines and 0.5-mm (0.020-in.) spacing. The circuits were given 51 $\times$ 10^{-6}-cm (20 $\times$ 10^{-6}-in.) gold plating as corrosion protection.

The circuit boards are stacked one on top of the other with ground planes shielding the stack in the desired places and are separated by lightweight epoxy spacers. Holes are drilled through the boards; the interior is plated; and No. 30 gauge insulated magnetic wire is used for electrically connecting the layers of the stack assembly. Interconnect topology is such that the boards can be unstacked and folded out to permit access to any component without disturbing the interconnection (Figures 5 and 6).

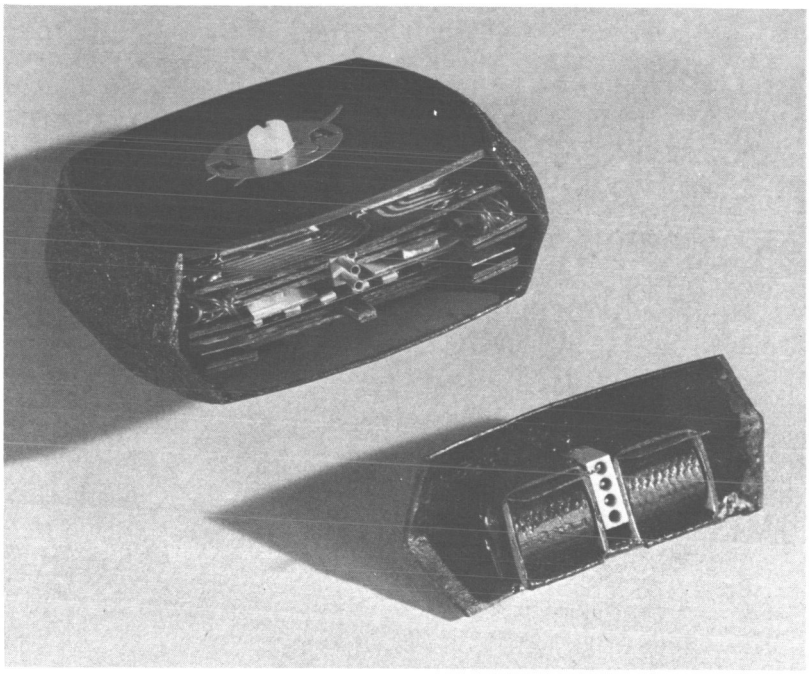

Figure 4. Biotelemeter with battery disconnected revealing circuit board stack assembly

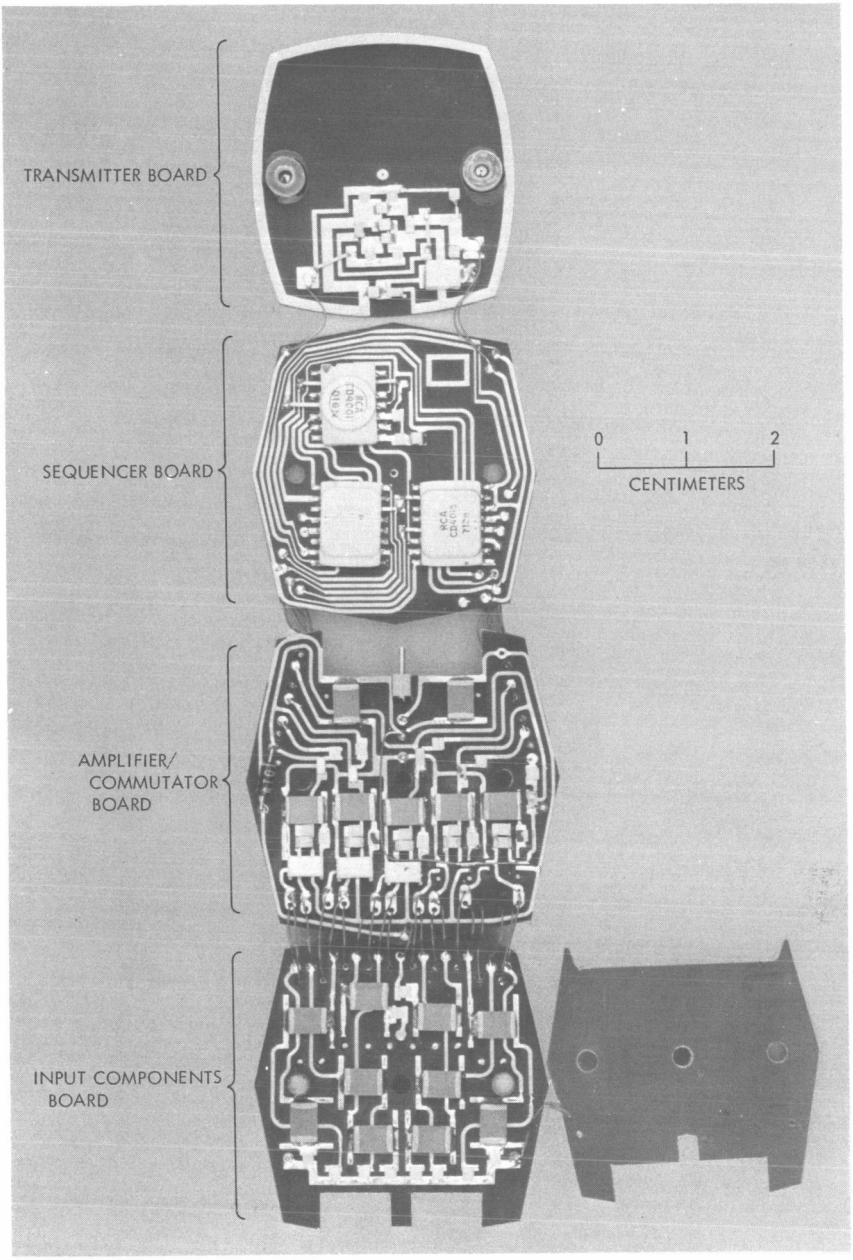

Figure 5. Bottom view of unfolded circuit boards

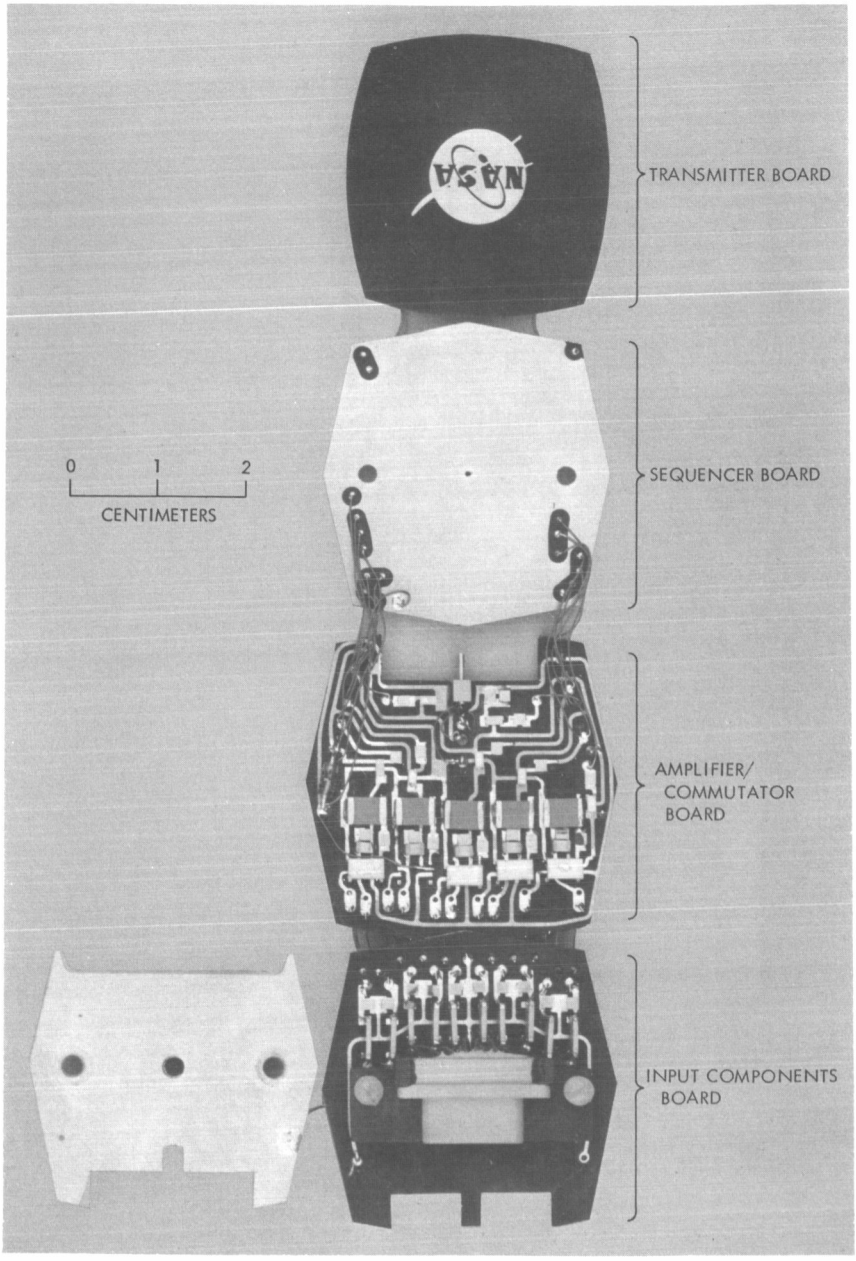

Figure 6. Top view of unfolded circuit boards

Parts Attachment Technique

The operational amplifiers and FET switches are bought in chip form and mounted on separate microminiature ceramic carriers [leadless inverted devices (LIDs)] (Figure 7). This process involves a sequence of operations that includes die bonding the chips to the carrier, thermocompression bonding of wire leads connecting die pads to carrier pads (the die end of the wire is ball-bonded and the carrier end wedge-bonded), and encapsulation. LID assembly was done in the JPL Hybrid Circuits Laboratory in a clean room environment with quality assurance inspection and test support.

Once the LID is encapsulated, it may be soldered directly to the miniature circuit boards. The thick film resistors, monolithic capacitors, and transistors are commercially available, mounted in hermetically sealed solderable carriers. The three COS/MOS digital chips are mounted as flat packs. Thus, all parts are mounted onto the circuit board by simple soldering, requiring only a miniature iron and low-temperature solder paste.

Module Housing

Because the module housing should be lightweight, rigid, low cost, and easily adaptable to different shapes, the housing was fabricated from low-pressure laminated glass-epoxy 0.5 mm (0.020 in.) thick. Each housing was made from a universal construction ring. Segments were cut from the ring in different lengths depending on what final shape was required. The bonded assembly is flexible enough so that the electronic assembly can be inserted, but rigid enough to hold the envelope dimensions accurately.

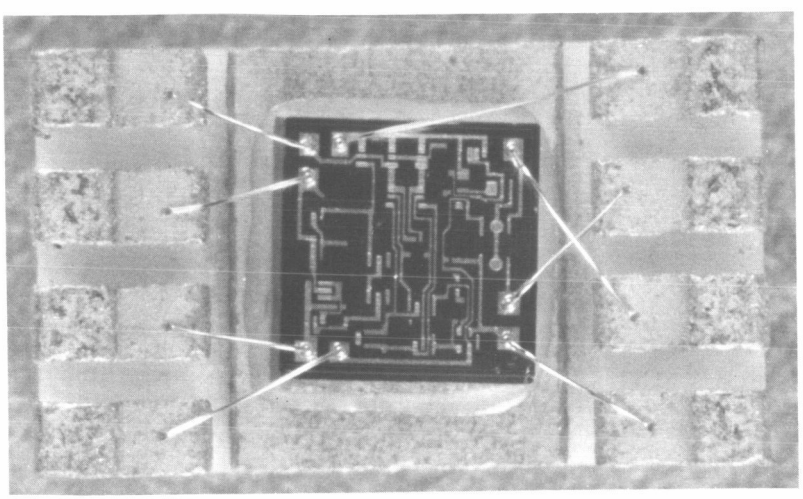

Figure 7. Operational amplifier chip mounted on ceramic carrier

Battery

The battery is constructed of laminated epoxy cylinders and boxes. The boxes each hold one cylinder, which in turn holds two small 1.5-V hearing-aid cells. The epoxy boxes are lined on two sides with gold-plated copper-clad epoxy laminate to form all contacts. The inherent spring of the epoxy laminate box is sufficient to hold the contacts against the cells. There are two flexible tabs bonded to the boxes to facilitate removal of the cylinders. The battery is mated to the board stack with a miniature connector and a built-in probe and slot. The slot is in the battery; the probe protrudes from the input board edge.

Receiver/Decommutator Design

The receiver/decommutator is pictured, functionally, in Figure 8. The receiver utilizes a commercial television front end. An IF amplifier was added to the front end to increase sensitivity, and a wideband (5 MHz) limiter and discriminator were substituted in place of the relatively narrowband (±25 kHz) television audio FM detector. The signal-to-noise ratio in the IF amplifier is high enough so that noise suppression will occur in both the limiter and the discriminator. By assuring that the incoming signal is of sufficient amplitude to saturate the limiter circuitry, the output signal level becomes independent of changes in received signal amplitude. The discriminator output is the reproduced PAM composite waveform.

The composite PAM waveform is presented to the decommutator for separation into samples corresponding to each input channel. This separation is accomplished by a level detector which senses a sync pulse sent every 10 samples. A sequencer circuit in the decommutator (identical to the telemeter COS/MOS sequencer) is phase-locked to the periodic sync pulse through the action of a simple phase-locked loop. The loop achieves decommutator frequency and phase synchronization with the telemeter and tracks any small shifts in the sampling rate.

The sampling pulses (used to gate the analog switches) are made narrower than the original telemeter sampling pulses (2.1 μs versus 4.2 μs) to reduce adjacent channel crosstalk. The sequence of sampled values corresponding to each input is smoothed by low-passing through an interpolation filter. The output waveforms of the 10 interpolation filters represent amplified reproductions of the 10 telemeter data input signals and are of sufficient amplitude to drive recording and display equipment.

Testing

A three-stage approach was taken toward telemeter hardware development and test (see Figure 9). First, an operational breadboard was fabricated using discrete components. This device interfaced circuit design, checked system design concepts, and provided system performance test data. The discrete breadboard was developed, through test, into the final electrical configuration design.

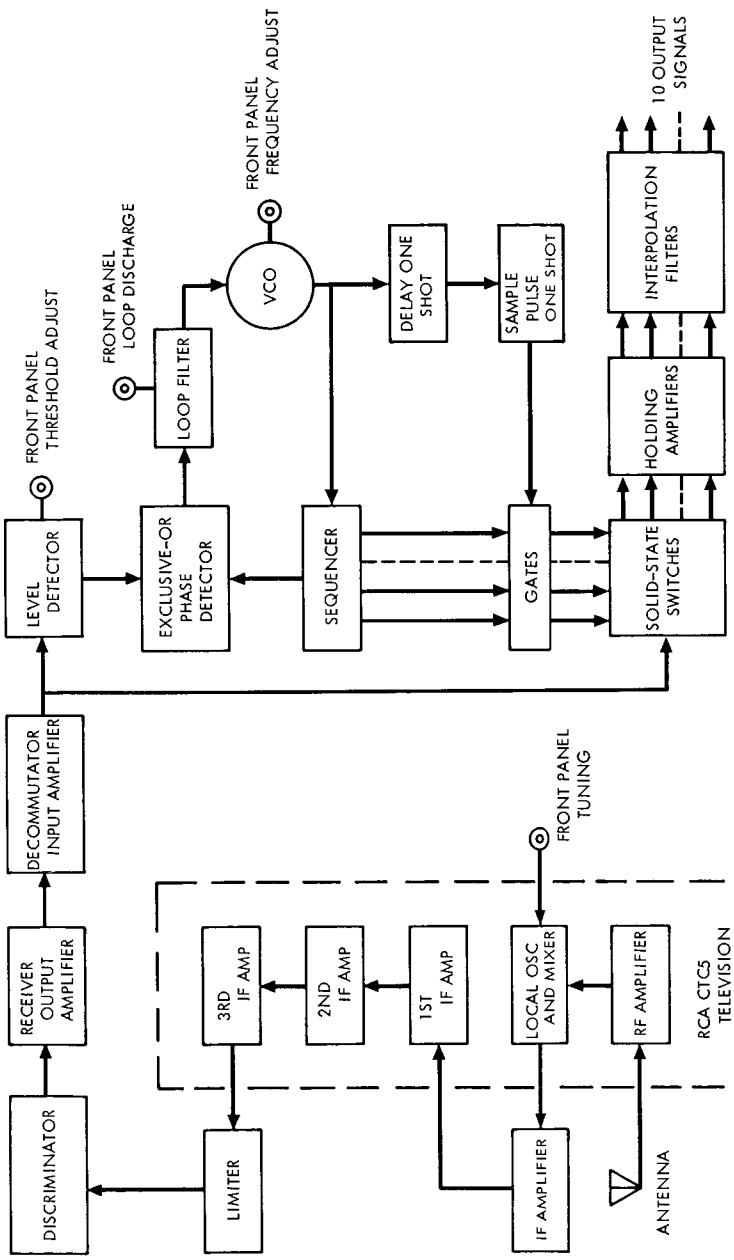

Figure 8. Biotelemeter receiver/decommutator

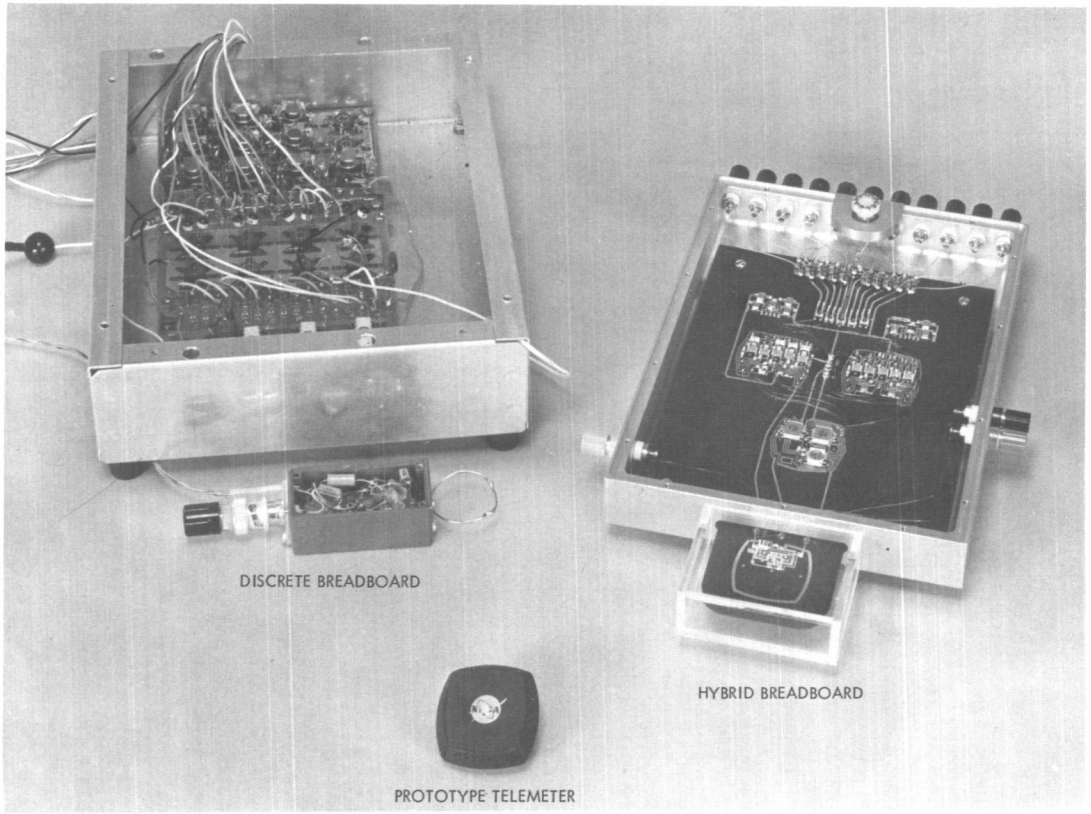

Figure 9. Three stages of hardware development

Stage two was the fabrication of a hybrid breadboard using miniaturized chip components mounted on a single board which was a two-dimensional layout of the third-stage printed circuit configuration. The hybrid breadboard tested IC mounting techniques, verified printed circuit layout, and established chip component performance characteristics.

The third and final stage of hardware development and test was the fabrication and test of a prototype miniature telemeter. The hybrid stack assembly was packaged and tested using simulated physiological signals (Figure 10). The approach chosen for evaluating the biotelemeter on a live source was to apply it to a particular user's requirements: those of Dr. James Olds of the Caltech Psychobiology Department.

Doctor Olds is a neurophysiologist, concerned with the monitoring of neuron waveforms in specific regions of the brain. His research is presently being carried out by using white rats that have been implanted with chronic electrodes in specific regions of their brains. The voltage spikes produced by neurons are wideband, extremely low-level signals coming from a high-impedance source and as such represent worst-case waveforms for a biotelemeter. In addition, environmental and size restrictions imposed by the use of rats for this research are worst case when compared to the use of larger subjects, such as dogs, cats, and humans. It was felt that the successful application of the miniature biotelemeter to this problem represented a realistic test of its limits of performance.

Figure 11 shows telemetered neuron waveforms from a live animal. Two channels of the 10 monitored by telemetry are shown together with signals from a hardwire system for comparison.

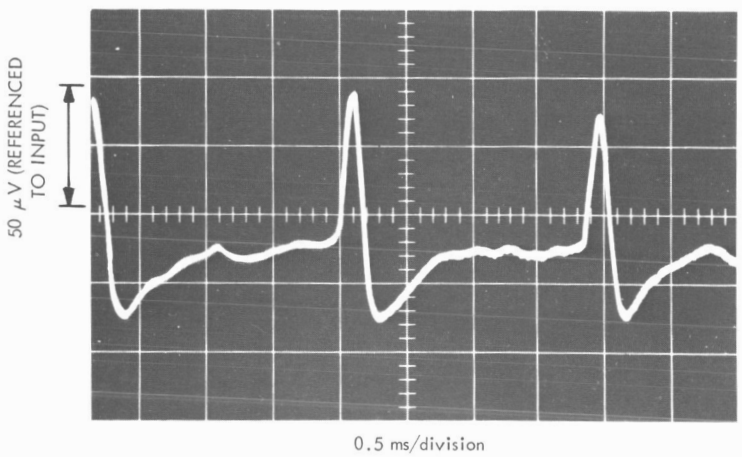

Figure 10. Telemetered simulated neuron firings

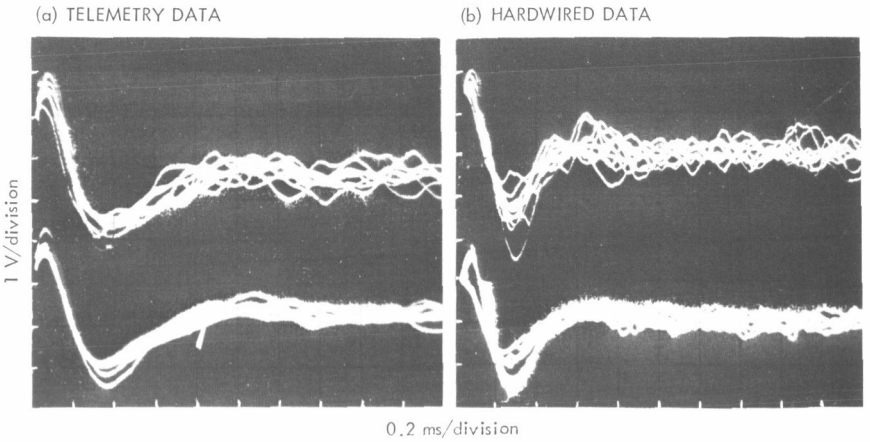

Figure 11. Neuron firings from chronically implanted rat (each photo superimposes tracings of 10 neuron firings)

Summary and Applications

A wideband, multichannel biotelemeter has been successfully designed, built, and tested. Two levels of breadboards were manufactured and tested in the evolution of the finished design. Imaginative component mounting and packaging techniques were developed to achieve a miniaturized telemeter that is economical, manufacturable, and maintainable.

The unique features of this miniature biotelemeter make it potentially useful in a wide variety of bioinstrumentation areas. Telemeter design anticipates its application to physiological signals of varying characteristics. Through use of functional circuit boards, variable sampling rate, and individual source signal conditioner/amplifiers, the telemeter design is sufficiently flexible to permit "customized" data channels with only minor telemeter reconfiguration.

Possible future development and users of this device are many. Follow-on applications of this advanced biotelemeter might well provide the critical step in significant discoveries in biomedical research and clinical fields.

Bibliography of Current Reporting

Author Index With Abstracts

AKLONIS, J. J.

A01 Viscoelastic Behavior of Polymers Undergoing Crosslinking Reactions

J. Moacanin and J. J. Aklonis (University of Southern California)

J. Polym. Sci., Pt. C: Polym. Sym., No. 35, pp. 71–76, 1971

For abstract, see Moacanin, J.

ANDERSON, J. D.

A02 Determination of Astrodynamic Constants and a Test of the General Relativistic Time Delay With S-Band Range and Doppler Data From Mariners 6 and 7

J. D. Anderson, P. B. Esposito, W. Martin, and D. O. Muhleman (California Institute of Technology)

Space Research XI, pp. 105–112, Akademie-Verlag, Berlin, 1971

Range and doppler tracking data from Mariners 6 and 7 have been used to obtain information on the ratio μ^{-1} of the mass of the Earth to the mass of the Moon and on the mass and ephemeris of Mars. Based on data from five Mariner and two Pioneer spacecraft, the best value for μ^{-1} is 81.3007 ± 0.0005. The best value of the ratio of the mass of the sun to the mass of Mars was obtained by Null from analyses of the Mariner 4 data. This value (3098714 ± 5) has been substantiated by the Mariner 6 data which give 3098697 ± 72. By combining the Mariner 6 range data with optical and radar data of the planets, it is possible to deduce that the mean equatorial radius of Mars is 3393.0 ± 1.7 km.

Range data around the time of solar superior conjunction have yielded a test of the general relativistic time delay to the level of

±10%. Additional post-conjunction data will significantly improve the accuracy of this test.

ANNO, G. H.

A03 Nuclear Radiation Sources On-Board Outerplanet Spacecraft

E. L. Noon, G. H. Anno, and M. A. Dore

IEEE Trans. Nucl. Sci., Vol. NS-18, No. 5, pp. 50–57, October 1971

For abstract, see Noon, E. L.

ANSPAUGH, B. E.

A04 ATS-5 Solar Cell Experiment Results After One Year in Synchronous Orbit

B. E. Anspaugh

Technical Memorandum 33-522, January 1, 1972

The results of the ATS-5 solar cell experiment after one year in synchronous orbit are reported. A partial failure in the experimental electronics package has caused a loss of data from half of the 80 experimental solar cells. Procedures for extracting data due to a partial spacecraft failure are described and discussed. Data from the remaining 40 solar cells, including 15 mounted on a thin flexible structure, are analyzed. Data are corrected to a solar intensity of 140 mW/cm^2 and a temperature of 25°C.

After one year in synchronous orbit: (1) cells with 1.52-mm-thick coverslides did not show a clear-cut advantage over those with 0.15-mm coverslides, (2) cells with solderless grid lines are degrading at the same rate as are cells with solder-dipped grid lines, (3) cells not quite completely covered with coverslides suffered a large power loss in comparison to cells fully covered, (4) no clear-cut advantage of 10-Ω-cm cells over 2-Ω-cm cells has yet been observed, (5) cells mounted on the flexible panel with relatively little backshielding did not degrade any faster than those with substantial backshielding, and (6) the flight data in large part confirms the adequacy of the ground-based techniques used in the preflight radiation test program.

AVIŽIENIS, A.

A05 The STAR (Self-Testing and Repairing) Computer: An Investigation of the Theory and Practice of Fault-Tolerant Computer Design

A. Avižienis, G. C. Gilley, F. P. Mathur, D. A. Rennels, J. A. Rohr, and D. K. Rubin

IEEE Trans. Computers, Vol. C-20, No. 11, pp. 1312–1321, November 1971

This article presents the results obtained in a continuing investigation of fault-tolerant computing being conducted at JPL. Initial studies led to the decision to design and construct an experimental computer with dynamic (standby) redundancy, including replaceable subsystems and a program rollback provision to eliminate transient errors. This system, called the STAR computer, began operation in 1969. The following aspects of the STAR system are described: architecture, reliability analysis, software, automatic maintenance of peripheral systems, and adaptation to serve as the central computer of an outer-planet spacecraft.

A06 Arithmetic Error Codes: Cost and Effectiveness Studies for Application in Digital System Design

A. Avižienis

IEEE Trans. Computers, Vol. C-20, No. 11, pp. 1322–1331, November 1971

The application of error-detecting or error-correcting codes in digital computer design requires studies of cost and effectiveness trade-offs to supplement the knowledge of their theoretical properties. General criteria for cost and effectiveness studies of error codes are developed, and results are presented for arithmetic error codes with the low-cost check modulus $2^a - 1$. Both separate (residue) and nonseparate (AN) codes are considered. The class of multiple arithmetic error codes is developed as an extension of low-cost single codes.

BACK, L. H.

B01 Viscous Slipstream Flow Downstream of a Centerline Mach Reflection

L. H. Back and R. F. Cuffel

AIAA J., Vol. 9, No. 10, pp. 2107–2109, October 1971

An important aspect of supersonic flows with shock waves is the reflections of these waves at boundaries such as along centerlines,

along surfaces, and along free jet extremities. The first of these interactions is considered in this article for a situation where the reflection from the centerline in an axisymmetric flow is through a shock stem (Mach reflection). The purpose of this investigation was to determine the mean structure of the viscous flowfield downstream of the intersection from Pitot and static pressure probe measurements. There was virtually no experimental information available on the structure of such a shear flow and on the size of the subsonic flow region that is imbedded in the supersonic flow.

B02 Turbulent Boundary Layer and Heat Transfer Measurements Along a Convergent-Divergent Nozzle

L. H. Back and R. F. Cuffel

Trans. ASME, Ser. C: J. Heat Transf., Vol. 93, No. 4, pp. 397–407, November 1971

This article presents boundary layer and heat transfer measurements along a cooled, conical nozzle with a convergent and a divergent half-angle of 10 deg. Semi-empirical analyses are considered in conjunction with the measurements. The heat transfer is found to be describable by using the integral form of the energy equation once the relationship between the Stanton number and energy thickness Reynolds number has been established from the measurements. The friction coefficient, however, is not described accurately along the entire nozzle by the existing formulations considered.

B03 Partially Ionized Gas Flow and Heat Transfer in the Separation, Reattachment, and Redevelopment Regions Downstream of an Abrupt Circular Channel Expansion

L. H. Back, P. F. Massier, and E. J. Roschke

Trans. ASME, Ser. C: J. Heat Transf., Vol. 94, No. 1, pp. 119–127, February 1972

Heat transfer and pressure measurements obtained in the separation, reattachment, and redevelopment regions along a tube and nozzle located downstream of an abrupt channel expansion are presented for a very-high-enthalpy flow of argon. The ionization energy fraction extended up to 0.6 at the tube inlet just downstream of the arc heater. Reattachment resulted from the growth of an instability in the vortex sheet-like shear layer between the central jet that discharged into the tube and the reverse flow along the wall at the lower Reynolds numbers, as indicated by water flow visualization studies which were found to dynamically model the high-temperature gas flow. A reasonably good prediction of the heat transfer in the reattachment region where the highest

heat transfer occurred and in the redevelopment region downstream can be made by using existing laminar-boundary-layer theory for a partially ionized gas. In the experiments, as much as 90% of the inlet energy was lost by heat transfer to the tube and the nozzle wall.

BAHM, E. J.

B04 Magnetic Tape Recorder for Long Operating Life in Space

E. J. Bahm and J. K. Hoffman

IEEE Trans. Magnetics, Vol. MAG-7, No. 3, pp. 517–520, September 1971

Magnetic tape recorders have long been used on satellites and spacecraft for onboard storage of large quantities of data. As satellites enter into commercial service, long operating life at high reliability becomes important. Also, the presently planned long-duration space flights to the outer planets require long-life tape recorders. Past satellite tape recorders have achieved a less-than-satisfactory performance record and the operating life of other spacecraft tape recorders has been relatively short and unpredictable. Most failures have resulted from malfunctions of the mechanical tape transport.

Recent advances in electric motors and static memories have allowed the development of the new tape recorder reported in this article. This recorder uses a very simple tape transport with few possible failure modes. It consists of only two brushless dc motors, two tape guides, and the recording heads. Relatively low tape tension, wide torque capability, and precise speed control facilitate design for mechanical reliability to match that of tape-recorder electronics.

BAUMAN, A. J.

B05 Isolation and Characterization of Keto-Carotenoids From the Neutral Extract of Algal Mat Communities of a Desert Soil

A. J. Bauman, H. G. Boettger, A. M. Kelly, R. E. Cameron, and H. Yokoyama (U.S. Department of Agriculture)

Eur. J. Biochem., Vol. 22, No. 2, pp. 287–293, September 1971

The carotenoid pigments of surficial algal mat communities of a California absolute subtropical desert were isolated and characterized principally by means of high resolution mass spectrometry.

The pigments were all oxidized keto-types, predominantly canthaxanthin, its isomers, and echinone. The carotenoid pattern suggests that the mats represent an old climax ecosystem in which the algal cells at the time of collection were starved for nitrogen.

B06 Absence of Porphyrins in an Apollo 12 Lunar Surface Sample

J. H. Rho, A. J. Bauman, T. F. Yen (University of Southern California), and J. Bonner (California Institute of Technology)

Proceedings of the Second Lunar Science Conference, Houston, Texas, January 11–14, 1971, Vol. 2, pp. 1875–1877, The M.I.T. Press, Cambridge, 1971

For abstract, see Rho, J. H.

B07 A Simple Electrostatic Model for the Chromatographic Behavior of the Primary Dithizonates

A. J. Bauman and J. H. Richards

Separ. Sci., Vol. 6, No. 5, pp. 715–725, October 1971

A simple electrostatic model of the reactive sites of primary metal dithizonates which fits their published chromatographic behavior is described. Coordination with a metal ion tends to increase the formal charge on the hindered imino hydrogens in the molecule. This increase is a function of the individual metal's Sanderson electronegativity. Plots of R_m versus electronegativity are rectilinear, have the same form for all systems and adsorbents described, and place dithizonates of similar molecular geometry on separate curves. The results of this study suggest that the dithizonates are a heterogeneous group of compounds which differ in coordination configuration and geometry.

BAUMERT, L. D.

B08 A Combinatorial Packing Problem

L. D. Baumert

SIAM/AMS (Society for Industrial and Applied Mathematics/ American Mathematical Society) Book Series, Vol. IV, pp. 97–108, 1970

This article is concerned with the efficient packing of squares of side two into the $p \times p$ torus. Of more general interest is the analogous n-dimensional problem: that of packing n-dimensional two-cubes efficiently into a $p \times p \times \ldots \times p$ torus. Of course, when p is even, the problem is trivial. (Then, the simplest possible

alignment of the cubes completely fills the torus.) Thus, p here is restricted to be an odd integer. Further, it should be pointed out that the primary interest here is in determining the maximum number [$=\alpha\ (C_p{}^n)$] of cubes which can be packed into the torus and of only secondary concern are the actual structural details of any particular maximal packing.

BECK, A. J.

B09 Jupiter Trapped Radiation Belts

A. J. Beck

JPL Quarterly Technical Review, Vol. 1, No. 4, pp. 78–88, January 1972

Previously developed models for trapped electron radiation belts and trapped proton radiation belts in the Jovian magnetosphere are described. The spatial distribution of flux and the L-shell dependence of the characteristic energy are displayed for both models. Based on these models, the fluence accumulated by a Jupiter flyby spacecraft is given in terms of the equivalent 3-MeV fluence for electrons and the equivalent 20-MeV proton fluence for protons. Finally, some impacts of these fluences on outer-planet missions are described.

BEER, R.

B10 Astronomical Infrared Spectroscopy With a Connes-Type Interferometer: I. Instrumental

R. Beer, R. H. Norton, and C. H. Seaman

Rev. Sci. Instr., Vol. 42, No. 10, pp. 1393–1403, October 1971

Shortly after P. and J. Connes had completed the first model of their now well-known Fourier spectrometer, JPL undertook the construction of a similar instrument. The JPL instrument differs significantly from the original. In this article, the construction and operation of the JPL instrument are discussed in an astronomical context, and a sample is given of the type of spectra obtained with the system.

BEJCZY, A. K.

B11 Analytical Methods for Performance Evaluation of Nonlinear filters

A. K. Bejczy and R. Sridhar (University of California, Los Angeles)

J. Math. Anal. Appl., Vol. 36, No. 3, pp. 477–505, December 1971

The investigation described in this article is addressed to the question of developing analytical methods for evaluating the performance of suboptimal nonlinear filters such that the filters' structure is fixed by postulating a simple form for it. The filtering problem is considered in the continuous time domain. The postulated simple suboptimal nonlinear filter structure closely parallels the structure of the Kalman–Bucy optimal linear filter algorithm.

Two filter performance evaluation methods are developed based on the Kolmogorov equations for the transition density of Markov processes. The expansions in the approximations for the nonlinear system and observation functions are, in effect, carried out up to second-order terms in both methods. The difference between the methods is the sequencing of expansions and averaging. The description of the filters' performance is sought in terms of second-order statistics (mean and covariance) in both methods. The equations for the mean and covariance of the filtering error resulting from the two methods are different. The resulting equations of both methods have, however, an important common feature: They are *deterministic* differential equations describing the time evolution of the mean and covariance of the filtering error process for the fixed filter structure in terms of the known (postulated) filter gain and system and noise parameters. The developed deterministic differential equations can also be utilized to determine appropriate (deterministic) filter gains for the fixed structure nonlinear filter. The salient features of the new performance evaluation (and filter gain construction) methods are illustrated with two examples.

BILLINGSLEY, F. C.

B12 Apollo 12 Multispectral Photography Experiment

A. F. H. Goetz, F. C. Billingsley, J. W. Head (Bellcomm, Inc.), T. B. McCord (Massachusetts Institute of Technology), and E. Yost (Long Island University)

Proceedings of the Second Lunar Science Conference, Houston, Texas, January 11–14, 1971, Vol. 3, pp. 2301–2310, The M.I.T. Press, 1971

For abstract, see Goetz, A. F. H.

BLAIR, P. M.

B13 Discoloration and Lunar Dust Contamination of Surveyor III Surfaces

W. F. Carroll and P. M. Blair (Hughes Aircraft Corporation)

Proceedings of the Second Lunar Science Conference, Houston, Texas, January 11–14, 1971, Vol. 3, pp. 2735–2742, The M.I.T. Press, Cambridge, 1971

For abstract, see Carroll, W. F.

BOETTGER, H. G.

B14 Isolation and Characterization of Keto-Carotenoids From the Neutral Extract of Algal Mat Communities of a Desert Soil

A. J. Bauman, H. G. Boettger, A. M. Kelly, R. E. Cameron, and H. Yokoyama (U.S. Department of Agriculture)

Eur. J. Biochem., Vol. 22, No. 2, pp. 287–293, September 1971

For abstract, see Bauman, A. J.

BONNER, J.

B15 Absence of Porphyrins in an Apollo 12 Lunar Surface Sample

J. H. Rho, A. J. Bauman, T. F. Yen (University of Southern California), and J. Bonner (California Institute of Technology)

Proceedings of the Second Lunar Science Conference, Houston, Texas, January 11–14, 1971, Vol. 2, pp. 1875–1877, The M.I.T. Press, Cambridge, 1971

For abstract, see Rho, J. H.

BOWERS, M. T.

B16 Dependence of the Rates on Ion Kinetic Energy for the Reactions $D_2^+ + D_2$ and $HD^+ + HD$

W. T. Huntress, Jr., D. D. Elleman, and M. T. Bowers (University of California, Santa Barbara)

J. Chem. Phys., Vol. 55, No. 11, pp. 5413–5414, December 1, 1971

For abstract, see Huntress, W. T., Jr.

BUECHLER, G.

B17 A Surface-Layer Representation of the Lunar Gravitational Field

L. Wong (Aerospace Corporation), G. Buechler (Aerospace Corporation), W. Downs (Aerospace Corporation), W. L. Sjogren, P. M. Muller, and P. Gottlieb

J. Geophys. Res., Vol. 76, No. 26, pp. 6220–6236, September 10, 1971

For abstract, see Wong, L.

CAMERON, R. E.

C01 Isolation and Characterization of Keto-Carotenoids From the Neutral Extract of Algal Mat Communities of a Desert Soil

A. J. Bauman, H. G. Boettger, A. M. Kelly, R. E. Cameron, and H. Yokoyama (U.S. Department of Agriculture)

Eur. J. Biochem., Vol. 22, No. 2, pp. 287–293, September 1971

For abstract, see Bauman, A. J.

CANNON, W. A.

C02 Fixation of Virgin Lunar Surface Soil

J. M. Conley, R. Frazer, and W. A. Cannon

Technical Memorandum 33-521, February 1, 1972

For abstract, see Conley, J. M.

C03 Physical Adsorption of Rare Gas on Terrigenous Sediments

F. P. Fanale and W. A. Cannon

Earth Planet. Sci. Lett., Vol. 11, No. 5, pp. 362–368, August 1971

For abstract, see Fanale, F. P.

CARON, L. G.

C04 Bernal Model: A Simple Equilibrium Theory of Close-Packed Liquids

L. G. Caron

J. Chem. Phys., Vol. 55, No. 11, pp. 5227–5232, December 1, 1971

The Bernal model of a hard-sphere liquid is used in conjunction with an extension of the cell method to predict the behavior of liquid argon near melting. The entropy of disorder associated with the Bernal state is deduced. The model is found to be applicable to liquid metals.

C05 Electron Correlations at Large Densities

L. G. Caron

Phys. Rev., Pt. B: Solid State, Vol. 5, No. 1, pp. 238–240, January 1, 1972

In two papers, Singwi, et al., presented a self-consistent scheme to calculate the dielectric function of an electron gas at metallic densities. An improvement made to obtain results that better satisfied the compressibility sum rules was presented in the second paper; this improvement, however, led to a great increase in computational time. In an attempt to reduce this time and yet retain the improved features of the dielectric function, an approximate scheme for numerical calculation of the dielectric function of an electron gas in the theory of Singwi, et al., was formulated. This scheme and the numerical results of its application are presented in this article.

CARROLL, W. F.

C06 Discoloration and Lunar Dust Contamination of Surveyor III Surfaces

W. F. Carroll and P. M. Blair (Hughes Aircraft Corporation)

Proceedings of the Second Lunar Science Conference, Houston, Texas, January 11–14, 1971, Vol. 3, pp. 2735–2742, The M.I.T. Press, Cambridge, 1971

As discussed in this article, the discoloration of Surveyor 3 surfaces observed by the Apollo 12 astronauts during their examination of the spacecraft on the Moon and clearly evident on the returned hardware has been analyzed and shown to be due to expected radiation darkening and a heavier-than-expected layer of lunar fines. Lunar surface material disturbed by the Apollo 12 lunar module (LM) landing 155 m away reached the Surveyor spacecraft and produced significant changes in its surfaces.

CHADWICK, H. D.

C07 A Markov Chain Technique for Determining the Acquisition Behavior of a Digital Tracking Loop

H. D. Chadwick

JPL Quarterly Technical Review, Vol. 1, No. 4, pp. 49–57, January 1972

Tracking loops have two characteristic modes of operation: acquisition and steady-state tracking. The steady-state behavior of such nonlinear tracking loops as the phase-locked loop has been the subject of considerable analysis. The acquisition behavior of a loop, the transition period between turning the loop on and the steady state, has resisted analysis for all but the simplest configurations. An iterative procedure is presented for determining the acquisition behavior of discrete or digital implementations of the tracking loop. The technique is based on the theory of Markov chains and provides the cumulative probability of acquisition in the loop as a function of time in the presence of noise and a given set of initial condition probabilities. A digital second-order tracking loop to be used in the Viking command receiver for continuous tracking of the command subcarrier phase has been analyzed using this technique, and the results agree closely with experimental data. Possible extensions of the technique include the analysis of continuous loops using discrete approximations.

C08 The Error Probability of a Wide-Band FSK Receiver in the Presence of Multipath Fading

H. D. Chadwick

IEEE Trans. Commun. Technol., Vol. COM-19, No. 5, pp. 699–707, October 1971

Calculations are made for the probability of error of a wide-band FSK (frequency-shift-keyed) receiver of the type used in space

telemetry when multipath reflections off the planetary surface cause signal fading. The error probability is found for both low and high fading bandwidths and for small or large reflected path delays.

CHAN, S. I.

C09 Ferromagnetic Resonance of Lunar Samples

F.-D. Tsay (California Institute of Technology),
S. I. Chan (California Institute of Technology), and
S. L. Manatt

Geochim. Cosmochim. Acta, Vol. 35, No. 9, pp. 865–875, September 1971

For abstract, see Tsay, F.-D.

C10 Magnetic Resonance Studies of Apollo 11 and Apollo 12 Samples

F.-D. Tsay (California Institute of Technology),
S. I. Chan (California Institute of Technology), and
S. L. Manatt

Proceedings of the Second Lunar Science Conference, Houston, Texas, January 11–14, 1971, Vol. 3, pp. 2515–2528, The M.I.T. Press, Cambridge, 1971

For abstract, see Tsay, F.-D.

CHAPMAN, A. K.

C11 DSN Progress Report for November–December 1971: Apollo Bistatic Radar Investigation

A. K. Chapman

Technical Report 32-1526, Vol. VII, pp. 190–194, February 15, 1972

The first bistatic Moon radar experiments were conducted by the Stanford Center for Radar Astronomy, using Lunar Orbiter spacecraft. Apollo not only provides stronger signals, but provides for conduct of the experiment on two frequency bands. The JPL 64-m-diameter tracking antenna at Goldstone is uniquely suited to the reception of the S-band signals involved, and has been used on both Apollo 14 and Apollo 15 for the bistatic investigation.

CHASE, S. C., JR.

C12 Mariner 1969 Infrared Radiometer Results: Temperatures and Thermal Properties of the Martian Surface

G. Neugebauer (California Institute of Technology),
G. Münch (California Institute of Technology),
H. Kieffer (University of California, Los Angeles),
S. C. Chase, Jr. (Santa Barbara Research Center), and
E. Miner

Astron. J., Vol. 76, No. 8, pp. 719–749, October 1971

For abstract, see Neugebauer, G.

CHELSON, P. O.

C13 Failure-Rate Computations Based on Mariner Mars 1969 Spacecraft Data

P. O. Chelson

Technical Report 32-1544, December 1, 1971

This report describes an analysis of in-flight spacecraft part hours and failure data from the Mariner Mars 1969 Project. It contains failure rates computed from these data for all electronic and electromagnetic parts on the Mariner 6 and 7 spacecraft. Also included are failure rates based on combining flight data from Mariner 4–7.

CHEN, C. J.

C14 Raman Scattering Cross Section for N_2O_4

C. J. Chen and F. Wu (State University of New York, Buffalo)

Appl. Phys. Lett., Vol. 19, No. 11, pp. 452–453, December 1, 1971

As reported in this article, the Raman scattering cross section for N_2O_4 at a Raman shift of 1360 cm^{-1} has been measured by using a Q-switched ruby laser as an excitation source. The cross section for N_2 at a Raman shift of 2330 cm^{-1} has also been measured. The latter measurement is compared with a previous measurement reported elsewhere, and the result is normalized to the wavelength.

C15 **Calculations of Geometries of Organic Molecules Using the CNDO/2 Method: I. Empirical Correlations Between Observed and Calculated Bond Lengths in Simple Acyclics, Strained Cycloalkenes and Some Polycyclic Molecules**

C. S. Cheung, M. A. Cooper, and S. L. Manatt

Tetrahedron, Vol. 27, No. 4, pp. 689–700, February 1971

In this article, it is shown that calculations of C—C and C—H bond lengths in hydrocarbons using the CNDO/2 semi-empirical MO method exhibit systematic deviations from the observed values. An empirical correlation relating the observed and calculated bond lengths with the number of substituents attached to the bond may be devised. This correlation is capable of providing theoretical bond lengths within 0.008 Å of the experimental for a wide range of simple acyclic molecules. Furthermore, calculations of molecular geometries for some strained cycloalkenes and also some larger molecules, e.g., naphthalene, biphenylene, and azulene, are similarly found to be in good agreement with experiment.

C16 **Calculations of Geometries of Organic Molecules Using the CNDO/2 Molecular Orbital Method: II. Structural Predictions for the Benzocycloalkenes, and a Theoretical Rationalization of Their Proton–Proton Spin–Spin Coupling Constants**

C. S. Cheung, M. A. Cooper, and S. L. Manatt

Tetrahedron, Vol. 27, No. 4, pp. 701–709, February 1971

In this article, the CNDO/2 semiempirical MO method is applied to calculations of the geometries of some strained benzocycloalkenes. The strain-induced bond-length distortions predicted are in disagreement with earlier work, although the lack of accurate experimental data precludes a decision as to the validity of either treatment. The CNDO/2 wavefunctions are examined for features which may throw light on previous qualitative descriptions which have been proposed to account for recent experimental data on this series, such as nuclear-magnetic-resonance and electron-spin-resonance spectra, and rates of electrophilic substitution. In particular, trends in the proton–proton spin–spin coupling constants in the benzocycloalkenes and also benzene, naphthalene, and biphenylene are well-accounted-for by the CNDO/2 wavefunctions.

CHITTY, W. H.

C17 Development and Testing of the Flight Command Subsystem for the Mariner Mars 1971 Spacecraft

W. H. Chitty

Technical Memorandum 33-531, March 15, 1972

The flight command subsystem for the Mariner Mars 1971 spacecraft is of the same basic design and construction as that for the Mariner Mars 1969 spacecraft, except for its expanded capability. Its primary purpose is to provide remote control for the spacecraft. This memorandum briefly describes the design changes, fabrication, and significant problems associated with the development of the Mariner Mars 1971 flight command subsystem.

CLEMENTS, P. A.

C18 DSN Progress Report for November–December 1971: Electrical Length Stability of Coaxial Cable in a Field Environment

P. A. Clements

Technical Report 32-1526, Vol. VII, pp. 97–100, February 15, 1972

Various environmental conditions will cause a coaxial cable to change electrical length. In the past, the effects of these changes were not important; however, recent requirements for future DSS accuracies have forced their consideration. Preliminary studies on the effects due to temperature changes and mechanical stress have been made. Results to date indicate some problem areas.

CONEL, J. E.

C19 Luminescence and Reflectance of Apollo 12 Samples

D. B. Nash and J. E. Conel

Proceedings of the Second Lunar Science Conference, Houston, Texas, January 11–14, 1971, Vol. 3, pp. 2235–2244, The M.I.T. Press, Cambridge, 1971

For abstract, see Nash, D. B.

C20 Objectives and Requirements of Unmanned Rover Exploration of the Moon

D. B. Nash, J. E. Conel, and F. P. Fanale

The Moon, Vol. 3, No. 2, pp. 221–230, August 1971

For abstract, see Nash, D. B.

CONLEY, J. M.

C21 Fixation of Virgin Lunar Surface Soil

J. M. Conley, R. Frazer, and W. A. Cannon

Technical Memorandum 33-521, February 1, 1972

Two systems have been shown to be suitable for fixing loose particulate soils with a polymer film without visually detectable disturbance of the soil particle spatial relationships. A two-component system uses a gas monomer condensible at the soil temperature and a gas-phase catalyst acting to polymerize the monomer. A one-component system uses a monomer which polymerizes spontaneously on and within the top few millimeters of the soil.

The two-component system may result in a simpler apparatus, but has been demonstrated to operate over a narrower temperature range, i.e., approximately −40 to −10°C. Other two-component polymer systems have been identified which may operate at soil temperatures as high as +100°C, but still over relatively narrow temperature ranges of approximately 30°C. The one-component system has been demonstrated to operate successfully with initial soil temperatures from −70°C or lower to +150°C.

CONNES, J.

C22 Fourier Spectroscopy With a One-Million-Point Transformation (Translation From the Original Published in the Nouvelle Revue d'Optique Appliquée, Vol. 1, pp. 3–22, 1970)

J. Connes (National Center for Scientific Research, Orsay, France), H. Delouis (National Center for Scientific Research, Orsay, France), P. Connes (National Center for Scientific Research, Orsay, France), G. Guelachvili (National Center for Scientific Research, Orsay, France), J.-P. Maillard (National Center for Scientific Research, Orsay, France), and G. Michel (National Center for Scientific Research, Orsay, France)

Technical Memorandum 33-525, March 15, 1972

A new type of interferometer for use in Fourier spectroscopy has been devised at the Aimé Cotton Laboratory of the National Center for Scientific Research (CNRS), Orsay, France. With this interferometer and with computational techniques developed by the Regional Interdisciplinary Center for Electronic Calculation

(CIRCE) at the CNRS, interferograms comprising as many as 10^6 samples can now be transformed. The techniques are described, and examples of spectra of thorium and holmium, derived from 10^6-point interferograms, are presented in this paper, which was translated by R. Beer of JPL.

CONNES, P.

C23 Fourier Spectroscopy With a One-Million-Point Transformation (Translation From the Original Published in the Nouvelle Revue d'Optique Appliquée, Vol. 1, pp. 3–22, 1970)

J. Connes (National Center for Scientific Research, Orsay, France), H. Delouis (National Center for Scientific Research, Orsay, France), P. Connes (National Center for Scientific Research, Orsay, France), G. Guelachvili (National Center for Scientific Research, Orsay, France), J.-P. Maillard (National Center for Scientific Research, Orsay, France), and G. Michel (National Center for Scientific Research, Orsay, France)

Technical Memorandum 33-525, March 15, 1972

For abstract, see Connes, J.

COOPER, M. A.

C24 Calculations of Geometries of Organic Molecules Using the CNDO/2 Method: I. Empirical Correlations Between Observed and Calculated Bond Lengths in Simple Acyclics, Strained Cycloalkenes and Some Polycyclic Molecules

C. S. Cheung, M. A. Cooper, and S. L. Manatt

Tetrahedron, Vol. 27, No. 4, pp. 689–700, February 1971

For abstract, see Cheung, C. S.

C25 Calculations of Geometries of Organic Molecules Using the CNDO/2 Molecular Orbital Method: II. Structural Predictions for the Benzocycloalkenes, and a Theoretical Rationalization of Their Proton–Proton Spin–Spin Coupling Constants

C. S. Cheung, M. A. Cooper, and S. L. Manatt

Tetrahedron, Vol. 27, No. 4, pp. 701–709, February 1971

For abstract, see Cheung, C. S.

CUFFEL, R. F.

C26 Viscous Slipstream Flow Downstream of a Centerline Mach Reflection

L. H. Back and R. F. Cuffel

AIAA J., Vol. 9, No. 10, pp. 2107–2109, October 1971

For abstract, see Back, L. H.

C27 Turbulent Boundary Layer and Heat Transfer Measurements Along a Convergent-Divergent Nozzle

L. H. Back and R. F. Cuffel

Trans. ASME, Ser. C: J. Heat Transf., Vol. 93, No. 4, pp. 397–407, November 1971

For abstract, see Back, L. H.

DALLAS, S. S.

D01 DSN Progress Report for November–December 1971: A Comparison of Cowell's Method and a Variation-of-Parameters Method for the Computation of Precision Satellite Orbits: Addendum 1

S. S. Dallas and E. A. Rinderle

Technical Report 32-1526, Vol. VII, pp. 32–36, February 15, 1972

Additional test cases using a precision special perturbations program employing either Cowell's method or a variation-of-parameters method to compute an elliptical orbit are analyzed to determine which method is more efficient. The results obtained indicate that the variation-of-parameters method with a predict-only integrator and Cowell's method with a predict-partial-correct integrator are equally efficient and both are significantly more efficient than Cowell's method with a predict-correct integrator. Either of these two methods for computing precision satellite orbits offers the potential for reducing the total costs of computations during orbit design and computer execution time during real-time mission operations for future orbiter projects.

DAVIS, D. P.

D02 Initiation System for Low Thrust Motor Igniter

L. D. Strand, D. P. Davis, and J. I. Shafer

Technical Memorandum 33-520, January 1, 1972

For abstract, see Strand, L. D.

DeGENNARO, L. I.

D03 DSN Progress Report for November–December 1971: Occultation Recording Assembly Implementation

L. I. DeGennaro

Technical Report 32-1526, Vol. VII, pp. 175–181, February 15, 1972

The Mariner Mars 1971 occultation experiment, in order to expedite data reduction and analysis, required real-time digital tape recordings of the Mars Deep Space Station (DSS) open loop receiver signal and nonreal-time digital tape conversion of the analog tapes (of the open loop receivers) produced by the Woomera DSS (Australia) and the Cebreros DSS (Spain). This article presents a description of the implementation of the two occultation recording assemblies, which were used to satisfy these requirements.

DELOUIS, H.

D04 Fourier Spectroscopy With a One-Million-Point Transformation (Translation From the Original Published in the Nouvelle Revue d'Optique Appliquée, Vol. 1, pp. 3–22, 1970)

J. Connes (National Center for Scientific Research, Orsay, France), H. Delouis (National Center for Scientific Research, Orsay, France), P. Connes (National Center for Scientific Research, Orsay, France), G. Guelachvili (National Center for Scientific Research, Orsay, France), J.-P. Maillard (National Center for Scientific Research, Orsay, France), and G. Michel (National Center for Scientific Research, Orsay, France)

Technical Memorandum 33-525, March 15, 1972

For abstract, see Connes, J.

DeMORE, W. B.

D05 Photolysis of CO_2 at 1849 Å

W. B. DeMore and M. M. Mosesman

J. Atmos. Sci., Vol. 28, No. 6, pp. 842–846, September 1971

Photolysis of CO_2 at 1849 Å (Hg lamp) has been studied at pressures in the range 65–800 psi at room temperature. The primary dissociation quantum yield is 1.0, as determined by experiments in which the atomic oxygen product was scavenged in the form of O_3. At high pressures (~400 psi), O_3 photolysis at 2537 Å gave appreciable CO_3 formation by the reaction

$$O(^1D) + CO_2 + M \rightarrow CO_3 + M$$

as evidenced by loss of O_3. To observe quantitative O_3 production, it was therefore necessary to filter out the 2537-Å light. The products CO and O_2 could not be recovered in 100% yield in most of the experiments. No satisfactory mechanism can be given for the product losses, although a number of possibilities can be ruled out. In particular, CO_3 did not oxidize CO to CO_2. The CO yield could be increased to nearly 100% by coating the cell walls with Kel-F grease, whereas the O_2 yield simultaneously dropped to zero. The quantum yield results at 1849 Å suggest that CO_2 dissociates at all wavelengths where absorption is appreciable.

DEVLIN, J. D.

D06 Dry-Heat Resistance of Bacillus Subtilis Var. Niger Spores on Mated Surfaces

G. J. Simko, J. D. Devlin, and M. D. Wardle

Appl. Microbiol., Vol. 22, No. 4, pp. 491–495, October 1971

For abstract, see Simko, G. J.

DORE, M. A.

D07 Nuclear Radiation Sources On-Board Outerplanet Spacecraft

E. L. Noon, G. H. Anno, and M. A. Dore

IEEE Trans. Nucl. Sci., Vol. NS-18, No. 5, pp. 50–57, October 1971

For abstract, see Noon, E. L.

DOWNS, G. S.

D08 Mars Radar Observations, a Preliminary Report

G. S. Downs, R. M. Goldstein, R. R. Green, and G. A. Morris

Science, Vol. 174, No. 4016, pp. 1324-1327, December 24, 1971

Radar observations of narrow belt of the surface of Mars, centered at 16° south latitude, show a very rugged terrain, with elevation differences greater than 13 km from peak to valley. For nearby points, the relative altitude is measured to 40 m at best; the precision is worse for points at different latitudes, or widely separated in longitude, because of orbital uncertainties. Some of the larger craters have been resolved, and their depth and, in some cases, the height of the raised rim have been measured. Where high-resolution photographs are available, the correlation is excellent.

DOWNS, W.

D09 A Surface-Layer Representation of the Lunar Gravitational Field

L. Wong (Aerospace Corporation), G. Buechler (Aerospace Corporation), W. Downs (Aerospace Corporation), W. L. Sjogren, P. M. Muller, and P. Gottlieb

J. Geophys. Res., Vol. 76, No. 26, pp. 6220-6236, September 10, 1971

For abstract, see Wong, L.

DUXBURY, T. C.

D10 In-Flight Calibration of an Interplanetary Navigation Instrument

T. C. Duxbury and H. Ohtakay

J. Spacecraft Rockets, Vol. 8, No. 10, pp. 1038-1042, October 1971

This article presents the results of an analytical investigation that demonstrates the feasibility of geometrically calibrating a navigation instrument during interplanetary flight to arc-sec accuracy. The instrument, similar to a television camera, would view selected natural satellites and reference stars simultaneously for navigating to the outer planets. An 11 × 11 reseau grid, etched onto the target raster of a vidicon tube, would be used to remove electromagnetic distortion from the satellite and reference star

data to less than 1.2 arc-sec (1σ) in each and every data frame, independent of reseau data from any other data frame. Taking advantage of expected optical distortion stability, 50 star images obtained from many data frames would be used to determine optical distortion to less than 4.3 arc-sec (1σ). Therefore, the use of the reseau grid and star images could enable the navigation measurements to be geometrically calibrated to an accuracy of 5 arc-sec (1σ).

DYER, P.

D11 A Computational Algorithm for Sequential Estimation

R. J. Hanson and P. Dyer (Imperial Chemical Industries Ltd.)

Comput. J., Vol. 14, No. 3, pp. 285–290, August 1971

For abstract, see Hanson, R. J.

EASTON, R. A.

E01 Centralized Data Handling for Grand Tour Missions

R. A. Easton

Advan. Astronaut. Sci., Vol. 29, No. II, pp. 367–376, 1971

This article describes an adaptive self-testing and repairing centralized data system incorporating the flexibility and reliability necessary for the Grand Tour class of deep-space missions. It was developed as part of the Thermoelectric Outer-Planet Spacecraft (TOPS) effort at JPL. The data system consists of a programmable adaptive computer-aided telemetry system (CATS) called the measurement processor, a 2×10^9-bit data storage system consisting of a buffer plus single-speed tape recorders, science instrument interface units customized to each instrument, a ground command decoder, a central timing source, and a self-testing and repairing (STAR) control computer that coordinates the operations of the other parts of the system and of the spacecraft.

This data system is organized such that the measurement processor performs all repetitive high-speed data gathering and reduction functions, alerting the STAR computer through a shared two-port memory if any abnormal readings are noted. It also routes compressed spacecraft data to data storage for periodic data dump transmissions to the ground while some data are transmitted to the ground in real time. Meanwhile, the STAR computer performs non-routine data handling functions and issues commands to the spacecraft as needed. It can also back-up failed portions of the

data system at a reduced capability. If the STAR computer is the spacecraft's brain, then CATS is its nervous system. This division of labor allows a substantial reduction in the power, weight, and complexity of the overall system as opposed to using one general-purpose computer for all functions. The CATS and STAR computer have been breadboarded at JPL.

ELLEMAN, D. D.

E02 Dependence of the Rates on Ion Kinetic Energy for the Reactions $D_2^+ + D_2$ and $HD^+ + HD$

W. T. Huntress, Jr., D. D. Elleman, and
M. T. Bowers (University of California, Santa Barbara)

J. Chem. Phys., Vol. 55, No. 11, pp. 5413–5414,
December 1, 1971

For abstract, see Huntress, W. T., Jr.

ERICKSON, D. E.

E03 DSN Progress Report for November–December 1971: The SAPDP Program Set for Sigma 5 Assembly

D. E. Erickson

Technical Report 32-1526, Vol. VII, pp. 91–96,
February 15, 1972

This article describes a set of programs that have been written to enable the Sigma 5 computer to assemble programs for the PDP-11 minicomputer. It consists of two parts: a system procedure deck, which allows SIGMA METASYMBOL to assemble a source language similar to PDP's own PAL-11; and a secondary loader, which reformats the Sigma 5 load module into PDP-11 absolute binary format and punches it onto paper tape. The syntactic differences between this assembler and PAL-11 are described, as well as the process of generating a PDP-11 program using this program set on the Sigma 5.

ERPENBACH, H.

E04 DSN Progress Report for November–December 1971: High Output Power for Hydrogen Maser Frequency Standards

H. Erpenbach and C. Finnie

Technical Report 32-1526, Vol. VII, pp. 106–108, February 15, 1972

This article describes the use of an FEP and TFE Teflon mixture to form duplicable storage bulb wall coatings for hydrogen maser frequency standards. The use of this mixture has resulted in wall coatings more efficient than previous coatings fabricated at this facility. A hydrogen maser has been optimized for high-power operation using these new storage bulbs, and a power output level of –80 dBmW has been achieved.

ESPOSITO, P. B.

E05 Determination of Astrodynamic Constants and a Test of the General Relativistic Time Delay With S-Band Range and Doppler Data From Mariners 6 and 7

J. D. Anderson, P. B. Esposito, W. Martin, and D. O. Muhleman (California Institute of Technology)

Space Research XI, pp. 105–112, Akademie-Verlag, Berlin, 1971

For abstract, see Anderson, J. D.

FANALE, F. P.

F01 Physical Adsorption of Rare Gas on Terrigenous Sediments

F. P. Fanale and W. A. Cannon

Earth Planet. Sci. Lett., Vol. 11, No. 5, pp. 362–368, August 1971

A physical-chemical explanation is offered for the paucity of Xe in the Earth's atmosphere and for the recently reported enrichments of heavy rare gases in shales. Brunauer-Emmett-Teller (BET) plots for N_2 adsorption at –195°C and Freundlich plots for Kr and Xe adsorption at 25 and 0°C were determined for shale samples. The results, together with geological considerations, suggest that Xe has been significantly depleted from the Earth's atmosphere, relative to other rare gases, by physical adsorption on terrigenous sediments.

F02 History of Martian Volatiles: Implications for Organic Synthesis

F. P. Fanale

Icarus, Vol. 15, No. 2, pp. 279–303, October 1971

As described in this article, a theoretical reconstruction of the history of Martian volatiles indicates that Mars probably possessed a substantial reducing atmosphere at the outset of its history and that its present tenuous and more oxidized atmosphere is the result of extensive chemical evolution. As a consequence, it is probable that Martian atmospheric chemical conditions, now hostile with respect to abiotic organic synthesis in the gas phase, were initially favorable. Evidence indicating the chronology and degradational history of Martian surface features, surface mineralogy, bulk volatile content, internal mass distribution, and thermal history suggests that Mars catastrophically developed a substantial reducing atmosphere as the result of rapid accretion. This atmosphere probably persisted—despite the direct and indirect effects of hydrogen escape—for a geologically short time interval during, and immediately following, Martian accretion. That was the *only* portion of Martian history when the atmospheric environment could have been chemically suited for organic synthesis in the gas phase. Subsequent gradual degassing of the Martian interior throughout Martian history could not sustain a reducing atmosphere due to the low intensity of planet-wide orogenic activity and the short atmospheric mean residence time of hydrogen on Mars. During the post-accretion history of Mars, the combined effects of planetary hydrogen escape, solar-wind sweeping, and reincorporation of volatiles into the Martian surface produced and maintained the present atmosphere.

F03 Objectives and Requirements of Unmanned Rover Exploration of the Moon

D. B. Nash, J. E. Conel, and F. P. Fanale

The Moon, Vol. 3, No. 2, pp. 221-230, August 1971

For abstract, see Nash, D. B.

FARMER, C. B.

F04 Global Studies of Atmospheric Pollutants and Trace Constituents

R. A. Toth (California Institute of Technology) and
C. B. Farmer (California Institute of Technology)

AIAA Preprint 71-1109, ACS (American Chemical Society)/ AIAA (American Institute of Aeronautics and Astronautics)/ EPA (Environmental Protection Agency)/IEEE (Institute of Electrical and Electronic Engineers)/ISA (Instrument Society of America)/NASA (National Aeronautics and Space Administration)/NOAA (National Oceanographic and Atmospheric Administration) Joint Conference on Sensing of Environmental Pollutants, Palo Alto, California, November 8–10, 1971

For abstract, see Toth, R. A.

F05 The Infrared Investigations on the Outer Planets Grand Tour

C. B. Farmer

Advan. Astronaut. Sci., Vol. 29, No. I, pp. 589–599, 1971

The infrared experiments being planned for the outer-planet Grand Tour include fundamental investigations in planetary radiation balance, atmospheric composition, structures and dynamics, and compositional and physical properties of the satellites. The multiple-planet missions to the outer solar system provide significant advantages to infrared experiments in terms of spatial resolution and planetary phase angle coverage over the limitations to Earth-based observations. The experiment and instrument design are based on the requirements of those investigations which can best exploit these advantages in a multiple-planet opportunity, as opposed to single-planet missions. The infrared instrument is a combined multi-channel radiometer and low-resolution spectrometer, covering the range from visible wavelengths out to 100 μ.

F06 The Strengths of H_2O Lines in the 8200 Å Region and Their Application to High Dispersion Spectra of Mars

C. B. Farmer

Icarus, Vol. 15, No. 2, pp. 190–196, October 1971

The improvement in the quality of spectroscopic plates taken in recent years in the search for water vapor in the atmosphere of Mars has dictated the need for improved laboratory data with which to interpret the spectra. This article presents the results of measurements of the strengths of 41 lines of the 8200-Å (211) water vapor band. The measured values show evidence of vibration–rotation interactions on the line intensities beyond the principal stretching effect. The value of the vibrational band strength derived from the results is $9.46 \pm 0.5 \times 10^{-22}$ cm^{-1}-mol^{-1}-cm^2.

FAVERO, M. S.

F07 Microbiological Sampling of Returned Surveyor III Electrical Cabling

M. D. Knittel, R. H. Green, and M. S. Favero (U.S. Public Health Department)

Proceedings of the Second Lunar Science Conference, Houston, Texas, January 11–14, 1971, Vol. 3, pp. 2715–2719, The M.I.T. Press, 1971

For abstract, see Knittel, M. D.

FINNEGAN, E. J.

F08 DSN Progress Report for November–December 1971: A New Crowbar Logic Unit

E. J. Finnegan

Technical Report 32-1526, Vol. VII, pp. 136–138, February 15, 1972

A new crowbar logic unit has been designed and installed for the Mars Deep Space Station 400-kW transmitter utilizing integrated circuits and plug-in modular construction. The logic unit of the crowbar consists of four detecting channels that generate and shape a new pulse which is used to trigger the crowbar. The crowbar is a device that short-circuits the power supply when a high-voltage arc threatens to destroy the output klystron.

FINNIE, C.

F09 DSN Progress Report for November–December 1971: High Output Power for Hydrogen Maser Frequency Standards

H. Erpenbach and C. Finnie

Technical Report 32-1526, Vol. VII, pp. 106–108, February 15, 1972

For abstract, see Erpenbach, H.

FJELDBO, G.

F10 Summary of Mariner 6 and 7 Radio Occultation Results on the Atmosphere of Mars

A. J. Kliore, G. Fjeldbo, and B. L. Seidel

Space Research XI, pp. 165–175, Akademie-Verlag, Berlin, 1971

For abstract, see Kliore, A. J.

FRAZER, R.

F11 Fixation of Virgin Lunar Surface Soil

J. M. Conley, R. Frazer, and W. A. Cannon

Technical Memorandum 33-521, February 1, 1972

For abstract, see Conley, J. M.

FYMAT, A. L.

F12 Jones's Matrix Representation of Optical Instruments: 2. Fourier Interferometers (Spectrometers and Spectropolarimeters)

A. L. Fymat

Appl. Opt., Vol. 10, No. 12, pp. 2711–2716, December 1971

The author's method of matrix synthesis of optical components and instruments is applied to the derivation of Jones's matrices appropriate for Fourier interferometers (spectrometers and spectropolarimeters). These matrices are obtained for both the source beam and the detector beam. In the course of synthesis, Jones's matrices of the various reflectors (plane mirrors; retroreflectors: roofed mirror, trihedral and prism cube corner, cat's eye) used by these interferometers are also obtained.

GALE, G.

G01 DSN Progress Report for November–December 1971: Overseas 64-m Hydrostatic Bearing Performance

G. Gale

Technical Report 32-1526, Vol. VII, pp. 154–158, February 15, 1972

The first azimuth rotation of the 64-m antenna under construction at the Ballima Deep Space Station (Australia) was made June 12, 1971. Film height records, profile records, and a bull gear reference level survey were made during this and subsequent rotations. This article includes the summary of data collected during these rotations.

GALLILY, I.

G02 On the Orientation of Nonspherical Particles at Solid Surfaces: A Method of Analysis

I. Gallily

J. Colloid Interface Sci., Vol. 37, No. 2, pp. 403–409, October 1971

The relation between the projected and true linear measures of nonspherical particles at solid surfaces is discussed in terms of an orientation distribution function. It is shown that this function can be determined by a geometric method, which is tested on spheroidal bacterial spores.

GILLEY, G. C.

G03 The STAR (Self-Testing and Repairing) Computer: An Investigation of the Theory and Practice of Fault-Tolerant Computer Design

A. Avižienis, G. C. Gilley, F. P. Mathur, D. A. Rennels, J. A. Rohr, and D. K. Rubin

IEEE Trans. Computers, Vol. C-20, No. 11, pp. 1312–1321, November 1971

For abstract, see Avižienis, A.

GOETZ, A. F. H.

G04 Apollo 12 Multispectral Photography Experiment

A. F. H. Goetz, F. C. Billingsley, J. W. Head (Bellcomm, Inc.), T. B. McCord (Massachusetts Institute of Technology), and E. Yost (Long Island University)

Proceedings of the Second Lunar Science Conference, Houston, Texas, January 11–14, 1971, Vol. 3, pp. 2301–2310, The M.I.T. Press, 1971

Apollo 12 carried a four-band camera system for orbital lunar surface photography. New image processing techniques were developed to delineate accurately subtle spectral reflectivity differences, independent of brightness differences within selected areas of the lunar surface. Ground-based photoelectric photometry was used to verify large area color differences.

In general, the highlands areas covered are quite uniform in normalized spectral reflectivity on a 200-m scale. Differences were detected in the Descartes region, which can be attributed to

exposed rock in the ejecta blanket of Dollond E. No color difference was detected across the mare-highland boundary at Fra Mauro. With few exceptions, the highlands areas studied are extremely uniform and the variation in spectral reflectivity in the wavelength region covered seen in any frame is less than that found in some Apollo 12 core samples.

GOLDSTEIN, R. M.

G05 Mars Radar Observations, a Preliminary Report

G. S. Downs, R. M. Goldstein, R. R. Green, and G. A. Morris

Science, Vol. 174, No. 4016, pp. 1324–1327, December 24, 1971

For abstract, see Downs, G. S.

GOODWIN, P. S.

G06 DSN Progress Report for November–December 1971: Helios Mission Support

P. S. Goodwin

Technical Report 32-1526, Vol. VII, pp. 17–24, February 15, 1972

Project Helios is a joint Deep Space Project between the Federal Republic of West Germany and the United States. Two solar orbiting spacecraft are planned: the first to be launched in mid-1974 and the second in late 1975. The spacecraft will have a perihelion of approximately 0.25 AU and an aphelion of 1.0 AU. These highly elliptical orbits will come closer to the Sun than any known or presently planned deep space venture to date. Prior volumes of this report have provided the reader with an overview of the division of responsibilities between West Germany and the United States, the Project management organization, and the spacecraft design—including a functional description of its radio system and the latter's interface with the Deep Space Network. This article highlights the supporting activities of the TDS organization during the Fifth Helios Joint Working Group meeting, which was held October 20–27, 1971 at Oberpfaffenhofen, West Germany.

GOTTLIEB, P.

G07 **A Surface-Layer Representation of the Lunar Gravitational Field**

L. Wong (Aerospace Corporation), G. Buechler (Aerospace Corporation), W. Downs (Aerospace Corporation), W. L. Sjogren, P. M. Muller, and P. Gottlieb

J. Geophys. Res., Vol. 76, No. 26, pp. 6220–6236, September 10, 1971

For abstract, see Wong, L.

GREEN, R. H.

G08 **Microbiological Sampling of Returned Surveyor III Electrical Cabling**

M. D. Knittel, R. H. Green, and M. S. Favero (U.S. Public Health Department)

Proceedings of the Second Lunar Science Conference, Houston, Texas, January 11–14, 1971, Vol. 3, pp. 2715–2719, The M.I.T. Press, 1971

For abstract, see Knittel, M. D.

GREEN, R. R.

G09 **Mars Radar Observations, a Preliminary Report**

G. S. Downs, R. M. Goldstein, R. R. Green, and G. A. Morris

Science, Vol. 174, No. 4016, pp. 1324–1327, December 24, 1971

For abstract, see Downs, G. S.

GUELACHVILI, G.

G10 **Fourier Spectroscopy With a One-Million-Point Transformation (Translation From the Original Published in the Nouvelle Revue d'Optique Appliquée, Vol. 1, pp. 3–22, 1970)**

J. Connes (National Center for Scientific Research, Orsay, France), H. Delouis (National Center for Scientific Research, Orsay, France), P. Connes (National Center for Scientific Research, Orsay, France), G. Guelachvili (National Center for Scientific Research, Orsay, France), J.-P. Maillard (National Center for Scientific Research, Orsay,

France), and G. Michel (National Center for Scientific Research, Orsay, France)

Technical Memorandum 33-525, March 15, 1972

For abstract, see Connes, J.

GULKIS, S.

G11 Radio Emission From the Major Planets—The Thermal Component

S. Gulkis

Advan. Astronaut. Sci., Vol. 29, No. I, pp. 203–222, 1971

Measurements of the radio emission from all the major planets have been reported at millimeter and centimeter wavelengths, and from Jupiter and Saturn at decimeter wavelengths as well. This achievement has become possible with the development of low-noise receivers and large aperture radiotelescopes. The measured brightness temperatures deduced from these measurements exceed the expected effective temperatures calculated from solar heating, and the observed spectra of the individual planets do not follow the classical blackbody spectral form. Nevertheless, the observed radiation is believed to be of thermal origin, except for the planet Jupiter, where a non-thermal component is known to contribute to its spectrum. The observed spectra are believed to depart from the simple blackbody form because of the dependence of the atmospheric emissivity on wavelength. The gross features of the major planet radio spectra can be explained in terms of thermal emission by an atmosphere whose temperature increases with depth and in which ammonia is assumed to be the principal source of opacity.

HAMILTON, G.

H01 DSN Progress Report for November–December 1971: Post-Detection Subcarrier Recording Equipment Implementation for Analog Recording Playback

G. Hamilton

Technical Report 32-1526, Vol. VII, pp. 182–184, February 15, 1972

The post-detection subcarrier recording reproduce capability has been implemented at the playback facility for playback of analog tapes recorded at stations in the Deep Space Instrumentation Facility. The primary purpose for this facility is to reproduce the analog tape data (which could not be played back at the stations) if a failure in the station subcarrier demodulator assembly or on the

spacecraft occurs. The analog data is used to produce digital data tapes and to generate data for input to the Space Flight Operations Facility. Reproduce modes of baseband playback and telemetry data bit stream playback are discussed.

HANSON, R. J.

H02 A Computational Algorithm for Sequential Estimation

R. J. Hanson and P. Dyer (Imperial Chemical Industries Ltd.)

Comput. J., Vol. 14, No. 3, pp. 285–290, August 1971

This article details a highly reliable computational algorithm for sequential least-squares estimation (filtering) with process noise. The various modular components of the algorithm are described in detail so that their conversion to computer code is straightforward. These components can also be used to solve any least-squares problem with possibly rank-deficient coefficient matrices.

HEAD, J. W.

H03 Apollo 12 Multispectral Photography Experiment

A. F. H. Goetz, F. C. Billingsley, J. W. Head (Bellcomm, Inc.), T. B. McCord (Massachusetts Institute of Technology), and E. Yost (Long Island University)

Proceedings of the Second Lunar Science Conference, Houston, Texas, January 11–14, 1971, Vol. 3, pp. 2301–2310, The M.I.T. Press, 1971

For abstract, see Goetz, A. F. H.

HOEHN, F. W.

H04 Liquid-Phase Mixing of Bipropellant Doublets

F. W. Hoehn, J. H. Rupe, and J. G. Sotter

Technical Report 32-1546, February 15, 1972

Comparisons of cold-flow mixing efficiency for sprays formed by unlike impinging doublet injector elements comprising circular and noncircular orifices have recently been reported by other investigators. It was concluded that noncircular elements produce significantly better mixing efficiencies than a circular unlike doublet at equivalent design conditions. The fact that the mixing efficiency for the circular-orifice unlike doublet was significantly lower than typical values for a number of other circular-orifice

doublets suggested that factors other than orifice shape might have been present in the comparisons.

Experimental results of unlike doublet mixing obtained at JPL are correlated with an analytically derived equation predicting fluid cavitation. The correlation relates the minimum orifice pressure drop required to initiate cavitation to the system back pressure, cold-flow simulant vapor pressure, and orifice flow discharge and contraction coefficients. Stream flow instabilities are also visually correlated with cavitation and orifice discharge coefficient measurements.

In addition, the influence of cavitation on the characteristic phenomenon of hydraulic flip is observed for both circular and noncircular orifices. For particular orifice lengths, some noncircular shapes are shown to produce more fully developed flows (shorter recovery lengths) and therefore provide slightly higher cold-flow mixing uniformities than circular orifices of equal length. The particular noncircular elements evaluated, however, are shown to be more sensitive to liquid-stream misimpingement than the corresponding circular orifices.

HOFFMAN, J. K.

H05 A Study of the Frictional and Stick–Slip Behavior of Magnetic Recording Tapes

S. H. Kalfayan, R. H. Silver, and J. K. Hoffman

Technical Report 32-1548, April 1, 1972

For abstract, see Kalfayan, S. H.

H06 Magnetic Tape Recorder for Long Operating Life in Space

E. J. Bahm and J. K. Hoffman

IEEE Trans. Magnetics, Vol. MAG-7, No. 3, pp. 517–520, September 1971

For abstract, see Bahm, E. J.

HOLDRIDGE, D. B.

H07 Simultaneous Solution for the Masses of the Principal Planets From Analysis of Optical, Radar, and Radio Tracking Data

J. H. Lieske, W. G. Melbourne, D. A. O'Handley, D. B. Holdridge, D. E. Johnson, and W. S. Sinclair

Celest. Mech., Vol. 4, No. 2, pp. 233–245, October 1971

For abstract, see Lieske, J. H.

HUGHES, R. S.

H08 Spacecraft S-Band 10–100 W rf Amplifier Tubes

R. S. Hughes

Progr. Astronaut. Aeronaut., Vol. 25, pp. 19–41, 1971

The results of electrical, environmental, and life tests on several S-band power amplifier tubes operated under saturated conditions are presented. These amplifiers operate in the 2.3-GHz region and are intended for spacecraft applications. The amplifiers tested include the amplitron, Raytheon Model QKS 1300; several traveling wave tubes, Hughes Aircraft Co. Models 216H and 242H; Watkins–Johnson Models 274-1, 274-6, and 395-3; and an electrostatically focused amplifier, Eimac Model X-3064. Overall efficiencies of 25 to 50% are exhibited; the Watkins–Johnson 395-3 and Eimac X-3064 100-W tubes exhibit overall efficiencies of 47 and 39%, respectively. The Eimac X-3064 tube employs a unique radiation-cooled collector which radiates heat through a sapphire window. Three 25-W amplitrons tested exhibited an average life of about 2350 h. Life tests on several 10- to 20-W traveling wave tubes have shown these tubes to have excellent life characteristics, which at present range up to 40,000 h.

HUNT, G. E.

H09 Laboratory Simulation of Absorption Spectra in Cloudy Atmospheres

D. J. McCleese, J. S. Margolis, and G. E. Hunt

Nature Phys. Sci., Vol. 233, No. 40, pp. 102–103, October 4, 1971

For abstract, see McCleese, D. J.

HUNTRESS, W. T., JR.

H10 Dependence of the Rates on Ion Kinetic Energy for the Reactions $D_2^+ + D_2$ and $HD^+ + HD$

W. T. Huntress, Jr., D. D. Elleman, and
M. T. Bowers (University of California, Santa Barbara)

J. Chem. Phys., Vol. 55, No. 11, pp. 5413–5414, December 1, 1971

The kinetic energy dependence of the reactions of H_2^+, D_2^+, and HD^+ ions with most of the isotopic variants of the hydrogen molecule has been studied, and several interesting dynamic features have been noted. There still remains some disagreement, however, on the kinetic energy dependence of the rates for some of the isotopic reactions. It is the purpose of this article to report some preliminary work which helps to alleviate some of this controversy.

HUTCHISON, R. B.

H11 Automated Analysis of Astronomical Spectra

R. B. Hutchison

Astron. J., Vol. 76, No. 8, pp. 711–718, October 1971

A description is given of a computer program that automates the analysis of high-resolution, infrared astronomical spectra. Procedures for the detection of spectral features and for the determination of accurate line frequencies, line depths, and equivalent widths are presented. Line profile analysis, identification, and other specialized operations are discussed.

H12 Turbulence Velocities in the Atmosphere of Alpha Orionis

R. B. Hutchison

Astrophys. J., Vol. 170, No. 3, Pt. 1, pp. 551–555, December 15, 1971

The curve of line-width correlation has been applied to OH lines in the spectrum of α Orionis, characteristic microturbulence, macroturbulence, and thermal velocities in the atmosphere of this star have been determined to be 9.9 ± 2.0, $\lesssim 3$, and $\cong 1.8$ km/s, respectively. Implications of these results are discussed in this article.

INGHAM, J. D.

I01 New Polymer Systems: Chain Extension By Dianhydrides

R. A. Rhein and J. D. Ingham

JPL Quarterly Technical Review, Vol. 1, No. 4, pp. 97–103, January 1972

For abstract, see Rhein, R. A.

JACKSON, E. B.

J01 DSN Progress Report for November–December 1971: DSN Research and Technology Support

E. B. Jackson

Technical Report 32-1526, Vol. VII, pp. 124–125, February 15, 1972

The major current activities of the Development Support Group at both the Venus Deep Space Station and the Microwave Test Facility are presented, and accomplishments and progress are described. Activities include pulsar measurements, tri-cone implementation, precision antenna gain measurement (26-m antenna), weak source observations, Faraday rotation measurements on Applications Technology Satellite 1 (ATS-1), clock synchronization transmissions, and Block IV receiver/exciter testing and demonstration.

JAFFE, L. D.

J02 Results of Recent Manned and Unmanned Lunar Exploration

L. D. Jaffe

Space Research XI, pp. 31–49, Akademie-Verlag, Berlin, 1971

Important data about the Moon obtained from spacecraft during the past year include the age-dating and chemical analyses of samples returned by Apollos 11 and 12. The material of the surface fragmental layer was differentiated 4.6×10^9 yr ago. The surfaces of Mare Tranquillitatis and Oceanus Procellarum solidified 3.7×10^9 and about 3×10^9 yr ago from lava of very low viscosity which had undergone extensive chemical fractionation. The lunar interior is of different composition from these surfaces. The Moon is tectonically rather quiet. The rate impact of moderate-sized objects was much greater before the mare formation than since. Micrometeorite impact has produced rock erosion, pitting, shock, melting, vitrification, and induration in the surface layer. Pictures, taken by Apollo astronauts, of the lunar surface disturbed by Surveyor 3 show that little change has occurred in 31 mo.

J03 Bearing Strength of Lunar Soil

L. D. Jaffe

The Moon, Vol. 3, No. 3, pp. 337–345, December 1971

Bearing load versus penetration curves have been obtained using a 1.3-g sample of lunar soil from the scoop of the Surveyor 3 soil

mechanics surface sampler and a circular indentor 2 mm in diameter. Measurements were made in an Earth laboratory, in air. This sample provided a unique opportunity to evaluate earlier, remotely controlled, in-situ measurements of lunar surface bearing properties. Bearing capacity, measured at a penetration equal to the indentor diameter, varied from 0.02–0.04 N-cm^{-2} at bulk densities of 1.15 g-cm^{-3} to 30–100 N-cm^{-2} at 1.9 g-cm^{-3}. Deformation was by compression directly below the indentor at bulk densities below 1.61 g-cm^{-3}, by outward displacement at bulk densities over 1.62 g-cm^{-3}. Preliminary comparison of in-situ remote measurements with those on returned material indicates good agreement if the lunar regolith at Surveyor 3 has a bulk density of 1.6 g-cm^{-3} at a depth of 2.5 cm. Definitive comparison awaits both better data on bulk density of the undisturbed lunar soil and additional mechanical-property measurements on returned material.

JET PROPULSION LABORATORY: MARINER MARS 1971 SCIENCE EXPERIMENTER TEAMS

J04 Mariner Mars 1971 Project Final Report: Preliminary Science Results

Mariner Mars 1971 Science Experimenter Teams

Technical Report 32-1550, Vol. II, February 1, 1972

This volume is the second of four volumes comprising the Mariner Mars 1971 Project Final Report. Presented in this volume are the preliminary science results for the Mariner 9 television, infrared spectroscopy, infrared radiometry, ultraviolet spectrometer, S-band occultation, and celestial mechanics experiments. These results, derived from data evaluation to December 14, 1971 (30 days after orbit insertion), have also been published in *Science*, Vol. 175, January 1972.

Volume I of this series describes project development through launch and the trajectory-correction maneuver; Volume III describes flight operations after the trajectory-correction maneuver and during the basic 90-day orbital mission; and Volume IV describes the science results derived from the basic 90-day orbital mission and the experimenters' interpretations of the data.

JOHNSON, D. E.

J05 Simultaneous Solution for the Masses of the Principal Planets From Analysis of Optical, Radar, and Radio Tracking Data

J. H. Lieske, W. G. Melbourne, D. A. O'Handley, D. B. Holdridge, D. E. Johnson, and W. S. Sinclair

Celest. Mech., Vol. 4, No. 2, pp. 233–245, October 1971

For abstract, see Lieske, J. H.

JOHNSTON, A. R.

J06 Stark-Effect Modulation of a CO_2 Laser by NH_2D

A. R. Johnston and R. D. S. Melville, Jr.

Appl. Phys. Lett., Vol. 19, No. 12, pp. 503–506, December 15, 1971

The molecular Stark effect in NH_2D was used to modulate the 10.6-μ $P(20)$ line of a CO_2 laser, yielding a modulation depth of 40% from a 200-V-cm^{-1} rms signal applied to a 19.7-cm gas cell external to the laser. NH_2D was prepared by mixing ND_3 and NH_3. The absorption coefficient of the $M = 4$ Stark-split line was measured as a function of mixing ratio and pressure. The observed pressure-broadening coefficient was 32.5 MHz/torr.

KALFAYAN, S. H.

K01 A Study of the Frictional and Stick-Slip Behavior of Magnetic Recording Tapes

S. H. Kalfayan, R. H. Silver, and J. K. Hoffman

Technical Report 32-1548, April 1, 1972

Methods were developed to determine the coefficient of friction and the extent of stick-slip of magnetic recording tapes. After a preliminary phase during which experimental procedures were established and screening of candidate tapes was carried out, the frictional and stick-slip behavior of four selected tapes, using four different kinds of magnetic heads, was studied at various temperatures, under dry and humid conditions, and in various gaseous atmospheres such as argon, helium, nitrogen, and air. The effects of tape speed and outgassing on the drag properties of the tapes were also studied.

A rank was assigned to each tape and magnetic head as a result of these tests. This study helped in the selection of a magnetic tape for a flight project and will be useful in the consideration of tapes and magnetic heads for future spacecraft applications.

KELLY, A. M.

K02 Isolation and Characterization of Keto-Carotenoids From the Neutral Extract of Algal Mat Communities of a Desert Soil

A. J. Bauman, H. G. Boettger, A. M. Kelly, R. E. Cameron, and H. Yokoyama (U.S. Department of Agriculture)

Eur. J. Biochem., Vol. 22, No. 2, pp. 287–293, September 1971

For abstract, see Bauman, A. J.

KIEFFER, H.

K03 Mariner 1969 Infrared Radiometer Results: Temperatures and Thermal Properties of the Martian Surface

G. Neugebauer (California Institute of Technology), G. Münch (California Institute of Technology), H. Kieffer (University of California, Los Angeles), S. C. Chase, Jr. (Santa Barbara Research Center), and E. Miner

Astron. J., Vol. 76, No. 8, pp. 719–749, October 1971

For abstract, see Neugebauer, G.

KLASCIUS, A. F.

K04 Microwave Radiation Protective Suit

A. F. Klascius

Am. Ind. Hygiene Assoc. J., Vol. 32, No. 11, pp. 771–774, November 1971

The use of a Navy-developed microwave radiation protective suit in a JPL project is described. The composition of the suit material is analyzed, and the amount of radiation absorbed by the various parts of the suit is measured. The effects of microwave radiation on the human body are considered, and the degree of protection provided by the suit during actual entry into a microwave field is evaluated.

KLIMASAUSKAS, C. C.

K05 DSN Progress Report for November–December 1971: The X930 Program Set for Sigma 5 Assembly

C. C. Klimasauskas

Technical Report 32-1526, Vol. VII, pp. 86–90, February 15, 1972

This article describes a set of programs that have been written to enable the Sigma 5 computer to assemble programs for the XDS 920/930 computers. It consists of two parts: a system procedure deck which allows SIGMA METASYMBOL to assemble a source language similar to the XDS 900-series METASYMBOL, and a secondary loader which reformats the Sigma 5 load module into the Universal Binary Language of the 900-series machines and writes it to cards or magnetic tape. The syntactic differences between this assembler and the 900-series METASYMBOL are described, as well as the process of generating a 920 program using this program set and the Sigma 5.

KLIORE, A. J.

K06 Summary of Mariner 6 and 7 Radio Occultation Results on the Atmosphere of Mars

A. J. Kliore, G. Fjeldbo, and B. L. Seidel

Space Research XI, pp. 165–175, Akademie-Verlag, Berlin, 1971

During the close flyby of Mars by Mariners 6 and 7 in the summer of 1969, their S-band radio beams were used to probe the atmosphere of Mars at four locations. These measurements indicate surface pressures ranging from a high of 7.3 mb in the Amazonis/Arcadia area to a low of 4.2 mb near the southern end of Hellespontus, indicating a range of local elevation differences of about 6 km. The surface temperatures range from about 250°K, measured near the equator in the afternoon, to about 173°K, in the north polar region at night. The temperature profiles suggest that condensation of CO_2 is probable at an altitude of about 15 km near the north pole and at altitudes ranging from 27 to 38 km in equatorial and temperate latitudes. The daytime measurements also show the existence of an ionosphere with a primary layer of about 1.7×10^5 el cm^{-3} at an altitude of about 135 km. The topside scale height indicates a plasma temperature of about 400–500°K if CO_2^+ is assumed to be the dominant ion.

KNITTEL, M. D.

K07 Microbiological Sampling of Returned Surveyor III Electrical Cabling

M. D. Knittel, R. H. Green, and M. S. Favero (U.S. Public Health Department)

Proceedings of the Second Lunar Science Conference, Houston, Texas, January 11–14, 1971, Vol. 3, pp. 2715–2719, The M.I.T. Press, 1971

A piece of electrical cabling was retrieved from the Surveyor 3 spacecraft by the crew of Apollo 12 and subjected to microbiological analysis for surviving terrestrial microorganisms. The experiment was done in a sealed environmental chamber to protect against contamination. No viable microorganisms were found on the wiring bundle samples.

KNOELL, A. C.

K08 Vibration and Buckling Analysis of Composite Plates and Shells

J. A. McElman (Lowell Technological Institute) and A. C. Knoell

J. Compos. Mater., Vol. 5, pp. 529–532, October 1971

For abstract, see McElman, J. A.

KROLL, G. G.

K09 DSN Progress Report for November–December 1971: Fire Protection and Safety Activities Throughout the Deep Space Network

G. G. Kroll

Technical Report 32-1526, Vol. VII, pp. 213–216, February 15, 1972

Comprehensive fire and safety studies have been initiated to determine the effort required to protect the tracking network from loss of life, property, and operational continuity due to fire. The studies recommend the installation of water storage tanks, new water mains and fire hydrants, fire hose cabinets, automatic early fire warning devices, automatic smoke detectors, and manual alarm stations. The protection offered to the Deep Space Network with the installation of this equipment will be equal to the highly protective risk category used by private industry to describe maximum installed protection against loss of life and property. This article describes the scope of the initial surveys, the follow-on preliminary engineering reports, and the design/construction efforts.

KRUGER, G. W.

K10 Experimental Evaluation of High-Thrust, Throttleable, Monopropellant Hydrazine Reactors

R. W. Riebling and G. W. Kruger

Technical Report 32-1551, March 1, 1972

For abstract, see Riebling, R. W.

LAESER, R. P.

L01 DSN Progress Report for November–December 1971: Mariner Mars 1971 Mission Support

R. P. Laeser

Technical Report 32-1526, Vol. VII, pp. 25–28, February 15, 1972

At the start of the Mariner 9 orbit operations, some confusion existed over the varying number of bit errors observed in the picture transmissions. This article presents a summary of observations made in an attempt to clarify the situation.

LAING, P. A.

L02 Lunar Gravity Analysis From Long-Term Effects

A. S. Liu and P. A. Laing

Science, Vol. 173, No. 4001, pp. 1017–1020, September 10, 1971

For abstract, see Liu, A. S.

LAYLAND, J. W.

L03 DSN Progress Report for November–December 1971: An Introduction to Minicomputer Software Support

J. W. Layland

Technical Report 32-1526, Vol. VII, pp. 84–85, February 15, 1972

This article discusses some problems associated with generating software for a possible deep space station configuration with a multiplicity of computers, and briefly describes an effort underway to help reduce those problems. It is a general introduction to "The X930 Program Set for Sigma 5 Assembly," and "The SAPDP

Program Set for Sigma 5 Assembly," which describe specific results from the development effort.

L04 A Flexible High-Speed Sequential Decoder for Deep Space Channels

J. W. Layland and W. A. Lushbaugh

IEEE Trans. Commun. Technol., Vol. COM-19, No. 5, pp. 813–820, October 1971

This article describes a sequential decoding machine, built at JPL, which uses a 3-bit quantization of the code symbols and achieves a computation rate of MHz. This machine is flexible and can be programmed to decode any complementary convolutional code with rates down to 1/4 and constraint lengths up to 32. In addition, metric programmability is provided for optimization of decoder performance with respect to channel parameter variations.

LEIBOWITZ, L. P.

L05 Nonequilibrium Ionization Measurements in Hydrogen–Helium Mixtures

L. P. Leibowitz

JPL Quarterly Technical Review, Vol. 1, No. 4, pp. 13–18, January 1972

Time-resolved emission measurements of several atomic line and continuum radiation channels have been made behind the incident shock wave of the JPL electric arc shock tube. Test times and nonequilibrium ionization times were obtained for shock velocities up to 2.5×10^4 m/s in a 0.2 H_2–0.8 He gas mixture. The shock-heated test gas was found to be free from driver gas contamination, and the test times were adequate to achieve steady-state conditions. An activation energy of 4 eV was obtained from the nonequilibrium ionization time measurements. Modifications to experimental technique to determine the effect of test gas impurity level on ionization time measurements are discussed.

LESH, J. R.

L06 DSN Progress Report for November–December 1971: Correlated Sampling With Application to Carrier Power Estimation Accuracy

J. R. Lesh

Technical Report 32-1526, Vol. VII, pp. 195–206, February 15, 1972

In this article the total sampling time and number of samples required to produce a sample mean having a specified variance is evaluated for various sampling intervals. The samples are assumed to be the correlated outputs of either a first- or second-order system having a white gaussian noise input. It is found that a reduction in both the total time and the number of samples can often be obtained for a given variance and sampling interval if the sampling is performed at the output of a second order system. These results are then applied to the automatic gain control sampling presently being used for carrier power estimation to show how its accuracy can be improved.

LEU, R. L.

L07 DSN Progress Report for November–December 1971: 400-kW Harmonic Filter

R. L. Leu

Technical Report 32-1526, Vol. VII, pp. 131–135, February 15, 1972

The low-power test data on the new 400-kW harmonic filter design shows that the new filter meets or exceeds the performance of the existing filters. This will not insure that the fourth harmonic from the 400-kW transmitter will not affect the X-band receiver performance. Additional fourth harmonic filters may be required.

LEVY, R.

L08 DSN Progress Report for November–December 1971: Improved Condensation Methods for Eigenvalue Problems

R. Levy

Technical Report 32-1526, Vol. VII, pp. 142–153, February 15, 1972

The conventional procedure used to condense the solution of eigenvalue problems for recovery of the lowest modes is tested by application to practical example structures. Evaluations are made of eigenvalue accuracy with respect to numbers of retained solution vectors. It is shown that solutions are likely to be inaccurate except in the special case of when prior knowledge of the mode shapes is available. One improvement for recovering the lowest modes is to supplement the retained vectors with static loading displacement functions. A further remedy is to perform iterative

repetitions of the solution procedure. Great improvements in accuracy can be achieved with only a few iterative cycles. These improvements are effective in the typical case of when only a few valid lowest-mode solutions are required and the order of the problem is large so that it becomes important to minimize the computational time by means of solution condensation.

LIESKE, J. H.

L09 Simultaneous Solution for the Masses of the Principal Planets From Analysis of Optical, Radar, and Radio Tracking Data

J. H. Lieske, W. G. Melbourne, D. A. O'Handley, D. B. Holdridge, D. E. Johnson, and W. S. Sinclair

Celest. Mech., Vol. 4, No. 2, pp. 233–245, October 1971

JPL has developed a set of computer programs known as the Solar System Data Processing System (SSDPS) which is employed in improving the ephemerides of the major planets and for improving the values of several associated astronomical constants. A group of solutions for the masses of the major planets, together with the AU and radii of Mercury, Venus, and Mars, is presented. These solutions based upon optical, radar, and spacecraft radio tracking data are preliminary. The relative power of radar and radio tracking data vis-à-vis purely optical data in a solution is shown. The problems which could arise by adopting solutions based upon a single data type are demonstrated.

LINDLEY, P. L.

L10 DSN Progress Report for November–December 1971: DSIF Tracking and Monitor and Control Subsystem: Prototype Implementation

P. L. Lindley

Technical Report 32-1526, Vol. VII, pp. 159–167, February 15, 1972

A developmental model Deep Space Instrumentation Facility Tracking and Monitor and Control Subsystem has been installed and used in the support of the Mariner Mars 1971 mission. The hardware and software necessary to support doppler measurements, including the ability to record the data locally as well as send it to the Space Flight Operations Facility both in real-time and recall (replay) modes, are operating. Checkout of other functions is in process.

LINNES, K. W.

L11 DSN Progress Report for November–December 1971: Radio Science Support

K. W. Linnes

Technical Report 32-1526, Vol. VII, pp. 29–31, February 15, 1972

Since 1967, radio scientists have used the Deep Space Network 26- and 64-m antenna stations to investigate pulsars, to study the effect of solar corona on radio signals, and to observe radio emissions from X-ray sources. More recently, very long baseline interferometry (VLBI) techniques have been used for high-resolution studies of quasars. During the reporting period, VLBI observations were made in support of investigations of quasars. Support was also provided from the 64-m antenna for the mapping of nearby spiral galaxies.

LIU, A. S.

L12 Lunar Gravity Analysis From Long-Term Effects

A. S. Liu and P. A. Laing

Science, Vol. 173, No. 4001, pp. 1017–1020, September 10, 1971

As described in this article, the global lunar gravity field was determined from a weighted least-squares analysis of the averaged classical element of the five Lunar Orbiter spacecraft. The observed-minus-computed residuals have been reduced by a factor of 10 from a previously derived gravity field. The values of the second-degree zonal and sectorial harmonics are compatible with those derived from libration data.

LOVELOCK, J. E.

L13 Rare Gases of the Atmosphere: Gas Chromatography Using a Thermal Conductivity Detector and a Palladium Transmodulator

J. E. Lovelock, P. G. Simmonds, and G. R. Shoemake

Anal. Chem., Vol. 43, No. 14, pp. 1958–1961, December 1971

This article reports on the application of the palladium transmodulator combined with a small-volume thermal conductivity detector to the determination of the rare gases in air. The analysis was performed directly on a 10-ml sample of air using a single column

operated at room temperature. A gain in sensitivity of 10^3 is demonstrated. The system described was developed for planetary atmospheric analysis, but is of general use wherever gas analysis at high sensitivity is required.

LUSHBAUGH, W. A.

L14 A Flexible High-Speed Sequential Decoder for Deep Space Channels

J. W. Layland and W. A. Lushbaugh

IEEE Trans. Commun. Technol., Vol. COM-19, No. 5, pp. 813–820, October 1971

For abstract, see Layland, J. W.

LUTES, G.

L15 DSN Progress Report for November–December 1971: Hydrogen Maser: Low Phase Noise, L-Band Frequency Multiplier

G. Lutes, J. MacConnell, and R. Meyer

Technical Report 32-1526, Vol. VII, pp. 81–83, February 15, 1972

A 100- to 1400-MHz discrete component ×14 frequency multiplier was developed to determine the lowest phase noise achievable with present technology. The $1/f$ phase noise spectrum of the multiplier measured 11 dB lower than the hydrogen maser frequency standard and 13 dB better than a high-quality step recovery diode multiplier.

MacCONNELL, J.

M01 DSN Progress Report for November–December 1971: Hydrogen Maser: Low Phase Noise, L-Band Frequency Multiplier

G. Lutes, J. MacConnell, and R. Meyer

Technical Report 32-1526, Vol. VII, pp. 81–83, February 15, 1972

For abstract, see Lutes, G.

MAILLARD, J.-P.

M02 Fourier Spectroscopy With a One-Million-Point Transformation (Translation From the Original Published in the Nouvelle Revue d'Optique Appliquee, Vol. 1, pp. 3-22, 1970)

J. Connes (National Center for Scientific Research, Orsay, France), H. Delouis (National Center for Scientific Research, Orsay, France), P. Connes (National Center for Scientific Research, Orsay, France), G. Guelachvili (National Center for Scientific Research, Orsay, France), J.-P. Maillard (National Center for Scientific Research, Orsay, France), and G. Michel (National Center for Scientific Research, Orsay, France)

Technical Memorandum 33-525, March 15, 1972

For abstract, see Connes, J.

MANATT, S. L.

M03 Ferromagnetic Resonance of Lunar Samples

F. D. Tsay (California Institute of Technology), S. I. Chan (California Institute of Technology), and S. L. Manatt

Geochim. Cosmochim. Acta, Vol. 35, No. 9, pp. 865-875, September 1971

For abstract, see Tsay, F.-D.

M04 Magnetic Resonance Studies of Apollo 11 and Apollo 12 Samples

F. D. Tsay (California Institute of Technology), S. I. Chan (California Institute of Technology), and S. L. Manatt

Proceedings of the Second Lunar Science Conference, Houston, Texas, January 11-14, 1971, Vol. 3, pp. 2515-2528, The M.I.T. Press, Cambridge, 1971

For abstract, see Tsay, F.-D.

M05 Calculations of Geometries of Organic Molecules Using the CNDO/2 Method: I. Empirical Correlations Between Observed and Calculated Bond Lengths in Simple Acyclics, Strained Cycloalkenes and Some Polycyclic Molecules

C. S. Cheung, M. A. Cooper, and S. L. Manatt

Tetrahedron, Vol. 27, No. 4, pp. 689–700, February 1971

For abstract, see Cheung, C. S.

M06 Calculations of Geometries of Organic Molecules Using the CNDO/2 Molecular Orbital Method: II. Structural Predictions for the Benzocycloalkenes, and a Theoretical Rationalization of Their Proton–Proton Spin–Spin Coupling Constants

C. S. Cheung, M. A. Cooper, and S. L. Manatt

Tetrahedron, Vol. 27, No. 4, pp. 701–709, February 1971

For abstract, see Cheung, C. S.

MANCINI, R. A.

M07 DSN Progress Report for November–December 1971: Data Decoder Assembly Implementation Status

R. A. Mancini

Technical Report 32-1526, Vol. VII, pp. 168–174, February 15, 1972

Twelve data decoder assemblies have been acceptance-tested, delivered to the Deep Space Network stations, and are undergoing installation/testing and incorporation of field modifications in preparation for the Pioneer F mission. Eight additional data decoder assemblies are in different stages of testing and implementation. This article describes their present status.

MARGOLIS, J. S.

M08 High Dispersion Spectroscopic Studies of Mars: V. A Search for Oxygen in the Atmosphere of Mars

J. S. Margolis, R. A. J. Schorn, and L. D. G. Young

Icarus, Vol. 15, No. 2, pp. 197–203, October 1971

In order to set a new upper limit on the amount of oxygen in the atmosphere of Mars, a number of high-dispersion spectra of the 7620-Å band of oxygen obtained during the 1969 apparition of Mars have been reduced by the authors. The new upper limit is w = 15 cm-atm (STP) for the Martian abundance in a single vertical path. This result confirms and lowers the 1963 upper limit of w = 70 cm-atm (STP) by Kaplan, Münch, and Spinrad. The features reported by Hunten and Belton do not appear in the authors' spectra. Furthermore, by measuring the pressure shift of the A band in the laboratory, the authors found that the shift required by

Hunten's and Belton's tentative identification of oxygen in the Martian atmosphere does not exist.

M09 Laboratory Simulation of Absorption Spectra in Cloudy Atmospheres

D. J. McCleese, J. S. Margolis, and G. E. Hunt

Nature Phys. Sci., Vol. 233, No. 40, pp. 102–103, October 4, 1971

For abstract, see McCleese, D. J.

MARTIN, W.

M10 Determination of Astrodynamic Constants and a Test of the General Relativistic Time Delay With S-Band Range and Doppler Data From Mariners 6 and 7

J. D. Anderson, P. B. Esposito, W. Martin, and D. O. Muhleman (California Institute of Technology)

Space Research XI, pp. 105–112, Akademie-Verlag, Berlin, 1971

For abstract, see Anderson, J. D.

MASSIER, P. F.

M11 Partially Ionized Gas Flow and Heat Transfer in the Separation, Reattachment, and Redevelopment Regions Downstream of an Abrupt Circular Channel Expansion

L. H. Back, P. F. Massier, and E. J. Roschke

Trans. ASME, Ser. C: J. Heat Transf., Vol. 94, No. 1, pp. 119–127, February 1972

For abstract, see Back, L. H.

MATHUR, F. P.

M12 The STAR (Self-Testing and Repairing) Computer: An Investigation of the Theory and Practice of Fault-Tolerant Computer Design

A. Avižienis, G. C. Gilley, F. P. Mathur, D. A. Rennels, J. A. Rohr, and D. K. Rubin

IEEE Trans. Computers, Vol. C-20, No. 11, pp. 1312–1321, November 1971

For abstract, see Avižienis, A.

M13 On Reliability Modeling and Analysis of Ultrareliable Fault-Tolerant Digital Systems

F. P. Mathur

IEEE Trans. Computers, Vol. C-20, No. 11, pp. 1376–1382, November 1971

The processes of protective redundancy, namely, standby replacement redundancy and hybrid redundancy (a combination of standby replacement and multiple-line voting redundancy), find application in the architecture of fault-tolerant digital computers and enable them to be ultrareliable and self-repairing. The claims to ultrareliability lead to the challenge of quantitatively evaluating and assigning a value to the probability of survival as a function of the mission durations intended. This article presents various mathematical models and derives and displays quantitative evaluations of system reliability as a function of various mission parameters of interest to the system designer.

McCLEESE, D. J.

M14 Laboratory Simulation of Absorption Spectra in Cloudy Atmospheres

D. J. McCleese, J. S. Margolis, and G. E. Hunt

Nature Phys. Sci., Vol. 233, No. 40, pp. 102–103, October 4, 1971

This article describes a laboratory investigation of diffuse reflectivity from a suspension of polymer latex spheres in a medium of variable absorption. This investigation was carried out in order to simulate the formation of absorption lines in cloudy planetary atmospheres. The experimental techniques derived may be generalized to situations which are too complicated for present computational techniques (for example, atmospheres which contain nonspherical scatterers, where the distribution of scatterers is inhomogeneous, or atmospheres with a complete structure).

McCORD, T. B.

M15 Apollo 12 Multispectral Photography Experiment

A. F. H. Goetz, F. C. Billingsley, J. W. Head (Bellcomm,

Inc.), T. B. McCord (Massachusetts Institute of Technology), and E. Yost (Long Island University)

Proceedings of the Second Lunar Science Conference, Houston, Texas, January 11–14, 1971, Vol. 3, pp. 2301–2310, The M.I.T. Press, 1971

For abstract, see Goetz, A. F. H.

McELIECE, R. J.

M16 DSN Progress Report for November–December 1971: Hiding and Covering in a Compact Metric Space

R. J. McEliece and E. C. Posner

Technical Report 32-1526, Vol. VII, pp. 101–105, February 15, 1972

This article investigates the relationship between games of search on a compact metric space X and the absolute epsilon entropy $I(X)$ of X. The main result is that

$$I(X) = -\log \nu_L^*,$$

ν_L^* being the lower value of a game on X we call "restricted hide and seek."

McELMAN, J. A.

M17 Vibration and Buckling Analysis of Composite Plates and Shells

J. A. McElman (Lowell Technological Institute) and A. C. Knoell

J. Compos. Mater., Vol. 5, pp. 529–532, October 1971

In the analysis of laminated composites, it is known that a coupling exists between extension and bending if the plies are not balanced in number and fiber orientation. This effect for the bending, vibration, and buckling of two-, four-, and six-ply laminates was examined elsewhere in the literature. The purpose of this article is to investigate the magnitude of this effect for buckling and vibration of doubly curved monocoque plates and shells of positive and negative gaussian curvature. In addition, the effect of stacking sequence (the order in which individual plies are laid up) is examined. This effect is considered since it is analogous to that of eccentric stiffening of isotropic cylinders. Solutions are presented

which provide a means of simply and economically assessing the magnitude of the coupling and stacking effects for various composite materials and geometric configurations.

McKINLEY, E. L.

M18 Mariner Venus–Mercury 1973 Midcourse Velocity Requirements and Delivery Accuracy

E. L. McKinley

JPL Quarterly Technical Review, Vol. 1, No. 4, pp. 104–115, January 1972

The Mariner Venus–Mercury 1973 mission represents the first attempt to navigate a single spacecraft to more than one planet. The primary mission consists of encounters with Venus and Mercury (with a second encounter with Mercury also possible). In this study, the expected navigation sequences are simulated with a Monte Carlo computer program for the purpose of determining midcourse correction velocity requirements and delivery accuracies. These simulations provide the sensitivity of the velocity requirements and delivery accuracies to the error sources affecting the navigation process. The orbit determination capability at the final pre-Venus maneuver is shown to be the dominant contributor to the velocity requirements for the primary mission. Similarly, the orbit determination capability at the final pre-Mercury maneuver is shown to be the dominant contributor to the delivery accuracy at Mercury.

McRONALD, A. D.

M19 On the Possibility of Earth Re-entry Simulation of Shallow Angle Jupiter Entry

A. D. McRonald

JPL Quarterly Technical Review, Vol. 1, No. 4, pp. 19–29, January 1972

Possible Earth re-entry simulation of shallow angle (3- to 30-deg) Jupiter entry has been investigated in terms of four parameters of the bow shock layer ahead of a blunt vehicle: peak (equilibrium) temperature, peak pressure, peak inward radiative flux, and time-integrated radiative flux. The comparison shows that simulation ranging from fair to good can be achieved, generally the easiest (lowest Earth re-entry speed) at steep Earth re-entry, in the Earth entry speed range of 15–22 km/s for both the Jupiter "nominal" and "cool" atmospheres. Increasing Earth speed is required, generally, for increasing Jupiter entry angle, and for temperature, radia-

tive flux, time-integrated flux, and pressure, in that order. It appears that a meaningful simulation test could be done using a launch vehicle with the speed and payload capability of the Titan IIID/Centaur/BII.

MELBOURNE, W. G.

M20 Simultaneous Solution for the Masses of the Principal Planets From Analysis of Optical, Radar, and Radio Tracking Data

J. H. Lieske, W. G. Melbourne, D. A. O'Handley, D. B. Holdridge, D. E. Johnson, and W. S. Sinclair

Celest. Mech., Vol. 4, No. 2, pp. 233–245, October 1971

For abstract, see Lieske, J. H.

MELVILLE, R. D. S., JR.

M21 Stark-Effect Modulation of a CO_2 Laser by NH_2D

A. R. Johnston and R. D. S. Melville, Jr.

Appl. Phys. Lett., Vol. 19, No. 12, pp. 503–506, December 15, 1971

For abstract, see Johnston, A. R.

MENARD, W. A.

M22 A Higher Performance Electric-Arc-Driven Shock Tube

W. A. Menard

AIAA J., Vol. 9, No. 10, pp. 2096–2098, October 1971

Simulation of Jupiter and Saturn atmospheric entry has been difficult because entry velocities range from 25 to 48 km/s. Shock tube velocities have been limited to about 15 km/s. The purpose of this article is to report the development of an electric arc-driven shock tube which has increased shock velocity by a factor of three. The new driver has a conical internal design of small volume and uses lightweight diaphragms. Data obtained from a 15.2-cm-diam driven tube show little shock wave attenuation. Shock velocities of 45 km/s with test times in excess of 4 μs have been attained.

MENICHELLI, V. J.

M23 Electrothermal Follow Display Apparatus for Electroexplosive Device Testing

L. A. Rosenthal (Rutgers University) and V. J. Menichelli

Technical Report 32-1554, March 15, 1972

For abstract, see Rosenthal, L. A.

M24 Fault Determinations in Electroexplosive Devices by Nondestructive Techniques

V. J. Menichelli and L. A. Rosenthal (Rutgers University)

Technical Report 32-1553, March 15, 1972

Several nondestructive test techniques have been developed for electroexplosive devices. The bridgewire responds, when pulsed with a safe-level current, by generating a characteristic heating curve. The response is indicative of the electrothermal behavior of the bridgewire–explosive interface. Bridgewires that deviate from the characteristic heating curve have been dissected and examined to determine the cause for the abnormality. Deliberate faults have been fabricated into squibs. The relationship of the specific abnormality and the fault associated with it is demonstrated.

M25 Detonation of Insensitive High Explosives by a Q-Switched Ruby Laser

L. C. Yang and V. J. Menichelli

Appl. Phys. Lett., Vol. 19, No. 11, pp. 473–475, December 1, 1971

For abstract, see Yang, L. C.

MEYER, R.

M26 DSN Progress Report for November–December 1971: Hydrogen Maser: Low Phase Noise, L-Band Frequency Multiplier

G. Lutes, J. MacConnell, and R. Meyer

Technical Report 32-1526, Vol. VII, pp. 81–83, February 15, 1972

For abstract, see Lutes, G.

MICCIO, J. A.

M27 DSN Progress Report for November–December 1971: DSN Traceability and Reporting Program: Micrographic Application

J. A. Miccio

Technical Report 32-1526, Vol. VII, pp. 185–189, February 15, 1972

Technology has advanced the development and utilization of higher and faster data rates for deep space satellite research; machine computation and analysis have been relied upon by investigators and analysts for a greater percentage of the data reduction. The investigator, analyst, and end user, however, still face a massive volume of output data. The longevity of spacecraft systems in high data transmission modes and the "one of a kind" nature of the data being returned increase the desire for extensive data acquisition and retention of scientific and engineering information. The result of increased volumes of data being processed with corresponding increases in magnetic tape and tab paper output poses cost and storage problems for the processing facility and the data analyst. An efficient and expeditious method for data reduction, retention, and retrieval is mandatory.

Micrographic technology, i.e., microfilm processes, microforms, and retrieval systems, combined with current computing techniques, affords the data user quick-look profiles and trend information in relatively short turnaround time, as well as accessibility to larger and more detailed data bases.

MICHEL, G.

M28 Fourier Spectroscopy With a One-Million-Point Transformation (Translation From the Original Published in the Nouvelle Revue d'Optique Appliquée, Vol. 1, pp. 3–22, 1970)

J. Connes (National Center for Scientific Research, Orsay, France), H. Delouis (National Center for Scientific Research, Orsay, France), P. Connes (National Center for Scientific Research, Orsay, France), G. Guelachvili (National Center for Scientific Research, Orsay, France), J.-P. Maillard (National Center for Scientific Research, Orsay, France), and G. Michel (National Center for Scientific Research, Orsay, France)

Technical Memorandum 33-525, March 15, 1972

For abstract, see Connes, J.

MINER, E.

M29 Mariner 1969 Infrared Radiometer Results: Temperatures and Thermal Properties of the Martian Surface

G. Neugebauer (California Institute of Technology),
G. Münch (California Institute of Technology),
H. Kieffer (University of California, Los Angeles),
S. C. Chase, Jr. (Santa Barbara Research Center), and
E. Miner

Astron. J., Vol. 76, No. 8, pp. 719–749, October 1971

For abstract, see Neugebauer, G.

MOACANIN, J.

M30 Viscoelastic Behavior of Polymers Undergoing Crosslinking Reactions

J. Moacanin and J. J. Aklonis (University of Southern California)

J. Polym. Sci., Pt. C: Polym. Sym., No. 35, pp. 71–76, 1971

A method was previously developed for predicting the viscoelastic response of polymers undergoing scission reactions. In this article, these results are now extended to include crosslinking reactions. As for scission, at any given time the character of the network chains is determined by the instantaneous crosslink density. For scission, all chains were assumed to carry the same stress; for crosslinking, however, the stress is distributed between the "new" and "old" chains. Equations for calculating the creep response of a system which experiences a step increase in crosslink density are derived.

MORRIS, G. A.

M31 Mars Radar Observations, a Preliminary Report

G. S. Downs, R. M. Goldstein, R. R. Green, and
G. A. Morris

Science, Vol. 174, No. 4016, pp. 1324–1327,
December 24, 1971

For abstract, see Downs, G. S.

MOSESMAN, M. M.

M32 Photolysis of CO_2 at 1849 Å

W. B. DeMore and M. M. Mosesman

J. Atmos. Sci., Vol. 28, No. 6, pp. 842–846, September 1971

For abstract, see DeMore, W. B.

MUHLEMAN, D. O.

M33 Determination of Astrodynamic Constants and a Test of the General Relativistic Time Delay With S-Band Range and Doppler Data From Mariners 6 and 7

J. D. Anderson, P. B. Esposito, W. Martin, and D. O. Muhleman (California Institute of Technology)

Space Research XI, pp. 105–112, Akademie-Verlag, Berlin, 1971

For abstract, see Anderson, J. D.

MULHALL, B. D.

M34 DSN Progress Report for November–December 1971: Local and Transcontinental Mapping of Total Electron Content Measurements of the Earth's Ionosphere

K. W. Yip and B. D. Mulhall

Technical Report 32-1526, Vol. VII, pp. 61–67, February 15, 1972

For abstract, see Yip, K. W.

MULLER, P. M.

M35 A Surface-Layer Representation of the Lunar Gravitational Field

L. Wong (Aerospace Corporation), G. Buechler (Aerospace Corporation), W. Downs (Aerospace Corporation), W. L. Sjogren, P. M. Muller, and P. Gottlieb

J. Geophys. Res., Vol. 76, No. 26, pp. 6220–6236, September 10, 1971

For abstract, see Wong, L.

MÜNCH, G.

M36 Mariner 1969 Infrared Radiometer Results: Temperatures and Thermal Properties of the Martian Surface

G. Neugebauer (California Institute of Technology), G. Münch (California Institute of Technology),

H. Kieffer (University of California, Los Angeles), S. C. Chase, Jr. (Santa Barbara Research Center), and E. Miner

Astron. J., Vol. 76, No. 8, pp. 719–749, October 1971

For abstract, see Neugebauer, G.

NASH, D. B.

N01 Luminescence and Reflectance of Apollo 12 Samples

D. B. Nash and J. E. Conel

Proceedings of the Second Lunar Science Conference, Houston, Texas, January 11–14, 1971, Vol. 3, pp. 2235–2244, The M.I.T. Press, Cambridge, 1971

The objectives of the laboratory measurements reported in this article were to: (1) compare the luminescence and reflectance properties of Apollo 12 surface and core-sample material with those of the surface material of Apollo 11, (2) obtain a better estimate of the average luminescence characteristics of the lunar surface under solar irradiation, and (3) obtain additional spectral reflectance data on lunar samples for more accurate interpretation of telescopic observations of the lunar surface. It was found that luminescence, thermoluminescence, and spectral reflectance properties of samples from Oceanus Procellarum are qualitatively similar to those of Mare Tranquillitatis samples. Detailed differences are controlled by mineralogy; fines from Procellarum have higher plagioclase content relative to glass and opaques and higher pyroxene content relative to plagioclase than fines from Tranquillity. Luminescence properties and reflectance do not vary systematically with depth in the core. The variations observed are attributable to differences in relative abundances of mineral and glass phases and are not indicative of variations in particle size, radiation damage, or surface coatings on individual grains.

N02 Objectives and Requirements of Unmanned Rover Exploration of the Moon

D. B. Nash, J. E. Conel, and E. P. Fanale

The Moon, Vol. 3, No. 2, pp. 221–230, August 1971

The scientific value of unmanned rovers for continued lunar exploration is considered in light of Apollo findings which suggest that the Moon's surface is more heterogeneous than expected. Major questions and investigations involving composition, internal structure, and thermal history are presented that form a scientific rationale for use of unmanned rovers in the post-Apollo period of

lunar exploration. Visual, petrologic, chemical, and geophysical measurements that are essential for an unmanned rover traverse over previously unexplored lunar terrain are discussed. Unmanned rovers are well-suited for low-cost, low-risk preliminary reconnaissance where measurement of a few definitive parameters over a wide area is more important than obtaining a wide array of detailed results at a given site.

NEUGEBAUER, G.

N03 Mariner 1969 Infrared Radiometer Results: Temperatures and Thermal Properties of the Martian Surface

G. Neugebauer (California Institute of Technology),
G. Münch (California Institute of Technology),
H. Kieffer (University of California, Los Angeles),
S. C. Chase, Jr. (Santa Barbara Research Center), and
E. Miner

Astron. J., Vol. 76, No. 8, pp. 719–749, October 1971

The reduced data of the Mariner 6 and 7 infrared radiometer experiments are presented, along with a discussion of the reduction and calibration procedures. Evidence is presented showing that the surface of Mars is strongly nonhomogeneous in its thermal properties, on scales ranging from those of the classical light and dark areas to the limit of resolution of the radiometers. On the sunlit side, the mean thermal inertia, for admissible bolometric albedos, is 0.006 (cal-cm^{-2}-s$^{-1/2}$-°K^{-1}). The dark areas Syrtis Major and Mare Tyrrhenum, observed at night, require thermal inertias as high as 0.010. The temperatures measured over the circular basin Hellas require a bolometric albedo of 0.40 and also a high thermal inertia. The temperature measured over the south polar cap, 148°K, provides evidence that the major constituent of the frost deposit is CO_2.

NICKLE, N. L.

N04 Surveyer III Material Analysis Program

N. L. Nickle

Proceedings of the Second Lunar Science Conference, Houston, Texas, January 11–14, 1971, Vol. 3, pp. 2683–2697, The M.I.T. Press, Cambridge, 1971

The Surveyor 3 components returned from the Moon by the Apollo 12 astronauts were released for scientific investigation by NASA on June 18, 1970. This article provides background information on return of the Surveyor 3 material and subsequent plans for

analysis of the returned parts. Also discussed are the environmental conditions to which the returned material was subjected, exposure of the spacecraft and the returned parts to solar radiation, orientation of the spacecraft, results of investigations, and future plans for the remaining parts.

NOON, E. L.

N05 Nuclear Radiation Sources On-Board Outerplanet Spacecraft

E. L. Noon, G. H. Anno, and M. A. Dore

IEEE Trans. Nucl. Sci., Vol. NS-18, No. 5, pp. 50–57, October 1971

Radioisotope thermoelectric generators (RTGs) and radiation heater units (RHUs) are presently being used or considered for sources of electrical power and heat for the Apollo, Pioneer, and Viking Projects. Both RTGs and RHUs have considerable merit if proper precautions are taken to compensate for overall system response to the nuclear radiation sources.

This article summarizes the nuclear characteristics of plutonium fuel, which gives rise to the radiation from both RTGs and RHUs; gives Monte Carlo estimates of the neutron and gamma isodose profiles from a 2200-W(th) HELIPAK (General Electric Co. conceptual-model tradename) thermoelectric generator; and concludes with a presentation summary of shield thicknesses required for several sensitive radiation experiments due to combined RTG–RHU fields. This study is a part of a continuing program of analysis at JPL on the evaluation of RTG radiation fields on an outerplanet spacecraft.

NORTON, R. H.

N06 Astronomical Infrared Spectroscopy With a Connes-Type Interferometer: I. Instrumental

R. Beer, R. H. Norton, and C. H. Seaman

Rev. Sci. Instr., Vol. 42, No. 10, pp. 1393–1403, October 1971

For abstract, see Beer, R.

O'HANDLEY, D. A.

001 Simultaneous Solution for the Masses of the Principal Planets From Analysis of Optical, Radar, and Radio Tracking Data

J. H. Lieske, W. G. Melbourne, D. A. O'Handley, D. B. Holdridge, D. E. Johnson, and W. S. Sinclair

Celest. Mech., Vol. 4, No. 2, pp. 233–245, October 1971

For abstract, see Lieske, J. H.

OHTAKAY, H.

002 In-Flight Calibration of an Interplanetary Navigation Instrument

T. C. Duxbury and H. Ohtakay

J. Spacecraft Rockets, Vol. 8, No. 10, pp. 1038–1042, October 1971

For abstract, see Duxbury, T. C.

ONDRASIK, V. J.

003 DSN Progress Report for November–December 1971: Improved Navigation Capability Utilizing Two-Station Tracking Techniques for a Low-Declination Distant Spacecraft

K. H. Rourke and V. J. Ondrasik

Technical Report 32-1526, Vol. VII, pp. 51–60, February 15, 1972

For abstract, see Rourke, K. H.

004 Application of New Radio Tracking Data Types to Critical Spacecraft Navigation Problems

V. J. Ondrasik and K. H. Rourke

JPL Quarterly Technical Review, Vol. 1, No. 4, pp. 116–132, January 1972

This article is concerned with newly envisioned Earth-based radio tracking data types involving simultaneous or near-simultaneous spacecraft tracking from widely separated tracking stations. These data types are conventional tracking instrumentation analogs of the very-long-baseline interferometry (VLBI) of radio astronomy—hence, the name quasi-VLBI. Quasi-VLBI promises to help alleviate two particularly troublesome problems encountered in interplanetary orbit determination: the zero declination and process

noise problems. This article motivates quasi-VLBI with a preliminary analysis using simplified tracking data models. The results of accuracy analysis studies are then presented for a representative mission, Viking 1975. The results indicate that, contingent on projected, not overly optimistic future tracking system accuracy, quasi-VLBI can be expected to significantly improve navigation performance over that expected of conventional tracking data types.

OTOSHI, T. Y.

O05 A Precision Compact Rotary Vane Attenuator

T. Y. Otoshi and C. T. Stelzried

IEEE Trans. Microwave Theor. Techniq., Vol. MTT-19, No. 11, pp. 843–854, November 1971

The accurate attenuation range of many precision rotary vane attenuators is limited to about 40 dB because of a transmission error term not accounted for in the familiar $\cos^2$ attenuation law. This article presents a modified law that makes it possible to extend the useful dynamic attenuation range. The same modified law also makes it practical to reduce the length of the rotor section and, therefore, to develop compact rotary vane attenuators that are accurate over reduced dynamic attenuation ranges. The modified law requires the additional calibrations of the incremental attenuation and incremental phase change at the 90-deg vane angle setting.

To verify the modified law, a precision compact WR 112 rotary vane attenuator was fabricated and tested. The attenuator has a total dynamic attenuation range of about 30 dB and a rotor section length approximately one-third that of a conventional WR 112 attenuator. Application of the modified law resulted in good agreement between theoretical and measured incremental attenuations over the total dynamic attenuation range.

PLAUNT, J. R.

P01 Adaptive Variable-Length Coding for Efficient Compression of Spacecraft Television Data

R. F. Rice and J. R. Plaunt

IEEE Trans. Commun. Technol., Vol. COM-19, No. 6, pp. 889–897, December 1971

For abstract, see Rice, R. F.

POSNER, E. C.

P02 DSN Progress Report for November–December 1971: Hiding and Covering in a Compact Metric Space

R. J. McEliece and E. C. Posner

Technical Report 32-1526, Vol. VII, pp. 101–105, February 15, 1972

For abstract, see McEliece, R. J.

RATHBUN, T. W.

R01 DSN Progress Report for November–December 1971: High Voltage Control for 400-kW Transmitter

T. W. Rathbun

Technical Report 32-1526, Vol. VII, pp. 139–141, February 15, 1972

This article describes a high-voltage control unit, whose functions are to bring the high voltage to a required level, provide voltage regulation, and reduce beam modulation. This unit, which has been installed in the 400-kW transmitter subsystem at two deep space stations, utilizes all solid-state devices mounted on printed circuit boards. The motorized potentiometer is modularized for ease of replacement. This feature and the printed-circuit-board replacement capability necessitate a minimum of maintenance by the operators, and repairs are made by module replacement at the field level.

REIER, M.

R02 The Response of Covered Silicon Detectors to Monoenergetic Gamma Rays

M. Reier

Technical Memorandum 33-524, January 15, 1972

Measurements have been made of the efficiency in detecting gamma rays of 0.3-, 3-, and 5-mm silicon detectors covered with different absorbers. Calibrated sources covering the range from 279 keV to 2.75 MeV were used. The need for the absorbers to obtain meaningful results and their contribution to the response of the detectors at electron biases from 50 to 200 keV are discussed in detail. It is shown that the results are virtually independent of the atomic number of the absorber. In addition, the role of the absorber in increasing the efficiency with increasing photon energy for low bias settings is demonstrated for the 0.3-mm crystal. Quali-

tative explanations are given for the shapes of all curves of efficiency versus energy at each bias.

RENNELS, D. A.

R03 The STAR (Self-Testing and Repairing) Computer: An Investigation of the Theory and Practice of Fault-Tolerant Computer Design

A. Avižienis, G. C. Gilley, F. P. Mathur, D. A. Rennels, J. A. Rohr, and D. K. Rubin

IEEE Trans. Computers, Vol. C-20, No. 11, pp. 1312–1321, November 1971

For abstract, see Avižienis, A.

RENZETTI, N. A.

R04 DSN Progress Report for November–December 1971: DSN Functions and Facilities

N. A. Renzetti

Technical Report 32-1526, Vol. VII, pp. 1–4, February 15, 1972

The Deep Space Network (DSN), established by the NASA Office of Tracking and Data Acquisition and under the system management and technical direction of JPL, is designed for two-way communications with unmanned spacecraft traveling approximately 16,000 km (10,000 mi) from earth to planetary distances. The objectives, functions, and organization of the DSN are summarized, and its three facilities—the Deep Space Instrumentation Facility, the Ground Communications Facility, and the Space Flight Operations Facility—are described.

R05 Tracking and Data System Final Report for the Mariner Mars 1971 Project

N. A. Renzetti

Technical Memorandum 33-523, Vol. I, March 15, 1972

The Tracking and Data System support for the Mariner Mars 1971 Project was planned and implemented in close cooperation with the project's Mission Operations and Spacecraft Systems. The configuration of each Deep Space Network system supporting the project is described.

Also described are new features of the Tracking and Data System for this project, such as the new Deep Space Network command

system, the high-rate telemetry system, the 4800-bit/s modem high-speed data lines from all deep space stations to the JPL Space Flight Operations Facility and the Goddard Space Flight Center, and the 50,000-bit/s wideband data lines from the Mars Deep Space Station to the Space Flight Operations Facility.

The Tracking and Data System performed prelaunch training and testing and provided support for the Mariner Mars 1971/Mission Operations System training and testing. The facilities of the Air Force Eastern Test Range, the Deep Space Network Compatibility Test Station at Cape Kennedy, and Manned Space Flight Network stations provided flight support coverage at launch and during the near-Earth phase. The Deep Space Network provided the deep-space phase support from the launch date, May 30, 1971, through the first trajectory correction maneuver on June 4, 1971, the end of the period covered in this volume.

Analysis of the support performance shows that all tracking and telemetry data received on Earth were acquired, processed, and delivered to the project. All commands were transmitted successfully.

REY, R. D.

R06 DSN Progress Report for November–December 1971: Automatic Angle Tracking: Angle Error Analysis and Tests

R. D. Rey

Technical Report 32-1526, Vol. VII, pp. 207–212, February 15, 1972

Tests are being developed to measure the angle errors of the 26-m-diameter antenna stations. Analysis is performed in order to define performance requirements. Receiver degradation due to the mean and variance of the angle error is determined using an approximation of the antenna gain pattern. The equation for the angle error variance is determined. Measured data were compared with the theoretical results and were found to agree well.

RHEIN, R. A.

R07 New Polymer Systems: Chain Extension By Dianhydrides

R. A. Rhein and J. D. Ingham

JPL Quarterly Technical Review, Vol. 1, No. 4, pp. 97–103, January 1972

New highly stable polymers are required for materials applications on future long-term planetary missions. This article presents the

results of a systematic investigation on the use of anhydrides to prepare stable elastomeric materials using mild reaction conditions. The three anhydrides investigated were found to provide effective chain extension of hydroxy-terminated poly(alkylene oxides) and poly(butadienes). These were tetrahydrofuran tetracarboxylic dianhydride, pyromellitic dianhydride, and benzophenone tetracarboxylic dianhydride. The most effective catalyst investigated was ferric acetylacetonate, which resulted in chain extension at 333 K (60°C). A novel feature of these anhydride reactants is that they are difunctional as anhydrides, but tetrafunctional if conditions are selected that lead to reaction of all carboxyl groups. Therefore, chain extension can be effected and then followed by crosslinking via the residual carboxyl groups.

RHO, J. H.

R08 Absence of Porphyrins in an Apollo 12 Lunar Surface Sample

J. H. Rho, A. J. Bauman, T. F. Yen (University of Southern California), and J. Bonner (California Institute of Technology)

Proceedings of the Second Lunar Science Conference, Houston, Texas, January 11–14, 1971, Vol. 2, pp. 1875–1877, The M.I.T. Press, Cambridge, 1971

As described in this article, no porphyrins were found in 15 g of the Apollo 12 lunar fines from the Ocean of Storms under the conditions in which porphyrins would have been detected had they been present in amounts as small as 10^{-14} mole. An instrumental artifact at 600, 630, and 680 nm that resembled porphyrin peaks was observed in the control sample in which no porphyrins were present. This was produced by the interaction of grating anomalies with light scattering materials and was associated with a definite plane of polarization. When the data from the grating monochromator were corrected, or when prism monochromator data were used, no fluorescence attributable to the presence of porphyrins was found.

However, in the organic phase of the lunar sample extract, species which fluoresced at 365 to 380 nm when activated at 300 nm were found to be present. The corresponding aqueous phase of the sample extract also contained a material which exhibits a fluorescence maximum at 415 nm. All fluorescence attributable to organic materials in the lunar sample was also found in the Lunar Receiving Laboratory sand blank in equivalent amounts.

RICE, R. F.

R09 Adaptive Variable-Length Coding for Efficient Compression of Spacecraft Television Data

R. F. Rice and J. R. Plaunt

IEEE Trans. Commun. Technol., Vol. COM-19, No. 6, pp. 889–897, December 1971

An adaptive variable-length coding system is presented. Although developed primarily for the proposed Grand Tour missions, many features of this system clearly indicate a much wider applicability.

Using sample-to-sample prediction, the coding system produces output rates within 0.25 bit/picture element (pixel) of the one-dimensional difference entropy for entropy values ranging from 0–8 bits/pixel. This is accomplished without the necessity of storing any code words. Performance improvements of 0.5 bit/pixel can be simply achieved by utilizing previous line correlation.

A basic compressor, using concatenated codes, adapts to rapid changes in source statistics by automatically selecting one of three codes to use for each block of 21 pixels. The system adapts to less frequent, but more dramatic, changes in source statistics by adjusting the mode in which the basic compressor operates on a line-to-line basis. Furthermore, the compression system is independent of the quantization requirements of the pulse-code modulation system

RICHARDS, J. H.

R10 A Simple Electrostatic Model for the Chromatographic Behavior of the Primary Dithizonates

A. J. Bauman and J. H. Richards

Separ. Sci., Vol. 6, No. 5, pp. 715–725, October 1971

For abstract, see Bauman, A. J.

RIEBLING, R. W.

R11 Experimental Evaluation of High-Thrust, Throttleable, Monopropellant Hydrazine Reactors

R. W. Riebling and G. W. Kruger

Technical Report 32-1551, March 1, 1972

Throttleable monopropellant hydrazine catalytic reactors of a size applicable to a planetary landing vehicle have been designed, fabricated, and tested. An experimental evaluation of two 2670-N

(600-lbf) reactor designs has been conducted. The steady-state and dynamic characteristics of the thruster/valve combinations have been determined. The results of the testing, including the engine characteristic velocity, smoothness of combustion, insensitivity to heat sterilization, and response during various simulated duty cycles, are presented and discussed. No problems of a fundamental nature were encountered as a result of rapid dynamic throttling of these large hydrazine reactors.

RINDERLE, E. A.

R12 **DSN Progress Report for November–December 1971: A Comparison of Cowell's Method and a Variation-of-Parameters Method for the Computation of Precision Satellite Orbits: Addendum 1**

S. S. Dallas and E. A. Rinderle

Technical Report 32-1526, Vol. VII, pp. 32–36, February 15, 1972

For abstract, see Dallas, S. S.

ROHR, J. A.

R13 **The STAR (Self-Testing and Repairing) Computer: An Investigation of the Theory and Practice of Fault-Tolerant Computer Design**

A. Avižienis, G. C. Gilley, F. P. Mathur, D. A. Rennels, J. A. Rohr, and D. K. Rubin

IEEE Trans. Computers, Vol. C-20, No. 11, pp. 1312–1321, November 1971

For abstract, see Avižienis, A.

ROSCHKE, E. J.

R14 **Partially Ionized Gas Flow and Heat Transfer in the Separation, Reattachment, and Redevelopment Regions Downstream of an Abrupt Circular Channel Expansion**

L. H. Back, P. F. Massier, and E. J. Roschke

Trans. ASME, Ser. C: J. Heat Transf., Vol. 94, No. 1, pp. 119–127, February 1972

For abstract, see Back, L. H.

ROSENTHAL, L. A.

R15 Electrothermal Follow Display Apparatus for Electroexplosive Device Testing

L. A. Rosenthal (Rutgers University) and V. J. Menichelli

Technical Report 32-1554, March 15, 1972

By employing a self-balancing bridge, it is possible to ascertain the electrothermal and nonlinear behavior of an electroexplosive device. A sinusoidal current is passed through the device that provides a signal in the form of a unique Lissajous display. This display can be qualitatively evaluated, and abnormal units can be readily detected. This technique for evaluating electroexplosive devices is described in this report.

R16 Fault Determinations in Electroexplosive Devices by Nondestructive Techniques

V. J. Menichelli and L. A. Rosenthal (Rutgers University)

Technical Report 32-1553, March 15, 1972

For abstract, see Menichelli, V. J.

ROURKE, K. H.

R17 DSN Progress Report for November–December 1971: Improved Navigation Capability Utilizing Two-Station Tracking Techniques for a Low-Declination Distant Spacecraft

K. H. Rourke and V. J. Ondrasik

Technical Report 32-1526, Vol. VII, pp. 51–60, February 15, 1972

This article presents the results of an uncompromised accuracy analysis study investigating the advantages of using two-station simultaneous tracking (quasi very long baseline interferometry) techniques to determine the far-approach orbit of a distant spacecraft at a low declination angle. The analysis is restricted to batch filtering techniques, but includes the effects of unmodeled spacecraft accelerations. By properly processing the simultaneous doppler and simultaneous range data, the errors resulting from the low-declination geometry are reduced by a factor of two to four, and the errors resulting from unmodeled spacecraft accelerations are reduced by two orders of magnitude.

R18 Application of New Radio Tracking Data Types to Critical Spacecraft Navigation Problems

V. J. Ondrasik and K. H. Rourke

JPL Quarterly Technical Review, Vol. 1, No. 4, pp. 116–132, January 1972

For abstract, see Ondrasik, V. J.

ROWE, W. M.

R19 Stress Analysis and Design of Silicon Solar Cell Arrays and Related Material Properties

A. M. Salama, W. M. Rowe, and R. K. Yasui

Technical Report 32-1552, March 1, 1972

For abstract, see Salama, A. M.

RUBIN, D. K.

R20 The STAR (Self-Testing and Repairing) Computer: An Investigation of the Theory and Practice of Fault-Tolerant Computer Design

A. Avižienis, G. C. Gilley, F. P. Mathur, D. A. Rennels, J. A. Rohr, and D. K. Rubin

IEEE Trans. Computers, Vol. C-20, No. 11, pp. 1312–1321, November 1971

For abstract, see Avižienis, A.

RUPE, J. H.

R21 Liquid-Phase Mixing of Bipropellant Doublets

F. W. Hoehn, J. H. Rupe, and J. G. Sotter

Technical Report 32-1546, February 15, 1972

For abstract, see Hoehn, F. W.

SALAMA, A. M.

S01 Stress Analysis and Design of Silicon Solar Cell Arrays and Related Material Properties

A. M. Salama, W. M. Rowe, and R. K. Yasui

Technical Report 32-1552, March 1, 1972

Mechanical failures that may arise in components of composite solar cell arrays in a thermal environment can be avoided by

properly selecting compatible material for the components and introducing certain geometric changes in a proposed design. This report provides the solar cell array designer with a rational systematic approach. A prerequisite to this approach is the characterization of material properties at different temperatures. Significant data were obtained for the thermal behavior of the silicon solar cell material and adhesives. Upon determining the mechanical and thermal material properties of the components of the solar cell array, utilizing a finite-element idealization for predicting the stress fields in the components, and employing the von Mises failure criterion, potential failure areas in various design configurations in a given thermal environment can be identified. Guidelines and means to optimize a given design are illustrated by two examples.

SCHORN, R. A. J.

S02 High Dispersion Spectroscopic Studies of Mars: V. A Search for Oxygen in the Atmosphere of Mars

J. S. Margolis, R. A. J. Schorn, and L. D. G. Young

Icarus, Vol. 15, No. 2, pp. 197–203, October 1971

For abstract, see Margolis, J. S.

SCHURMEIER, H. M.

S03 The 1969 Mariner View of Mars

H. M. Schurmeier

Proceedings of the Twenty-First International Astronautical Congress, Constance, Germany, October 4–10, 1970, pp. 193–210, North-Holland Publishing Co., Amsterdam, 1971

The second step in the U.S. program to explore Mars by spacecraft was completed by the Mariner mission in 1969. This article presents a brief summary of that mission, highlighting the planetary encounter and discussing the various scientific experiments. The scientific results analyzed to date are also summarized.

SEAMAN, C. H.

S04 Astronomical Infrared Spectroscopy With a Connes-Type Interferometer: I. Instrumental

R. Beer, R. H. Norton, and C. H. Seaman

Rev. Sci. Instr., Vol. 42, No. 10, pp. 1393–1403, October 1971

For abstract, see Beer, R.

SEIDEL, B. L.

S05 Summary of Mariner 6 and 7 Radio Occultation Results on the Atmosphere of Mars

A. J. Kliore, G. Fjeldbo, and B. L. Seidel

Space Research XI, pp. 165–175, Akademie-Verlag, Berlin, 1971

For abstract, see Kliore, A. J.

SHAFER, J. I.

S06 Initiation System for Low Thrust Motor Igniter

L. D. Strand, D. P. Davis, and J. I. Shafer

Technical Memorandum 33-520, January 1, 1972

For abstract, see Strand, L. D.

S07 Solid-Propellant Motors for High-Incremental-Velocity Low-Acceleration Maneuvers in Space

J. I. Shafer

Technical Memorandum 33-528, March 1, 1972

Recent advancements in motor technology offer promise of extending the applicability of solid-propellant rockets into a regime of high-performance long-burning tasks beyond the capability of existing motors. Successful static test firings have demonstrated the feasibility of: (1) utilizing fully case-bonded end-burning propellant charges without mechanical stress relief, (2) using an all-carbon radiative nozzle markedly lighter than the flight-weight ablative nozzle it replaces, and (3) producing low spacecraft acceleration rates during the thrust transient through a controlled-flow igniter that promotes operation beyond the L^* combustion limit. It remains now to show that a 350-kg-sized motor, with all features integrated, performs reliably and produces the predicted motor performance, a mass fraction of 0.92 with a vacuum specific impulse of 2840 N/kg.

SHINOZUKA, M.

S08 On the First Excursion Probability in Stationary Narrow-Band Random Vibration

J.-N. Yang and M. Shinozuka (Columbia University)

Trans. ASME, Ser. E: J. Appl. Mech., Vol. 38, No. 4, pp. 1017–1022, December 1971

For abstract, see Yang, J.-N.

SHOEMAKE, G. R.

S09 Rare Gases of the Atmosphere: Gas Chromatography Using a Thermal Conductivity Detector and a Palladium Transmodulator

J. E. Lovelock, P. G. Simmonds, and G. R. Shoemake

Anal. Chem., Vol. 43, No. 14, pp. 1958-1961, December 1971

For abstract, see Lovelock, J. E.

SIEGMETH, A. J.

S10 DSN Progress Report for November–December 1971: Pioneer Mission Support

A. J. Siegmeth

Technical Report 32-1526, Vol. VII, pp. 5–16, February 15, 1972

The Pioneer F and G missions are planned to extend the exploration of the solar system toward the outer planets. The major objectives will be the first penetration of the asteroid belt and a Jupiter flyby. Since Jupiter missions require new types of solar orbits, some adaptations of the tracking and data acquisition capabilities and resources are necessary to meet effectively the requirements of these new challenges. The Pioneer F and G mission characteristics and the near-Earth and deep-space phase support plans are delineated in this article.

SILVER, R. H.

S11 A Study of the Frictional and Stick–Slip Behavior of Magnetic Recording Tapes

S. H. Kalfayan, R. H. Silver, and J. K. Hoffman

Technical Report 32-1548, April 1, 1972

For abstract, see Kalfayan, S. H.

SIMKO, G. J.

S12 Dry-Heat Resistance of Bacillus Subtilis Var. Niger Spores on Mated Surfaces

G. J. Simko, J. D. Devlin, and M. D. Wardle

Appl. Microbiol., Vol. 22, No. 4, pp. 491–495, October 1971

Bacillus subtilis var. *niger* spores were placed on the surfaces of test coupons manufactured from typical spacecraft materials (stainless steel, magnesium, titanium, and aluminum). These coupons were then juxtaposed at the inoculated surfaces and subjected to test pressures of 0, 1000, 5000, and 10,000 psi. Tests were conducted in ambient, nitrogen, and helium atmospheres. While under the test pressure condition, the spores were exposed to 125°C for intervals of 5, 10, 20, 50, or 80 min, with survivor data being subjected to a linear regression analysis that calculated decimal reduction times. Differences in the dry-heat resistance of the test organism resulting from pressure, atmosphere, and material were observed.

SIMMONDS, P. G.

S13 Rare Gases of the Atmosphere: Gas Chromatography Using a Thermal Conductivity Detector and a Palladium Transmodulator

J. E. Lovelock, P. G. Simmonds, and G. R. Shoemake

Anal. Chem., Vol. 43, No. 14, pp. 1958–1961, December 1971

For abstract, see Lovelock, J. E.

SIMON, M. K.

S14 On the Selection of an Optimum Design Point for Phase-Coherent Receivers Employing Band-Pass Limiters

M. K. Simon

JPL Quarterly Technical Review, Vol. 1, No. 4, pp. 69–77, January 1972

In the design of phase-coherent receivers employing band-pass limiters, it is customary to specify system performance relative to its value at a fixed design point. For a given design point, an

optimum tradeoff can be found between the power allocated to the carrier and the sideband signals. This article describes an attempt to further improve the performance of such coherent carrier systems by optimizing the design point based upon a given practical optimizing criterion. The single-channel system is treated in detail, and a brief discussion is given on how to extend the technique to a two-channel system.

SIMON, W.

S15 Nozzle Exhaust Plume Backscatter Experiment Using the JPL Molsink Facility

W. Simon

JPL Quarterly Technical Review, Vol. 1, No. 4, pp. 89–96, January 1972

The flow field of gases and scattered particulates in the forward direction from a rocket nozzle is not presently predictable on a quantitative basis. Qualitative tests have been made with water injected through the nozzle wall and the droplet trajectories observed photographically. These tests were conducted for nozzles where the boundary layer is a significant portion of the flow. The tests indicated that both gases and particulate matter will be found in the region outside of the plume boundaries that can be calculated using current analytical techniques. A test program is being conducted in the JPL Molsink facility to measure the distribution of exhaust gases from small nozzles using an electron beam/photomultiplier system and a matrix of quartz crystal microbalances. Analysis of data from these tests, using nitrogen, will result in a better understanding of the backscattering flow field. Calibration tests of the Molsink, using simulated hydrazine exhaust product gas mixtures, have also been conducted, and future tests with small hydrazine thrusters are being considered. The test program and results of the pumping calibration tests with hydrazine (simulated hydrazine exhaust products) are reported.

SINCLAIR, W. S.

S16 Simultaneous Solution for the Masses of the Principal Planets From Analysis of Optical, Radar, and Radio Tracking Data

J. H. Lieske, W. G. Melbourne, D. A. O'Handley, D. B. Holdridge, D. E. Johnson, and W. S. Sinclair

Celest. Mech., Vol. 4, No. 2, pp. 233–245, October 1971

For abstract, see Lieske, J. H.

SJOGREN, W. L.

S17 A Surface-Layer Representation of the Lunar Gravitational Field

L. Wong (Aerospace Corporation), G. Buechler (Aerospace Corporation), W. Downs (Aerospace Corporation), W. L. Sjogren, P. M. Muller, and P. Gottlieb

J. Geophys. Res., Vol. 76, No. 26, pp. 6220–6236, September 10, 1971

For abstract, see Wong, L.

S18 Lunar Gravity Estimate: Independent Confirmation

W. L. Sjogren

J. Geophys. Res., Vol. 76, No. 29, pp. 7021–7026, October 10, 1971

Reduction of 2½ days of Lunar Orbiter 4 radio tracking data has provided an independent estimate of the low-degree spherical harmonic coefficients in the lunar potential model. The estimate is in good agreement with previous results and confirms that the Moon is essentially homogeneous. These doppler data, never incorporated in other gravity estimates, were obtained at relatively high spacecraft altitudes (2700–6000 km). These high-altitude data allowed the model to fit to the noise level of 1 mm/s unlike previous results, where systematic residuals of tens of millimeters per second occurred, owing to local gravity anomalies detectable at low spacecraft altitudes (≈100 km).

SLAUGHTER, D. W.

S19 DSN Progress Report for November–December 1971: Hi-Rel Integrated Circuit Packaging Development

D. W. Slaughter

Technical Report 32-1526, Vol. VII, pp. 113–123, February 15, 1972

Standardized modular hardware for the packaging of Deep Space Instrumentation Facility integrated circuit logic systems is described. The status of development is reported, and a schedule is given for the production of station-quality hardware.

SMITH, J. G.

S20 Bias and Spread in Extreme Value Theory Measurements of Probability of Error

J. G. Smith

JPL Quarterly Technical Review, Vol. 1, No. 4, pp. 58–68, January 1972

Performance tests of communication systems characterized by low bit rates and high data reliability requirements frequently utilize classical extreme value theory (EVT) to avoid the excessive test times required by bit error rate (BER) tests. If the underlying noise is gaussian or perturbed gaussian, EVT will produce results either biased or with excessive spread if an insufficient number of test samples are used. This article examines EVT to explain the cause of the bias and spread, gives experimental verification, and points out procedures that minimize these effects. Even under these conditions, however, EVT test results are not particularly more significant than BER test results.

SOTTER, J. G.

S21 Liquid-Phase Mixing of Bipropellant Doublets

F. W. Hoehn, J. H. Rupe, and J. G. Sotter

Technical Report 32-1546, February 15, 1972

For abstract, see Hoehn, F. W.

SRIDHAR, R.

S22 Analytical Methods for Performance Evaluation of Nonlinear filters

A. K. Bejczy and R. Sridhar (University of California, Los Angeles)

J. Math. Anal. Appl., Vol. 36, No. 3, pp. 477–505, December 1971

For abstract, see Bejczy, A. K.

STELZRIED, C. T.

S23 A Precision Compact Rotary Vane Attenuator

T. Y. Otoshi and C. T. Stelzried

IEEE Trans. Microwave Theor. Techniq., Vol. MTT-19, No. 11, pp. 843–854, November 1971

For abstract, see Otoshi, T. Y.

STIVER, R. A.

S24 DSN Progress Report for November–December 1971: Mark IIIA IBM Computer Configuration Expansion

R. A. Stiver

Technical Report 32-1526, Vol. VII, pp. 126–130, February 15, 1972

In order to meet Pioneer Project requirements while continuing to support the Mariner Mars 1971 mission, it has been necessary to expand the Space Flight Operations Facility computer configuration. This expansion has been implemented in the following areas: high-speed data input/output interface, display control and switching, subchannel extension and user device switching, and magnetic tape drives. Expansion was accomplished with minimum impact on operating system design.

STRAND, L. D.

S25 Initiation System for Low Thrust Motor Igniter

L. D. Strand, D. P. Davis, and J. I. Shafer

Technical Memorandum 33-520, January 1, 1972

A test program was carried out to demonstrate an igniter motor initiation system utilizing the bimetallic material Pyrofuze (trademark of Pyrofuze Corporation) for a solid-propellant rocket with controlled low rate of thrust buildup. The program consisted of a series of vacuum ignition tests using a slab burning window motor that simulated the principal initial ballistic parameters of the full-scale igniter motor. A Pyrofuze/pyrotechnic igniter system was demonstrated that uses a relatively low electrical current level for initiation and that eliminates the necessity of a pyrotechnic squib, with its accompanying accidental firing hazards and the typical basket of pyrotechnic pellets. The Pyrofuze ignition system does require an initial constraining of the igniter motor nozzle flow, and, at the low initiating electrical current level, the ignition delay time of this system was found to be quite sensitive to factors affecting the local heat generation or loss rates.

SWARD, A.

S26 Measurement of the Power Spectral Density of Phase of the Hydrogen Maser

A. Sward

JPL Quarterly Technical Review, Vol. 1, No. 4, pp. 30–33, January 1972

Hydrogen masers are being developed by JPL to satisfy the needs of the Deep Space Network for improved frequency standards in order to achieve better timing accuracies, reduced doppler residuals, and lower phase noise in the tracking system. Performance data for the JPL hydrogen masers are given in two forms: time-domain performance, useful for analyzing time-keeping systems and doppler systems; and frequency-domain performance, useful for analyzing tracking systems. Particular attention is given to frequency-domain performance, as obtained from both time-domain measurements and direct measurements.

THOMAS, J. B.

T01 DSN Progress Report for November–December 1971: An Analysis of Long Baseline Radio Interferometry

J. B. Thomas

Technical Report 32-1526, Vol. VII, pp. 37–50, February 15, 1972

The VLBI (very long baseline interferometer) cross-correlation procedure is analyzed for both a natural point source and a completely incoherent extended source. The analysis is based on a plane wave description of a radio signal that consists of stationary random noise. A formulation of the time delay is developed on the basis of plane wave phase. A brief discussion is devoted to small time delay corrections that are generated by relativistic differences in clock rates in the various coordinate frames. The correlation analysis, which includes electronic factors such as amplitude and phase modulation and the heterodyne process, leads to expressions for fringe amplitude and fringe phase. It is shown that the cross-correlation function for an extended source is identical to the point-source expression if one adjusts the fringe amplitude to include the transform of the brightness distribution. Examples of diurnal paths in the u–v plane are presented for various baselines and source locations. Finally, delay and delay rate measurement accuracy is briefly discussed.

THOMPSON, T. W.

T02 Map of Lunar Radar Reflectivity at 7.5-m Wavelength

T. W. Thompson (Cornell-Sydney University Astronomy Center)

Icarus, Vol. 13, No. 3, pp. 363–370, November 1970

The radar reflectivity of a substantial portion of the Earth-visible lunar surface has been mapped at a wavelength of 7.5 m. This mapping—the first to use interferometric techniques in lunar observations—demonstrated that delay-doppler mapping of the Moon is possible at wavelengths of several meters. In the map that was obtained, the maria at a given angle of incidence had echo powers approximately half of those of highlands at the same angle of incidence. Also, an enhancement associated with the lunar crater Tycho was observed.

TOTH, R. A.

T03 Global Studies of Atmospheric Pollutants and Trace Constituents

R. A. Toth (California Institute of Technology) and
C. B. Farmer (California Institute of Technology)

AIAA Preprint 71-1109, ACS (American Chemical Society)/AIAA (American Institute of Aeronautics and Astronautics)/EPA (Environmental Protection Agency)/IEEE (Institute of Electrical and Electronic Engineers)/ISA (Instrument Society of America)/NASA (National Aeronautics and Space Administration)/NOAA (National Oceanographic and Atmospheric Administration) Joint Conference on Sensing of Environmental Pollutants, Palo Alto, California, November 8–10, 1971

A high-speed, high-resolution, Fourier interferometer operating in the 1- to 5-μ spectral region can best meet the needs for remotely detecting and monitoring various molecular species in the atmosphere. An operational breadboard version of the instrument exists. Spectra obtained from ground sites in the Los Angeles area demonstrate the presence of several gases in the atmosphere. Spectra in the 2.1- and 2.3-μ regions are presented, from which relative abundances of carbon dioxide and carbon monoxide are derived. Ground-based operations and aircraft flights with the present instrument verify the potential operational capacity for a satellite instrument. A discussion is presented on the use of the instrument from a spacecraft.

T04 Line Strengths of N_2O in the 2.9 Micron Region

R. A. Toth

J. Molec. Spectrosc., Vol. 40, No. 3, pp. 588–604, December 1971

The line strengths of the bands 10^01–00^00, 02^01–00^00, and 11^11–01^10 of N_2O have been measured with low sample pressures and high resolution (0.031–0.33 cm^{-1}). The data are analyzed to determine the band strengths and dipole moment matrix elements. At 300°K the strengths of the two Σ–Σ bands in order of increasing frequency are 1.77 and 36.9 cm^{-2}-atm^{-1}. The band strength of the π–π band is 4.25 cm^{-2}-atm^{-1} at 300°K. Five lines of the band 06^00–00^00 and two lines of the 06^0–00^00 bands have been observed in the spectrum of the 10^01–00^00 band. The strengths and frequencies of these lines have been measured. These results are used in conjunction with perturbation theory to determine the Fermi interaction term W. Molecular constants and the band strength of the 06^00–00^00 band are obtained from W and the data. The band strength of the 06^00–00^00 band is 0.0092 cm^{-2}-atm^{-1} at 300°K.

T05 Self-Broadened and N_2 Broadened Linewidths of N_2O

R. A. Toth

J. Molec. Spectrosc., Vol. 40, No. 3, pp. 605–615, December 1971

The self and N_2-broadened linewidths of N_2O have been measured directly in the 10^01–00^00 and 02^01–00^00 bands of N_2O at 297°K with a resolution of 0.03 cm^{-1}. The experimental results are compared with linewidths calculated from Anderson's impact theory as amplified by Tsao and Curnutte. The agreement between experiment and theory is good for both types of broadening. Best-fit values for the quadrupole moments and hard-sphere diameters of N_2O and N_2 are listed and compared with previous values. The best-fit values were used to calculate the N_2O + N_2 linewidths at temperatures of 180, 220, and 260°K.

TSAY, F.-D.

T06 Ferromagnetic Resonance of Lunar Samples

F.-D. Tsay (California Institute of Technology),
S. I. Chan (California Institute of Technology), and
S. L. Manatt

Geochim. Cosmochim. Acta, Vol. 35, No. 9, pp. 865–875, September 1971

Evidence is presented to show that the electron-spin-resonance spectra observed for a selection of Apollo 11 lunar samples arise from the ferromagnetic centers consisting of metallic Fe. A model study to simulate the polycrystalline spectra has been carried out, from which it was possible to ascertain with some degree of certainty the size and shape of the ferromagnetic centers as well as the metallic iron content. Some variations in the metallic Fe content have been noted in these samples, e.g., between rocks and fine soil.

T07 Magnetic Resonance Studies of Apollo 11 and Apollo 12 Samples

F.-D. Tsay (California Institute of Technology),
S. I. Chan (California Institute of Technology), and
S. L. Manatt

Proceedings of the Second Lunar Science Conference, Houston, Texas, January 11–14, 1971, Vol. 3, pp. 2515–2528, The M.I.T. Press, Cambridge, 1971

This article describes the electron-spin-resonance (ESR) studies at both X-band (9.5 GHz) and K-band (34.8 GHz) frequencies that have been carried out on a selection of Apollo 11 and Apollo 12 lunar samples. On the basis that no significant temperature dependence of the absorption intensity is noted, together with the result that the signal intensity is at least three orders of magnitude greater than that expected for possible paramagnetism, the broad, asymmetric resonance signal centered at $g = 2.09 \pm 0.03$ has been assigned to ferromagnetic centers. A model study to simulate the polycrystalline spectra using computer simulation techniques has been carried out, from which it was possible to ascertain with some degree of certainty the size and shape of the ferromagnetic centers and to ascertain that the ferromagnetism is due to metallic Fe particles. Metallic Fe contents have been measured for all lunar samples studied, and these range in concentration from 0.001 to 0.50 wt%. These results suggest an apparent correlation between the metallic Fe contents and the geological and surface exposure ages of the samples.

Weak paramagnetic resonances attributable to octahedrally coordinated Mn^{2+} ions have also been observed in some samples in which the metallic Fe content is either low or partially removed. From the g value (2.002 ± 0.002) and the nuclear hyperfine coupling constant (-95.0 ± 2.0 gauss), it appears that these resonances originate from $Mn(H_2O)_6^{2+}$. No ESR signals ascribable to free

electrons and/or holes, which would be indicative of radiation damage, or Ti^{3+} have been detected in these samples.

VAN DER CAPELLEN, A. G.

V01 Development of a 20-W Solid-State S-Band Power Amplifier

A. G. van der Capellen

JPL Quarterly Technical Review, Vol. 1, No. 4, pp. 43–48, January 1972

As an alternative to the use of traveling-wave-tube amplifiers in spacecraft with long-life mission requirements, JPL is developing a solid-state 20-W S-band power amplifier. Traveling-wave-tube amplifiers have limited reliability because of the relative short life of the cathode and the complexity of the power supply. A solid-state amplifier with an output of 20 W at 2295 MHz, a dc/RF efficiency of 38%, and a gain of 27 dB has been developed. This article describes the physical and electrical performance of the solid-state amplifier.

VON ROOS, O. H.

V02 Method for the Solution of Electromagnetic Scattering Problems for Inhomogeneous Dielectrics as a Power Series in the Ratio (Dimension of Scatterer)/Wavelength

O. H. von Roos

J. Appl. Phys., Vol. 42, No. 11, pp. 4197–4201, October 1971

In this article, the definitive work of Stevenson for the Rayleigh series expansion of electromagnetic scattering from homogeneous scatterers is extended to inhomogeneous scatterers. Furthermore, it is shown that a determination of the strength of the multipoles induced by the incident radiation is sufficient to determine the far field and, therefore, the scattering cross section, without relying on an awkward expansion and subsequent matching of far and near fields. The calculations are thus enormously simplified.

WANG, J. T.

W01 Cold-Welding Test Environment

J. T. Wang

Technical Report 32-1547, February 1, 1972

Spacecraft designers concerned with the development of excessive friction or cold-welding in mechanisms with moving parts operating in space vacuum for an extended period should consider cold-weld qualification tests. To establish requirements for effective test programs, a flight test was conducted, and the results were compared with ground test data from various facilities. Sixteen typical spacecraft material couples were mounted on an experimental research satellite (ERS-20), where a motor intermittently drove the spherical moving specimens across the faces of the flat fixed specimens in an oscillating motion. Friction coefficients were measured over a period of 14-mo orbital time. Surface-to-surface sliding was found to be the controlling factor of generating friction in a vacuum environment. Friction appears to be independent of passive vacuum exposure time.

Prelaunch and postlaunch tests identical to the flight test were performed in a TRW oil-diffusion-pumped ultrahigh vacuum (1.33×10^{-6} N/m^2) chamber. Only 50% of the resultant data agreed with the flight data due to pump oil contamination. Subsequently, identical ground tests were run in the JPL Molsink, a unique ultrahigh vacuum facility, and a TRW ion-pumped vacuum chamber. The agreement (90%) between data from these tests and the flight data established the adequacy of these test environments and facilities.

WARDLE, M. D.

W02 Dry-Heat Resistance of Bacillus Subtilis Var. Niger Spores on Mated Surfaces

G. J. Simko, J. D. Devlin, and M. D. Wardle

Appl. Microbiol., Vol. 22, No. 4, pp. 491–495, October 1971

For abstract, see Simko, G. J.

WELLS, R. A.

W03 DSN Progress Report for November–December 1971: High-Rate Telemetry Preprocessor for the SFOF 360/75 Computers

R. A. Wells

Technical Report 32-1526, Vol. VII, pp. 109–112, February 15, 1972

The concluding phase has been reached for an advanced development task to determine the feasibility of implementing a computer-based system to preprocess digitally encoded block-format-

ted video data at serial rates up to 250 kbits/s. A software model has been completed showing that under typical mission conditions the Space Flight Operations Facility (SFOF) 360/75 primary computer would be virtually preempted by raw video data at this rate. A high-rate telemetry preprocessor or some similar concept would relieve the primary computer in the central processing system of the severe loading that could result from injecting unpreprocessed video information directly into the SFOF 360/75 serial input channels in a real-time or near-real-time environment. A recommendation is made that the technique of video preprocessing be pursued in order to meet the known objectives of future missions.

WILLIAMS, W. F.

W04 Reduction of Near-In Sidelobes Using Phase Reversal Aperture Rings

W. F. Williams

JPL Quarterly Technical Review, Vol. 1, No. 4, pp. 34–42, January 1972

Spacecraft antennas having high gain and extremely low sidelobes will be needed for communications satellites. Low sidelobe performance is needed to isolate beams of multibeam systems using the same carrier frequency (frequency re-use). Because of a limited allowable spectrum for transmission, frequency re-use may be necessary. A technique for reducing near-in lobes by cancellation is described. This technique takes a small portion of the radiation from the antenna aperture and generates the near-in lobes, which are then fed out-of-phase relative to the main signal. Results of sample cases indicate that the first three lobes can be nearly eliminated at a 40% reduction in aperture efficiency.

WINKELSTEIN, R.

W05 DSN Progress Report for November–December 1971: Spectral Estimate Variance Reduction by Averaging Fast-Fourier Transform Spectra of Overlapped Time Series Data

R. Winkelstein

Technical Report 32-1526, Vol. VII, pp. 74–80, February 15, 1972

An analysis is made of the variance of the spectral estimates calculated in the DSN by two methods, namely the correlation method and the Fast Fourier Transform (FFT) method. It is shown that the FFT method using consecutive sequences of data samples produces the same variance as the correlation method. However, a

reduction of over 20% in variance can be obtained by using the FFT method with overlapped sequences of data. A relationship is derived giving the variance reduction as a function of the amount of data sequence overlap.

WINN, F. B.

W06 DSN Progress Report for November–December 1971: Tropospheric Refraction Calibrations and Their Significance on Radio-Metric Doppler Reductions

F. B. Winn

Technical Report 32-1526, Vol. VII, pp. 68–73, February 15, 1972

This article describes the tropospheric refraction algorithm used in the Mariner Mars 1971 tracking data reductions and orbit determination effort; this algorithm differs from models used to support past missions and performs two times better than the stated mission requirement. Although single-pass reductions of doppler tracking data are extremely influenced by tropospheric refraction models, fits to doppler acquired over large time periods, weeks or months, are influenced only slightly, in that the tropospheric refraction corruption of the doppler observables simply is left in the after-the-fit observed minus computed residuals.

WONG, L.

W07 A Surface-Layer Representation of the Lunar Gravitational Field

L. Wong (Aerospace Corporation), G. Buechler (Aerospace Corporation), W. Downs (Aerospace Corporation), W. L. Sjogren, P. M. Muller, and P. Gottlieb

J. Geophys. Res., Vol. 76, No. 26, pp. 6220–6236, September 10, 1971

A surface-layer representation of the lunar gravitational field has been derived dynamically from the analysis of doppler observations on both polar and equatorial lunar orbiters. The force model contained 600 discrete masses located on the mean lunar surface between the approximate boundaries of ±60-deg latitude and ±95-deg longitude. The derived major mascons were generally in agreement with a model based on polar orbits alone. A technique for combining the discrete mass gravitational field for the front side with a spherical harmonics expansion for the back side is described. Harmonic analysis of the resultant field shows that the higher end of the power spectrum roughly follows the decay rule predicted by W. M. Kaula in 1963.

WU, F.

W08 Raman Scattering Cross Section for N_2O_4

C. J. Chen and F. Wu (State University of New York, Buffalo)

Appl. Phys. Lett., Vol. 19, No. 11, pp. 452–453, December 1, 1971

For abstract, see Chen, C. J.

YANG, J.-N.

Y01 Nonstationary Envelope Process and First Excursion Probability

J.-N. Yang

JPL Quarterly Technical Review, Vol. 1, No. 4, pp. 1–12, January 1972

A definition of the envelope of nonstationary random processes is proposed. The establishment of the envelope definition makes it possible to simulate the nonstationary random envelope directly. The envelope statistics, such as the density function, the joint density function, the moment function, and the level crossing rate, relevant to the analyses of the catastrophic failure, fatigue, and crack propagation of structures, are derived. Applications of the envelope statistics to the prediction of structural reliability under random loadings are demonstrated in detail.

Y02 On the First Excursion Probability in Stationary Narrow-Band Random Vibration

J.-N. Yang and M. Shinozuka (Columbia University)

Trans. ASME, Ser. E: J. Appl. Mech., Vol. 38, No. 4, pp. 1017–1022, December 1971

Dealing with a stationary narrow-band gaussian process $X(t)$ with mean zero, this paper derives a number of approximate solutions on the basis of the point-process approach. In particular, upper and lower bounds sharper than those presently available are established, an approximation based on the Markov point process is obtained, and the clump size approach is also used for approximation. These approximations are checked against the results of semisimulations performed elsewhere. Some remarks are also made on the use of the principle of maximum entropy.

YANG, L. C.

Y03 Detonation of Insensitive High Explosives by a Q-Switched Ruby Laser

L. C. Yang and V. J. Menichelli

Appl. Phys. Lett., Vol. 19, No. 11, pp. 473–475, December 1, 1971

Immediate longitudinal detonations have been observed in confined small-diameter columns of PETN, RDX, and tetryl by using a focused *Q*-switched ruby laser. The energy ranged from 0.8 to 4.0 J in a pulse width of 25 ns. A 1000-Å-thick aluminum film deposited on a glass window was used to generate a shock wave at the window-explosive interface when irradiated by the laser. In some cases steady-state detonations were reached in less than 1/2 μs with less than 10% variation in the detonation velocity.

YASUI, R. K.

Y04 Stress Analysis and Design of Silicon Solar Cell Arrays and Related Material Properties

A. M. Salama, W. M. Rowe, and R. K. Yasui

Technical Report 32-1552, March 1, 1972

For abstract, see Salama, A. M.

YEN, T. F.

Y05 Absence of Porphyrins in an Apollo 12 Lunar Surface Sample

J. H. Rho, A. J. Bauman, T. F. Yen (University of Southern California), and J. Bonner (California Institute of Technology)

Proceedings of the Second Lunar Science Conference, Houston, Texas, January 11–14, 1971, Vol. 2, pp. 1875–1877, The M.I.T. Press, Cambridge, 1971

For abstract, see Rho, J. H.

YIP, K. W.

Y06 DSN Progress Report for November–December 1971: Local and Transcontinental Mapping of Total Electron Content Measurements of the Earth's Ionosphere

K. W. Yip and B. D. Mulhall

Technical Report 32-1526, Vol. VII, pp. 61–67,
February 15, 1972

The interchangeability of total electron content data for the purpose of ionospheric calibration of deep space radio metric data, both locally and across the North American Continent, is demonstrated. Comparisons were made between calibrations produced from Faraday rotation data recorded at Stanford and Goldstone in California and at Hamilton in Massachusetts for simulated missions to Mars. The results, in terms of equivalent station location errors, are shown. The averages of the differences between the tracking station spin radius errors are below 1 m with standard deviations of about 1 m for both data sources. The averages of the differences of ionospheric effect on longitude changes are also less than 1 m with uncertainties of 2–3 m. Transcontinental mapping of Faraday rotation measurements is concluded to be a competitive calibration scheme with local mapping. However, because of the large scatter in the longitude changes, the improvement in this coordinate using the electron data from another station is at best marginal.

The geomagnetic latitude factor used in the mapping is also investigated. This factor is found essential to the mapping procedure.

YOKOYAMA, H.

Y07 Isolation and Characterization of Keto-Carotenoids From the Neutral Extract of Algal Mat Communities of a Desert Soil

A. J. Bauman, H. G. Boettger, A. M. Kelly,
R. E. Cameron, and H. Yokoyama (U.S. Department of Agriculture)

Eur. J. Biochem., Vol. 22, No. 2, pp. 287–293,
September 1971

For abstract, see Bauman, A. J.

YOST, E.

Y08 Apollo 12 Multispectral Photography Experiment

A. F. H. Goetz, F. C. Billingsley, J. W. Head (Bellcomm, Inc.), T. B. McCord (Massachusetts Institute of Technology), and E. Yost (Long Island University)

Proceedings of the Second Lunar Science Conference, Houston, Texas, January 11–14, 1971, Vol. 3, pp. 2301–2310, The M.I.T. Press, 1971

For abstract, see Goetz, A. F. H.

YOUNG, L. D. G.

Y09 High Dispersion Spectroscopic Studies of Mars: V. A Search for Oxygen in the Atmosphere of Mars

J. S. Margolis, R. A. J. Schorn, and L. D. G. Young

Icarus, Vol. 15, No. 2, pp. 197–203, October 1971

For abstract, see Margolis, J. S.

Subject Index

Subject Categories

Subjects

Publication Index

Technical Reports

DSN Progress Report for November–December 1971 (Technical Report 32-1526, Vol. VII)

Technical Memorandums

JPL Quarterly Technical Review, Vol. 1, No. 4

Open Literature Reporting

ACS/AIAA/EPA/IEEE/ISA/NASA/NOAA Joint Conference on Sensing of Environmental Pollutants, Palo Alto, California, November 8–10, 1971

Advan. Astronaut. Sci.

AIAA J.

NASA — JPL — Coml., L.A., Calif.

A15 84209

N72-28941

TECHNICAL REPORT STANDARD TITLE PAGE

1. Report No. Vol. 2, No. 1	2. Government Accession No.	3. Recipient's Catalog No.
4. Title and Subtitle JPL QUARTERLY TECHNICAL REVIEW		5. Report Date April 1972 6. Performing Organization Code
7. Author(s) JPL Staff		8. Performing Organization Report No.
9. Performing Organization Name and Address JET PROPULSION LABORATORY California Institute of Technology 4800 Oak Grove Drive Pasadena, California 91103		10. Work Unit No. 11. Contract or Grant No. NAS 7-100 13. Type of Report and Period Covered JPL Quarterly Technical Review
12. Sponsoring Agency Name and Address NATIONAL AERONAUTICS AND SPACE ADMINISTRATION Washington, D.C. 20546		14. Sponsoring Agency Code

15. Supplementary Notes

16. Abstract

The QTR is comprised of two parts: (1) brief technical articles describing recent JPL-sponsored work, and (2) a bibliography of the Laboratory's recently distributed external publications and those open literature articles written under JPL sponsorship.

17. Key Words (Selected by Author(s))	18. Distribution Statement
Not applicable for this type of report	Unclassified -- Unlimited

19. Security Classif. (of this report)	20. Security Classif. (of this page)	21. No. of Pages	22. Price
Unclassified	Unclassified	286	